

**FES Joint Facilities Research Milestone 2010**  
*by the Alcator C-Mod, DIII-D, and NSTX Research Staffs*

**Annual Target:** Conduct experiments on major fusion facilities to improve understanding of the heat transport in the tokamak scrape-off layer (SOL) plasma, strengthening the basis for projecting divertor conditions in ITER. The divertor heat flux profiles and plasma characteristics in the tokamak scrape-off layer will be measured in multiple devices to investigate the underlying thermal transport processes. The unique characteristics of C-Mod, DIII-D, and NSTX will enable collection of data over a broad range of SOL and divertor parameters (e.g., collisionality  $\nu^*$ , beta  $\beta$ , parallel heat flux  $q_{\parallel}$ , and divertor geometry). Coordinated experiments using common analysis methods will generate a data set that will be compared with theory and simulation.

**Quarter 4 Milestone**

Complete necessary experiments, data analysis and associated interpretive modeling. Prepare a joint report on the empirical understanding gained, the connections to edge transport models, and the opportunities for more detailed and extensive comparisons to theory and simulation. Identify critical research areas to improve extrapolation to ITER.

**Completion of 4<sup>th</sup> Quarter Milestone – Brief Summary**

The targeted goal for the fourth quarter was achieved, as documented in the remainder of this report. All three devices find that the mapped heat flux width  $\lambda_q^{\text{mid}}$  varied with plasma current  $I_p^{-\alpha}$ , with the weakest dependence in Alcator C-Mod Enhanced  $D_{\alpha}$  H-mode ( $\alpha=0.17$ ), and stronger dependences in Alcator C-Mod L-modes, and DIII-D and NSTX H-modes (all  $\alpha \geq 1$ ). In addition, all three devices show no dependence of  $\lambda_q^{\text{mid}}$  on power flowing into the scrape-off layer, or on toroidal field.

Modeling of these datasets was done with the SOLT, UEDGE, and XGC-0 codes, as described in the appendices. For ITER, confirmation and understanding of the  $I_p$  scaling is identified as a critical step for projections of its divertor performance.

## EXECUTIVE SUMMARY

### Statement of Overall Goals

The goals of the FY 2010 Joint Research Target were clearly laid out with its wording: “Conduct experiments on major fusion facilities to improve understanding of the heat transport in the tokamak scrape-off layer (SOL) plasma, strengthening the basis for projecting divertor conditions in ITER. The divertor heat flux profiles and plasma characteristics in the tokamak scrape-off layer will be measured in multiple devices to investigate the underlying thermal transport processes. The unique characteristics of C-Mod, DIII-D, and NSTX will enable collection of data over a broad range of SOL and divertor parameters (e.g., collisionality  $\nu^*$ , beta  $\beta$ , parallel heat flux  $q_{\parallel}$ , and divertor geometry). Coordinated experiments using common analysis methods will generate a data set that will be compared with theory and simulation.”

More succinctly, the goal was to improve understanding of SOL thermal transport by measuring heat flux profiles and relevant quantities in Alcator C-Mod, DIII-D, and NSTX. These datasets would serve as the basis for detailed comparisons with models. These high level goals were met, as described below.

### Coordinated Experimental Planning and Analysis

The planning of experiments was accomplished in a coordinated manner through three mechanisms: periodic (approximately monthly) conference calls, group discussions at various domestic meetings (e.g. the American Physical Society meeting in Nov. 2009, the Plasma-Surface Interactions Conference meeting in May 2010), as well as personal visits between participants from different sites. The Edge Coordinating Committee also facilitated planning with dedicated conference calls and a dedicated session at the Transport Task Force meeting. Note that preparatory discussions actually began before in FY 2009, and additional in-depth analysis of these data will continue into FY 2011.

These discussions identified that infrared (IR) thermography would be the central technique used to measure the temperature profiles, from which heat flux would be computed. In addition, the discussions also identified an “integral definition” of the heat flux profile footprint as the best way to facilitate comparison across devices.

Experimentally it was agreed that each facility would measure the parametric dependences of the heat flux footprint on externally controllable parameters, including plasma current ( $I_p$ ), toroidal field ( $B_t$ ), and heating power ( $P_{\text{heat}}$ ), in the high confinement or H-mode. In addition, all three devices would measure the heat flux footprint in a common poloidal cross-sectional shape. Moreover, those experiments in C-Mod and DIII-D would try to also match the normalized dimensionless parameters collisionality  $\nu^*$ , normalized poloidal beta  $\beta_{\text{pol}}$ , and normalized gyroradius  $\rho^*$ , at the separatrix, and possibly at the top of the pedestal,.

### **Diagnostic Preparations**

Each device added and/or upgraded diagnostics to make the critical measurements.

In the Alcator C-Mod, a number of new diagnostic systems were installed to measure tile temperatures and plasma characteristics at the plasma facing surfaces. Specifically, a fast time response IR camera was installed to measure the surface temperature, and new 2-D heat flux calculation algorithms were implemented. In addition, divertor bolometry to measure the radiated power profile was upgraded. Also, a range of new in-vessel sensors were installed to measure tile temperatures and plasma characteristics: 14 calorimeter probes, 10 surface temperature probes, 10 tile thermocouples, and 10 Langmuir probes were commissioned. Substantial effort was placed on cross-calibrating the IR thermography with the thermocouples.

A fast time-response IR camera was recently commissioned in DIII-D, and a substantial in-situ calibration was accomplished. In addition, edge reciprocating probes were refurbished to measure plasma characteristics in the scrape-off layer.

A new fast time-response IR camera was also recently commissioned in NSTX, as well as a new set of high spatial resolution Langmuir probes. In addition, a multi-color capability was developed in house for this camera, to reduce the effect of variable lithium IR emissivity on the absolute temperature calibrations.

### **Experimental Activities**

Dedicated experiments in each facility measured the heat flux profile shapes as a function of  $I_p$ ,  $B_t$ , and  $P_{\text{heat}}$ , in H-mode discharges. All three devices found that the

mapped heat flux width,  $\lambda_q^{\text{mid}}$ , varied with  $I_p^{-\alpha}$ , with the weakest dependence in Alcator C-Mod Enhanced  $D_\alpha$  (EDA) H-mode ( $\alpha \sim 0.2$ ), and stronger dependences in ELMy H-modes in DIII-D ( $\alpha \sim 1.0$  averaged over ELMs, or  $\alpha \sim 1.2$  between ELMs) and NSTX ( $\alpha \sim 1.6$  averaged over ELMs). The weaker dependence in C-Mod might be attributable to the differences in edge stability: edge particle transport in the EDA H-mode in Alcator C-Mod is regulated by a continuous quasi-coherent mode, as opposed to discrete ELMs. Hence the time averaged heat flux profiles in EDA H-mode may be naturally broader. In separate experiments in C-Mod, it was found that  $\alpha \sim 1$  in L-mode discharges. The reason for the stronger dependence in NSTX is under investigation.

In addition, all three devices showed no dependence of  $\lambda_q^{\text{mid}}$  on power flowing into the scrape-off layer, or on  $B_t$ . Additional experiments in DIII-D demonstrated no difference in the footprint width comparing electron cyclotron heating (ECH) and neutral beam heating. Finally additional experiments in NSTX showed that the same trends mentioned above were also observed in ELM-free discharges with lithium conditioning.

### **Modeling Activities**

The data sets described above were modeled with the XGC-0, SOLT, and UEDGE codes. Each of these modeling activities that targeted multiple devices is summarized below, and described in individual sections in the appendices.

Modeling of the narrowing of the heat flux width with  $I_p$  was done with the XGC-0 code for discharges from each device. The XGC-0 is a kinetic, guiding-center code, and it was used to investigate the basic kinetic neoclassical behavior of the heat and particle fluxes on divertor plates in tokamaks with realistic divertor geometries. The simulations of NSTX and DIII-D with neoclassical transport only predict  $\lambda_q^{\text{mid}} \sim I_p^{-1}$ , in reasonable agreement with the observations on those devices; this reduction of the heat flux width is correlated with a reduction of the width of the radial electric field well as  $I_p$  increases. Quantitatively, the predicted neoclassical widths are up to 50% narrower than the measured widths. The addition of neutrals and turbulent diffusive transport tends to broaden the computed heat flux profiles, in closer agreement with data. In addition, a

weaker dependence of the heat flux width on  $I_p$  in the simulation C-Mod follows roughly the experimental observation and is attributed to higher collisionality.

The role of cross-field turbulent heat transport in the midplane SOL was investigated with the SOLT code for both NSTX and C-Mod data. For NSTX the scaling of the near- $\lambda_q^{\text{mid}}$ , with  $P_{\text{heat}}$  and  $I_p$  was investigated. The simulated  $\lambda_q^{\text{mid}}$ , as well as the midplane SOL profiles of density and temperature were compared with gas-puff imaging data, reciprocating Langmuir probe data, and midplane-mapped divertor heat flux data. It was concluded that the midplane turbulence simulated in SOLT explains some, but not all, of the experimentally observed  $\lambda_q^{\text{mid}}$  scaling. Additionally, a new convective cell mechanism that determines the SOL width was identified. In related theoretical work, a transition from a diffusive to a convective SOL heat transport regime was found at critical values of power and connection length. For C-Mod, an EDA H-mode discharge was simulated. The SOLT code produced a heat flux SOL width of about  $\lambda_q \sim 1$  mm, somewhat shorter than the experimental measurement. Most of the edge turbulence was in a single mode with a poloidal wavelength  $\sim 6$  cm, which might be related to the quasi-coherent mode found experimentally in C-Mod EDA H-modes.

The UEDGE 2-D plasma and neutral gas transport code was used to simulate DIII-D and C-Mod dedicated discharges that used a common poloidal cross-section and attempted to match dimensionless parameters near the separatrix. The C-Mod profiles can be matched when plasma drifts are included, and require a particle diffusivity varying with radius; the required cross-field diffusive transport coefficients are quite low, because the plasma drifts provide most of the needed transport. Simulations of the DIII-D discharges as part of this comparison are ongoing. Plasma drifts play a major part in the DIII-D simulations as well.

## Conclusions

For ITER, confirmation and understanding of the  $I_p$  scaling is identified as a critical step for projections of its divertor performance. There does seem to be an increase in the SOL width with minor radius (from C-Mod, to DIII-D and NSTX which have the same minor radius). The extent to which increases in the SOL width that correlate with the machine size/normalized gyroradius offset the adverse  $I_p$  scaling requires additional

work. In this regard, a collaborative effort with European devices (e.g. JET, ASDEX-Upgrade, MAST) would increase the range of device sizes upon which a regression analysis would be based. Finally, the absence of heat-flux width dependences upon power flowing into the SOL and upon toroidal field strength are also important for projections of divertor performance on ITER.

## TABLE OF CONTENTS

Executive Summary	2
C-Mod Contribution (B. Labombard, J.L. Terry, <i>et al.</i> )	8
DIII-D Contribution (C.J. Lasnier, <i>et al.</i> )	55
NSTX Contribution (R. Maingi, <i>et al.</i> )	67
Appendix A: DIII-D PSI 2010 paper (C.J. Lasnier, <i>et al.</i> )	97
Appendix B: DIII-D PSI 2010 paper (M.A. Makowski, <i>et al.</i> )	116
Appendix C: DIII-D PSI 2010 paper (D.N. Hill, <i>et al.</i> )	134
Appendix D: DIII-D IAEA paper (C.J. Lasnier, <i>et al.</i> )	152
Appendix E: DIII-D Interpretive 2-D Modeling (M.E. Rensink, <i>et al.</i> )	163
Appendix F: C-Mod Interpretive 2-D Modeling (G.D. Porter, <i>et al.</i> )	180
Appendix G: Lodestar turbulence modeling (J.R. Myra, <i>et al.</i> )	190
Appendix H: CPES neoclassical modeling (A.Y. Pankni, <i>et al.</i> )	201

## **Boundary Layer Heat Transport Experiments in Alcator C-Mod in Support of the FY2010 US DoE Joint Research Target**

B. LaBombard<sup>1</sup>, J.L. Terry<sup>1</sup>, J.W. Hughes<sup>1</sup>, D. Brunner<sup>1</sup>, J. Payne<sup>1</sup>, M.L. Reinke<sup>1</sup>,  
I. Cziegler<sup>1</sup>, S. Zweben<sup>2</sup>, R. Granetz<sup>1</sup>, M. Greenwald<sup>1</sup>, I.H. Hutchinson<sup>1</sup>, J. Irby<sup>1</sup>,  
Y. Lin<sup>1</sup>, B. Lipschultz<sup>1</sup>, Y. Ma<sup>1</sup>, E.S. Marmor<sup>1</sup>, N. Mucic<sup>1</sup>, W. Parkin<sup>1</sup>, S. Pierson<sup>1</sup>,  
R. Rosati<sup>1</sup>, R. Rowan<sup>3</sup>, H. Savelli<sup>1</sup>, J. Stillerman<sup>1</sup>, N. Tsujii<sup>1</sup>, R. Vieira<sup>1</sup>, G. Wallace<sup>1</sup>,  
D.G. Whyte<sup>1</sup>, S. Wolfe<sup>1</sup>, S. Wukitch<sup>1</sup>, G. Wurden<sup>4</sup>, J. Zaks<sup>1</sup> and the Alcator C-Mod  
Team

<sup>1</sup>*MIT Plasma Science and Fusion Center, Cambridge, MA 02139 USA*

<sup>2</sup>*Princeton Plasma Physics Laboratory, P.O. Box 451, Princeton, NJ 08540 USA*

<sup>3</sup>*University of Texas, Fusion Research Center, Austin, TX 78712*

<sup>4</sup>*Los Alamos National Laboratory, Los Alamos, NM 87545 USA*

September 2010

Physics-based transport models that can accurately simulate heat-flux power widths in the tokamak boundary plasma are lacking at the present time. Existing empirical scaling laws for heat-flux power widths appear to be ambiguous and not well formulated. Yet this information is of fundamental importance for ITER and of utmost importance for DEMO, where the lifetime of the first-wall will be a limiting factor. Recognizing this gap in understanding, Alcator C-Mod, in coordination with DIII-D and NSTX, conducted experiments in FY2010 aimed at characterizing divertor heat flux ‘footprints’ and their connections to conditions in the boundary and core plasmas. This research was performed in support of a Joint Research Target (JRT) established by the US DoE Office of Fusion Energy Sciences.†

This report summarizes Alcator C-Mod’s contributions to the JRT and constitutes completion of the FY2010 milestone.

---

†**US DoE Office of Fusion Energy Sciences JRT for FY2010:** Conduct experiments on major fusion facilities to improve understanding of the heat transport in the tokamak scrape-off layer (SOL) plasma, strengthening the basis for projecting divertor conditions in ITER. The divertor heat flux profiles and plasma characteristics in the tokamak SOL will be measured in multiple devices to investigate the underlying thermal transport processes. The unique characteristics of C-Mod, DIII-D, and NSTX will enable collection of data over a broad range of SOL and divertor parameters (e.g., collisionality, beta, parallel heat flux, and divertor geometry). Coordinated experiments using common analysis methods will generate data that will be compared with theory and simulation.

## 1. Project Overview

The physics of boundary layer heat transport and its associated ‘heat flux footprint’ at divertor strike-point regions is of fundamental importance for the attainment of magnetic fusion energy production, yet it is poorly understood. Recognizing this fact, Alcator C-Mod initiated an aggressive program in FY2009 aimed at contributing to this key science area, first by developing an extensive array of heat flux instrumentation for C-Mod’s outer divertor strike point region and second by performing dedicated experiments to explore boundary layer heat transport. This program was designed to not only support the FY2010 DoE JRT milestone but also to expand the breadth of C-Mod’s boundary layer research capabilities.

### 1.1 Time-line of JRT research activities

June 25, 2008 – Initial planning meeting for C-Mod’s new outer divertor heat flux instrumentation, targeting installation during the FY2009 extended maintenance break

July 2008 to May 2009 – Extended C-Mod maintenance break. Divertor heat-flux instrumentation, ‘ramped tiles’ and IR camera systems installed; new CPCI-based data acquisition system and infrastructure installed for embedded sensors and Langmuir probes.

July 2009 – Commissioning of new divertor heat flux instrumentation (MP#557)

August to October 2009 – Initial L-mode heat flux experiments (MP#570)

October 8, 2009 – FY2010 JRT milestone officially established by US DoE OFES

November 2009 to February 2010 – Development of C-Mod’s IR image stabilization algorithms and heat flux analysis software packages; Development of C-Mod EDA H-mode mini-proposal (MP#591), in coordination with NSTX and DIII-D

February 9 and 11, 2010 – DIII-D joint facility experiments (D3DMP No. 2010-62-02), including DIII-D/C-Mod ‘similarity discharges’

February 12 to March 10, 2010 – C-Mod EDA H-mode joint facility experiments (MP#591), including DIII-D/C-Mod ‘similarity discharges’

April to June 2010 – C-Mod up-to-air maintenance break. Refurbished and installed improved divertor ‘ramped tiles’ and heat flux sensor arrays. New ramped-tile Langmuir probes installed. Initial analysis of EDA H-mode data performed; data published at PSI and HTPD conferences.

July 2010 – C-Mod EDA H-mode data ported to modelers (CPES, Lodestar, LLNL) and distributed to JRT team.

July to August 2010 – Second round of L-mode heat flux experiments with repaired/improved diagnostic set (MP#570)

August 2010 – Final set of EDA H-mode experiments (MP#591)

October 2010 – Final JRT report (including this document) sent to US DoE OFES

## 1.2 Key results

- Divertor heat flux profiles exhibit a two zone structure: a narrow heat flux channel near the strike point (FWHM  $\sim 2$  mm) and a tail in the far scrape-off layer, similar to other tokamaks (section 5.1).
- C-Mod's heat flux widths challenge empirical scalings that are currently used to project to ITER. Widths based on Kirnev *et al.* [1] are a factor of  $\sim 4$  too small while those from Loarte *et al.* [2] appear to be more consistent (section 5.2).
- Yet, C-Mod's favorable comparison with the Loarte scaling appears fortuitous. Neither scaling captures the dependencies seen in C-Mod's heat flux widths, i.e., no dependence on  $P_{SOL}$  and  $B_\phi$ , both for EDA H-modes (sections 5.4, 5.5) and ohmic L-modes (section 6).
- Contrary to transport models that assume a fixed cross-field heat diffusivity, divertor heat flux profiles are found insensitive to magnetic field line length. In plasmas where the magnetic connection length was changed by a factor of two (via magnetic topology changes), the shape of the heat flux profile remains invariant (section 5.3). These data indicate that the heat flux profile is set dynamically by the plasma; a critical-gradient model for heat transport may be needed to account for this observation. These results make contact with turbulence observations and earlier investigations of edge particle transport behaviors (section 7.1).
- Heat flux widths are found to be intimately connected to the behavior of the H-mode pedestal. This observation is clearly illustrated in discharges where the pedestal conditions evolve in time; changes in  $P_{SOL}$  do not affect the heat flux widths, while changes in pedestal conditions do (section 5.4). The quasi-coherent mode may be a key player in setting the heat flux widths in C-Mod's EDA H-modes; its importance in the particle transport channel is highlighted in edge turbulence observations (section 7.1).
- EDA H-mode heat flux widths are most strongly correlated with the stored plasma energy of the discharge and statistically uncorrelated with  $P_{SOL}$  and  $B_\phi$  (section 5.5). A weak inverse correlation with plasma current is seen. Forcing a power-law

fit to plasma current as a control variable yields an exponent (-0.17) that is much weaker than that reported from JRT experiments in DIII-D and NSTX.

- Heat flux widths in ohmic L-mode discharges are also found independent of  $B_\phi$ , testing a factor of 2 variation in this parameter up to 8 tesla. However, unlike in EDA H-modes, a clear inverse scaling of heat flux widths with plasma current is observed (section 6).

## 2. Background and Motivation

ITER is expected to operate with steady-state, time-averaged SOL parallel heat fluxes ( $\sim 1 \text{ GW m}^{-2}$ ) that are up to an order of magnitude higher than those observed in most present-day tokamaks (with the exception of Alcator C-Mod, which attains about  $\frac{1}{2}$  the ITER level) – a significant extrapolation from our collective operating experiences. At this power level, the width ( $\lambda_q$ ) of power channel arriving at the divertor plate becomes a critical scaling parameter. Because of the hard engineering constraint of not exceeding  $\sim 10 \text{ MW m}^{-2}$  steady-state power densities to material surfaces, the value of  $\lambda_q$  directly sets the acceptable fraction of the total scrape-off layer (SOL) power exhaust that may be allowed to come into contact with the divertor surface ( $f_{div}$ ). Based on ITER design parameters and simple geometric constraints, one arrives at the relationship  $f_{div} \sim 0.04 \lambda_q$  [3], with  $\lambda_q$  expressed in millimeters, magnetically mapped to the outboard midplane location. Thus a 5 mm power e-folding length mandates that 80% of the SOL power must be dissipated (i. e.,  $1 - f_{div}$ ), in order to avoid damage to divertor surfaces and associated coolant structures (a typical projection that is assumed for ITER). This in turn demands that the ITER divertor must be operated in a partially detached regime – a regime that is not guaranteed to be compatible with the desired core plasma performance (QDT  $\sim 10$ ). However, the empirical basis behind the extrapolation of  $\lambda_q$  values from present day experiments to a  $\sim 5 \text{ mm}$  value in ITER is very uncertain. Of primary concern are the ambiguities in the present set of empirical scalings for  $\lambda_q$  with respect to major radius, scrape-off layer power density and engineering parameters such as magnetic field and plasma current [1-3].

Figures C2-1 and C2-2 serve to illustrate some of these ambiguities and to motivate further experimentation. Multi-machine scalings based on heat flux ‘footprints’ measured at the outer divertor surface of ELMy H-modes (Fig. C2-1) suggested very weak or no scaling with machine size. Power-law regression analyses yielded the expressions [2]:

$$\lambda_q^{H-1}(m) = (5.2 \pm 1.3)10^{-3} P(MW)_{div}^{0.44 \pm 0.04} B(T)_\phi^{-0.45 \pm 0.07} q_{95}^{0.57 \pm 0.16} \quad (1)$$

$$\lambda_q^{H-2}(m) = (5.3 \pm 1.4)10^{-3} P(MW)_{TOT}^{0.38 \pm 0.04} B(T)_\phi^{-0.71 \pm 0.08} q_{95}^{0.30 \pm 0.15} \quad (2)$$

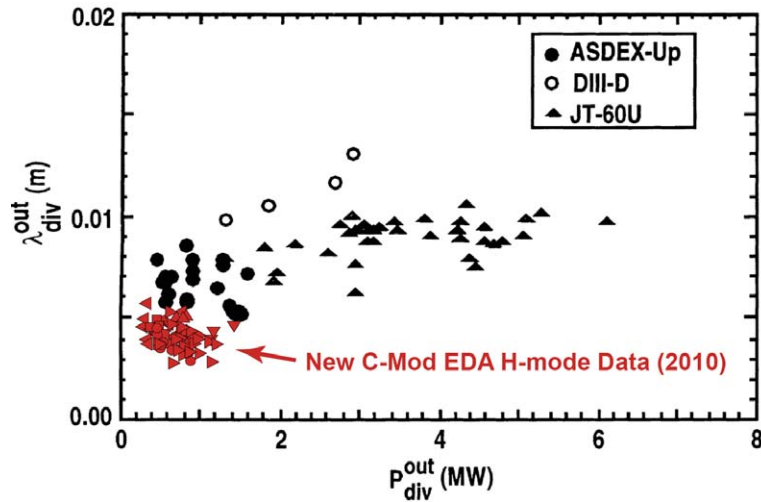


Fig. C2-1. Integral heat flux e-folding width measurements from ASDEX-Upgrade, DIII-D and JT-60U, as reported in [2] (black data points), suggest weak or no statistical dependence on machine size. Data from recent C-Mod experiments provide a valuable ‘anchor’ for machine size dependences, suggesting that there does indeed exist an imbedded machine-size scaling for the divertor heat flux footprint.

Yet, multi-machine scaling studies of the temperature e-folding lengths at the last-closed flux surface (LCFS) at the outer midplane (Fig. C2-2) revealed that major radius was the dominant scale parameter. These observations stand in contrast to scalings of Eqs. (1) and (2), given that the ‘upstream’ electron temperature profile is expected to play such a dominant role in setting the width of the power exhaust channel.

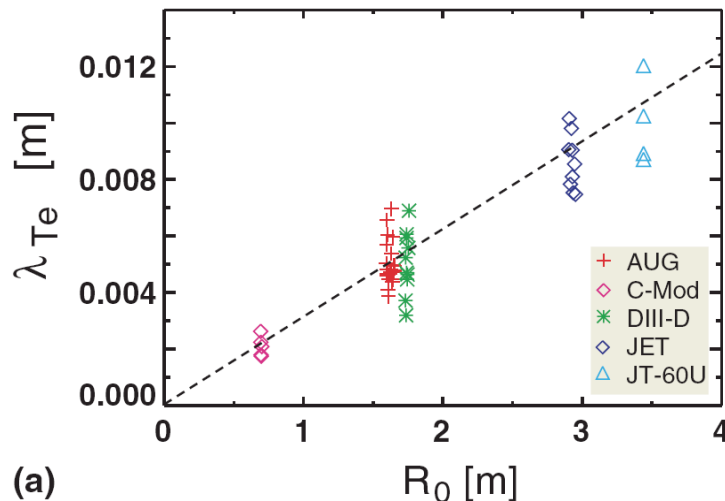


Fig. C2-2. H-mode electron temperature e-folding lengths near the last-closed flux surface, as measured by Thomson scattering diagnostics on five different tokamaks [4]. The dominant scaling parameter in these data was found to be major radius.

Adding to these ambiguities, detailed analyses of the power exhaust channel in JET produced yet another set of empirical scaling projections for  $\lambda_q$  [1]

$$\lambda_q^{cond} \propto B_\phi^{-1} P_{SOL}^{-0.5} n_{e,u}^{0.25} q_{95} R^2 \quad (3)$$

$$\lambda_q^{conv} \propto B_\phi^{-1} P_{SOL}^{-0.5} n_{e,u}^{0.25} q_{95}^{0.5} R^{1.5} \quad (4)$$

exhibiting an explicit  $R^2$  dependence for the conduction-limited case. This scaling has been used to project to  $\lambda_q \sim 4$  mm for ITER (the current design value) via an extrapolation from JET results. Nevertheless, the authors appropriately point out: “The main problem in the extrapolation ... is the scaling of  $\lambda_q$  with the major radius, which cannot be inferred from experiments and simulations on JET alone.” This ambiguous state of affairs was a strong motivator for the establishment of the FY2010 DoE JRT milestone and for Alcator C-Mod to become fully engaged in the new experiments that are described in this report. As stated plainly in the 2007 ITER Physics basis document [3]: “...there is a need for improved experimental measurements and a theory-oriented approach for making extrapolations for the target heat flux in ITER...”

Overlaid in Fig. C2-1 are recent (FY2010) Alcator C-Mod measurements of  $\lambda_q$  from a wide range of EDA H-mode discharges [5]. These data immediately suggest that  $\lambda_q$  does indeed have an embedded machine-size dependence, highlighting the value of performing these experiments in C-Mod. Moreover, a new experimental infrastructure has been developed for C-Mod, which will enable boundary layer heat transport studies to be conducted beyond the FY2010 milestone.

### 3. Divertor Heat Flux Instrumentation

In support of the experimental program, an extensive array of divertor diagnostics was installed during C-Mod’s 2009 extended maintenance period, including IR thermography, embedded calorimeters, tile thermocouples and surface thermocouples. These systems were operated from July 2009 to April 2010. In addition, a new CPCI-based data acquisition was installed, both to upgrade and expand the existing Langmuir probe data acquisition system and also to handle the new sensor signals. Custom-made analog electronics cards and backplanes were fabricated to accommodate the new range

of signal types. During the most recent April-June 2010 vacuum break, a new and improved set of ramped tiles and embedded sensors were installed.

### **3.1 Ramped tiles, embedded sensors, IR camera – June 2009 installation**

An array of embedded heat-flux sensor probes (tile thermocouples, calorimeters, surface thermocouples) combined with a new IR camera (ElectroPhysics Titanium 550M) was installed during C-Mod's 2009 maintenance period (see Fig. C3-1). This camera, now sold as the FLIR SC7000, was supplied through C-Mod's collaboration with LANL, DoE Award DE-AC52-06NA25396. Instrumented tiles on the outer divertor consist of two vertical columns, tilted in the toroidal direction by  $\sim 2$  degrees and 'ramped up' by 2 mm relative to standard tiles. This ensures that the instrumented tiles will not be shadowed by misalignments that are extremely difficult to avoid since field lines strike the C-Mod targets at grazing angles as small as  $1^\circ$ . It also increases the thermal load to the ramped tiles, improving signal-to-noise for sensor-based diagnostics.

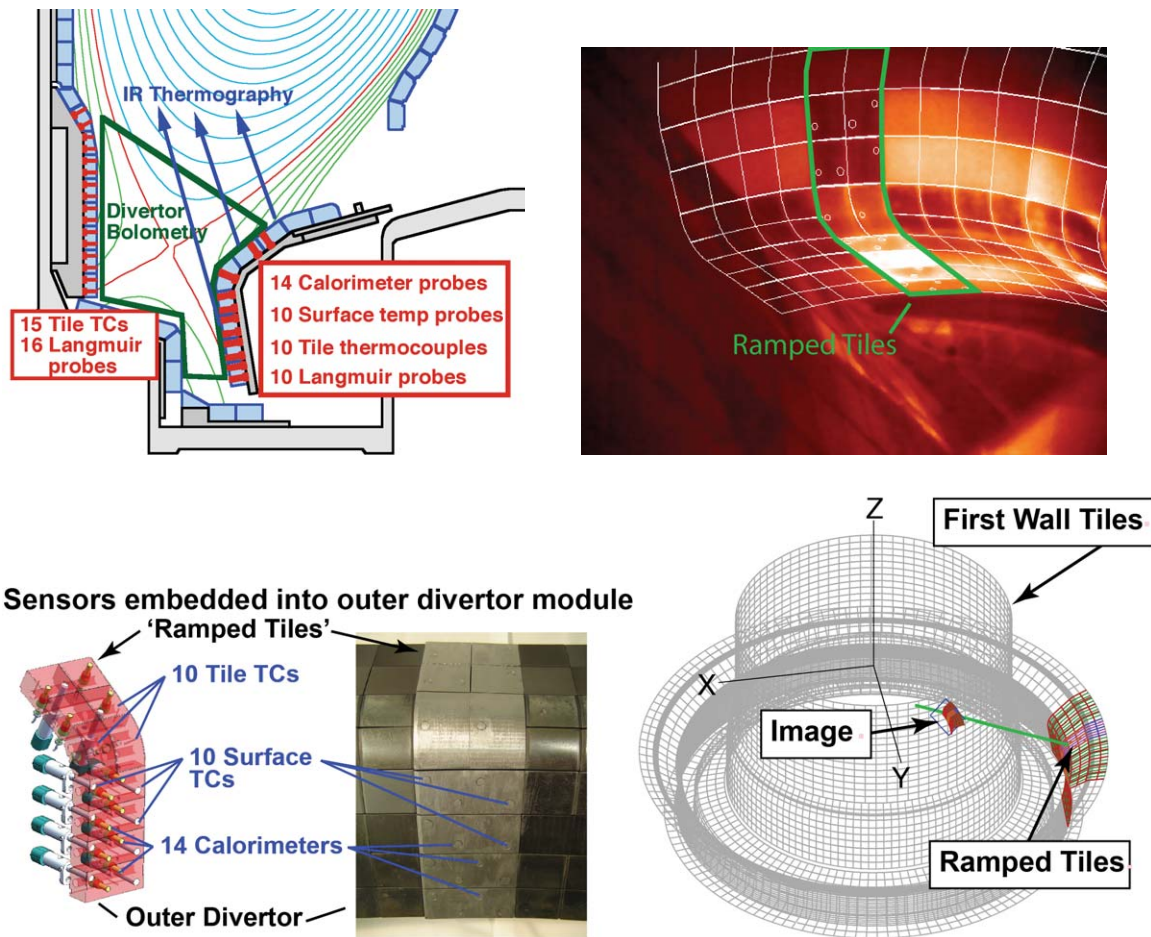


Fig. C3-1. Divertor heat flux diagnostic set installed during the 2009 extended maintenance period. An array of calorimeters plus surface and tile temperature sensors is embedded into two vertical columns of ‘ramped tiles’ on a sector of the outer divertor (poloidal cross-section in top left panel, image in bottom left panel). Langmuir probes (indicated in red) are located in a different sector, displaced 90 degrees toroidally. IR camera/periscope system views a portion of the outer divertor and ramped tiles at an oblique angle (top right panel). A virtual 3-D model of C-Mod’s first-wall tiles and periscope location is used to generate an artificial image (bottom right panel), yielding a reference tile grid for image alignment (seen projected onto the IR image in the upper right panel).

The IR camera views the ramped tiles by looking both down and in the toroidal direction from a periscope [6], which is located in a vertical port ~90 degrees away. An example image and the schematic viewing geometry are shown in Fig. C3-1. IR thermography is challenging in C-Mod with its shiny, low emissivity tile surfaces and oblique observations angles [7] – an environment that is similar to ITER. Additional

complications include low-Z surface films (e.g. boron) that change in time and image movement due to relative machine/periscope/camera motion that routinely exceeds 20 pixels in the image. To compensate for the image movement, the overall tile pattern is used as a landmark to numerically stabilize the image (see section 4.1), necessitating the wide field-of-view seen in Fig. C3-1. Nevertheless, the camera/periscope system resolves  $\sim 1$  mm scale features on the ramped-tile surfaces. In-situ cross calibrations of the IR emission with the embedded thermocouples are performed after each shot while the tiles are still hot, correcting for changes in emissivity due to surface film evolution and for degradations in periscope transmission [7].

An array of 10 Langmuir probes is embedded in divertor tiles at a toroidal location that is 90 degrees away from the ramped tiles with similar poloidal spacing as the thermal sensors. These record profiles of plasma density and electron temperature at  $\sim 5$  ms intervals and, in principal, can yield estimates of parallel heat fluxes via standard sheath models. In this way, Langmuir probe and calorimeter data can provide valuable cross-checks on the IR-inferred heat flux profiles and allow basic tests of plasma-sheath heat transmission [8].

### **3.2 Upgraded ramped tiles and embedded sensors – June 2010 installation**

Experiments performed during the time period of August 2009 through October 2009 (MP#557 [9] and MP#570 [10]) focused on commissioning embedded heat flux sensor diagnostics and initiating boundary layer heat transport studies in ohmic L-mode discharges. Unfortunately, these experiments uncovered some problems with the embedded thermal sensor and Langmuir probe arrays. Consequently, plans were immediately formulated to address these problems via component redesign and to implement these improvements at the first vacuum-opening opportunity in FY2010. Additional improvements to the arrangement of the ramped-tile were also realized as operational experience has gained:

(1) Surface thermocouple sensors began to fail over time, appearing to lose electrical isolation of their cable shields with respect to vacuum vessel ground. The sensor signals also exhibited sensitivity to currents flowing into the divertor surface, generating an EMF that was comparable to the thermal EMFs.

(2) Tile and calorimeter thermocouples exhibited poor thermal response times ( $\sim 10$

seconds). This was tracked to a high thermal resistance layer between the thermocouple junction and the tile/calorimeter surface.

(3) A cross-calibration of Langmuir probe sensors (indicated in Fig. C3-1) performed divertor strike point sweeps (MP#570) revealed that sensors ‘below the nose’ on the outer divertor were being shadowed by misalignments of the local divertor cassette. Langmuir probe data taken during this time period were therefore discarded and treated as unreliable [11].

(4) Concern arose that, due to heat-flux focusing effects [12], the heat flux ‘footprint’ on the ramped tiles might not represent the true heat flux profile on a set on axis-symmetric tiles, with the trailing edge of the ramped tile receiving an enhanced heat flux.

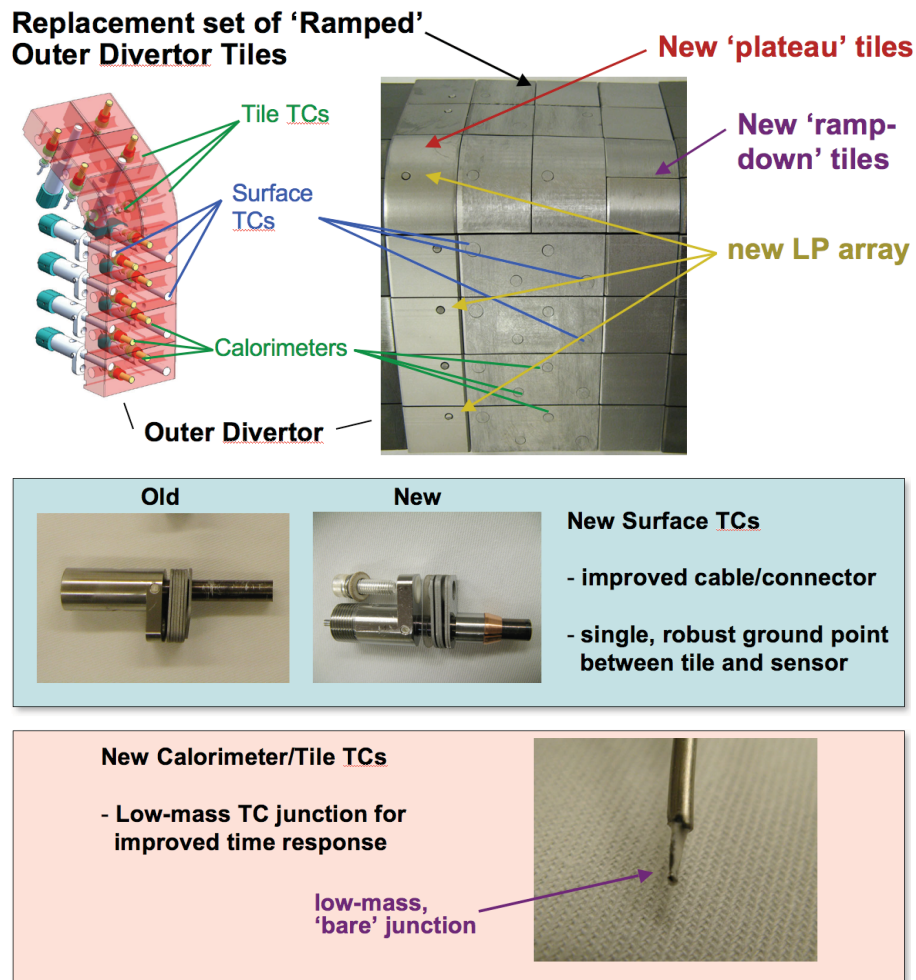


Fig. C3-2. A refurbished set of divertor heat flux sensors and ramped tiles were installed during April-June 2010 vacuum break, addressing a number of diagnostic issues. In addition, a new Langmuir probe array was installed on the ramped tiles.

(5) In some situations, portions of ‘shadowed’ regions of the outer divertor exhibited a significant amount of IR light in the camera view, indicating that this light was not originating from graybody emission but was rather some combination of reflected light and plasma emission. A reliable means for subtracting this contribution to the IR signal was desired.

To address these issues, an upgraded set of ramped-tiles and embedded sensors were installed during the April-June vacuum break (Fig. C3-2). The ramped tiles were extended toroidally, having a flat ‘plateau’ tile at the trailing edge and a ‘ramp-down’ tile and the leading edge of the ramp. The ‘plateau’ tile both eliminated concern about heat flux focusing effects on the ramp and allowed a set of Langmuir probes to be installed at this location, which would not be shadowed by divertor cassette misalignments. IR emission from the shadowed ‘ramp-down’ tiles provide a direct measure of the background light since these tiles are hidden with respect to parallel heat fluxes. Low-mass, bare thermocouple sensors were installed for the tile/calorimeter sensors and improvements to the grounding and cabling for the surface thermocouples were implemented (Fig. C3-2).

Upgrades to the IR thermography system were also instituted during this maintenance period. The most important of these was provision for a two-speed clock that externally triggered each IR image-acquisition. Since shot-to-shot cross-calibration with the embedded thermocouple systems required IR data ~30 sec after each discharge, single rate image-acquisition at the maximum full-frame rate for the camera was not practical – an enormously large data file would result. The two-speed clock upgrade allowed image-acquisition at the maximum full-frame rate (380 frames/s) for the discharge duration followed by post-discharge image-acquisition at 10 frames/s with manageable data file sizes.

#### **4. Measurement of Heat Flux Footprints**

In order to convert the raw, unstabilized IR images into time-resolved heat flux profiles across the outer divertor, a significant effort was expended during the November 2009 to January 2010 time frame to develop a suite of customized data analysis tools. The goal was to have these tools in place in time for the initial JRT experiments on EDA

H-mode heat flux footprints, the first of which occurred on February 12, 2010.

#### 4.1 IR image registration and stabilization

Due to vacuum vessel flexure during a C-Mod discharge, the IR periscope system experiences movement, causing the raw IR image to dynamically shake and shift on the order of  $\sim 20$  pixels. This effect was handled by the new data analysis software in two steps: (1) define a set of ‘virtual pixels’ that are fixed in space and registered with respect to the ramped tiles and (2) populate these pixels by shifting user-defined “regions-of-interest” (ROIs) in the raw images, so as to bring them into alignment, starting from the last IR image frame and proceeding back in time to the first. Image alignment at the sub-pixel level is performed by computing a 2-D cross correlation function between two edge-enhanced images, using fast Fourier transform techniques (see Fig. C4-1). Only translational corrections in two orthogonal dimensions were necessary; correction for image rotation was not required. Applying this image-alignment algorithm in the post-discharge processing stage provides the crucial image-stabilization. A typical time-history of image-shifts is shown in Fig. C4-2.

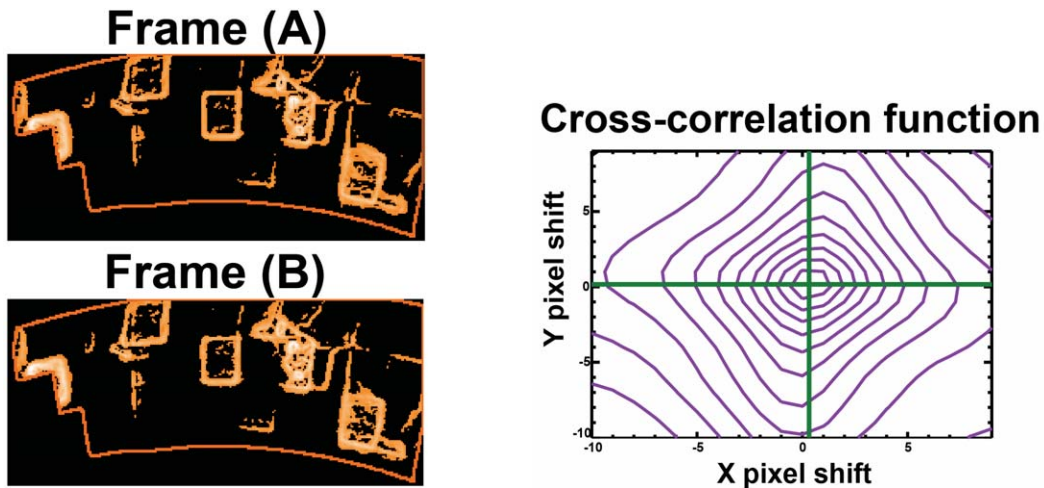


Fig. C4-1. A 2D cross-correlation (from FFT methods) between subsequent images is performed to correct for camera/periscope motion during a discharge. The IDL SOBEL function is used for edge enhancement, keeping only the upper 20% of pixels by intensity. Masking is performed based on predefined regions of interest (ROIs – the yellow outline shown).

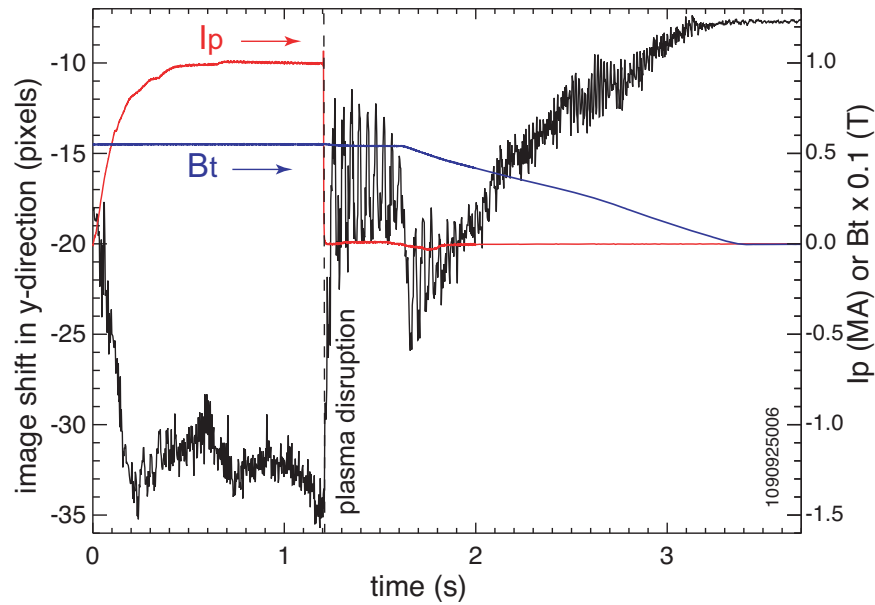


Fig. C4-2. Typical shifts in the “up-down” dimension needed to stabilize the IR camera image. Note the variations in the shift in response to a plasma disruption and to changes plasma current ( $I_p$  in red) and toroidal field ( $B_t$  in blue).

#### 4.2 In situ calibration of IR thermography

The camera and viewing-periscope were initially calibrated “on the bench” using heated Mo tiles prior to deployment of the system on C-Mod. The bench calibrations showed: (1) that the clean Mo tiles emit as “graybodies” over the range of interest, i.e. follow a blackbody curve times a constant, and (2) that the camera signal,  $S$ , can be well characterized by the expression

$$S(T_{\text{surf}}, T_{\text{camera}}, \tau_{\text{int}}) = \text{Offset}(\tau_{\text{int}}) + \alpha(\tau_{\text{int}})B(T_{\text{camera}}) + \beta(\tau_{\text{int}})B(T_{\text{surf}}) \quad (5)$$

where  $B(T)$  is blackbody emission within the spectral bandpass of the camera for a temperature  $T$ ,  $\alpha$  is a constant times  $\tau_{\text{int}}$ , (determined by varying the temperature of the camera housing,  $T_{\text{camera}}$ , while viewing a cold plate), and  $\beta$  is a calibration parameter (also linear in  $\tau_{\text{int}}$ ) that depends on the viewed surface emissivity, the periscope transmission, the detector sensitivity, and the angle with which the surface is viewed. It can be different for each pixel. “Offset( $\tau_{\text{int}}$ )” is an experimentally-determined parameter dependent only upon  $\tau_{\text{int}}$ . The “graybody” emission measured in the bench calibration of a heated Mo tile is shown in Fig. C4-3.

The IR periscope’s viewing angles of the ramped-tiles (Fig. C3-1) are large, ranging from 35 to 80 degrees away from normal to the target surfaces. The bench calibrations also showed that the

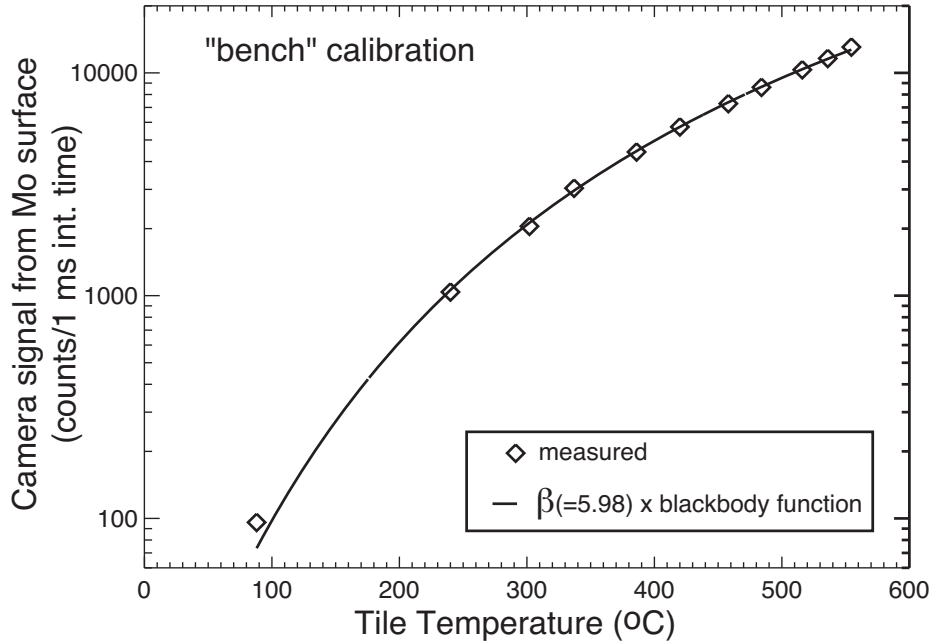


Fig. C4-3 Camera signal from tile surface (i.e.  $S\text{-Offset}-\alpha B_{\text{camera,periscope}}$ ) vs temperature of a clean Mo tile measured on the “bench”, compared to the graybody curve.  $\tau_{\text{int}}$  in this case was  $500 \mu\text{s}$ .

emissivity from a clean Mo surface increases sharply as the view angle increases beyond about 55 degrees. While this effect is present in the C-Mod measurements, another source for significant variation in surface emissivity is also present – changing low-Z surface coatings (e.g., boron). A clean Mo target surface has a low emissivity ( $\sim 0.1\text{-}0.2$ ), and the coatings increase the emissivity significantly, making in-situ calibrations necessary [7].

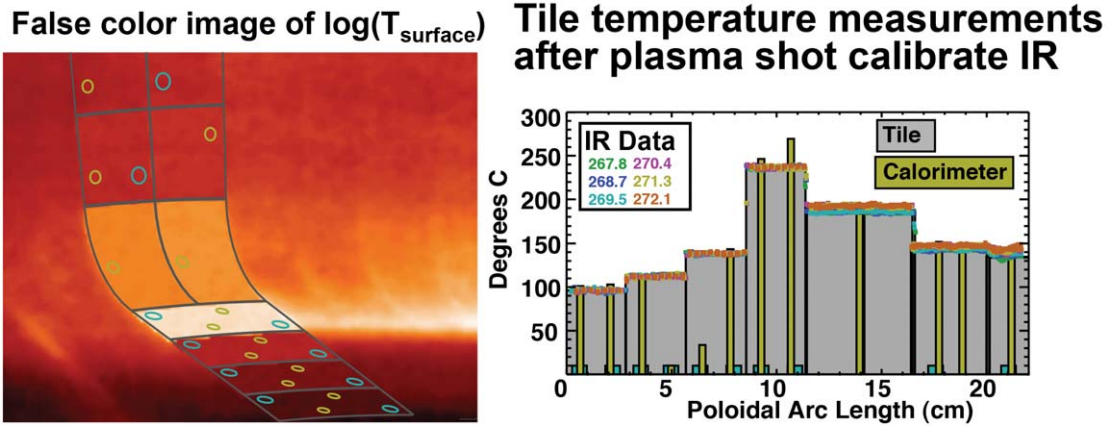
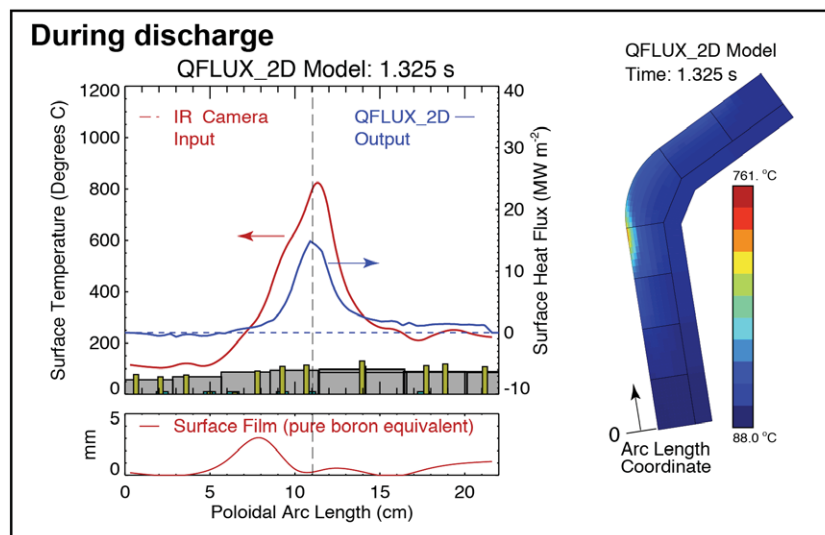


Fig. C4-4. Aligned and calibrated temperature image (left); IR camera calibration is based on matching the embedded sensor temperatures (right).

In-situ calibrations are produced after each tokamak pulse by taking IR camera data and tile thermocouple data for at least 25 seconds after the discharge termination, at which time the individual tiles have thermally equilibrated yet are still hot, as shown in Fig. C4-4.

### 4.3 Thermal analyses: QFLUX\_1D and QFLUX\_2D

1-D and 2-D finite-element heat transfer models (QFLUX\_1D and QFLUX\_2D) were developed to infer surface heat fluxes from surface temperature measurements and to simulate the long time thermal behavior of calorimeter and surface thermocouple sensors. These codes were benchmarked against cases where analytic solutions could be obtained and against a commercial 3-D thermal heat transport code (ALGOR [13])



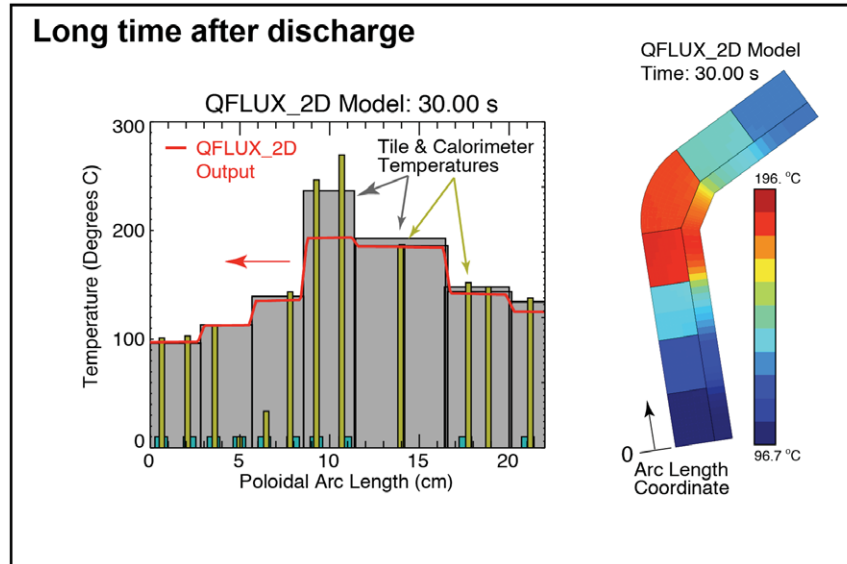


Fig. C4-5. Thermal analysis of ramped tiles using QFLUX\_2D

QFLUX\_2D contains a dimensionally accurate 2-D description of C-Mod's ramped-tile geometry, including tile gaps, at a cross-section corresponding to the ramped tile's midsection in toroidal angle. QFLUX\_2D employs a fully implicit time-integration, accounts for temperature-dependent materials properties and allows a thermal resistance layer (film) profile to be specified on the tile surface. Figure C4-5 shows an example of a QFLUX\_2D simulation. During the discharge (top panel), QFLUX\_2D imposes the IR-measured surface temperatures as a time-dependent boundary condition and computes the implied surface heat flux profiles. Peak surface heat fluxes exceeding  $10 \text{ MW m}^{-2}$ , corresponding to parallel heat fluxes exceeding  $200 \text{ MW m}^{-2}$ , are routinely observed. Immediately after the discharge, the surface heat flux is set to zero and the temperatures are allowed to evolve, arriving at a tile temperature distribution that can be compared to that measured by embedded thermocouples (lower panel of Fig. C4-5). This technique serves as a cross-check between IR and thermocouple diagnostics. For example, some discrepancy in temperature is noted in Fig. C4-5, on the fourth tile from the bottom.

#### 4.4 Surface films

Surface films can dramatically alter the relationship between surface temperature and heat flux, and if not properly considered, can lead to erroneous negative heat fluxes [14]. We have implemented a novel Fourier analysis method to estimate the thermal resistance of films: (1) compute the complex thermal impedance of a bare surface using

measured temperatures and modeled heat fluxes and (2) add to this a minimal amount of surface thermal resistance to eliminate negative heat fluxes. The top panel of Fig. C4-5 shows the output of this computation, expressing the surface thermal resistance in terms of its equivalent thickness of a pure boron film.

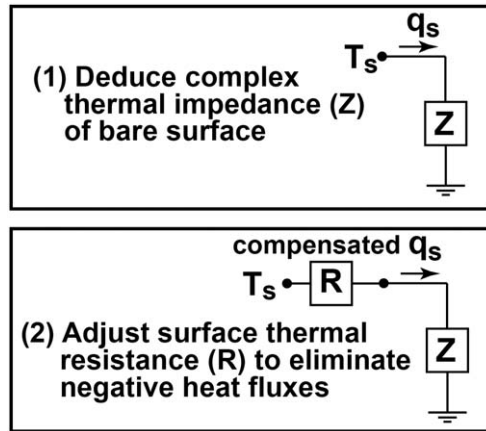


Fig. C4-6. Surface film compensation algorithm.

#### 4.5 Comparison of IR and embedded sensors

Embedded calorimeters can provide an independent measurement of the discharge-integrated energy deposition profile on the ramped tile surfaces, yielding another valuable cross-check on IR thermography-inferred heat flux profiles. Prior to the installation of improved thermocouple sensors in June 2010 (see section 3.2), the calorimetry analysis had to account for the poor time-response of the thermocouples [8]. Nevertheless, good agreement between the IR thermography and calorimeter profiles has been obtained (Fig. C4-7), lending confidence in the IR thermography analysis that was used to study heat flux footprints in EDA H-mode discharges (reported in section 5).

After the June 2010 installation of the new surface thermocouples, the IR-derived temperatures could be compared directly with the lowest-noise surface thermocouple. This comparison depends on good IR image registration and stabilization since the surface TC is only 8 pixels in the image. Such a comparison is shown in Figure C4-8.

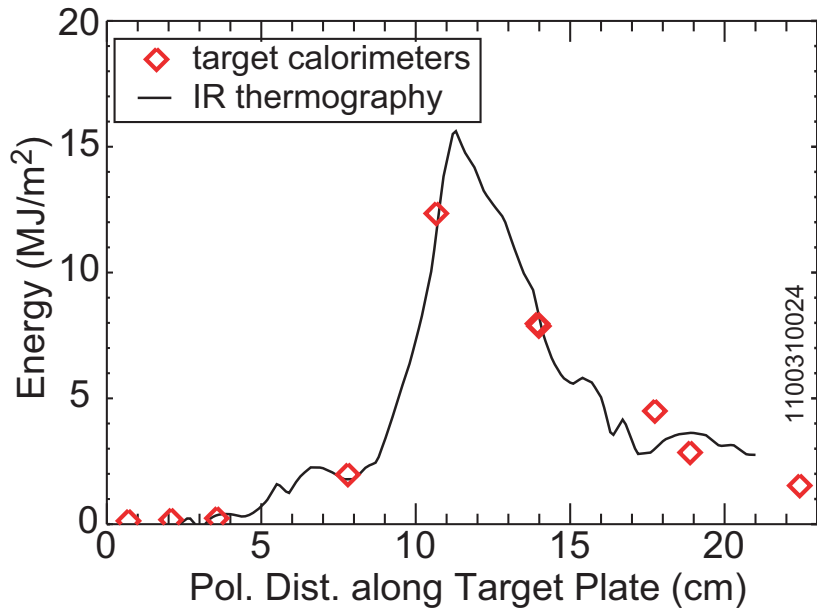


Fig. C4-7. Cross-check of thermal energy deposition as inferred from embedded target calorimeters and IR thermography [8].

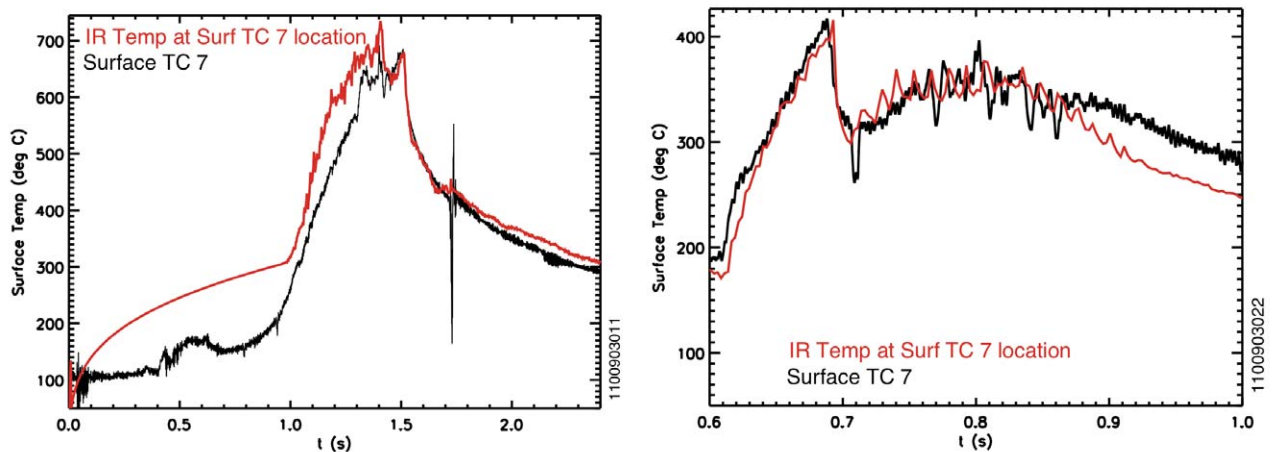


Fig. C4-8. Comparison of IR surface temperatures (red) and surface thermocouple temperatures (black). Left panel – The time-history over the discharge duration. (The smooth portion of the IR temperature between  $t \sim 0$  and  $t \sim 1.0$  s is interpolated, since subtraction of the “background” emission could not be performed over those times.) Right panel – Detail of a time-history comparison from a different discharge. The sharp drop in temperature at  $t \sim 0.7$  is the result of a L-to-H-mode transition, while the semi-periodic small changes in the IR temperature between  $0.75 < t < 0.92$  s are correlated with sawtooth crashes that are presumably expelling heat into the SOL.

#### 4.6 Comparison of Langmuir probe and surface thermocouple inferred heat fluxes

With the new Langmuir probe array installed on the plateau section of the ramped tiles, cross-comparisons of parallel heat flux profiles from these probes and the surface thermocouples (also newly improved) could be performed. Reasonable agreement has been obtained between these diagnostics in sheath-limited and moderate recycling conditions using a standard sheath transmission factor of  $\sim 7$  (Fig.C4-9). However, some significant discrepancies have been uncovered as the plasma transitions into a high-recycling regime – a topic currently under investigation [15].

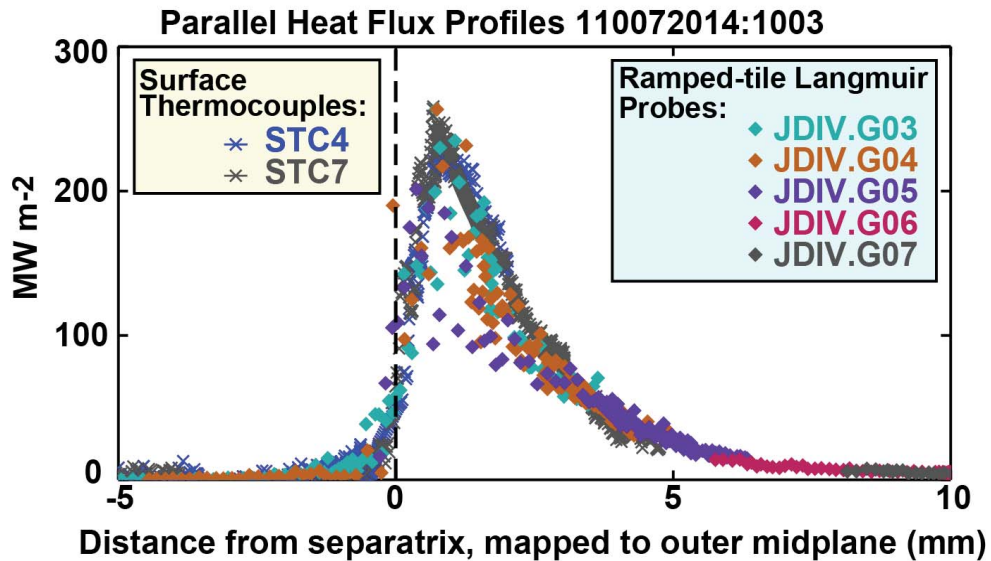


Fig. C4-9. Comparison of parallel heat profiles as inferred from the new Langmuir probes installed on the ‘plateau tiles’ (see section 3.2) and two surface thermocouples, obtained during a strike-point sweep experiment (MP#570, August 2010).

#### 5. Heat flux footprints in EDA H-modes – MP#591

Starting in February 2010, an experimental program was begun to investigate heat flux footprints in EDA H-modes and their corresponding midplane-mapped boundary layer profiles over a wide range of parameters. C-Mod mini-proposal #591 [16] was developed for this purpose, in consultation with DIII-D and NSTX team members. It should be noted that EDA H-modes are steady-state discharges in which the pedestal is regulated by a continuous ‘quasi-coherent’ edge mode, rather than by a regular procession of ELMs [17]. Thus, one must be careful in relating these results to discharges whose heat flux profiles are obtained during ELMy (time-averaged) or ELM-free

conditions. In addition, these discharges were operated with no extrinsic impurity seeding and with only modest divertor radiation (attached outer divertor) so as to yield a clean measure of the divertor heat flux footprints.

### **5.1 Experimental program – similarity discharges, $I_p$ , $B_T$ & $P_{ICRF}$ scans**

A total of seven run days were devoted to studying heat flux footprints in EDA H-modes, covering the engineering parameter space indicated in Fig. C5-1. The investigation also included ‘dimensionless similarity discharges’, which matched boundary layer shape and dimensionless plasma physics parameters ( $v^*$ ,  $\rho^*$ ,  $\beta$ ) with companion DIII-D discharges [18]. Five runs were performed in the February-March 2010 time frame, with the initial set of heat flux diagnostics. The remaining two were performed in August 2010, with the refurbished diagnostic set. The DIII-D companion similarity discharges were executed on February 9 and February 11, 2010. In addition to these parameter scans, the effect of magnetic connection length on power e-folding widths was explored by comparing lower single null versus near double null discharges under otherwise identical conditions. This technique was used to help differentiate among the roles of plasma current, safety factor and connection length in empirical scalings. In all of these experiments, turbulence imaging diagnostics were employed to record fluctuation spectra in the boundary layer region (see results reported in section 7).

1100212024 EFT: 1.000

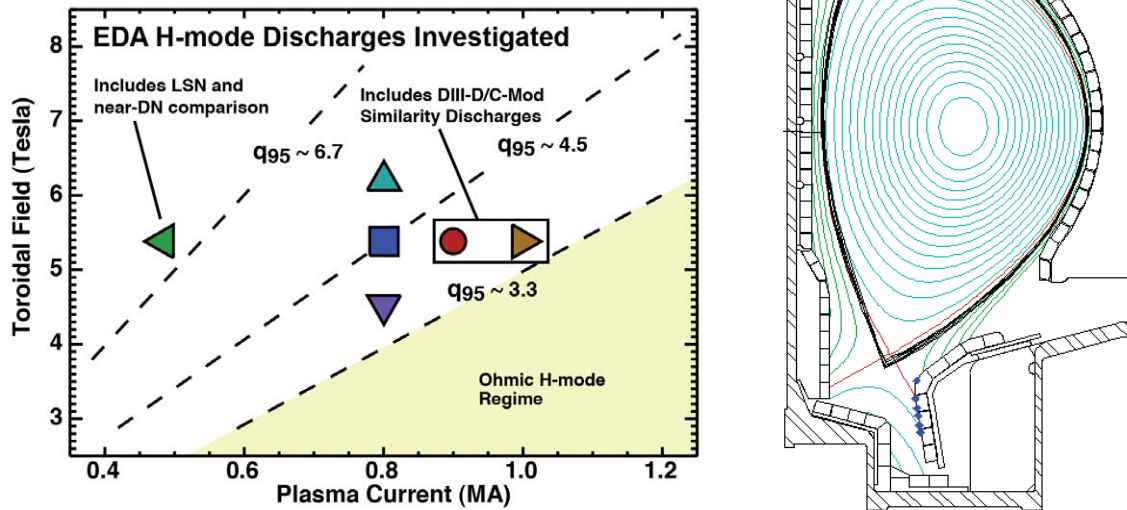


Fig. C5-1. Engineering parameter space explored during EDA H-mode studies (left) with boundary shape matched to DIII-D (right, with DIII-D overlay in black) – February-March 2010 (MP#591).

A good match of plasma boundary shape was been obtained between C-Mod and DIII-D for the similarity discharge set (see Fig. C5-1). Stable EDA H-modes were obtained at  $I_p = 0.9$  MA and 1.0 MA. Auxiliary ICRF heating power was varied between 1 and 4 MW, with fixed and swept strike point and a variety of pedestal profiles were obtained. A comparison of C-Mod’s edge temperature and density profiles with the appropriately scaled profiles from DIII-D for the similar discharges are shown in Fig. C5-2. Edge profiles of the dimensionless quantities  $v^*$ ,  $\rho^*$ , and  $\beta$  for two of the DIII-D shots and one C-Mod shot are also shown.

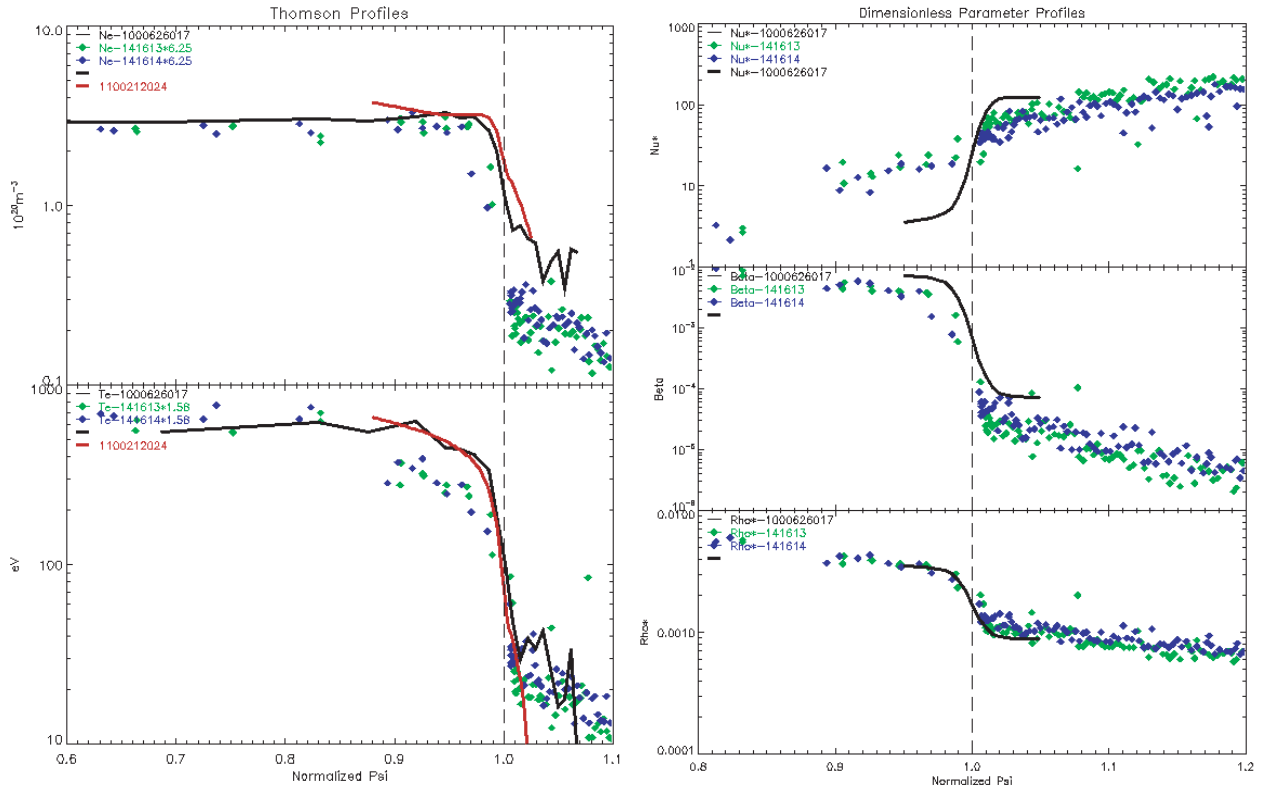


Figure C5-2. Left – Edge electron density and temperature profiles from C-Mod’s similarity discharges (black and red lines) compared to the appropriately scaled profiles from the DIII-D similarity discharges (blue and green points). The red line is a C-Mod profile from the recent set of similarity experiments while the black line is from a C-Mod discharge (from CY 2000 [19]) that served as the target. Right – Edge profiles of the dimensionless quantities  $\nu^*$ ,  $\beta$ , and  $\rho^*$  from the DIII-D (blue and green points) and C-Mod (black line) similarity discharges. The abscissa are normalized  $\psi$ .

## 5.2 Heat flux profiles

Figure C5-3 shows results from a representative 0.9 MA, 5.4 tesla EDA H-mode discharge, with 4 MW of ICRF power (80 MHz, second-harmonic, hydrogen-minority). Radiated power from the confined plasma ( $P_{RAD}$ ) is deduced from a resistive bolometer system [20], providing an estimate of the power into the scrape-off layer ( $P_{SOL}$ ). Power onto the outer divertor ( $P_{ODIV}$ ) is computed from the IR-inferred divertor heat flux profiles. Data from this particular discharge has been shared with external collaborators for modeling studies (section 8).

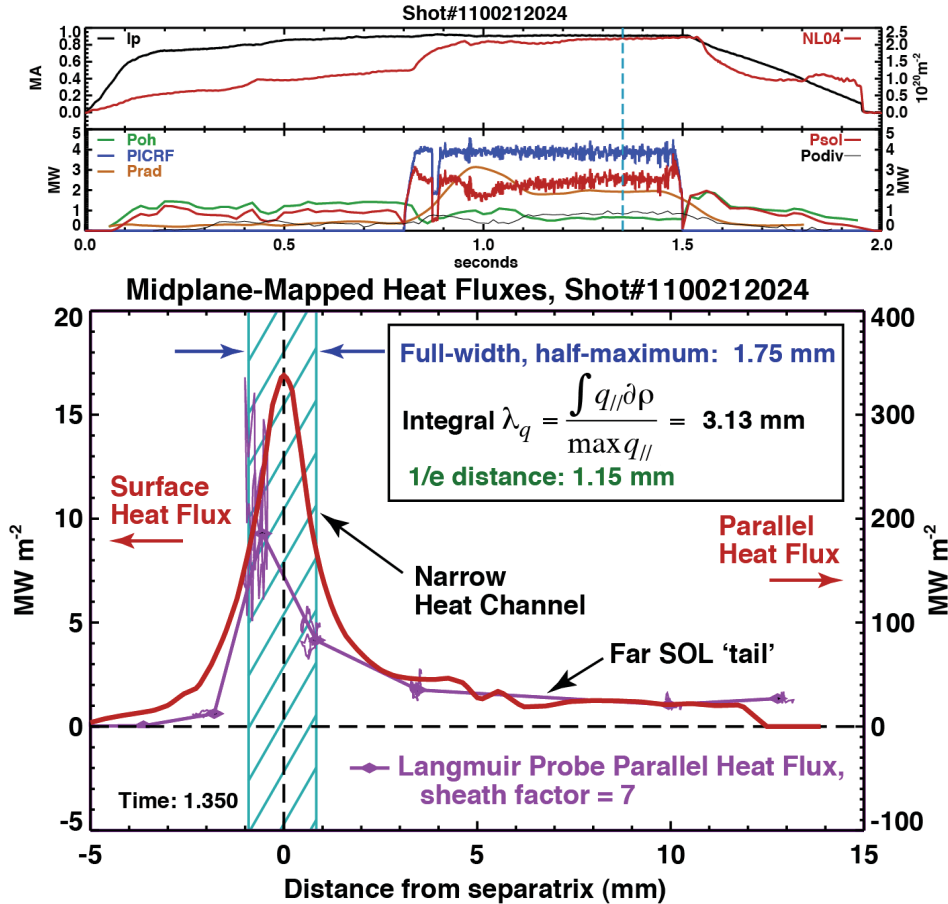


Fig. C5-3. Representative time traces (top panels) and a corresponding divertor heat flux footprint from a steady EDA H-mode discharge. Heat flux profiles from IR camera (red line, bottom panel) and Langmuir probe array (purple line) are shown, mapped to the outer midplane. (Note: Langmuir probe measurements near the strike point may be partially shadowed by divertor misalignments in this discharge – see section 3.2.)

Heat flux footprints are found to exhibit a two zone structure: a narrow ‘power channel’ near the separatrix of approximately  $\sim 2$  mm wide (characterized by its full-width at half-maximum, FWHM), and a ‘tail’ that extends into the far SOL region. This behavior is similar to what has been seen in other tokamaks [21, 22]. It should be noted that the exact location of the separatrix relative to the narrow heat flux channel is uncertain, with shot-to-shot variation on the order of  $\sim 1$  mm and systematic offsets on the same order. Langmuir probe data verify that the ‘tail’ feature in the heat-flux profile is real and not some artifact of the IR-inferred heat flux profile. Langmuir probes are not able to spatially resolve the narrow feature without sweeping the strike point, however; parallel heat fluxes in this region ( $> \sim 300 \text{ MW m}^{-2}$ ) often exceed the range in which

tungsten probes can operate without melt damage.

Following the definition by Loarte [2], the integral heat flux width (also defined in Fig. C5-3) is found to be  $\sim 3$  mm for this discharge. This value differs substantially from the scalings of Kirnev *et al.* [Eqs. (3) and (4)], which project to 0.55 mm (conduction-limited case, the one relevant here) and 1.0 mm (convection-limited case) for the discharge shown in Fig. C5-3. On the other hand, empirical scaling laws of Loarte *et al.* [Eqs. (1) and (2)] yield integral  $\lambda_q$  estimates that appear to correspond to the C-Mod observations, projecting to 5.2 mm [based on  $PDIV$ ] and 3.4 mm [based on  $PSOL$ ]. It is important to point out that if the Loarte scaling were to hold true for ITER, integral  $\lambda_q$  values would be  $\sim 20$  mm rather than the assumed  $\sim 4$  mm. However, one must be careful here. The connection of the Loarte scalings to the C-Mod data may be just fortuitous; these scalings have explicit dependencies on  $PSOL$  (or  $PDIV$ ) and  $B_\phi$ , and, as noted in the following sections, such scaling relationships are not observed in C-Mod's heat flux footprints.

### 5.3 Effect of magnetic connection length

In addition to the experiments described above, a small set of discharges ( $I_p = 0.5$ , 1.0 MA,  $B_T = 5.4$  tesla) were run with the x-point balance changed dynamically; the magnetic equilibrium was programmed to start in lower single-null and to sweep to a double-null configuration. The goal of these experiments was to document changes in the divertor heat flux footprint as the magnetic connection length changed (a factor of  $\sim 2$  longer for single-null versus double-null). One might expect that, as the connection is shortened by a factor of two, which occurs in the SOL region beyond the secondary separatrix, the heat flux profile in the common flux region would show a corresponding break in slope, yielding a shorter e-folding length there. However, as documented in Figure C5-4, no such response was seen in the experiment – the shapes of the heat flux profiles are robustly insensitive to the location of the secondary x-point.

This result may seem puzzling at first but is consistent with previous C-Mod observations of scrape-off layer (SOL) profiles in response to magnetic topology changes [23]: in changing from single to double-null, the electron pressure profiles in the low-

field side SOL remained similar. Taken together, these observations tell us that heat transport in the SOL cannot be simply described as a fixed cross-field diffusivity that is balanced by parallel losses, which change according to magnetic connection length. Rather, the heat flux profile on the outer divertor appears to be rigidly set by ‘critical gradient’ phenomena on the low-field side; whether the field line connects a long way around to the inner divertor (single-null) or a short way to the upper divertor (double null) is apparently not of primary importance.

Recognizing the significance of this observation, a follow-up set of experiments was performed on August 24, 2010, using the improved ramped tile diagnostics. Secondary x-point sweeps were performed across the lower divertor in 1.1 MA ohmic L-mode discharges and 0.5 MA EDA H-mode discharges. Care was taken to make sure that the magnetic equilibrium was swept beyond double-null into upper-single null to accommodate possible errors in EFIT mapping. Preliminary analysis indicates very similar results: the shape of the heat flux profile is found to be insensitive to the location of the secondary x-point flux surface.

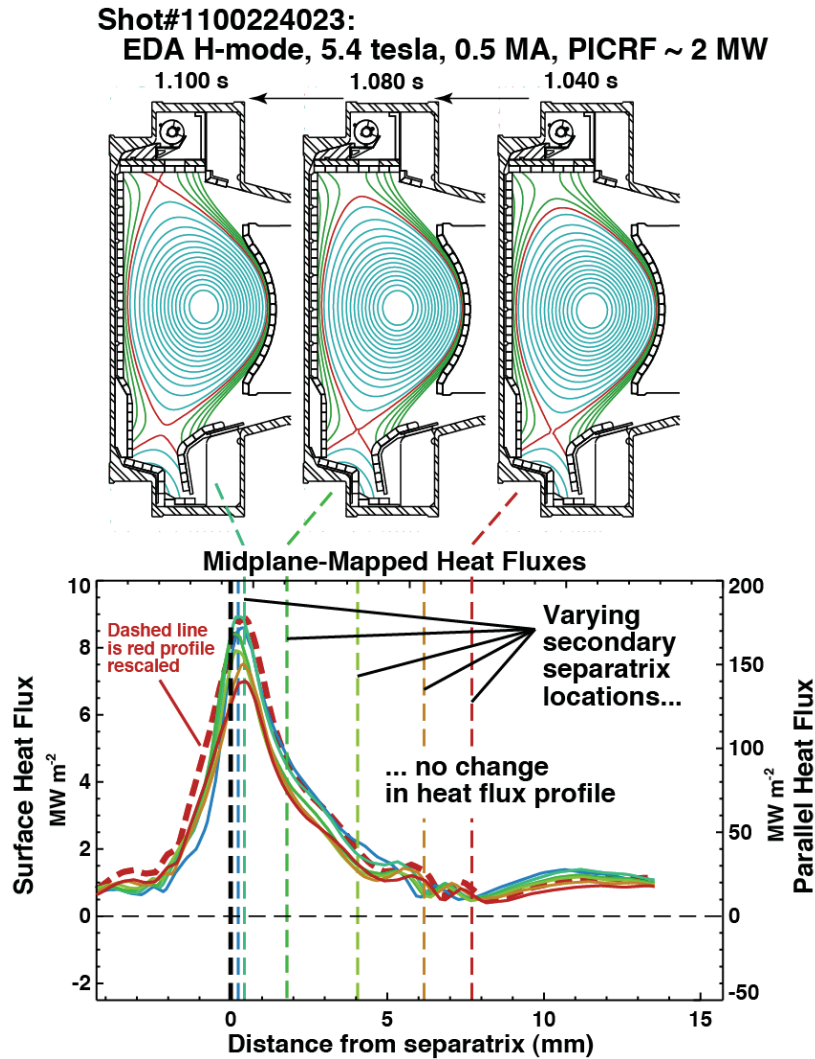


Fig. C5-4. Divertor heat flux profiles (bottom) obtained dynamically during a secondary separatrix sweep (top). The shape of the heat flux profiles is found to be remarkably insensitive to the change in magnetic topology. Note: Modulation in the peak heat flux is caused by changes in  $PSOL$ , which varied during the sweep.

#### 5.4 Insensitivity of $\lambda_q$ to $PSOL$ , correlation with pedestal behavior

Figure C5-5 shows time traces from a 1.0 MA, 5.4 tesla EDA H-mode discharge that highlight some important heat flux footprint observations; these are been born out in the full data set (section 5.5). This plasma exhibited two separate EDA phases (see time-slice sample times marked EDA 1 or EDA 2), with a clear quasi-coherent mode present in both. The heat footprints and pedestal profiles corresponding to the time slices are shown in Fig. C5-5. During EDA 1, the ramp-up in ICRF power combined with increasing  $P_{RAD}$  resulted in a 50% modulation in the peak heat flux arriving at the outer

divertor. The heat flux profiles in Fig. C5-6 show this modulation (red curves), yet, the shape of the normalized heat flux profiles is found to be invariant during this phase. [Note: Data from EDA1 and EDA 2 time slices have been ported to external modelers for detailed study (section 8).]

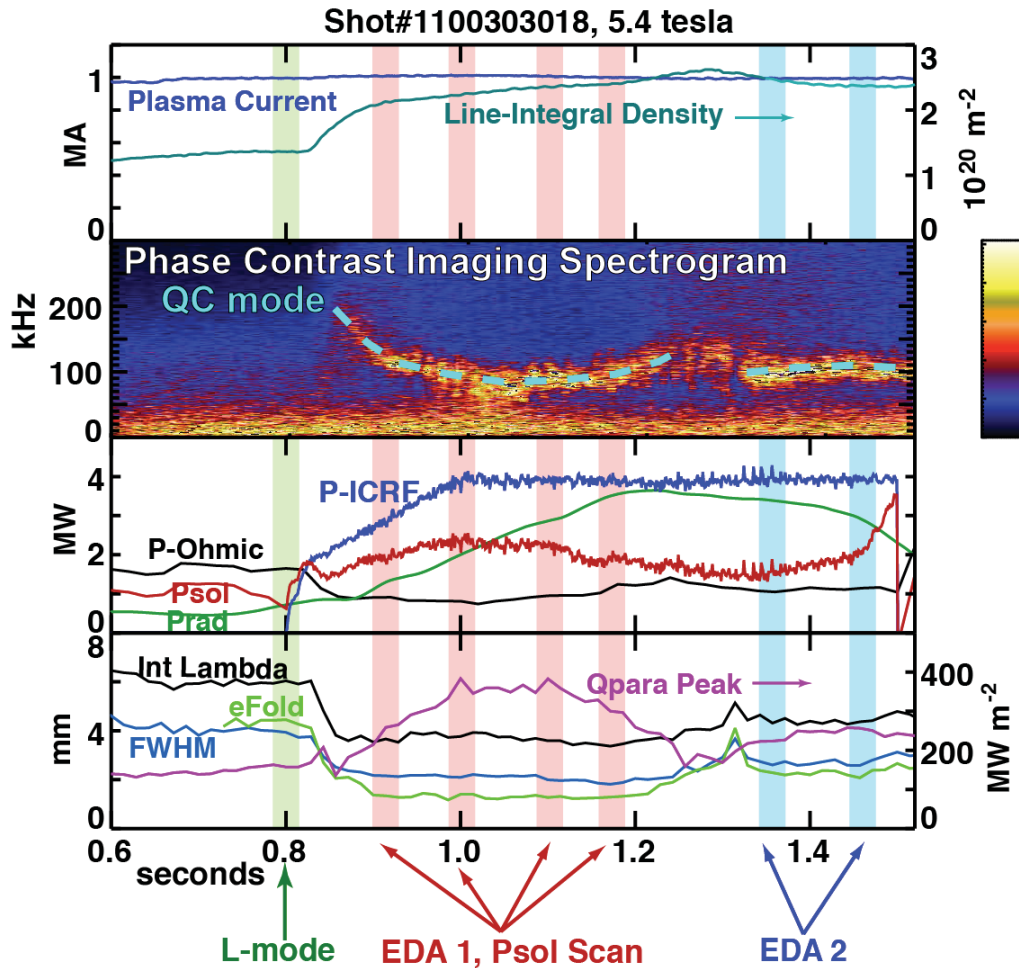


Fig. C5-5. Time traces from H-mode discharge with two different time-evolving EDA phases. Heat flux profiles corresponding to the time slices indicated are shown in Fig. C5-6.

Thus, the level of power into the scrape-off layer ( $PSOL$ ) does not explicitly influence the width of the heat flux footprint. Moreover, the time traces of heat flux widths in Fig. C5-5 change from EDA 1 to EDA 2 with essentially no change in external control parameters – integral  $\lambda_q$  steps up from 4 mm (EDA 1) to 5 mm (EDA 2); normalized profiles in Fig. C5-6 show a clear change in widths. These observations clearly confound efforts to characterize  $\lambda_q$  as a simple power-law function of global

engineering quantities.

As shown in Fig. C5-6, electron pressures at the top of the pedestal were significantly reduced in the transition from EDA 1 to EDA 2. Associated with this is a flattened pressure profile in the SOL. This behavior has been noted before in C-Mod – as confinement improves, SOL pressure gradient scale lengths become shorter [24]. ASDEX-Upgrade examined similar relationships, producing an explicit power-law scaling of heat flux widths in terms of H-mode confinement factor [2]. The message here is clear: one must look to the physics of the edge transport barrier and pedestal as controlling the width of the power channel in the SOL.

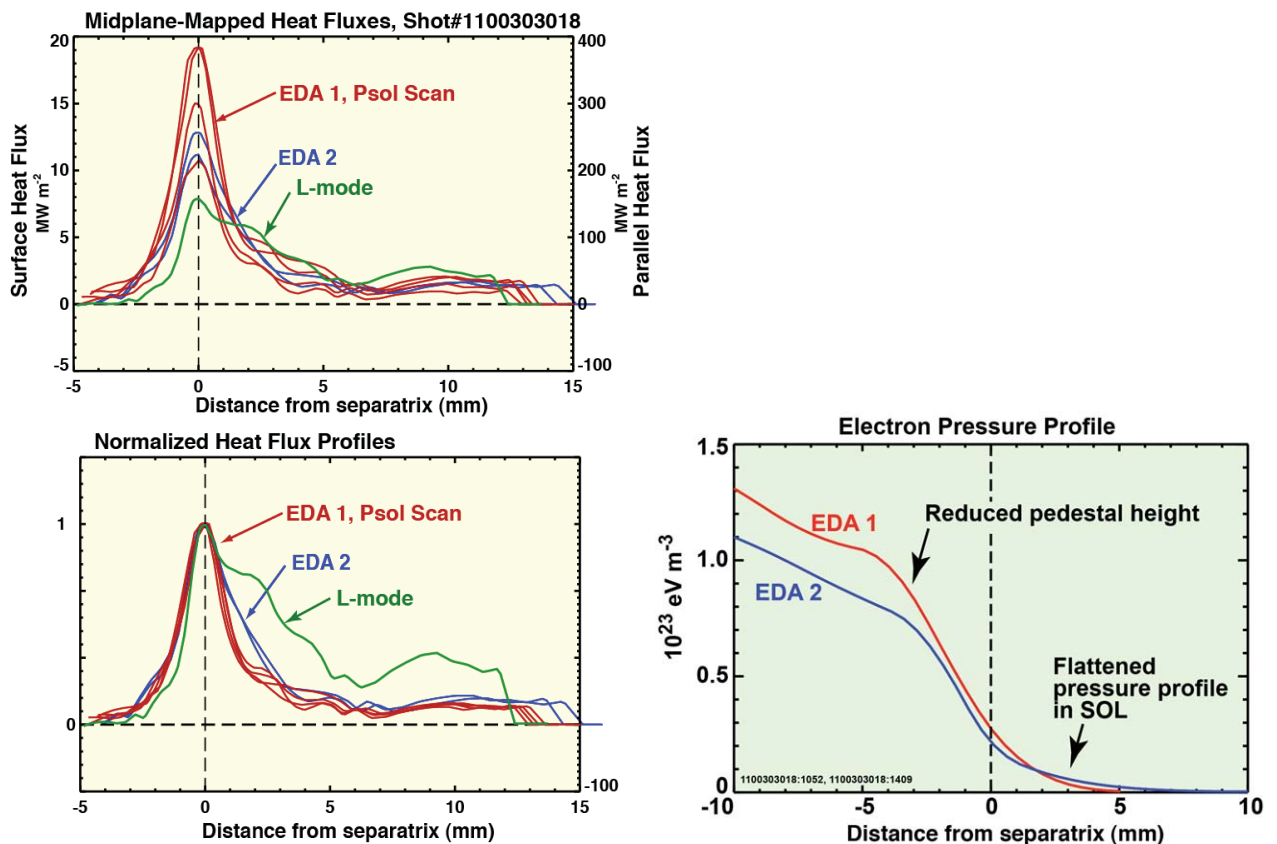


Fig. C5-6. Divertor heat flux profiles from L-mode, EDA 1 and EDA 2 phases (top left) and their corresponding normalized shapes (bottom left). Pedestal electron pressure profiles, averaged over EDA 1 and EDA 2 phases (bottom right).

### 5.5 Statistical trends

Data from the full set of EDA H-mode discharges are compiled in Fig. C5-7. Heat flux widths are found to systematically decrease with increasing plasma thermal energy, consistent with the above pedestal observations (note locations of EDA 1 and EDA 2 data

points). Since plasma thermal energy increases roughly with plasma current squared, heat flux widths have a general tendency to decrease with increasing plasma current. While the variation of toroidal field in the present data set is modest (factor of 1.5), no explicit dependence on this parameter is evident – an observation that also makes contact with the pedestal, where pressure gradients are insensitive to toroidal magnetic field strength [25].

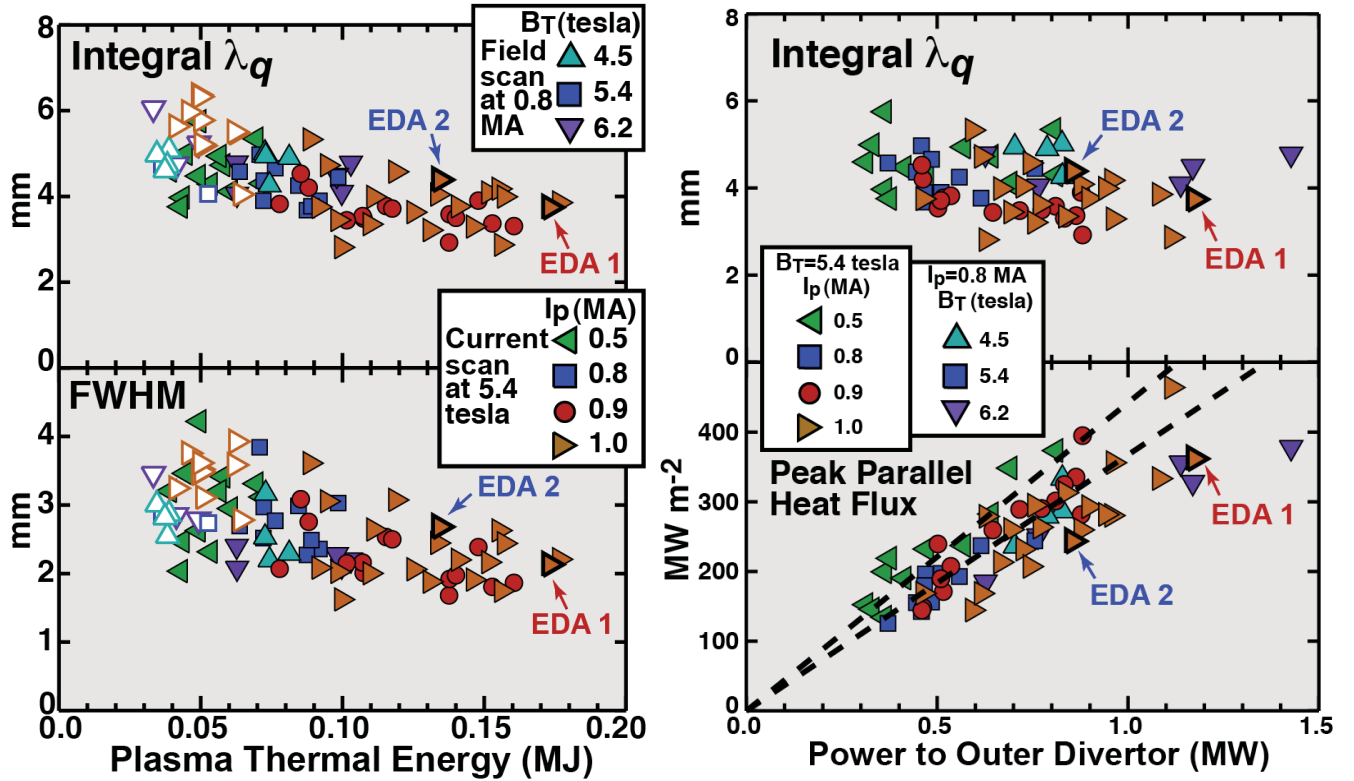


Fig. C5-7. Integral heat flux footprint widths are well correlated with plasma thermal energy (top left panel). Data from all conditions studied thus far follow a similar scaling, even accommodating L-mode discharges (open symbols). Full-width, half-maximum values show a similar trend with more scatter (bottom left panel). Because of these trends, heat flux widths in H-mode discharges tend to decrease with increasing plasma current. Integral widths are insensitive to power arriving at the outer divertor (top right), yielding a  $\sim$ linear relationship between the peak parallel heat flux and power on the outer divertor (bottom right, with dashed lines to guide the eye). No explicit dependence on toroidal magnetic field strength is evident.

These trends can be examined more formally by statistical analysis. Here we adopt the traditional strategy of trying to describe integral  $\lambda_q$  in terms of a power-law function of the usual set of regressors,

$$\lambda_q^{EDA}(\text{mm}) = C I_p^\alpha B_\phi^\beta P_{sol}^\gamma W_{mhd}^\delta q_{95}^\epsilon, \quad (6)$$

with the addition of plasma stored energy,  $W_{mhd}$ . The units of dimensional quantities in

Eq. (6) are:  $\lambda_q^{EDA}$  [mm],  $I_p$  [MA],  $B_\phi$  [tesla],  $P_{sol}$  [MW], and  $W_{mhd}$  [MJ]. Within this framework, regressors that are statistically the most relevant in determining  $\lambda_q$  can be identified by examining the  $\chi^2$  of the fit as these terms are included in the power law formula (i.e., F statistic [26]). For this data sample size, an F-test result of  $\sim 4$  indicates that there is a 5% chance that the same statistical result would have been obtained from a random regressor. Therefore, regressors with an F-test much less than 4 should be treated

Table 1 – Results from power-law regression analysis of  $\lambda_q^{EDA}$  (integral  $\lambda_q$  in C-Mod EDA H-modes)

85 data points included			Power-law exponent					F-test result				
Case #	$R_{mul}^2$	C	$I_p$	$B_\phi$	$P_{sol}$	$W_{mhd}$	$q_{95}$	$I_p$	$B_\phi$	$P_{sol}$	$W_{mhd}$	$q_{95}$
1	0.04	4.14	-0.17					3.4				
2	0.00	4.31		0.00					0.0			
3	0.04	4.10	-0.17	0.01				3.4	0.0			
4	0.01	4.22			0.04					0.5		
5	0.05	4.06	-0.17		0.05			3.5		0.5		
6	0.01	3.78		0.06	0.05				0.0	0.5		
7	0.05	3.56	-0.17	0.08	0.05			3.5	0.1	0.6		
8	0.47	2.16				-0.27					74.5	
9	0.50	2.01	0.17			-0.31		4.6			75.9	
10	0.48	2.66		-0.13		-0.27			0.3		74.2	
11	0.50	2.61	0.17	-0.16		-0.31		4.8	0.5		75.9	
12	0.48	2.12			0.05	-0.27				0.9	74.6	
13	0.51	1.97	0.17		0.04	-0.31		4.5		0.9	75.6	
14	0.48	2.36		-0.07	0.04	-0.27			0.1	0.7	73.7	
15	0.51	2.36	0.17	-0.11	0.04	-0.31		4.6	0.2	0.6	74.9	
16	0.02	3.56					0.13					1.8
17	0.06	6.69	-0.53				-0.37	3.2				1.6
18	0.02	4.35		-0.13			0.14		0.2			2.0
19	0.21	1.28	-3.37	3.20			-3.35	18.6	15.1			16.9
20	0.03	3.42			0.06		0.14			0.7		2.1
21	0.06	6.30	-0.50		0.02		-0.34	2.5		0.1		1.1
22	0.03	3.74		-0.06	0.05		0.14		0.0	0.6		2.1
23	0.21	1.27	-3.36	3.19	0.01		-3.33	17.6	14.8	0.0		16.0
24	0.51	2.53				-0.31	-0.18				81.1	5.8
25	0.51	2.75	-0.06			-0.31	-0.24	0.1			74.3	1.2
26	0.51	2.46		0.02		-0.31	-0.18		0.0		79.8	5.4
27	0.52	1.92	-0.81	0.80		-0.29	-0.99	1.3	1.2		51.3	1.9
28	0.51	2.48			0.03	-0.31	-0.17			0.4	79.5	5.2
29	0.51	2.53	-0.02		0.03	-0.31	-0.19	0.0		0.4	73.8	0.7
30	0.51	2.25		0.06	0.03	-0.31	-0.18		0.1	0.5	78.6	5.1
31	0.52	1.82	-0.74	0.77	0.03	-0.29	-0.92	1.0	1.1	0.3	51.0	1.6

as statistically irrelevant.

Table 1 shows the results, considering all possible combinations of regressors in Eq. (5). The F-test results clearly identify  $W_{mhd}$  as the most relevant regressor (case #8);  $B_\phi$  and  $P_{sol}$  are statistically irrelevant. A weak correlation with  $I_p$  is indicated (case #1). Case #24 is statistically the best, with  $W_{mhd}$  and  $q_{95}$  as the regressors. However, in all cases, the multiple regression coefficient,  $R_{mul}^2$ , is  $\sim 0.5$  or less, suggesting that the power-law model expression is a poor representation of the physics and/or there are other hidden control parameters that are not being tracked. Note that cases #19 and #23 are spurious, reflecting the covariance among  $B_\phi$ ,  $I_p$  and  $q_{95}$ .

Figure C5-8 shows data points and corresponding regression fits for cases #1 and #8. It should be noted that the scaling of integral  $\lambda_q$  with respect to  $I_p$  (exponent  $\sim -0.17$ ) is considerably weaker than in DIII-D [27] (exponent  $\sim -1.0$ ) and NSTX [28] (exponent  $\sim -1.6$ ).

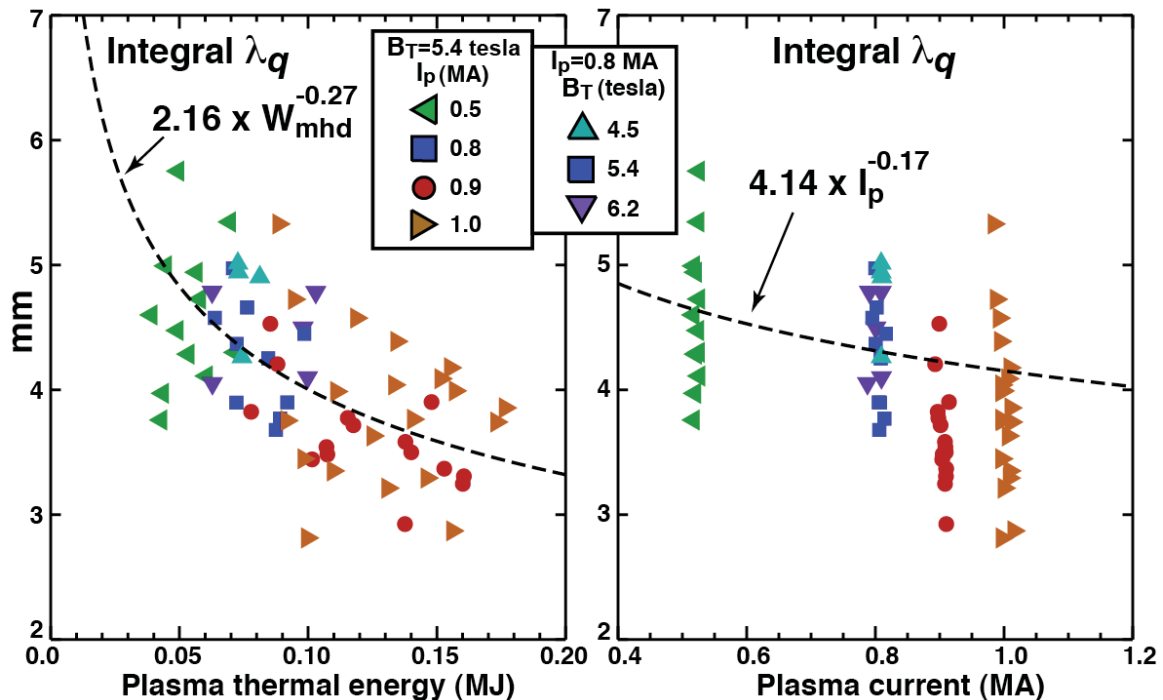


Fig. C5-8. Integral heat flux widths in C-Mod's EDA H-modes are better correlated statistically with plasma thermal energy (left) than plasma current (right). The power-law exponent with  $I_p$  is weak ( $\sim -0.17$ ), compared to that seen for ELMy H-modes in NSTX [28] and DIII-D [27].

## 6. Heat flux footprints in L-modes – MP#570

Because of the initial problems encountered with the embedded heat flux sensor diagnostics (see section 3.2), experimental work on MP#570 had to be postponed until after the April-June 2010 opening, when appropriate repairs and improvements could be made. Following initial re-commissioning experiments, which demonstrated that the refurbishments were quite successful, experimental work on MP#570 resumed (July 16, 2010). Four run days were devoted to MP#570 during the remaining summer run campaign, with discharges spanning a wide range of currents and fields, as shown in Fig. C6-1.

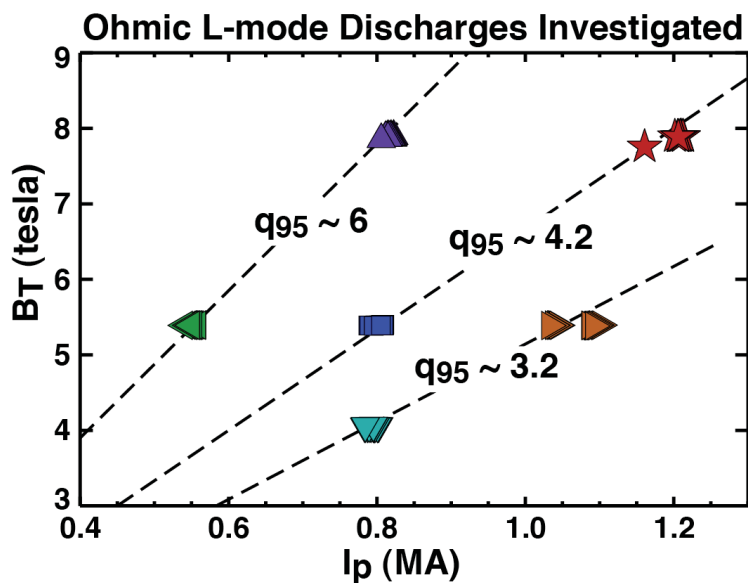


Fig. C6-1. Engineering parameter space explored during resumed Ohmic L-mode studies, executed on four run days – July, August 2010 (MP#570). For each current-field pair, density scans were performed, spanning normalized densities over the range  $0.12 < n/n_G < 0.31$ .

Outer divertor strike-point sweeps were performed while holding discharge parameters otherwise unchanged. In this way, parallel divertor heat flux profiles could be recorded on embedded Langmuir probes and surface thermocouple sensors (see Fig. C3-2). Good agreement was obtained between these two diagnostics in low and moderate recycling regimes. However, some substantial deviations are seen in high recycling regimes, with Langmuir probes recording anomalously high heat fluxes. Such cross-comparisons among diagnostics have been found essential to weed-out potentially erroneous heat flux measurements in the data set. Although a careful analysis of the data

remains to be performed, preliminary analysis reveals that, unlike in EDA H-modes, heat flux widths in ohmic L-modes exhibit a  $\sim 1/I_p$  scaling. Figure C6-2 shows heat flux profiles recorded by embedded Langmuir probes for normalized discharge densities in the range of  $0.12 < n/n_G < 0.17$ , a regime where the two diagnostics are in agreement. The corresponding e-folding distances in the common flux zone (Fig. C6-3), display an approximate inverse scaling with  $I_p$  and no sensitivity to magnetic field strength.

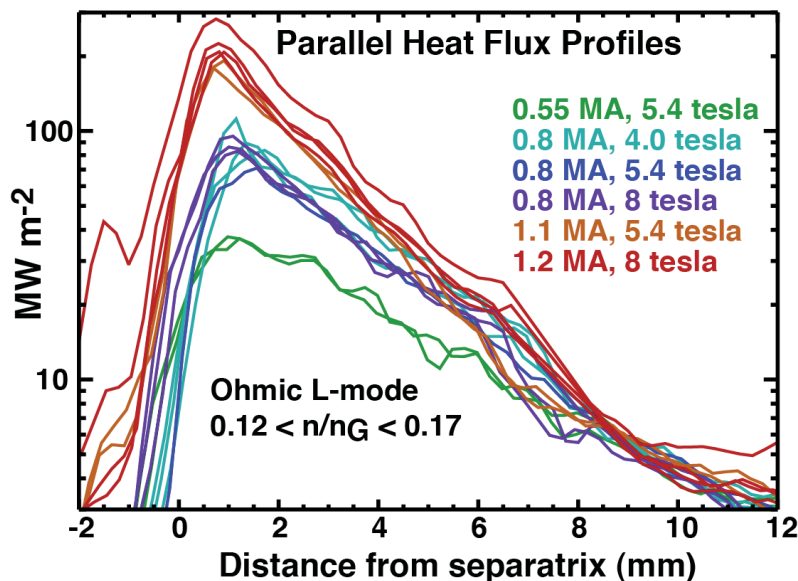


Fig. C6-2. Parallel heat flux profiles on the outer divertor surface as recorded by embedded Langmuir probes. Data are flux-surface mapped to the outer midplane.

These data make contact with previous investigations of boundary layer pressure profiles in ohmic L-modes [29]. In that study, normalized pressure gradients ‘upstream’ at outer midplane (i.e., normalized by plasma current squared) were found to be invariant at a fixed collisionality; no sensitivity to magnetic field strength was detected. An in-depth analysis of these discharges is presently underway, with the goal of presented the latest results at the 2010 November APS meeting.

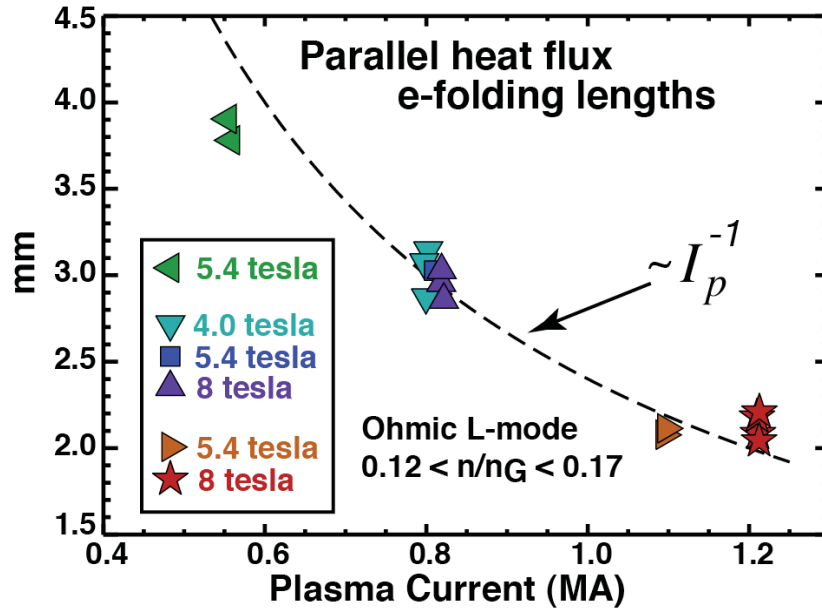


Fig. C6-3. Parallel heat flux profile e-folding lengths on the outer divertor, plotted versus plasma current. These data show an approximately inverse scaling with plasma current and no scaling with toroidal field strength.

## 7. Measurements of Boundary Layer Turbulence

We are not able to predict heat-flux widths from first-principles' theory and modeling. This is the case partly because turbulent transport – also not yet predicted from first principles' modeling - no doubt plays an important role in setting this important measure. The study of the edge and SOL turbulence was therefore recognized as an essential part of this JRT research; diagnostics sensitive to turbulence in the edge and SOL were engaged for almost all of the runs dedicated to the heat-flux footprint investigations. On C-Mod, Gas-Puff-Imaging (GPI) was the primary turbulence diagnostic in the study. Phase Contrast Imaging (PCI) and three scanning Langmuir probes were also active turbulence diagnostics. Two GPI systems view the outboard edge of the plasma near the plasma midplane. One is a 9x10 array of views coupled to Avalanche Photo-Diodes (APDs)[30]. Each view images a 3.5 mm diameter spot in the (R,θ) plane at the toroidal location of a local gas-puff nozzle. This sensitive, low-noise system has a Nyquist frequency of 1 MHz. The second GPI system images a 2D region slightly larger than that viewed by the APD array onto an ultra-fast framing camera. The spatial resolution of the camera imaging is ~2 mm. Over the course of these experiments,

cameras with maximum Nyquist frequencies of 125 kHz and 200 kHz were employed. The camera views the plasma with sightlines approximately aligned with the local magnetic field when  $q_{95}=3.5$ , while the APD system views are purely toroidal. Some of the results are summarized here, although much of the turbulence data is still being analyzed.

We make the distinction in this section between the ‘edge region’, i.e. the region  $\sim 2$  cm just inside the separatrix, and the ‘near’ and ‘far’ SOL. The near SOL is the  $\sim 3$  mm just beyond the separatrix carrying most of the parallel SOL heat-flux, and the far SOL is the region beyond that where blobs/filaments are the dominant manifestation of particle transport. The edge region also contains the pedestal of H-mode plasmas. Figure C7-1 shows these regions, as well as a raw image from the GPI fast-camera containing a clear ‘blobby’ transport event.

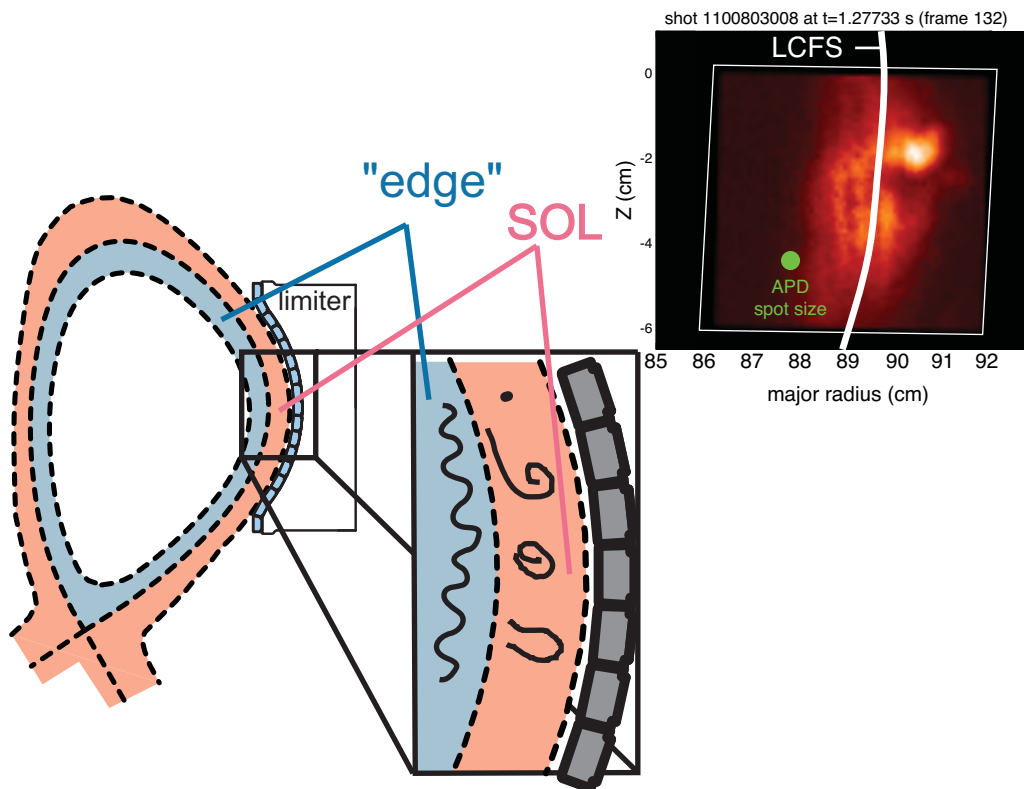
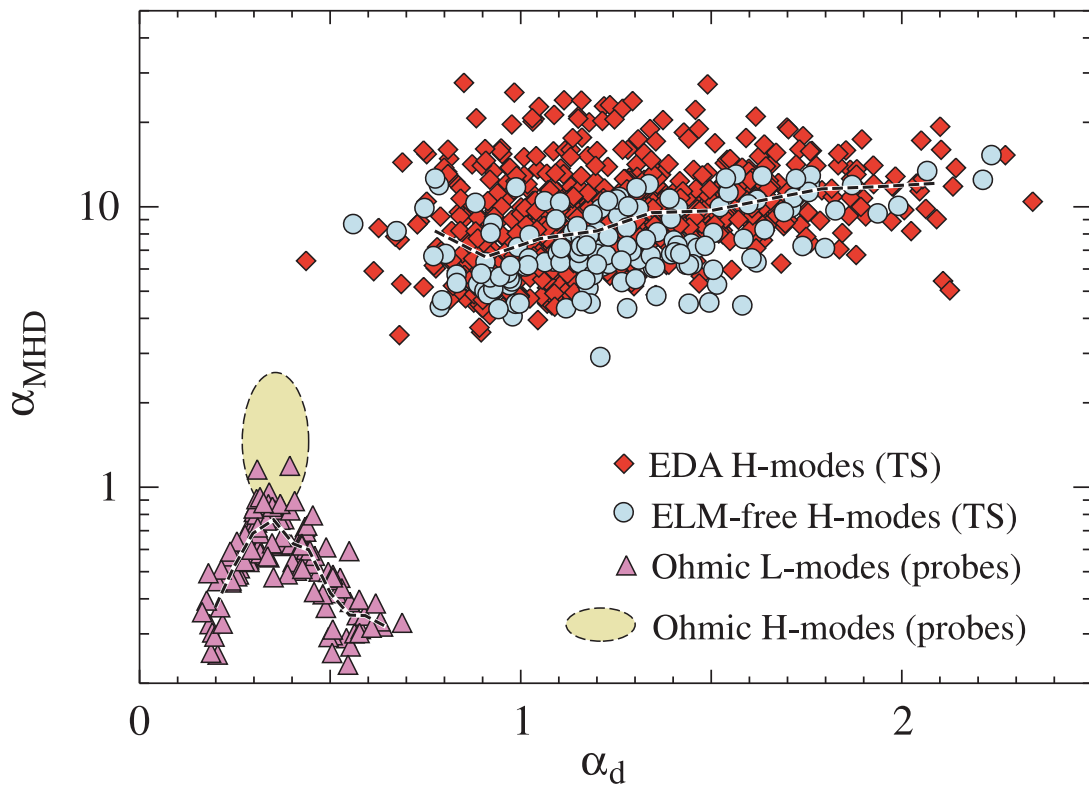


Fig. C7-1. Schematic of edge and SOL regions in GPI diagnostics' views, illustrating “wavelike” turbulence in the edge emerging as blobs and propagating out through the SOL. In the upper right is a raw GPI camera image with a blob present in the SOL at  $R_{maj} \sim 90.5$  cm.

### 7.1 Turbulence near the last-closed flux surface

It is reasonable to ask why we are investigating the turbulence in the *edge* (in addition to the SOL), when the heat-flux width in the SOL and footprint on the target are the primary subjects of interest. The answers to that question are: (1) there is evidence (see section 5.4) that the pedestal transport “spills over” into the near SOL affecting the heat flux width, and we seek to determine the physics of this phenomenon, (2) the edge fluctuation dominating the pedestal particle transport in EDA H-mode plasmas is the Quasi-Coherent Mode (QCM) [31], and, while the QCM is strongest in the edge region, GPI measurements show that it extends into the near SOL, and (3) both the H-mode pedestal [25] and the near SOL [29] exhibit “critical-gradient”-like transport responses,



*Fig. C7-2. Near SOL (using probes) and H-mode pedestal data cast into a dimensionless phase space suggested by electromagnetic fluid drift turbulence theory. SOL data are taken at the point of minimum pressure gradient scale length in the near SOL of ohmic discharges with  $I_P$  ranging from 0.5 to 1.0 MA. H-mode points are from discharges with  $0.4 < I_P < 1.7$  MA at various  $B_r$ . The dashed lines represent the median value of measured  $\alpha_{MHD}$  as a function of  $\alpha_d$  (from [25]).*

i.e., pressure gradients normalized by the square of the poloidal field ( $\alpha_{\text{MHD}} = 2\mu_0 R \nabla p / B_p^2$ ) tend to be invariant for the same value of normalized (inverse) collisionality parameter ( $\alpha_d \sim 1/q \times (\lambda_{\text{ei}}/R)^{0.5}$ ). This behavior is shown for both the pedestal and the near SOL in Fig. C7-2.

The QCM has been shown to be localized in the edge region, although GPI measurements also show that it extends into the near SOL. The QCM has also been shown to affect particle transport through the pedestal, increasing the particle loss rate over ELM-free H-mode levels, such that core density and impurity levels are regulated and held nearly constant in time. Evidence of this role in edge particle transport is shown in Fig. C7-3. The QCM is measured by GPI to be a mode propagating in the electron diamagnetic drift direction with  $k_{\text{pol}}^{\text{QCM}} \rho_s \sim 0.1$ . A typical conditional ( $k_{\text{pol}}, f$ ) spectrum of the GPI edge fluctuations during EDA H-mode is shown in Fig. C7-4. The changes that occur in the frequency spectra of the electron-diamagnetic drift-directed (EDD) fluctuations through the transitions from L-mode to ELM-free H-mode to EDA H-mode are shown in Fig. C7-4. The  $\sim \times 10$  increase in the fluctuation levels in going from ELM-

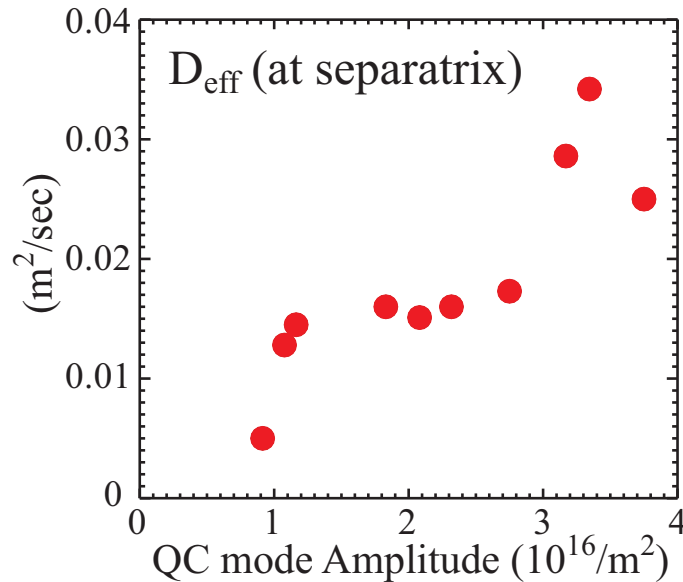


Fig. C7-3. Increase of  $D_{\text{eff}}$  with the increase of the QCM amplitude. Here  $D_{\text{eff}} \equiv -\Gamma_{\text{perp}} / \nabla n_e$ ,  $\nabla n_e$  is determined from probe measurements and  $\Gamma_{\text{perp}}$  is inferred from spatially-resolved measurements of the ionization source. The QCM amplitude is the line integral of the density fluctuation within the QCM frequency feature (from [30]).

free to EDA is further evidence for the QCM and EDD turbulence in the edge driving particle transport. Of special interest for this work is the role of the QCM in the heat-flux width; this is presently under investigation.

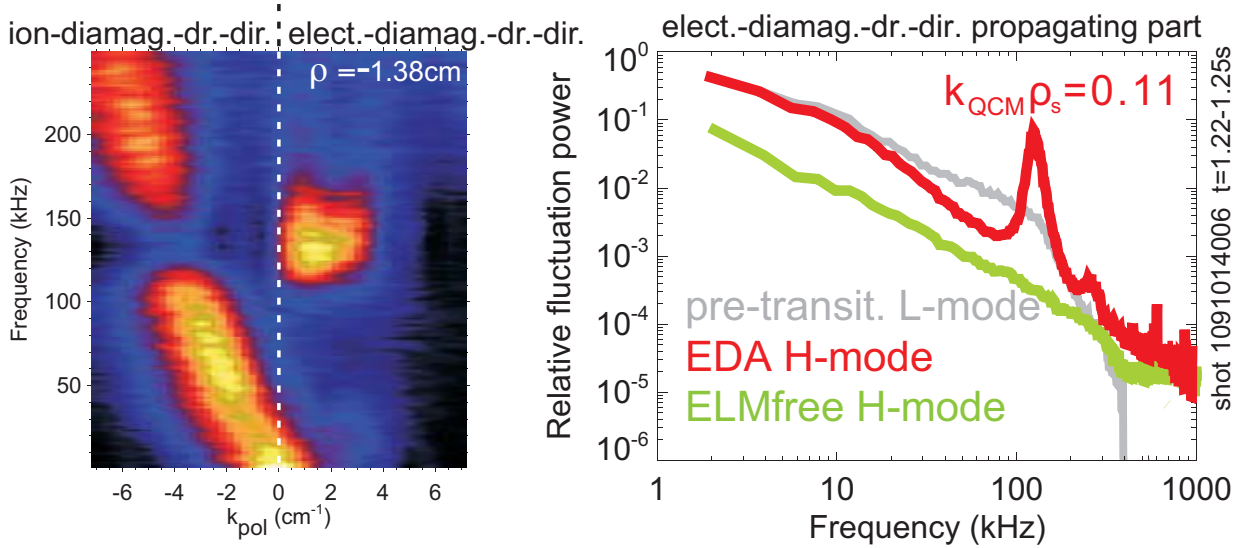


Fig. C7-4. Left – conditional  $(k_{pol}, f)$  spectrogram of the edge turbulence in an ICRF-heated EDA H-mode, showing the EDD propagating QCM, as well as broadband turbulence propagating in the ion-diamagnetic-drift direction. Right – spectra of the EDD edge turbulence in the pre-H-mode phase (gray), the ELM-free H-mode phase (green), and the EDA H-mode phase (red) with the QCM at  $f=130$  kHz. Note the  $\sim 10$  decrease in the fluctuation level in ELM-free H-mode.

In L-mode discharges the QCM is not seen, but turbulence with similar size scales is present under these conditions as well. Bispectral analyses of the spectra show that the energy input to the EDD fluctuations is occurring with the same spatial scale for both L- and EDA H-modes, i.e. with  $k_{pol}^{input} \rho_s \sim 0.1$ . The evolution of the EDD turbulence as a function of normalized density in L-mode is shown in Figure C7-5.

As is evident, the power in the EDD edge turbulence increases with increased normalized density and/or with increased  $\beta_p$ , plotted in Figure C7-6. The particle flux through the SOL also increases with these parameters, as can be seen in Figure C7-7. We take this as additional evidence that the *EDD edge* turbulence is responsible for transport into the SOL.

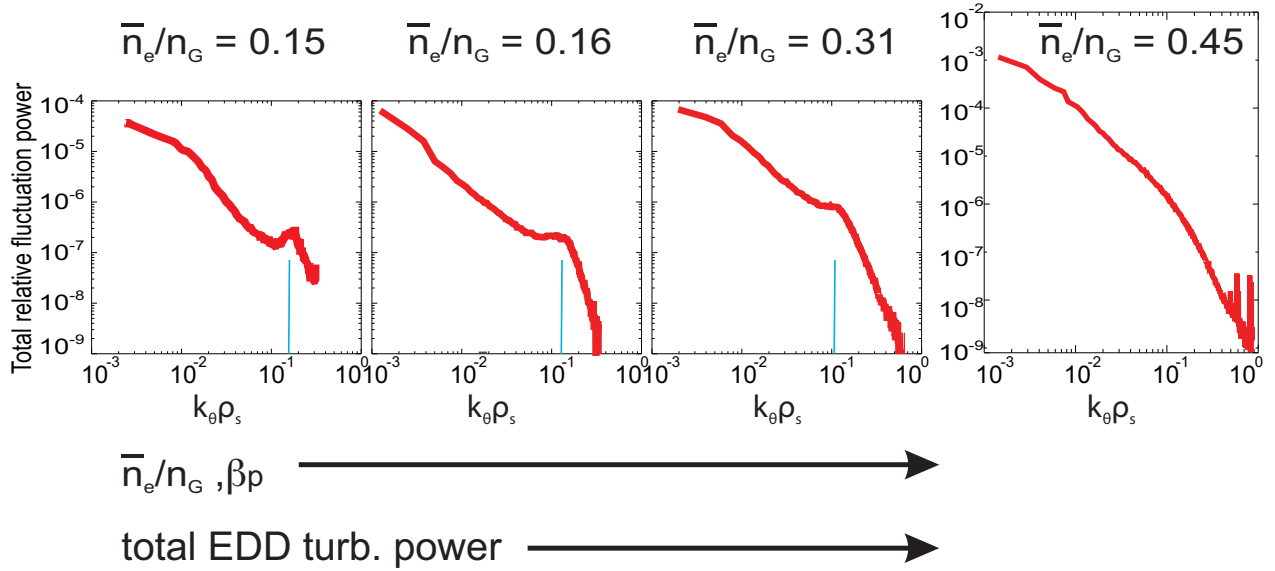


Fig. C7-5. The total spectral power in the EDD edge turbulence shows a strong dependence on normalized density,  $n_e/n_G$ , and on  $\beta_p$  (see Fig. C7-6) in L-mode discharges. The spectral distribution also shows strong dependence on these quantities. There is a clear local maximum or break-in-slope at  $k_{pol} \rho_s \sim 0.1$  in each of these spectra (blue line). Bispectral analyses of the spectra show that the energy input to the EDD turbulence has the same spatial scale for both L- and EDA H-modes.

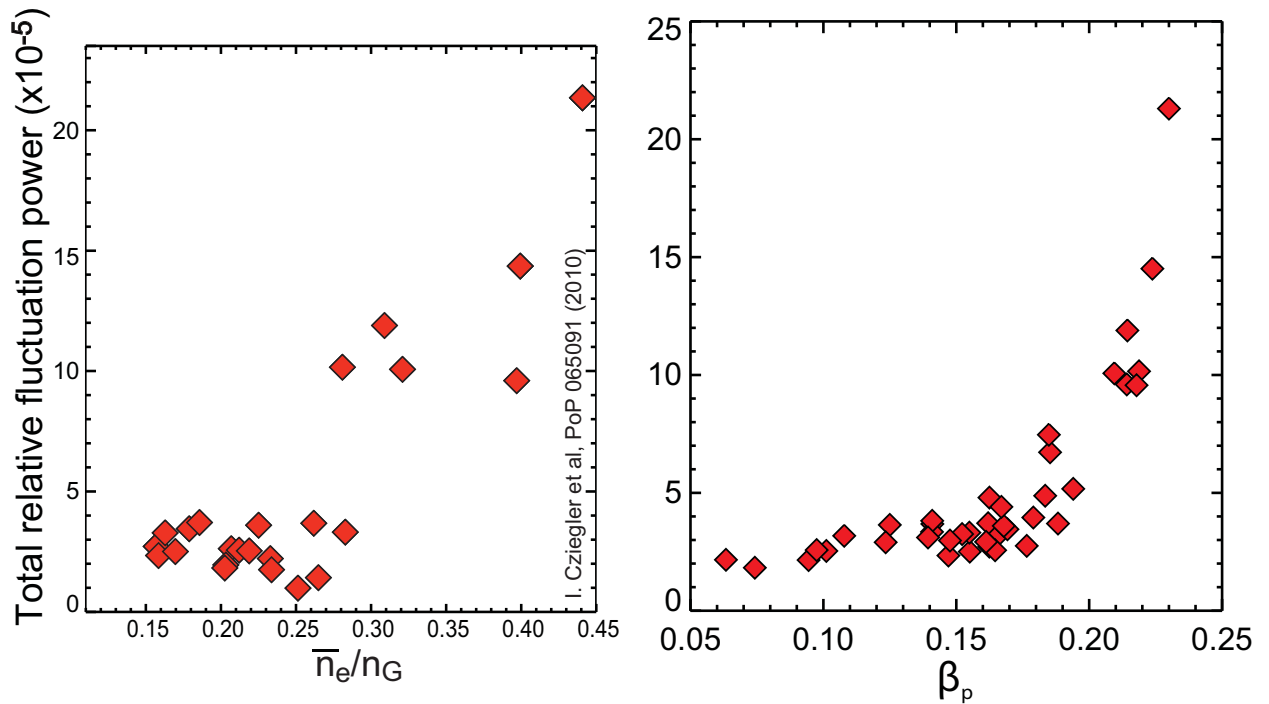


Fig. C7-6. (left) Power in the EED edge turbulence vs normalized density,  $n_e/n_G$ . (right) Power in the EED edge turbulence vs  $\beta_p$ . The physical variable  $\beta_p$  seems to parameterize the increase in turbulence power more sensitively than  $n_e/n_G$ .

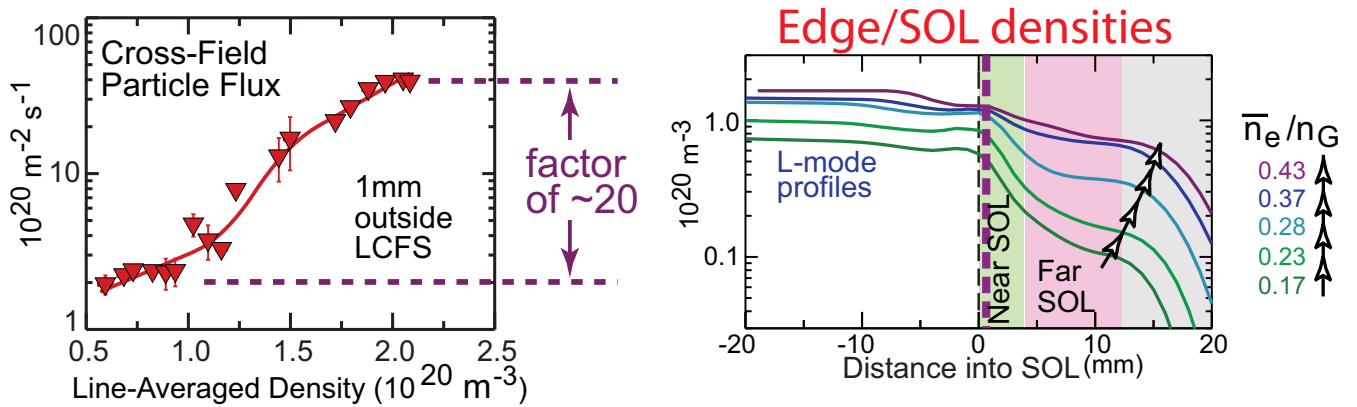


Fig. C7-7. Changes seen in the near SOL flux (left) and the SOL density profiles (right) as a function of normalized density. Combined with the scaling of the EDD edge turbulence shown in Fig. C7-6, we interpret the large increases in particle fluxes into the SOL shown here as evidence that the EDD propagating edge turbulence is a major driver of transport into the SOL.

## 7.2 Turbulence in the Far SOL

Far SOL turbulence is dominated by blobs and blob transport. An analysis of GPI camera data from the far SOL has been done [31] in order to estimate the effect of the convective radial transport of SOL turbulence on the SOL density scale length,  $\lambda_n$ . Results were obtained for a series of ohmic discharges covering  $I=0.4\text{-}1.1$  MA at constant  $q_{95}$  and moderate density. The average radial turbulence speed within  $\rho=1\text{-}2$  cm near the outer midplane was calculated by a 2-D cross-correlation technique to be  $V_r \sim 0.2\text{-}0.3$  km/sec. Assuming this to be the local convective plasma velocity, the SOL density scale length was evaluated using a simple convective model to be  $\lambda_n \sim 4\text{-}7$  cm, which is  $\sim 2\text{-}3$  times higher than that measured using one of the scanning Langmuir probes (see Fig. C7-8). The GPI-derived result has at least a factor-of-two uncertainty; for example, the average parallel connection length is taken to be  $L_{||} \sim 5$  m, but is actually varying by a factor-of-two over  $\rho=1\text{-}2$  cm, and is also different by factor-of-two in the two different directions along the magnetic field. The probe-derived results for  $\lambda_n$  are also uncertain by up to a factor-of-two. Thus the level of disagreement shown in Fig. C7-8 is not too surprising, given these uncertainties. We also note that the convective velocity measured this way is  $\sim 2\text{-}3$  times lower than the velocities estimated from analytic blob-dynamic

models [32-34], but exhibits a scaling similar to the models with plasma current at constant  $q_{95}$ .

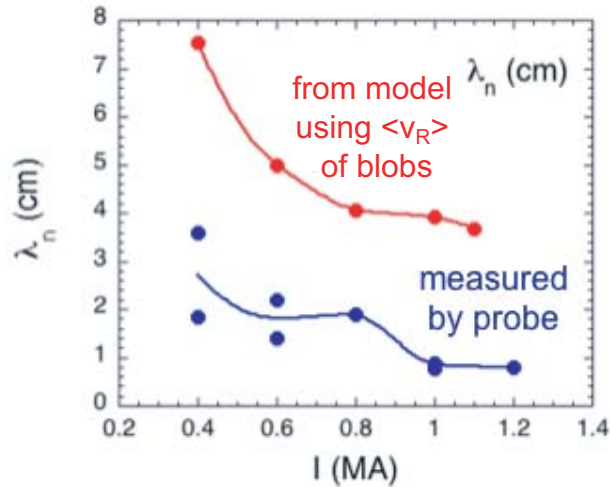


Fig. C7-8. The density profile scrape-off-layer scale lengths as a function of plasma current, where the scale lengths are calculated using the radial velocity of the emission structures (see text). These are compared with the scale lengths that were measured with a scanning probe. The SOL region investigated is  $\rho=1-2$  cm.

## 8. Modeling activities initiated through external collaborations

Guidance from theoretical models and numerical simulations is essential to understand the physics that determines the heat-flux footprint widths in tokamaks. As stated in the FY2010 milestone text, an important component of the JRT was to generate high-quality data that could be compared with theory and simulation. Indeed, representatives of the theory/modeling community participated fully in the JRT organizational meetings, the experimental planning and the discussions of initial results that were obtained by the three experiments. At C-Mod, special provisions were made to share experimental data directly with interested external modeling groups. In order to facilitate this, a data receptacle was set up where all processed data files relevant to modeling efforts were placed. This framework for data storage and transfer will help support subsequent JRT modeling efforts. Local directories were organized according to the C-Mod discharge (shot number) and time-in-the-discharge. With each data set were associated an ASCII file, an IDL save set file, and an explanatory text file. In addition to the experimental values, the files contained explanations of what the tabulated quantities were, the units of the quantities, how and when the files were generated. At the present

time directories for three key shot/time-slices have been populated. The directory files for the relevant time-slices were subsequently e-mailed to the participating modeling groups. In parallel, we are evaluating different methods for sharing this data repository directly over the internet with our external collaborators.

The groups that are presently participating in the modeling of C-Mod JRT results are (in no particular order), the Center for Plasma Edge Simulation (CPES) group using the XGC0 code, Gary Porter (LLNL) using the UEDGE code, D. D'Ippolito, J. Myra, and D. Russell of Lodestar Corporation using the SOLT code, and R. Goldston (PPPL) using analytical modeling of parallel and perpendicular heat-flux. Results from initial modeling efforts are reported by each group in individual sections of the FY2010 JRT final report. Here we summarize the set of C-Mod experiments that were targeted for modeling and the data that were supplied to these groups.

CPES – using the XGC0 code, a time-slice from the C-Mod/DIHD similarity discharge (see Sections 5.1 and 5.2) is being modeled. Supplied processed data were: core, edge, and SOL profiles of  $n_e$  and  $T_e$ , high-resolution EFIT equilibrium, profiles of heating powers, radiated power profile, toroidal rotation profile, and Zeff.

LLNL – using the UEDGE code, a time-slice from the C-Mod/DIHD similarity discharge is being modeled. Supplied processed data were: edge and SOL profiles of  $n_e$  and  $T_e$ , high-resolution EFIT equilibrium, heat-flux profile on the outer target, and divertor Langmuir probe measurements.

Lodestar Corp. – using the SOLT turbulence code, two time-slices (EDA 1 and EDA 2 – see Section 5.4) from an EDA H-mode discharge are being modeled. Supplied processed data were: edge and SOL profiles of  $n_e$ ,  $T_e$ , the profiles of the connection lengths in the SOL,  $P_{SOL}$ , profiles of  $B_t$  and  $B_p$ . Future work with this group will include the exchange of measured and simulated GPI images, GPI analyses, as well as additional modeling of L-mode discharges of varying plasma currents, toroidal magnetic fields and collisionalities (i.e., a subset of the discharges presented in section 6).

R. Goldston – Dr. Goldston's research on the subject on heat-flux parallel and perpendicular to B was published in references[12, 35]. He visited C-Mod in March 2010 and discussed his ideas and research with C-Mod staff. Subsequent communications with C-Mod centered around ideas about how to determine the separatrix location from power

balance arguments and about the heat-flux on leading edges on material surfaces that are intersected by open field lines (so-called “scrapers”).

### Acknowledgements

We wish to thank the entire Alcator C-Mod team for their excellent work that makes these experiments possible. This research is supported by U.S. D.o.E. Coop. Agreement DE-FC02-99ER54512.

### References

- [1] Kirnev, G., Fundamenski, W., and Corrigan, G., "*Modelling of ELM-averaged power exhaust on JET using the EDGE2D code with variable transport coefficients*," Plasma Physics and Controlled Fusion 49 (2007) 689.
- [2] Loarte, A., Bosch, S., Chankin, A., Clement, S., Herrmann, A., Hill, D., Itami, K., Lingertat, J., Lipschultz, B., McCormick, K., Monk, R., Porter, G.D., Shimada, M., and Sugihara, M., "*Multi-machine scaling of the divertor peak heat flux and width for L-mode and H-mode discharges*," Journal of Nuclear Materials 266-269 (1999) 587.
- [3] Loarte, A., Lipschultz, B., Kukushkin, A.S., Matthews, G.F., Stangeby, P.C., Asakura, N., Counsell, G.F., Federici, G., Kallenbach, A., Krieger, K., Mahdavi, A., Philipps, V., Reiter, D., Roth, J., Strachan, J., Whyte, D., Doerner, R., Eich, T., Fundamenski, W., Herrmann, A., Fenstermacher, M., Ghendrih, P., Groth, M., Kirschner, A., Konoshima, S., LaBombard, B., Lang, P., Leonard, A.W., Monier-Garbet, P., Neu, R., Pacher, H., Pegourie, B., Pitts, R.A., Takamura, S., Terry, J., and Tsitroni, E., "*Chapter 4: Power and particle control*," Nuclear Fusion 47 (2007) S203.
- [4] Kallenbach, A., Asakura, N., Kirk, A., Korotkov, A., Mahdavi, M.A., Mossessian, D., and Porter, G.D., "*Multi-machine comparisons of H-mode separatrix densities and edge profile behaviour in the ITPA SOL and Divertor Physics Topical Group*," Journal of Nuclear Materials 337-339 (2005) 381.
- [5] LaBombard, B., Terry, J.L., Hughes, J.W., Brunner, D., Payne, J., Reinke, M., Lin, Y., and Wukitch, S., "*Divertor heat flux footprints in EDA H-mode discharges on Alcator C-Mod*," accepted for publication in Journal of Nuclear Materials (2010).
- [6] Maqueda, R.J., Wurden, G.A., Terry, J.L., and Stillerman, J.A., "*The new infrared imaging system on Alcator C-Mod*," Rev. Sci. Instrum. 70 (1999) 734.

- [7] Terry, J.L., LaBombard, B., Brunner, D., and Payne, J., "*Measurements of heat-flux profiles on the divertor target of Alcator-C-Mod using IR thermography*," accepted for publication in Review of Scientific Instruments (2010).
- [8] Brunner, D., LaBombard, B., Payne, J., and Terry, J.L., "*Comparison of heat flux measurements by IR thermography and probes in the Alcator C-Mod divertor*," to be published in Journal of Nuclear Materials (2010).
- [9] LaBombard, B., Terry, J.L., Reinke, M.L., Brunner, D., and Payne, J., *MP#557: Commissioning of new divertor heat flux diagnostics*. 2009: <http://www.psf.mit.edu/cm/operations/miniproposals/557.pdf>.
- [10] LaBombard, B., Terry, J.L., Reinke, M.L., Brunner, D., Payne, J., Cziegler, I., Greenwald, M., Hughes, J.W., Lipschultz, B., Whyte, D., and Zweben, S., *MP#570: Boundary layer heat transport experiments in L-mode plasmas*. 2009: <http://www.psf.mit.edu/research/alcator/miniproposals/570.pdf>.
- [11] LaBombard, B., Brunner, D., Payne, J., Reinke, M., Terry, J.L., Hughes, J.W., Lipschultz, B., and Whyte, D., "*Initial results from divertor heat-flux instrumentation on Alcator C-Mod*," Bull. Amer. Phys. Soc. <http://meetings.aps.org/link/BAPS.2009.DPP.PP8.20> (2009).
- [12] Goldston, R.J., "*Downstream heat flux profile vs. midplane T profile in tokamaks*," submitted to Journal of Nuclear Materials (2010).
- [13] Algor simulation software, <http://www.algor.com/>.
- [14] Hermann, A., "Limitations for divertor heat flux calculations of fast events in tokamaks," presented at the 28th EPS Conference on Controlled Fusion and Plasma Physics, Madeira, Portugal, 2001.
- [15] Brunner, D., LaBombard, B., Terry, J.L., and Reinke, M., "*Measurements of plasma sheath heat flux in the Alcator C-Mod divertor*," to be presented at the November 2010 APS meeting in Chicago. (2010).
- [16] LaBombard, B., Terry, J.L., Hughes, J.W., Lasnier, C., Maingi, R., Brunner, D., Payne, J., Reinke, M., Cziegler, I., Zweben, S., Lin, Y., and Wukitch, S., *MP#591: Boundary layer heat transport experiments in H-mode plasmas*. 2010: <http://www.psf.mit.edu/research/alcator/miniproposals/591.pdf>.
- [17] Greenwald, M., Boivin, R., Bonoli, P., Budny, R., Fiore, C., Goetz, J., Granetz, R., Hubbard, A., Hutchinson, I., Irby, J., LaBombard, B., Lin, Y., Lipschultz, B., Marmor, E., Mazurenko, A., Mossessian, D., Sunn Pedersen, T., Pitcher, C.S., Porkolab, M., Rice, J., Rowan, W., Snipes, J., Schilling, G., Takase, Y., Terry, J., Wolfe, S., Weaver, J., Welch, B., and Wukitch, S., "*Characterization of enhanced*

- D alpha high-confinement modes in Alcator C-Mod,*" AIP. Physics of Plasmas 6 (1999) 1943.
- [18] Lasnier, C.J., Boedo, J.A., Leonard, A.W., Makowski, M.A., and Watkins, J.G., *Inter-machine comparisons for heat flux scaling & ELM heat.* 2010: D3DMP No. 2010-62-02.
- [19] Mossessian, D., Hubbard, A.E., Pedersen, T.S., Granetz, R.S., Boivin, R.L., Greenwald, M., Hughes, J., Irby, J., Johnson, D., LaBombard, B., Lin, Y., Mazurenko, A., Nazikian, R., Pitcher, C.S., Taylor, G., and Wolfe, S.M., *"Measurements and scalings of the H-mode pedestal on Alcator C-Mod,"* IOP Publishing. Plasma Physics & Controlled Fusion 42 (2000) 27.
- [20] Reinke, M.L. and Hutchinson, I., *"Two dimensional radiated power diagnostics on Alcator C-Mod,"* Rev. Sci. Instrum. 79 (2008) 10F306.
- [21] Soukhanovskii, V.A., Maingi, R., Gates, D.A., Menard, J.E., Paul, S.F., Raman, R., Roquemore, A.L., Bell, R.E., Bush, C.E., Kaita, R., Kugel, H.W., LeBlanc, B.P., and Mueller, D., *"Divertor heat flux mitigation in high-performance H-mode discharges in the national spherical torus experiment,"* Nuclear Fusion 49 (2009) 095025 (10 pp.).
- [22] Lasnier, C.J., Hill, D.N., Petrie, T.W., Leonard, A.W., Evans, T.E., and Maingi, R., *"Survey of target plate heat flux in diverted DIII-D tokamak discharges,"* Nuclear Fusion 38 (1998) 1225.
- [23] LaBombard, B., Rice, J.E., Hubbard, A.E., Hughes, J.W., Greenwald, M., Irby, J.H., Lin, Y., Lipschultz, B., Marmor, E.S., Smick, N., Wolfe, S.M., and Wukitch, S.J., *"Transport-Driven Scrape-off Layer Flows and the Boundary Conditions Imposed at the Magnetic Separatrix in a Tokamak Plasma,"* Nuclear Fusion 44 (2004) 1047.
- [24] LaBombard, B., Goetz, J.A., Hutchinson, I., Jablonski, D., Kesner, J., Kurz, C., Lipschultz, B., McCracken, G.M., Niemczewski, A., Terry, J., Allen, A., Boivin, R.L., Bombarda, F., Bonoli, P., Christensen, C., Fiore, C., Garnier, D., Golovato, S., Granetz, R., Greenwald, M., Horne, S., Hubbard, A., Irby, J., Lo, D., Lumma, D., Marmor, E., May, M., Mazurenko, A., Nachtrieb, R., Ohkawa, H., O'Shea, P., Porkolab, M., Reardon, J., Rice, J., Rost, J., Schachter, J., Snipes, J., Sorci, J., Stek, P., Takase, Y., Wang, Y., Watterson, R., Weaver, J., Welch, B., and Wolfe, S., in Plasma Physics and Controlled Fusion Research 1996 (Proc. 16th Int. Conf., Montreal, 1996), Vol. 1, IAEA, Vienna (1997) 825.
- [25] Hughes, J.W., LaBombard, B., Terry, J., Hubbard, A., and Lipschultz, B., *"Edge profile stiffness and insensitivity of the density pedestal to neutral fuelling in Alcator C-Mod edge transport barriers,"* Nuclear Fusion 47 (2007) 1057.

- [26] Bevington, P.R., *Data reduction and error analysis for the physical sciences* (McGraw-Hill, New York, 1969).
- [27] Lasnier, C., Makowski, M.A., Boedo, J.A., Allen, S.L., Brooks, N.H., Hill, D., Leonard, A.W., Watkins, J.G., and West, W.P., "*Scaling of divertor heat flux profile widths in DIII-D,*" to be published in *Journal of Nuclear Materials* (2010).
- [28] Maingi, R., *Presentation at the NSTX PAC meeting.* 2010: February 3-5, 2010.
- [29] LaBombard, B., Hughes, J.W., Smick, N., Graf, A., Marr, K., McDermott, R., Reinke, M., Greenwald, M., Lipschultz, B., Terry, J.L., Whyte, D.G., and Zweben, S.J., "*Critical gradients and plasma flows in the edge plasma of Alcator C-Mod,*" *Physics of Plasmas* 15 (2008) 056106.
- [30] Terry, J.L., Basse, N.P., Cziegler, I., Greenwald, M., Grulke, O., LaBombard, B., Zweben, S., Edlund, E.M., Hughes, J.W., Lin, L., Porkolab, M., Sampsell, M., Veto, B., and Wukitch, S.J., "*Transport phenomena in the edge of Alcator C-Mod plasmas,*" *Nuclear Fusion* 45 (2005) 1321.
- [31] Zweben, S.J., Terry, J.L., LaBombard, B., Agostini, M., Greenwald, M., Grulke, O., Hughes, J.W., D'Ippolito, D.A., Krasheninnikov, S.I., Myra, J.R., Russell, D.A., Stotler, D.P., and Umansky, M., "*Estimate of Convective Radial Transport due to SOL Turbulence as Measured by GPI in Alcator C-Mod,*" accepted for publication in *Journal of Nuclear Materials* (2010).
- [32] Krasheninnikov, S.I., D'Ippolito, D.A., and Myra, J.R., "*Recent theoretical progress in understanding coherent structures in edge and SOL turbulence,*" *Journal of Plasma Physics* 74 (2008) 679.
- [33] Myra, J.R., D'Ippolito, D.A., Stotler, D.P., Zweben, S.J., LeBlanc, B.P., Menard, J.E., Maqueda, R.J., and Boedo, J., "*Blob birth and transport in the tokamak edge plasma: Analysis of imaging data,*" *Physics of Plasmas* 13 (2006) 092509.
- [34] Myra, J.R., D'Ippolito, D.A., Krasheninnikov, S.I., and Yu, G.Q., "*Convective transport in the scrape-off-layer by nonthermalized spinning blobs,*" *Physics of Plasmas* 11 (2004) 4267.
- [35] Goldston, R.J., "*Downstream heat flux profile versus midplane T profile in tokamaks,*" *Physics of Plasmas* 17 (2010) 012503.

**DIII-D CONTRIBUTION TO  
2010 OFES JOINT RESEARCH  
TARGET  
DIVERTOR HEAT FLUX PROFILE  
WIDTH**

**FINAL REPORT**

**BY**

**C.J. LASNIER, M.A. MAKOWSKI, J.A. BOEDO, D.N.  
HILL, A.W. LEONARD, G.D. PORTER, M.E. RENSINK,  
J.G. WATKINS, AND DIII-D STAFF**

## DESCRIPTION OF DELIVERABLE

Conduct experiments on major fusion facilities to improve understanding of the heat transport in the tokamak scrape-off layer (SOL) plasma, strengthening the basis for projecting divertor conditions in ITER. In FY10, FES will measure the divertor heat flux profiles and plasma characteristics in the tokamak scrape-off layer in multiple devices to investigate the underlying thermal transport processes. The unique characteristics of C-Mod, DIII-D, and NSTX will enable collection of data over a broad range of SOL and divertor parameters (e.g., collisionality, beta, parallel heat flux, and divertor geometry). Regimes similar to the ITER operating scenarios will be among those studied and characterized. Coordinated experiments using common analysis methods will generate a data set that will be compared with theory and simulation.

## DEFINITION OF COMPLETION

Final Report

## I. INTRODUCTION

Heat in a tokamak is transported from the confined core plasma to the edge in a process characterized by the energy confinement time. Energy crossing from the closed field lines to the open field lines at the edge is carried along field lines by ions and electrons while continuing to move outward across field lines due to particle collisions, drifts, and instabilities. Some fraction of the energy is radiated by collisionally excited ions along the way. The open field lines, which form a region called the scrape-off layer (SOL) connect to a limiter or to one or more divertors, where the remaining particle energy is deposited on plasma facing components. Most present and planned tokamaks are designed with divertors, a physical structure combined with a magnetic configuration that gives superior control of impurities. In a divertor the heating of the solid surface is concentrated at the strike points, where the field lines intersect that surface.

The width of the heat flux profile in the divertor  $\lambda_{q,div}$  is important to know for the design of future high-power tokamaks. The divertor must be carefully designed to survive the heating by the plasma. To facilitate such designs, we must be able to predict the heat flux by understanding the physics controlling the heat flux profile width on present-day tokamaks, and understand how increases in size, heating power, and plasma temperature will affect that profile in future machines. Prior work studying the parametric dependence of  $\lambda_{q,div}$  have arrived at a variety of scalings [1] for JET [2], ASDEX-Upgrade [3], JT60-U [4,5], DIII-D [6,7], and NSTX [8], which are not all in agreement. The work discussed here is intended to solidify the foundation for the physics understanding of the processes governing  $\lambda_{q,div}$ .

Experiments were performed in DIII-D both independently and jointly with the National Spherical Torus Experiment (NSTX) at PPPL and the C-Mod experiment at MIT. The C-Mod experiments were most closely coordinated since we were able to match more of the relevant plasma parameters between C-Mod and DIII-D than between NSTX and DIII-D. By matching those parameters and examining the differences in the resulting SOL transport, we expect to gain new understanding of those transport mechanisms. The analysis and modeling of this data from the joint experiments is still ongoing and we expect it to be fruitful for some time to come.

The experiments in DIII-D were aimed at both extracting an empirical scaling of the divertor heat flux profile width, and measuring fundamental plasma characteristics to enable detailed numerical modeling of energy transport in the scrape-off layer (SOL). We performed multiple overlapping scans in which most plasma parameters were held fixed while some other parameter was varied, including density, toroidal field, plasma current,

edge safety factor, and input power. Empirical scaling of the divertor heat flux width has been derived. We found that the heat flux width was dependent mainly upon the plasma current, varying inversely as the 1.2 power of the plasma current. We also obtained edge fluctuation data of the electron density and temperature, to identify the effect of fluctuations on SOL energy transport.

Ultimately the best prediction of the heat flux profile should be obtained by using numerical models that have been shown to contain the appropriate physics by comparing the model with a wide variety of data from existing experiments. Preliminary numerical modeling of these data has begun, using the UEDGE code.

## II. EXPERIMENTS AND DATA

The initial heat flux experiments discussed here were carried out in 2008. We performed measurements in lower single-null H-mode diverted configurations operated with edge localized modes (ELMs). We varied toroidal field ( $B_T$ ) at constant plasma current ( $I_p$ ),  $I_p$  at constant  $B_T$ , and  $B_T/I_p$  at constant  $q_{95}$ . The neutral beam injected power  $P_{inj}$  was changed at constant  $I_p$  and  $B_T$ . Line-averaged density  $\bar{n}_e$  was varied at constant  $I_p$  and  $B_T$ . The divertor heat flux was calculated from infrared camera measurements using a new high-resolution fast-framing IR camera.

### A. Analysis averaged over ELMS

The initial analysis was carried out by averaging over ELMs. This is reasonable because the ELMs carry less than 20% of the time-averaged heat flux [7]. Time windows in the discharges were chosen for nearly constant conditions except for ELMs, and heat flux profiles were averaged over each interval. The full width of the heat flux profile at half-maximum was extracted from each averaged profile and analyzed. The detailed results of this analysis are given in Appendix A.

We found essentially no dependence of  $\lambda_{q,div}$  on total input power  $P_{in} = P_{inj} + P_{Ohmic}$ . We illustrate this in Fig. 1, where peak heat flux averaged over ELMs is plotted against input power. The peak heat flux increases linearly with input power. By conservation of energy, the heat flux profile width stays fixed. The result is in agreement with data from NSTX, JET and ASDEX-Upgrade (DIVII).

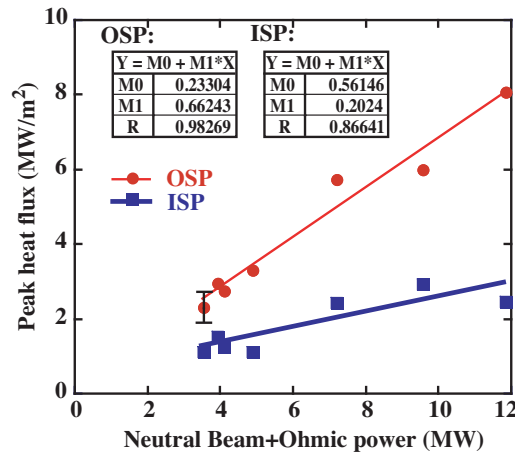


Fig. 1. ELM-averaged peak heat flux at the ISP and OSP plotted against the input power. Linear fits to the data are plotted, with fitting parameters shown in the boxes. The dependence on input power appears linear. A representative error bar is shown.

At low density,  $\lambda_{q,div}$  was independent of density, up to a threshold signifying the onset of detachment. The effect of radiation from the outboard divertor on the strike point heat flux profile is small for the low-density attached discharges. It becomes significant at the onset of detachment where we see the profile broadening, and in fully detached divertor (not considered here), the radiated power absorbed by the divertor plate accounts for nearly all the measured heat flux.

The profile width decreased inversely with increasing plasma current with a very strong correlation (Fig. 2). Density increased with plasma current in these discharges, but remained below the threshold for onset of detachment except at the highest plasma current, where the density was just approaching that threshold. Therefore plots of heat flux profile width versus plasma current are only slightly affected by the density variation.

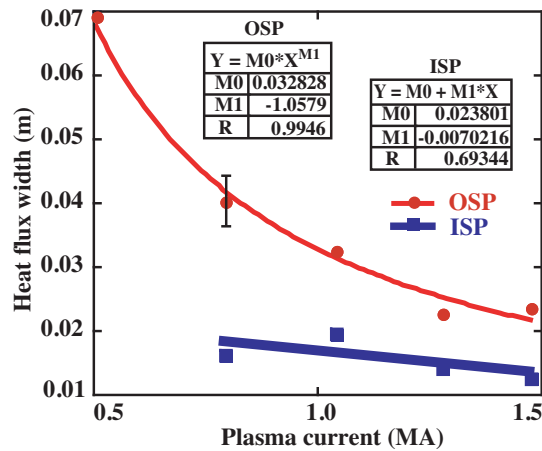


Fig. 2. Widths of profiles, averaged over ELMs, plotted against plasma current. The outer strike point (OSP) shows a clear inverse dependence of width on  $I_p$ . The inner strike point (ISP) dependence is less clear, in part because the heat flux is very small at low plasma current. A representative error bar is shown.

## B. Inter-ELM analysis

Subsequent analysis was performed by averaging only data falling between ELMS. In this averaging the analysis interval was from 20% to 95% of the relative interval between successive ELMs. Heat flux profiles from these intervals were averaged to form the final result. The heat flux profiles derived in this way were mapped along field lines to the outer midplane by using the magnetic equilibrium reconstruction from the EFIT code.

After the field line mapping, both the outside and inside of each profile were fitted with offset exponentials  $(a_0 + a_1 e^{x/\lambda})$  as shown in Fig. 3. The heat flux width  $\lambda_{q,div,midplane}$  is taken to be the sum of the two exponential widths. In this plot the region to the left of the peak is in the private flux region, so-called because the field lines do not traverse the rest of the poloidal cross-section. The right side is in the SOL. The

cause of the offsets from zero heat flux seen in the private flux region and the far SOL are still under investigation. Some heating is known to occur there due to absorption in the surface of radiated power and interaction with very low-density plasma. This heating is calculated to be too small to explain the offset, which is likely to be instrumental.

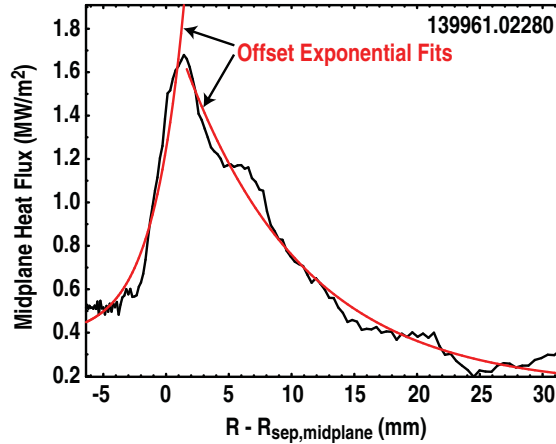


Fig. 3. Typical heat flux profile after mapping to the midplane as a function of distance from the separatrix at the midplane,  $R - R_{sep,mp}$ , showing offset exponential fits.

The widths,  $\lambda_{q,div,midplane}$ , were used in a multi-parameter fit with independent variables of  $B_T$ ,  $I_p$ ,  $P_{in}$ ,  $\bar{n}_e$ ,  $P_{SOL}$  (the power crossing into the SOL from the main plasma). The detailed results of this analysis are shown in Appendices B and D. The only significant correlation shown by this fitting process, as seen in Fig. 4, was a dependence of  $\lambda_{q,div,midplane}$  on the plasma current:

$$\lambda_{q,div,midplane} \text{ (mm)} = 6.38 / I_p^{1.24} \text{ (MA)} \quad (1)$$

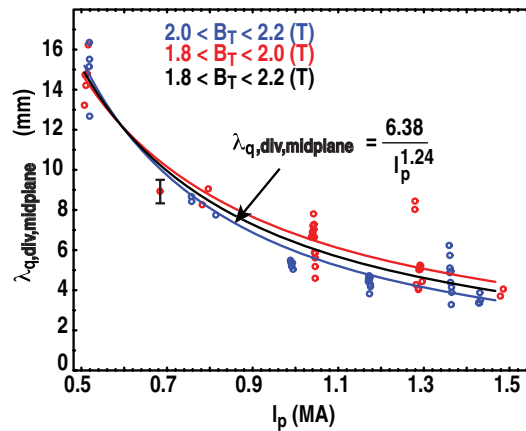


Fig. 4. Dependence of heat flux width (mapped to the midplane) on plasma current. The red and blue symbols denote two ranges of toroidal field, showing little effect from changing  $B_T$ . A representative error bar is shown.

The blue and red data points of Fig. 4 are taken from different ranges of toroidal field in various discharges. The blue and red curves are fit to those data sets, and the black curve is a fit to the full set, showing no significant effect of changing  $B_T$  on  $\lambda_{q,div,midplane}$ .

We note that the multi-parameter fits also show no trend with  $B_T$ . This means that although the connection length is increasing as  $B_T$  increases, the transport of energy across field lines is inhibited so that the profile width at the divertor remains nearly unchanged.

Equation (1) contains no scaling for machine size because we have not yet compared the DIII-D heat flux data in detail with that from NSTX and C-Mod. Therefore it is incorrect to apply Eq. (1) to a larger machine without modification.

### C. Effect of upstream $T_e$ profile on heat flux profile

Thomson scattering was used to measure upstream temperature and density profiles in the boundary plasma. Magnetic equilibrium reconstructions were once again used to map these profiles to the outer midplane. The profiles just inside and just outside the separatrix were fitted separately with exponential functions. It was found that the SOL-side fits had lower scatter, and it was these that were used in comparisons with  $\lambda_{q,div,midplane}$ . Electron temperature and density profiles mapped to the outer midplane are shown in Fig. 5, with the respective core-side and SOL-side exponential fits.

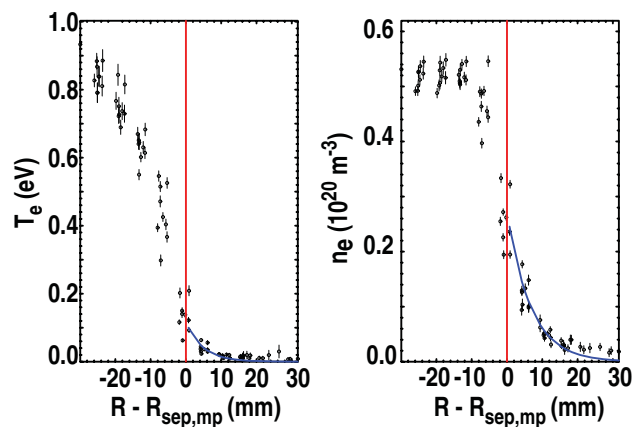


Fig. 5. Typical outer midplane electron temperature and density profiles mapped from Thomson scattering measurements to the outer midplane. The curves show the exponential fits.

In Fig. 6 we show  $\lambda_{q,div,midplane}$  plotted against the temperature gradient scale length on the SOL-side of the separatrix,  $\lambda_{T_e}^{SOL}$ . The scatter is large and the correlation is weak. This is in contradiction to simple two-point models of SOL transport [9], which would predict  $\lambda_{q,div}$  and  $\lambda_{T_e}$  are closely related,  $\lambda_{T_e} = (7/2) \lambda_{q,div}$ .

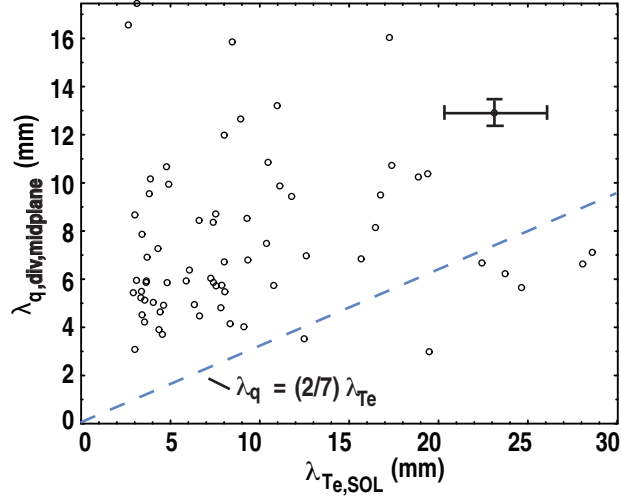


FIG. 6. Plot of the heat flux width,  $\lambda_{q,div,midplane}$ , versus the Thomson electron temperature profile e-folding length in the scrape off layer,  $\lambda_{Te}^{SOL}$ . The lengths are larger than expected from a two point model,  $\lambda_q = (2/7) \lambda_{Te}$ , which is shown by the blue dashed line.

We conclude that the heat flux profiles for the most part are wider than predicted by the two-point model. Departures from that model are to be expected due to the presence of radial transport, radiation within the transport volume, and recycling in the divertor, which these two-point models neglect.

These results are consistent with UEDGE simulations that explored the correlation between midplane  $T_e$  and divertor heat flux profiles. That work also shows that the divertor heat flux is much wider than expected from the two-point SOL model. Details can be found in Appendix C.

#### D. Comparison with other scaling results

The results of the present scaling study are in qualitative agreement with trends given by the JET scaling of conduction limited heat flux widths [10], given by

$$\lambda_{q,miplane}^{JET} \text{ (mm)} = 2.41 \times 10^{-5} B_T^{-1} \text{ (T)} P_{SOL}^{-1/2} \text{ (MW)} n_e^{1/4} \text{ (m}^{-3}) q_{95} R^2 \text{ (m)} \quad (2)$$

The dominant dependence is in  $q_{95}/B_T \sim 1/I_p$ . The density dependence is weak in the JET scaling law, in agreement with our observations. However, our fits show no dependence on  $P_{SOL}$ , the power crossing the separatrix. With no machine size variation in our data to compare with the  $R^2$  dependence from JET, we are left with  $1/I_p$  from Eq. (2), which is similar to our finding.

### E. Comparison of Divertor Heat Flux profiles with UEDGE Modeling

Preliminary modeling of discharges from the plasma current scan shown in Fig. 4 has begun, using the UEDGE code [11]. These results are discussed in detail in Appendices B and E. The power flow through the SOL, and the midplane electron temperature and density profiles are taken from the experimental data, from a 1.5 MA discharge. Transport coefficients in UEDGE are adjusted until the upstream profiles agree with the experiment. In the results reported here, best agreement with the heat flux width was obtained when SOL particle drifts were turned on at 20% of full value, and poor agreement when drifts were turned off. The drifts have a strong effect on particle flow, convective heat transport, divertor density, and divertor radiative losses. The experimentally determined heat flux is much lower than that in the model result, a discrepancy we are working to resolve.

Adding the drifts improved the match between the simulated radiated power (300 kW) and the total measured SOL radiation loss (350 kW). These results show that drifts are important, but further work is needed to match both the drifts and the measured profile values.

### F. Joint experiment between DIII-D and C-Mod

We performed a set of experiments in DIII-D in a configuration close to one which could be run on C-Mod, and closest to a shape that NSTX could run. We used a shape very close to that developed by Groebner, Mossesian, Moyer et al., for “Edge Similarity Experiments on C-Mod and DIII-D.” This equilibrium is similar to the ITER shape. C-Mod later made a shape similar to this, with the same elongation ( $\kappa$ ), triangularity  $\delta$  (upper and lower), squareness ( $\xi$ ), and edge safety factor  $q_{95}$ . NSTX has data in a shape that matched some of these parameters.

We varied  $P_{in}$ ,  $I_p$ , and  $B_T$  in a stepwise manner. Each value was held long enough to perform a small strike point sweep for divertor Langmuir probe profile data. The lower single null shape placed the outer strike point on top of the shelf at  $R = 145$ -150 cm in order to make it visible to an IR camera viewing it from an  $R + 2$  port. We measured both ELM and inter-ELM heat flux. By making comprehensive measurements we will be able to calculate  $P_{SOL}$  and use that as a scaling parameter more appropriate than  $P_{in}$ . We will also find how the scalings are affected by ELM frequency.

The C-Mod discharges are ICRF-heated. To match this as well as we were able, we used ECH heating during the first half of the day. During the second half we used neutral beam injection heating only. For ECH shots, the range of toroidal field scanning was limited in order to keep a resonance inside the separatrix. The weakest toroidal field allowed for the ECH-heated discharges was  $B_T = -1.6$  T. This put the resonance off-axis on the inboard side, but we were still able to place the power inside the separatrix with efficient absorption. The strongest field allowed was  $B_T = -2.1$  T, limited by magnet

operation.

The lower cryopump provided some pumping of the private flux region, and the upper pumps contributed a small amount of pumping.

The sequence of shots for the scans was patterned on the sequence developed by W.P. West for the heat flux scaling experiment on July 23, 2008 in DIII-D. Preliminary modeling of these C-Mod discharges is discussed in Appendix F.

### III. CONCLUSION

Experiments have been carried out in DIII-D in coordination with experiments at NSTX and C-Mod, measuring the divertor temperature profiles from which were derived divertor heat flux profiles, and plasma characteristics in the respective scrape-off layer of each machine. ITER-like operating regimes are within the covered range of plasma parameters. This data set satisfies the deliverable requirement for this milestone.

This data set will enable detailed study of the mechanisms of heat flux transport in the scrape-off layer that govern the divertor heat flux profile width, and evaluation of modeling codes against data covering a wide range of collisionality, beta, parallel heat flux, and divertor geometry. Data sets are being exchanged between the research staff of the various facilities to enable all to investigate the full range of experimental parameters. Comparison of full 2D numerical models to this data is now in progress. This will result in models adapted to handle this wider range of parameters, and allow more confident and accurate extrapolation of the models to future machines. We have found that a simple two-point model is not adequate to describe transport in the SOL.

DIII-D data has been examined for empirical scaling of divertor heat flux profile widths. We find that the primary dependence is heat flux profile width varying inversely as the 1.24 power of the plasma current. We anticipate improved understanding of the physics responsible for this effect from numerical modeling now in progress. Ongoing comparisons of data from the three machines will result in additional information about the scaling with machine size. SOL electron temperature and density fluctuations were also measured in DIII-D, so that SOL heat flux transport can be compared with fluctuation levels over the full range of experimental parameters. This will allow benchmarking of codes that calculate fluctuation levels from first principles, and in turn allow us to quantify the effect of these fluctuations on SOL transport.

## ACKNOWLEDGMENT

This work is supported by the U.S. Department of Energy under DE-AC52-07NA27344, DE-FG02-07ER54917, DE-FC02-04ER54698, and DE-AC04-94AL85000.

## REFERENCES

- [1] A. Loarte, *et al.*, Nucl Fusion **47**, S203 (2007).
- [2] T. Eich, *et al.*, J. Nucl. Mater. **333-339**, 669 (2005).
- [3] A. Herrmann, Plasma Phys. Control. Fusion **44**, 883 (2002).
- [4] ITER Physics Basis Editors, Nucl. Fusion **39**, 2137 (1999).
- [5] A. Loarte, *et al.*, J. Nucl. Mater. **266-269**, 587 (1999).
- [6] D.N. Hill, *et al.*, J. Nucl. Mater. **196-198**, 204 (1992).
- [7] C.J. Lasnier, *et al.*, Nucl. Fusion **38**, 1225 (1998).
- [8] R. Maingi, *et al.*, J. Nucl. Mater. **363-365**, 196 (2007).
- [9] C.S. Pitcher and P.C. Stangeby, Plasma Phys. Control. Fusion **39**, 779 (1997).
- [10] G. Kirnev, *et al.*, Plasma Phys. Control. Fusion **49**, 689 (2007).
- [11] T. Rognlien, *et al.*, J. Nucl. Mater. **196-198**, 347 (1992).

## **NSTX contribution to the Joint Facilities Research Milestone 2010**

*by R. Maingi, J-W. Ahn, T.K. Gray, A.G. McLean, V.A. Soukhanovskii*

**Annual Target:** Conduct experiments on major fusion facilities to improve understanding of the heat transport in the tokamak scrape-off layer (SOL) plasma, strengthening the basis for projecting divertor conditions in ITER. The divertor heat flux profiles and plasma characteristics in the tokamak scrape-off layer will be measured in multiple devices to investigate the underlying thermal transport processes. The unique characteristics of C-Mod, DIII-D, and NSTX will enable collection of data over a broad range of SOL and divertor parameters (e.g., collisionality  $\nu^*$ , beta  $\beta$ , parallel heat flux  $q_{\parallel}$ , and divertor geometry). Coordinated experiments using common analysis methods will generate a data set that will be compared with theory and simulation.

### **Quarter 4 Milestone**

Complete necessary experiments, data analysis and associated interpretive modeling. Prepare a joint report on the empirical understanding gained, the connections to edge transport models, and the opportunities for more detailed and extensive comparisons to theory and simulation. Identify critical research areas to improve extrapolation to ITER.

### **Completion of 4<sup>th</sup> Quarter Milestone – Executive Summary for NSTX**

The targeted goal for the fourth quarter was achieved, as documented in the remainder of the joint report. All three devices find that the mapped heat flux width  $\lambda_q^{\text{mid}}$  varied with plasma current  $I_p^{-\alpha}$ , with the weakest dependence in C-Mod Enhanced  $D_{\alpha}$  H-mode ( $\alpha=0.17$ ), and stronger dependences in C-Mod L-modes, and DIII-D and NSTX H-modes (all  $\alpha \geq 1$ ). In addition, all three devices show no dependence of  $\lambda_q^{\text{mid}}$  on power into the scrape-off layer (SOL) or toroidal field.

The trends above in NSTX were documented in ELMy H-modes, and then confirmed qualitatively in ELM-free H-modes with lithium conditioning. A portion of these results were modeled with the XGC-0 and the SOLT codes (described in the full report), suggesting the importance of neoclassical transport scaling, and X-point effects, and turbulent cross-field transport in the SOL. For ITER, confirmation and understanding of the  $I_p$  scaling is identified as a critical step for divertor projections.

## N1. Introduction

Power is input into tokamaks via a variety of techniques, including neutral beam injection, radiofrequency heating, and resistive or ohmic heating, with the goal of simulating certain aspects of the conditions needed for thermonuclear fusion. In steady state, this power must be exhausted by the plasma facing components (PFC). Technology has progressed to enable steady heat flux removal up to  $10 \text{ MW/m}^2$ , including the ability to handle limited transients above that value. These heat fluxes are quite high: as a point of reference, rocket nozzles typically experience heat fluxes in the range of  $1 \text{ MW/m}^2$ .

The magnetic divertor concept used in fusion devices channels the power to PFCs that are specially designed to handle both the steady heat flux, and transients due to instabilities, such as Edge Localized Modes (ELMs)<sup>1</sup> and disruptions. The magnetic divertor has an additional benefit in that it facilitates access to an improved energy confinement regime known as H-mode. However the divertor also tends to concentrate

power in a relatively narrow region known as the divertor target. The plasma intercepts the divertor target in two geometrically separated regions: the outer and inner strike points (e.g. see Figure N1-1). For geometric and transport reasons, the outer strike point, i.e. the leg at larger major radius, tends to have higher heat flux than the inner strike point in tokamaks. Thus the focus of international research has been on characterization of the outer divertor heat flux, partly to improve the projection for next step devices, such as ITER.

Peak heat fluxes of magnitude  $\sim 10 \text{ MW/m}^2$  are predicted at the outer strike point in the ITER, based on 2-D calculations of the edge plasma and neutral gas transport<sup>2-4</sup>. Those calculations<sup>5</sup> assume that the transport along the magnetic field is mostly classical,

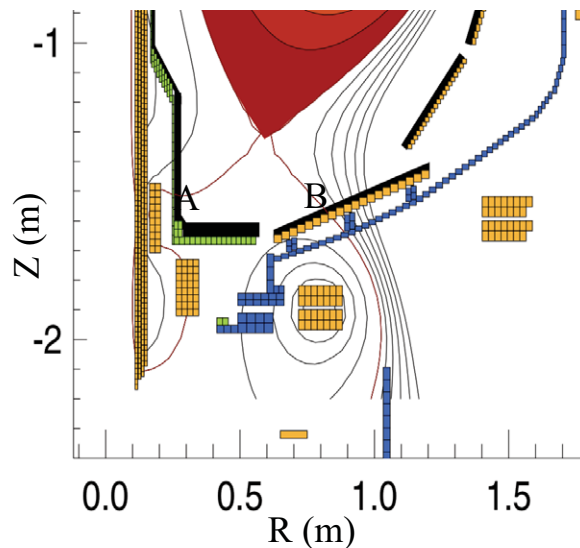


Figure N1-1: Equilibrium reconstruction for a low  $\delta$  discharge (shot# 132341, 0.41 s) with  $\delta \sim 0.44$ ,  $\kappa = 2.1$  and  $f_{exp} = 4$ . The inner and outer strike points are labeled as A and B.

with some modifications for kinetic effects, while transport across the field is governed by anomalous diffusion, characterized by fixed transport coefficients. The magnitude of those transport coefficients is based on values needed to simulate existing devices. However analysis of present experiments points to a wide range for those cross-field transport coefficients, leading to considerable uncertainty about the expected width or footprint of the heat flux profile<sup>6</sup>.

Multi-machine studies have been conducted to experimentally determine the scaling of the divertor heat flux width mapped to the midplane, as well as the electron temperature profile widths measured directly at the midplane<sup>7, 8</sup>. These studies point to a major radius scaling of the temperature width, and the midplane heat flux width in the parallel direction,  $\lambda_{q\parallel}^{\text{mid}}$  or  $\lambda_q$  for short, assuming that electron conduction dominates the power balance (e.g. Figure N1-2). However research in individual devices has pointed to several key parameters that affect the heat flux width, e.g. plasma current<sup>9-11</sup>,  $I_p$ .

The heat flux profiles in the outer divertor typically have an exponential or offset exponential shape, with the characteristic scale length in the scrape-off layer (SOL)

about 2-4 times longer than the scale falloff on the private flux region side, e.g. Figure N1-3. Note that the heat flux profiles in the inner divertor are often broad, due to a phenomenon known as partial detachment<sup>12, 13</sup>. Fitting the outer divertor profiles with exponential functions can make comparison across devices difficult, because of differing functional forms, error minimization schemes, etc. An alternate way to compare profiles

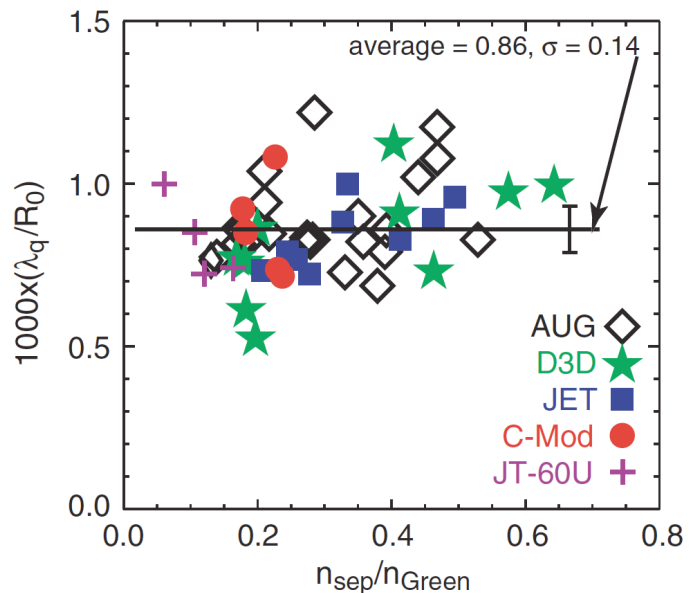


Figure N1-2: Ratio of  $\lambda_{q\parallel}^{\text{mid}}$  to machine major radius,  $R_0$ , as a function of separatrix density,  $n_{\text{sep}}$ , normalized by the Greenwald density,  $n_{\text{Green}}$ . The value is computed as  $2/7 \lambda_{Te}^{\text{mid}}$ , assuming electron conduction dominates parallel transport [B. Lipshultz, et al., Nucl. Fusion 47 (2007) 1189].

without the need for profile fitting is by using an integral definition of the divertor heat flux width<sup>14</sup>  $\lambda_q^{\text{div}}$ , which is given by:

$$\lambda_q^{\text{div}} = P_{\text{div}}^{\text{out}} / (2\pi r_{\text{div}}^{\text{out}} \times q_{\text{div,peak}}^{\text{out}})$$

where

$P_{\text{div}}^{\text{out}}$  = total power incident on outer divertor

$r_{\text{div}}^{\text{out}}$  = radius of peak heat flux

$q_{\text{div,peak}}^{\text{out}}$  = outer divertor peak heat flux

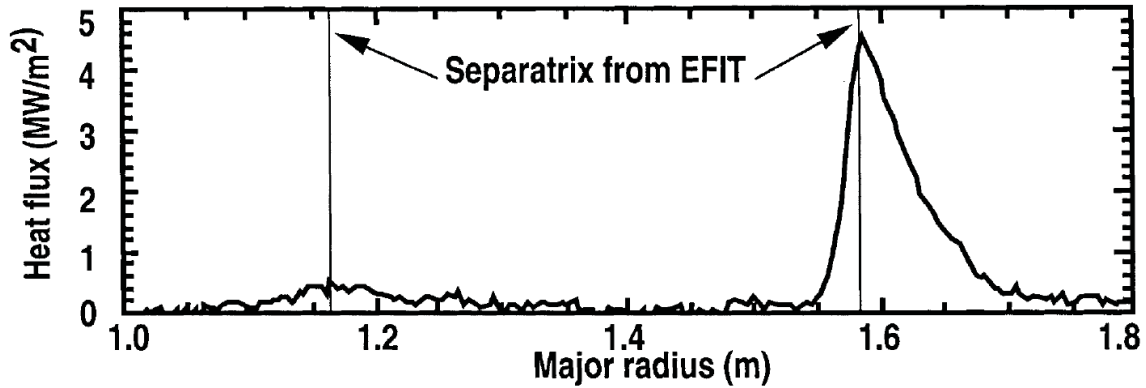


Figure N1-3: typical plot of heat flux profiles from the inner and outer divertors in DIII-D. The two vertical lines represent the inner and outer strike points. The outer divertor heat flux is typically higher, whereas dissipative processes, such as radiation, charge exchange, and recombination, reduce the peak heat flux on the inner side [C.J. Lasnier, et al., Nucl. Fusion 38 (1998) 1225].

This  $\lambda_q^{\text{div}}$  can be easily to a characteristic scale length at the outer midplane  $\lambda_q^{\text{mid}}$  via the magnetic flux expansion  $f_{\text{exp}}$ , i.e.

$$\lambda_q^{\text{mid}} = \lambda_{q,\text{div}}^{\text{out}} / f_{\text{exp}}$$

where

$$f_{\text{exp}} = r_{\text{mid}} B_o^{\text{mid}} / (r_{\text{div}}^{\text{out}} B_o^{\text{div}})$$

$r_{\text{mid}}$  =  $r_{\text{div}}^{\text{out}}$  mapped to the midplane

$B_o^{\text{mid}}$  = midplane poloidal field strength

$B_o^{\text{div}}$  = divertor poloidal field strength

Thus it was decided early in the research planning process to use  $\lambda_q^{\text{mid}}$  as defined above as the central way to compare data<sup>15-18</sup> across Alcator C-Mod, DIII-D, and NSTX. In NSTX, all the data presented are exclusively in H-mode.

In NSTX the scope of the experimental research effort was threefold. The first entailed diagnostic preparation to measure the heat flux profiles in the presence of lithium

wall conditioning, which complicates infrared (IR) interpretation. A fast IR camera installed in 2009 was upgraded to look at two different wavelength bands, as described in Section N2-2.

The second part involved detailed analysis of previous well-characterized sets of heat flux scaling experiments from 2004-2009 in terms of the midplane profile width. All of these data were obtained in ELMy discharges, mostly with small Type V ELMs, using an older 30 Hz IR camera. In 2008 and 2009, the datasets were obtained before lithium was applied as a wall coating technique, to facilitate interpretation of surface temperatures and heat fluxes from IR thermography. Much of this older dataset was obtained in low triangularity ( $\delta$ ) discharges. Analysis of the heat flux widths for this dataset is presented in Section N2-3.

The final part of NSTX research involved obtaining a comprehensive dataset in strongly shaped discharges with high  $\delta$  and elongation, as these are of interest to NSTX-Upgrade (Design:  $I_p = 2$  MA,  $B_t = 1$  T,  $P_{\text{NBI}} = 10$  MW, 5 sec pulse length) in particular and future spherical tokamaks in general. This involved fine scans in  $I_p$ , toroidal field  $B_t$ , neutral beam heating power  $P_{\text{NBI}}$ , radial separation between the two X-points at the outer midplane,  $\delta_r^{\text{sep}}$ , and measurements in a poloidal cross-section shape that matches a scaled C-Mod and DIII-D shape<sup>19, 20</sup>. These data were obtained at two different lithium deposition rates, with the plasmas being more ELMy with the lower deposition rates, and the preliminary data analysis for these new datasets are given in Section N2-4.

For completeness, we also describe experiments in NSTX to reduce the peak heat flux by use of the innovative ‘snowflake’ divertor shape<sup>21-23</sup> in Section N2-5, as well as investigation of the effect of applied non-axisymmetric magnetic perturbations on heat flux profiles. Analysis of the effective heat flux widths in these experiments is still in progress, but we anticipate that when properly optimized, each will result in an increase in the heat flux width, and hence a decrease in the peak heat flux.

## N2. Diagnostic preparations

Infrared (IR) thermography on NSTX was originally installed<sup>24, 25</sup> in 2002 to measure the surface temperature, from which the heat flux could be computed at a 30 Hz frame rate. In 2009, a fast IR camera was implemented<sup>26</sup> to allow measurement of the divertor heat flux carried by Edge Localized Modes (ELMs) in NSTX. This fast IR camera has a 128x128 pixel detector with 1.6 kHz full frame capture rate. It can be operated up to 6.3kHz, with a binned 96x32 frame size.

Each of the previously described IR systems measures the IR emission over a single wavelength or color band, typically 8-12  $\mu\text{m}$ . Unfortunately single color systems are sensitive to the tile emissivity, which changes strongly with lithium deposition. While graphite has relatively low optical reflectivity at infrared (IR) wavelengths ( $R < 0.15$ ), liquid Li is highly reflective ( $R > 0.9$ ). High reflectivity, combined with variable emissivity of Li as fuel and impurities are absorbed, greatly complicates critical interpretation of infrared photon flux from plasma-facing surfaces in NSTX which, near the divertor, may be subject to temperatures of  $> 1,000$  °C and heat fluxes of  $> 10$  MW/m<sup>2</sup>. This high heat flux makes the capability to diagnose surface conditions using IR with sufficient temporal and spatial resolution essential for successful operation of the LLD.

We note that past NSTX heat flux data were obtained before lithium coatings were used in any given calendar year. In 2010, the NSTX IR system was modified<sup>27</sup> to simultaneously view two wavelength bands or ‘colors’. A schematic of the optical layout is given in figure N2-1.

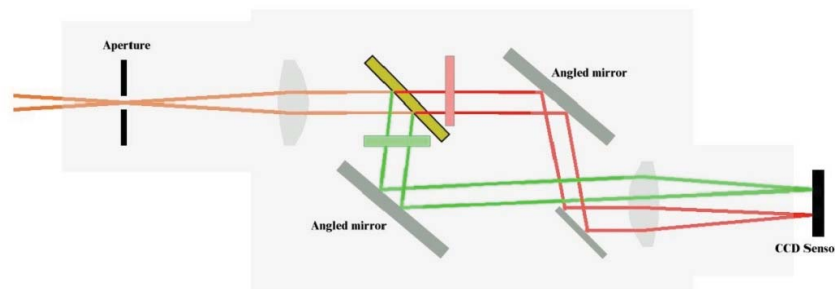
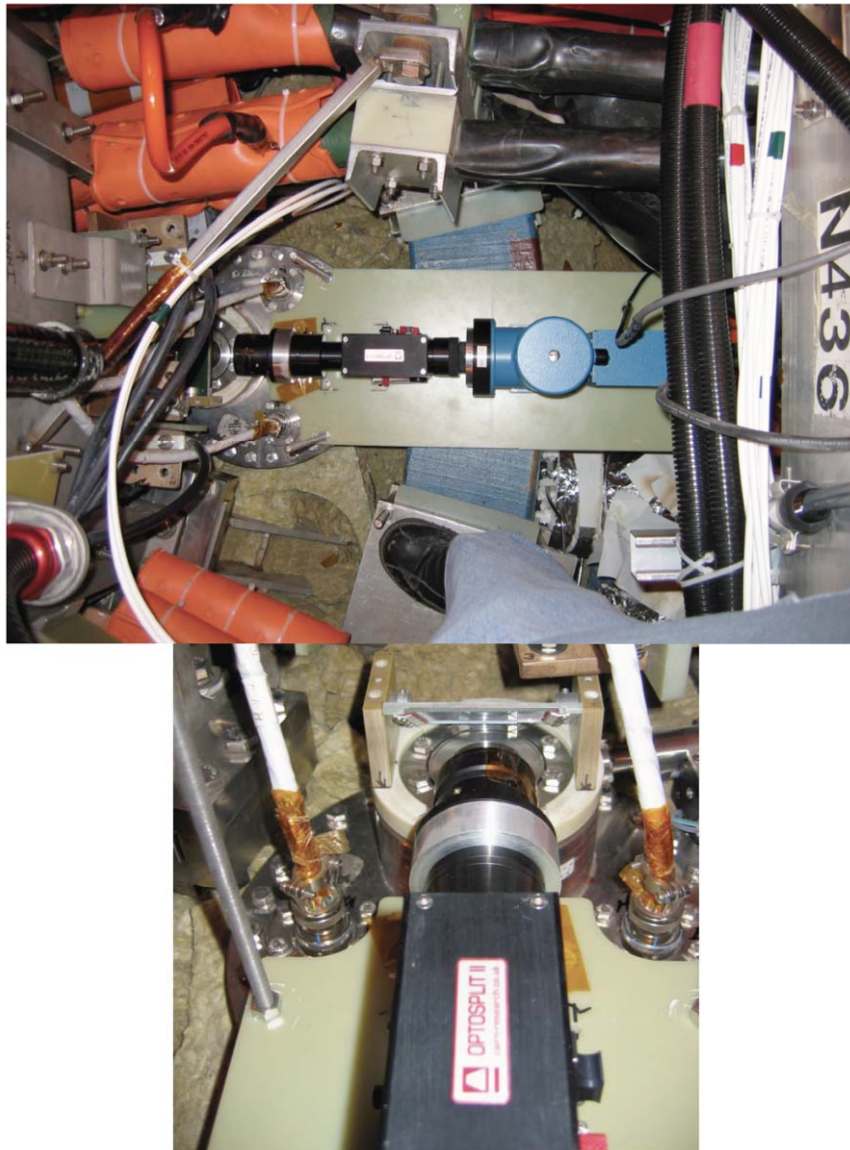


Figure N2-1: Optical layout of the Cairn Optosplit II image splitter

The beam-splitter divides the IR image into two beams using a custom IR dichroic beamsplitter, through separate bandpass filters, and then re-projects the two images side-by-side onto the existing camera detector. By assuming that the emissivity is the same in these two color ranges, the ratio of the signals becomes insensitive to emissivity; this is the basic premise of pyrometers. This upgrade allows for an assessment of the impact of lithium on the SOL heat flux width, as well as general measurements during lithium operation. Figure N2-2 shows the camera and splitter installed on NSTX.



*Figure N2-2: Camera layout on NSTX, including the custom designed optical splitter, which is positioned between the camera and the mirror.*

The key enabling technology for the dual-band imaging adapter is a long-wave pass dichroic beamsplitter which efficiently separates MWIR and LWIR photons. For this project, Lambda Research Optics developed a dichroic which, when mounted at  $45^\circ$  to the impinging optical path, transmits the  $7 - 10 \mu\text{m}$  (LWIR) spectral band with  $T_{avg} \sim 92\%$  efficiency, and reflects the  $4 - 6 \mu\text{m}$  (MWIR) spectral band with  $R_{avg} \sim 99\%$  efficiency. The splitting technique effectively divides the available pixels in one of the two directions by 2, since the images are displayed side-by-side. Thus either a wider toroidal view or radial view of the liquid lithium divertor (LLD)<sup>28</sup> is possible, as shown in Figure N2-3. Here, the reported heat flux results used the radial view.

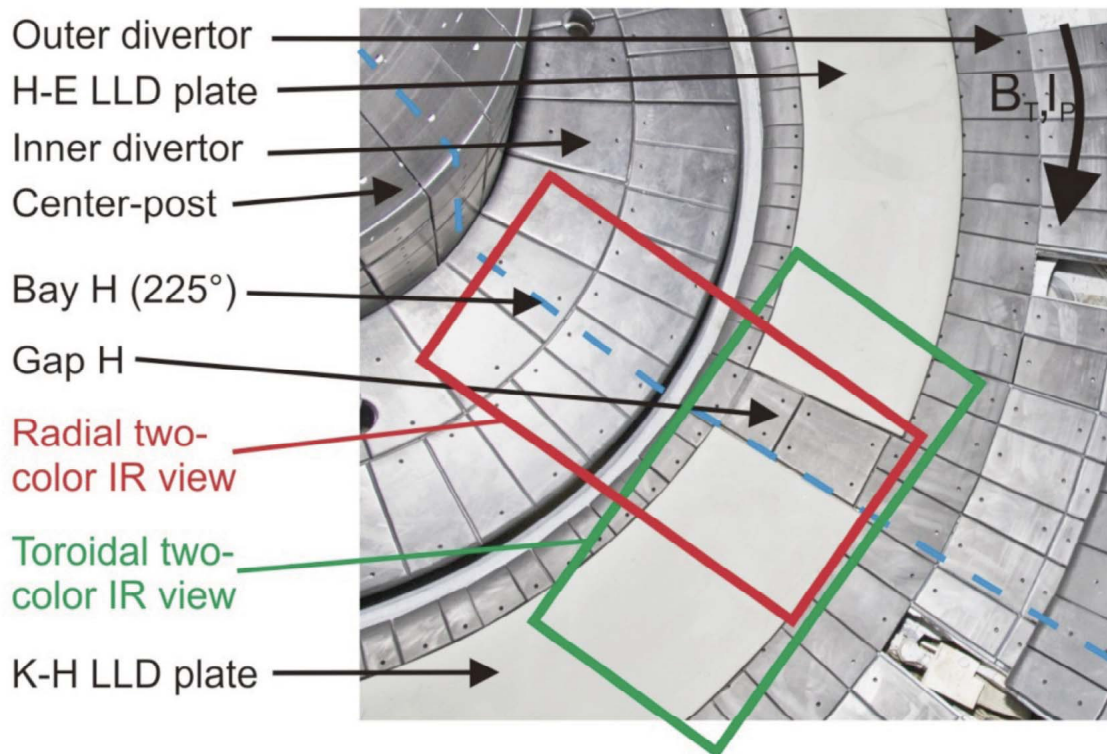


*Figure N2-3: Plan view showing possible IR camera views because of the 2-color splitting technique, that effectively reduces the pixels per view to about  $60 \times 120$ . The heat flux data presented in this report are from the radial view.*

The two-color system was put through an extensive set of bench calibrations, as well as in-situ calibrations. Figure N2-4 shows that the ratio of the intensities in the two colors from a bench calibration. The ratio of the intensities of the long wavelength ( $7-10\mu\text{m}$ ) IR to the mid-wavelength ( $4-6\mu\text{m}$ ) IR is a quantifiable function of temperature, with good sensitivity between  $50 \sim 500^\circ\text{C}$ , proving the validity of the two-color technique for this

application. A recent refinement has expanded the sensitivity of the two-color system up the range 30~800°C, which is sufficient for most NSTX discharges between ELMs and during smaller ELMs. We are now determining if cross-calibration between the

### SBFP 2-color intensity ratio calibration, blackbody source, 22 us integration time

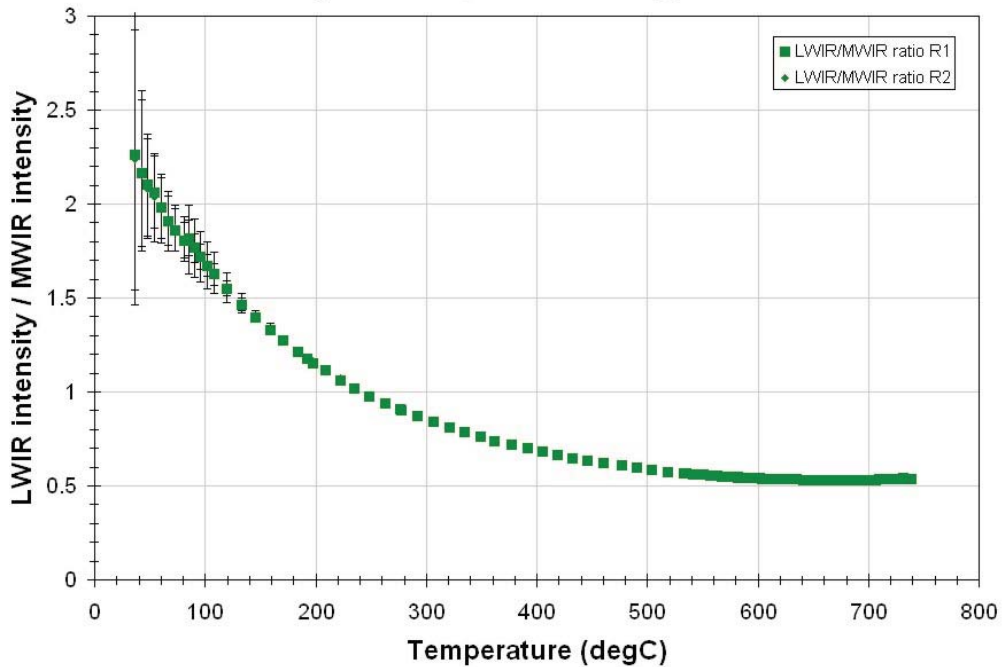


Figure N2-4. Ratio of the 2-band IR intensities ( $I_{LWIR}/I_{MWIR}$ ) of the NSTX 2-color IR camera system as a function of the temperature during a black body source calibration. Here LW=long wavelength, and MW=mid-wavelength.

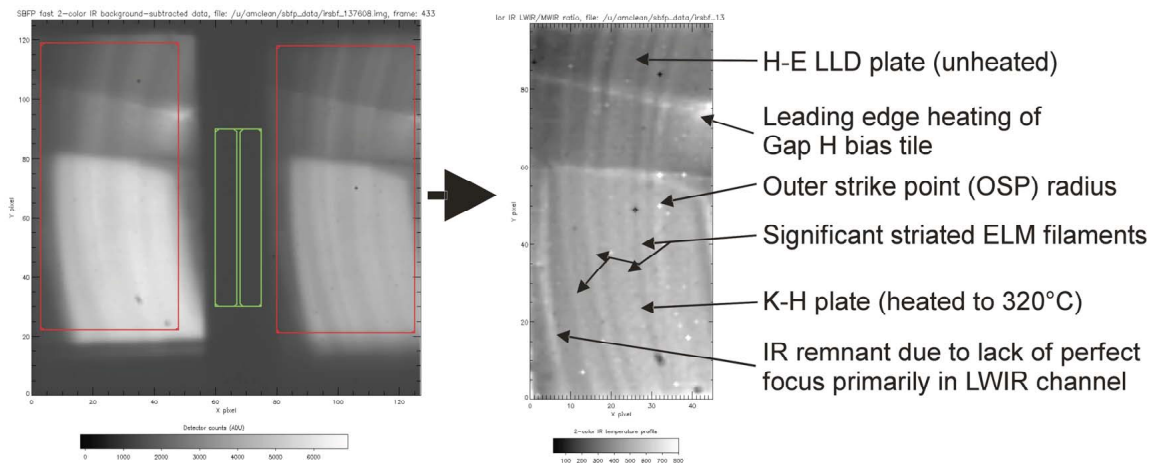


Figure N2-5: Example of the side-by-side projection using the beam splitter. The two color technique actually enhances contrast to LLD heating by ELM filaments. Note the IR remnant near the left edge of the analyzed image, which is not related to filamentary heating.

individual long and mid-wavelength data with the two-color ratios can provide the surface temperature and heat flux during the larger ELMs.

An example of the temperature data obtained from the two-color technique for the toroidal view is shown in Figure N2-5. As a point of interest, the two-color technique seems to enable detection of filamentary heating on the targets from ELM filaments. In much of the data from 2010, the plasma was operated in an ELM-free mode, because of the tendency of lithium to reduce the density profile and suppress ELMs<sup>29-32</sup>. In ELM-free discharges, there is no sign of filaments in the two-color data, demonstrating that the filament images are not an artifact of this technique.

The advantages of two-color technique are especially evident when the lithium in the LLD goes through a phase change<sup>27</sup>. Figure N2-6 shows the data from a discharge in which the LLD temperature remained at the freezing temperature, 180 °C, at the end of a discharge, as measured by thermocouples in the LLD. The two-color data showed the LLD temperature indeed stayed at the freezing point, but the single color data falsely indicated a decaying lithium temperature, likely because of the change in lithium emissivity across the freezing point.

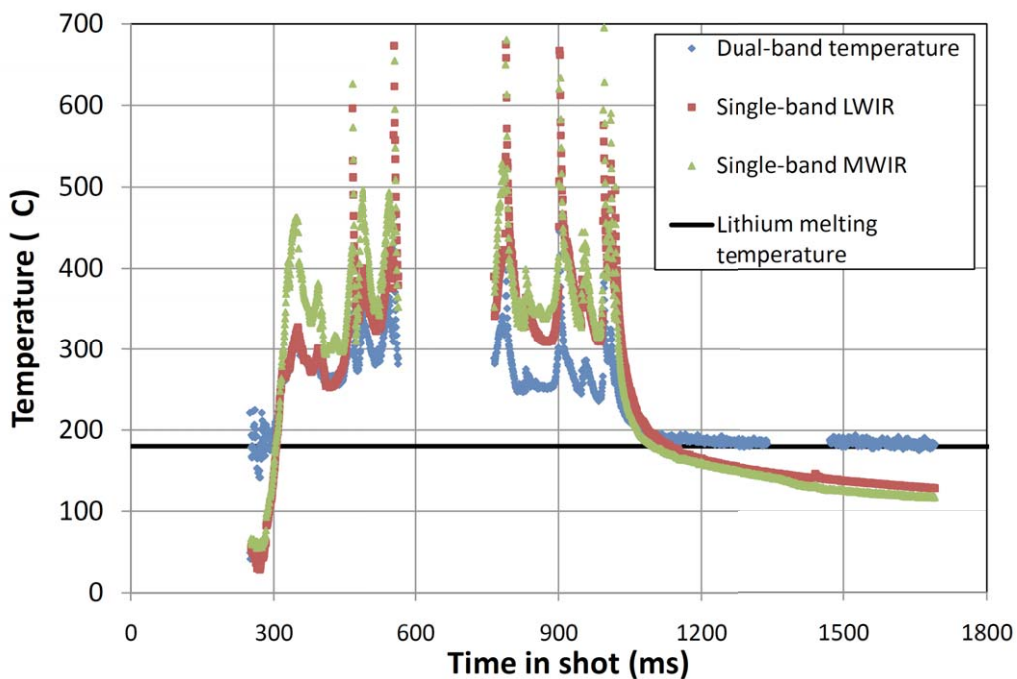


Figure N2-6: Comparison of two-color temperature and those obtained from the individual colors for a discharge where the lithium is passing through the freezing point at 180 °C at the end of the discharge at ~ 1.1 sec. The rapid peaks are due to a few ELMs and magnetohydrodynamic activity at the end of the discharge.

### N3. Heat flux width dependences in discharges without lithium conditioning

Substantial effort was given to detailed analysis<sup>18, 33</sup> of the heat flux widths from existing NSTX datasets<sup>10, 34-37</sup> that were focused on heat flux scaling experiments in H-

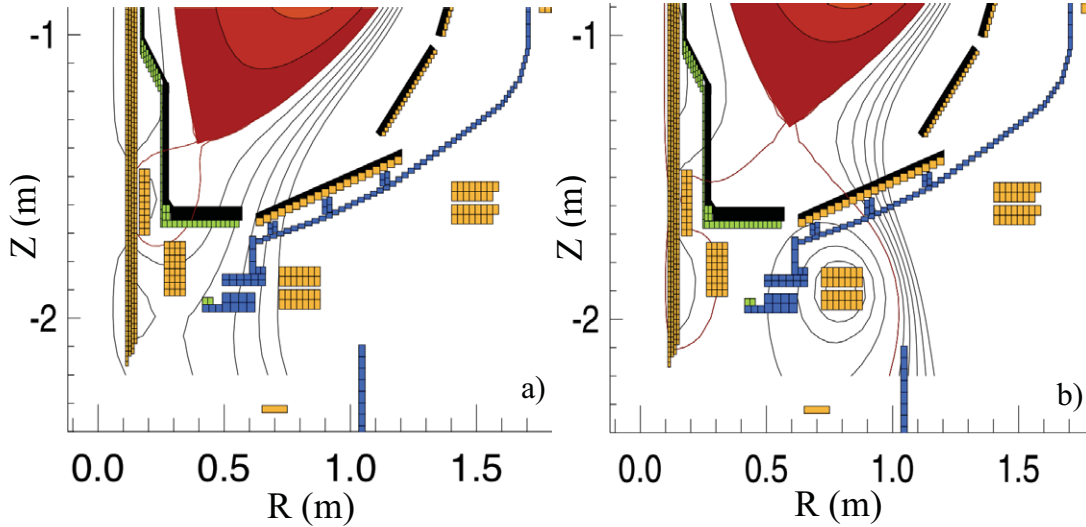


Figure N3-1: EFIT equilibrium reconstructions for 2 discharges with different plasma shapes. (a) High  $\delta$  discharge (shot# 128640, 0.4 s) with  $\delta \sim 0.7$ ,  $\kappa = 2.3$  and  $f_{exp} = 16$ . (b) Low  $\delta$  discharge (shot# 132341, 0.41 s) with  $\delta \sim 0.44$ ,  $\kappa = 2.1$  and  $f_{exp} = 4$ .

These datasets were all obtained without lithium wall conditioning; the operating scenario used periodic boronizations along with helium glow discharge cleaning between discharges. Nearly all of the discharges had small, Type V ELMs, and some of these also had large Type I ELMs. The temperatures were measured with an IR camera<sup>24</sup> operated at 30 Hz, and the heat flux was computed from a 1-D semi-infinite conduction model. The data from these existing datasets were obtained in a variety of shapes, including both low  $\delta$  and high  $\delta$ , e.g. are shown in Figure N3-1.

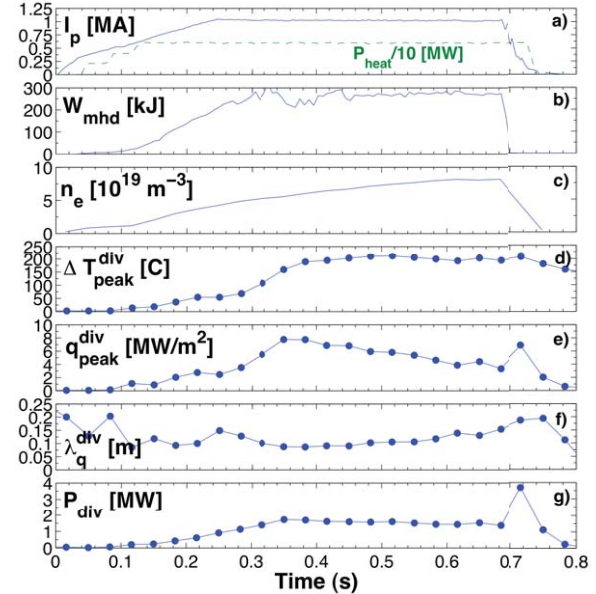
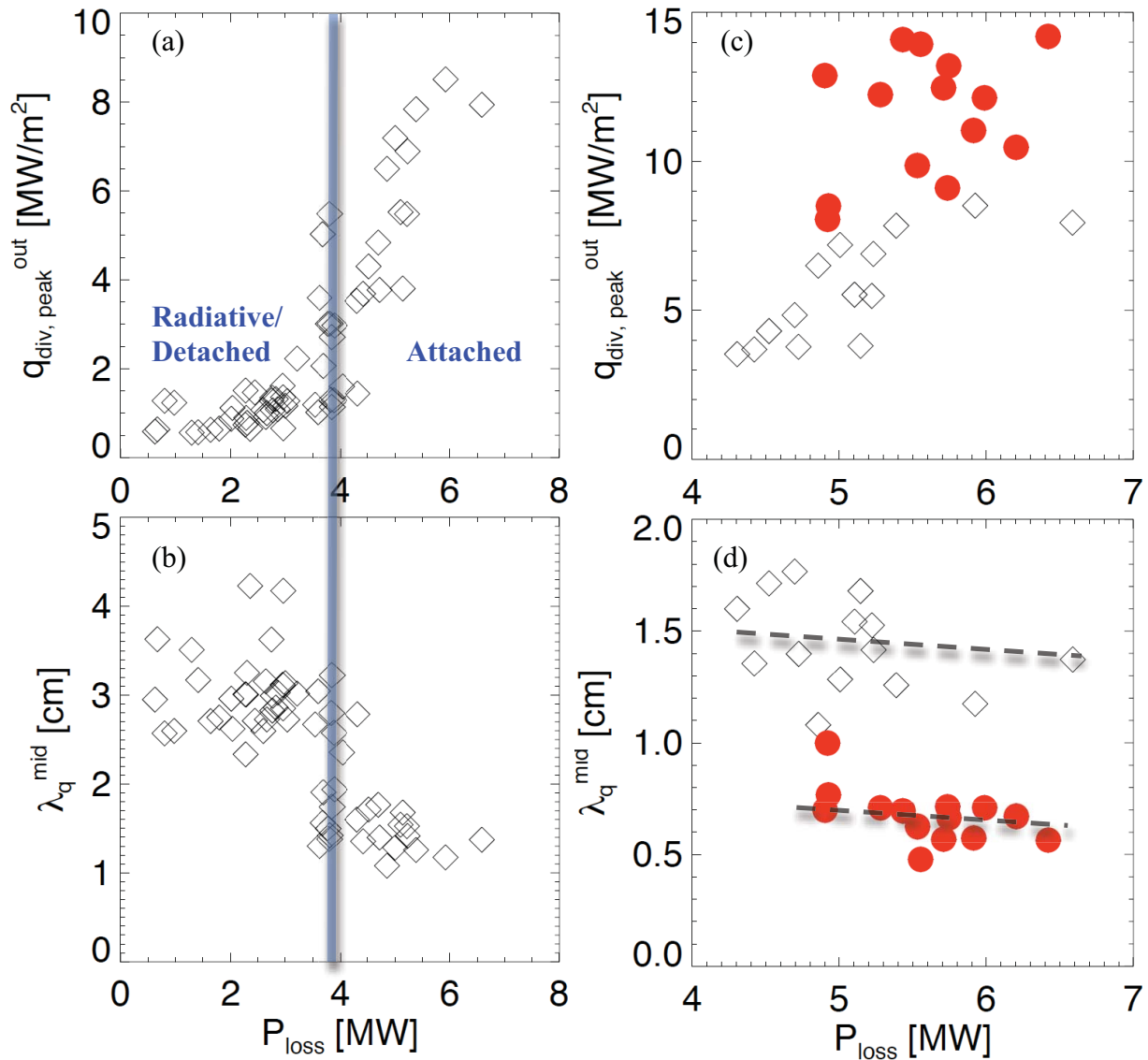


Figure N3-2: Typical progression of discharge parameters for NSTX (#128640) in a)  $I_p$  and  $P_{heat}$ , b) plasma stored energy,  $W_{MHD}$ , c)  $\bar{n}_e$ , d)  $\Delta T_{peak}^{div}$ , e)  $q_{div}^{peak}$ , f)  $\lambda_q^{div}$  and g) power to the outer divertor,  $P_{div}$ . To appear in T.K. Gray et al, J. Nucl. Mater. (2011) at press.

It should be noted that the heat flux profile does not stay constant during the evolution of NSTX discharges, which typically have a secular density ramp. Figure N3-2 shows a typical evolution of discharge parameters. Note in particular that the peak surface temperature rise,  $\Delta T_{\text{peak}}^{\text{div}}$ , flattens out, and that the peak divertor heat flux,  $q_{\text{peak}}^{\text{div}}$ , usually rolls over as the density increases, mostly due to a broadening of  $\lambda_q^{\text{div}}$ . The power incident on the outer divertor remains roughly constant. Thus, for the analysis presented here, we typically analyze a 100-150ms period of peak heat fluxes, which



*Fig. N3-3: dependence of peak outer divertor heat flux and midplane-equivalent widths on power flow into the SOL,  $P_{\text{loss}}$ . The black diamonds were obtained at intermediate triangularity  $\delta \sim 0.5$  and  $I_p = 0.8$  MA, whereas the red circles were obtained at high  $\delta \sim 0.7$  and  $I_p = 1.2$  MA. To appear in T.K. Gray et al, J. Nucl. Mater. (2011) at press.*

corresponds to the lowest  $\lambda_q^{\text{div}}$ . This choice is made to provide a conservative estimate for projections, and it anticipates success in the density control program, which is aimed partly at eliminating the density ramp.

Previously we reported<sup>10, 11</sup> that the peak heat flux increased with power flowing into the SOL,  $P_{\text{loss}}$ . A refined analysis of those data shows that  $\lambda_q^{\text{mid}}$  is relatively independent of power flowing into the SOL when the divertor is in the “attached” state, i.e. with relatively low radiated power and momentum loss. Figure N3-3a,b illustrates these points from a set of discharges at intermediate  $\delta=0.5$  and  $I_p=0.8$  MA: at  $P_{\text{loss}} \approx 4$  MW, there is a clear transition to a narrow footprint in terms of  $\lambda_q^{\text{mid}}$ . For higher  $P_{\text{loss}}$ , the  $\lambda_q^{\text{mid}}$  appears insensitive with a range between 1.0-1.8 cm. Figure N3-3c, N3-3d plots the dependences over the  $P_{\text{loss}}$ , range 4-7 MW, with data from a sequence of high  $\delta=0.7$  and  $I_p=1.2$  MA discharges. The relative insensitivity of  $\lambda_q^{\text{mid}}$  to  $P_{\text{loss}}$  is apparent in that dataset also. On the other hand, the large difference between  $\lambda_q^{\text{mid}}$  for these two conditions points to an  $I_p$  (or an edge safety factor,  $q_{95}$ ) dependence.

One of the main differences between the low and high  $I_p$  discharges above is the divertor flux expansion, which is much higher in the high  $I_p$  discharges. We therefore examined the dependence of  $\lambda_q^{\text{mid}}$  with  $f_{\text{exp}}$ . A wide scan in the divertor flux expansion was accomplished in past NSTX experiments<sup>37</sup> by variation of the X-point

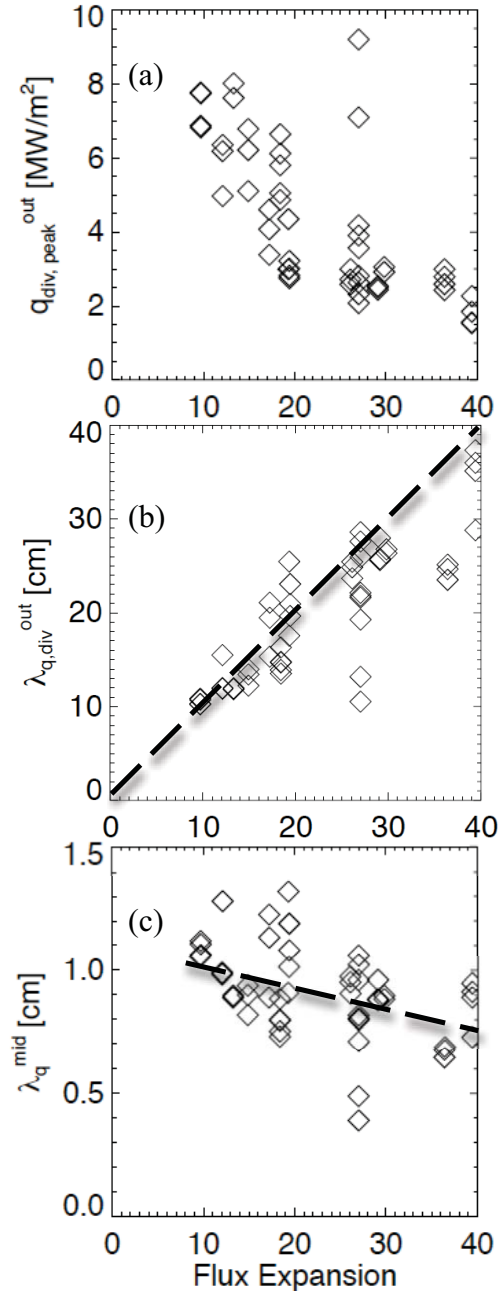


Fig. N3-4: dependence of (a) peak heat flux, (b) divertor heat flux width, (c) and (mapped) midplane heat flux widths on divertor magnetic flux expansion. To appear in T.K. Gray et al, *J. Nucl. Mater.* (2011) at press.

height<sup>37</sup>. The goal here is to evaluate the dependence of the divertor and midplane heat flux footprint widths on flux expansion. It was found that the  $q_{\text{div},\text{peak}}^{\text{out}}$  decreased inversely with flux expansion (Figure N3-4a), and that the total power incident on the outer divertor was approximately constant. Thus the outer divertor heat flux profile width,  $\lambda_q^{\text{div}}$ , scaled nearly linearly with flux expansion over a wide range (Figure N3-4b). Consequently, the  $\lambda_q^{\text{mid}}$  contracts only weakly on magnetic flux expansion, if at all (20% reduction over a factor of 4 change in flux expansion).

Using the results shown in the two preceding figures that the  $\lambda_q^{\text{mid}}$  is in relatively insensitive to  $P_{\text{loss}}$  (for high  $P_{\text{loss}}$ ) and flux expansion, data from different  $\delta$  and  $f_{\text{exp}}$  can be combined to quantify the dependence of  $q_{\text{div},\text{peak}}^{\text{out}}$  and  $\lambda_q^{\text{mid}}$  on  $I_p$ . This is shown in Figure N3-5. All of these discharges had a fixed  $B_t=0.45$  T. Here the  $\lambda_q^{\text{mid}} \sim I_p^{-1.6}$ , i.e. faster than inversely with  $I_p$ , consistent with past results<sup>10</sup>; in comparison, DIII-D<sup>9</sup> and JET<sup>38</sup> have reported an  $\lambda_q^{\text{mid}} \sim I_p^{-1}$  in the past. Part of the scatter in the NSTX data is related to the weak remnant dependence on  $P_{\text{SOL}}$  and  $f_{\text{exp}}$ , and partly due to slightly different fueling and divertor radiation regimes. Nonetheless the strong dependence of the SOL width on  $I_p$  is apparent, and therefore critical to understand in projection to higher future devices with higher  $I_p$ . One possibility of the underlying physics is a dependence on  $\beta_{\text{pol}}$ , which could originate from neoclassical transport considerations.

The data described in this section were shared between the three facilities. Looking ahead for NSTX-Upgrade, the prediction is for  $\sim 3$  mm SOL width at  $I_p=2$  MA, which will require very high flux expansion and/or partial detachment to handle for the 5 sec design pulse length.

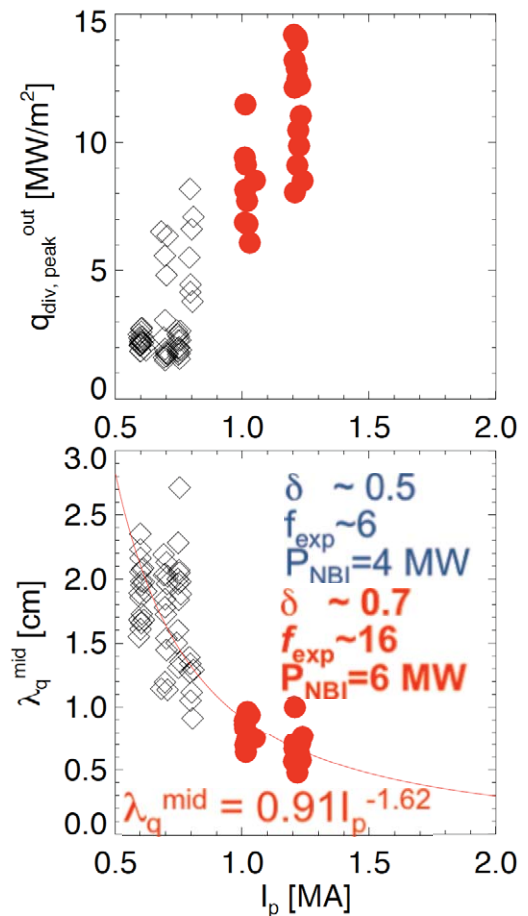


Fig. N3-5: dependence of peak outer divertor heat flux and midplane-widths on  $I_p$ . To appear in T.K. Gray et al, *J. Nucl. Mater.* (2011) at press.

#### N4. Heat flux width dependences in discharges with lithium coatings

Because all of the previous data were from discharges without lithium coatings, the focus of new experiments in 2010 was to measure the effect of lithium on SOL widths with the new two-color IR camera described in Section N2, in H-mode discharges. The biggest change due to the lithium was a transition from ELMy discharges (either Type V, Type I, or mixed Type I/V ELM regimes<sup>39</sup>) to ELM-free discharges. The new data included single-parameter scans in  $I_p$ ,  $B_t$ ,  $P_{NBI}$ ,  $\delta_r^{sep}$ , and measurements of the heat flux profile in a poloidal cross-section shape that matches a scaled C-Mod and DIII-D shape

used in small ELM similarity studies<sup>19, 20</sup>. Much of the data were obtained with a ‘high’ lithium evaporation rate of 300 mg per discharge, which tended to make the plasmas nearly completely ELM-free. Additional data were obtained with a ‘medium’ lithium evaporation rate of 150 mg per discharge, which tended to make the plasmas somewhat more prone to ELMs. All of the data analysis presented here was done with the 1-D semi-infinite slab conduction model mentioned above; however, the fast IR camera appears to be more sensitive to surface film effects (e.g. poor thermal contact) because of the fast framing speed. Hence,

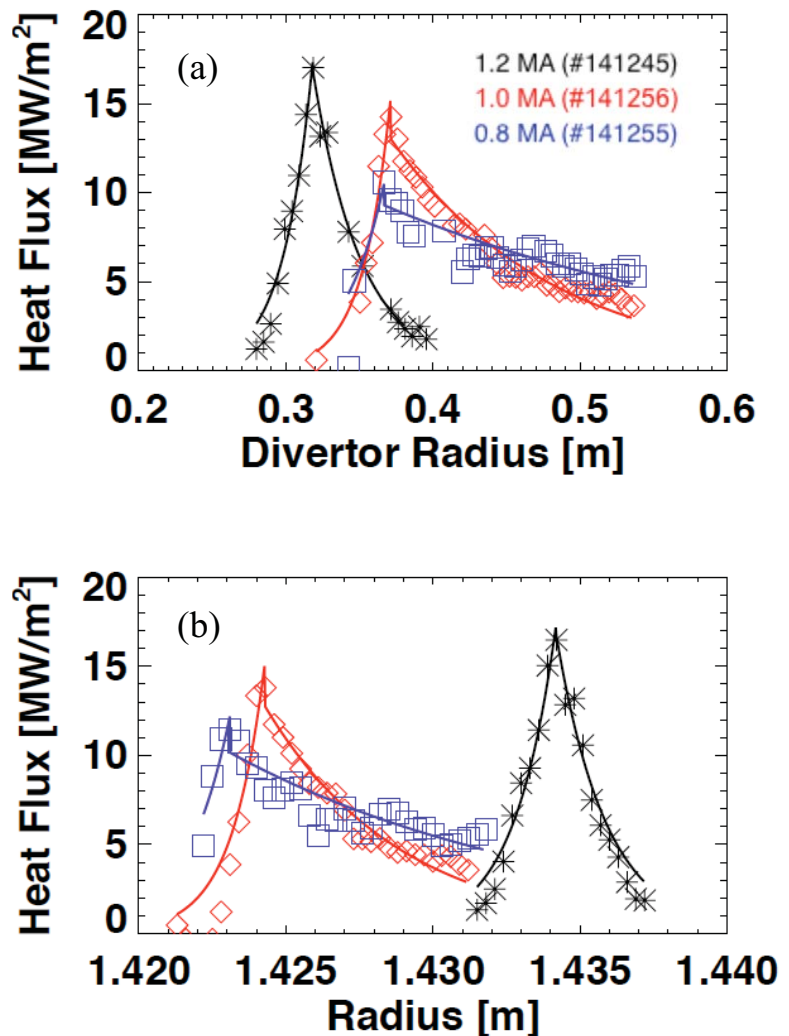


Figure N4-1: Dependence of (a) divertor and (b) midplane mapped heat flux profiles for three different  $I_p$ , demonstrating that the  $\lambda_q^{mid}$  also contracts with  $I_p$  in ELM-free discharges with lithium wall coatings.

the intensity calibrations and computed heat fluxes could be 100%-200% high, and those data should be considered preliminary, pending the application of a 2-D calculation with the THEODOR code<sup>40</sup>. The heat flux widths should be more reliable. In this section, the data from the ‘medium’ evaporation rate endpoints are shown, to illustrate the trends. All data are obtained between ELMs, if present, and averaged over 6-12 msec.

A fine  $I_p$  scan was obtained from 0.7 to 1.3 MA in 0.1 MA increments; the other discharge parameters were  $P_{NBI}=3$  & 4 MW,  $B_t=0.45$  T,  $\delta_r^{sep} \sim -5$ mm, and elongation  $\kappa \sim 2.4$ . Figure N4-1 compares the measured divertor profiles for 0.8, 1.0, and 1.2 MA, as well as the profiles mapped to the midplane. The trend presented in the previous section that  $\lambda_q^{mid}$  drops faster than inversely with  $I_p$  in ELM-free discharges is evident in these ELM-free discharges also.

A fine  $B_t$  scan was also obtained from 0.33 to 0.55 T, in increments of 0.025-0.05 T. The other discharge parameters were  $P_{NBI}=4$  MW,  $I_p=0.8$  MA,  $\delta_r^{sep} \sim -5$ mm, and elongation  $\kappa \sim 2.4$ . Figure N4-2 compares the heat flux profiles from two different  $B_t$  values: there is no discernible impact of the  $B_t$  magnitude on

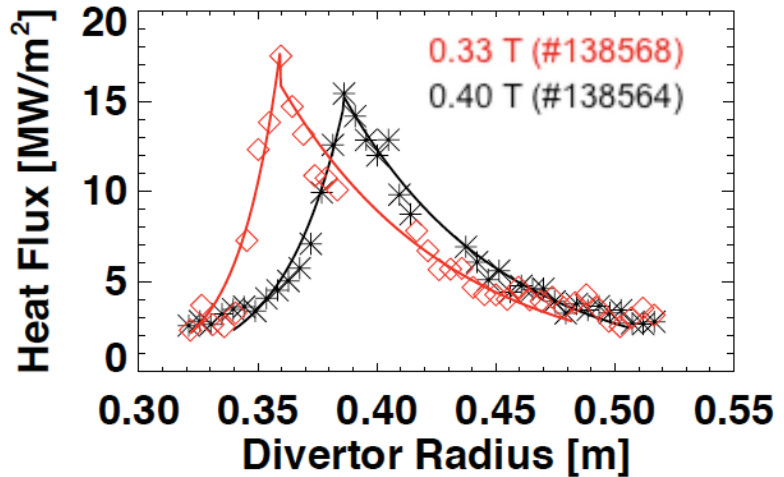


Figure N4-2: Dependence of divertor heat flux profiles for two different  $B_t$ , indicating that the  $\lambda_q^{mid}$  is independent of  $B_t$  in ELM-free discharges with lithium wall coatings.

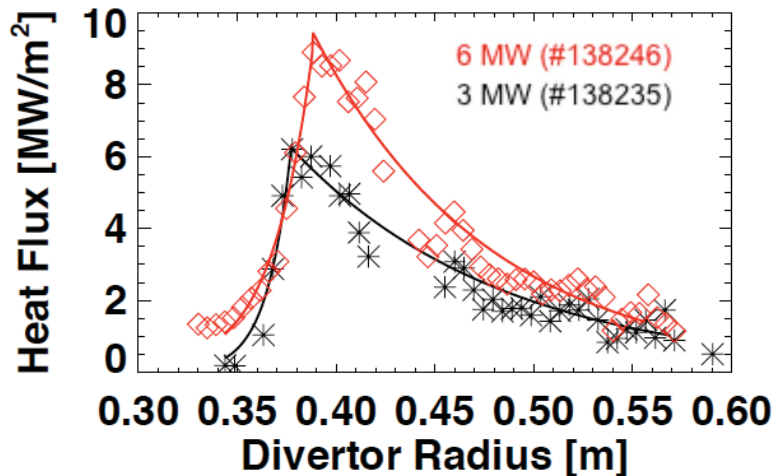


Figure N4-3: Dependence of divertor heat flux profiles for two different  $P_{NBI}$ , indicating that the  $\lambda_q^{mid}$  is largely independent of  $P_{NBI}$  in ELM-free discharges with lithium wall coatings.

the heat flux profile. From this, we conclude that the observed  $I_p$  dependence is not a  $q_{95}$  dependence. Clearly the higher  $B_t \geq 0.5$  T data will help clarify this, once the pending analysis is completed.

A  $P_{\text{NBI}}$  scan from 2 MW to 6 MW in 1 MW increments was obtained at both 0.8 MA and 1.2 MA. As expected the peak heat flux goes up with  $P_{\text{NBI}}$ , but  $\lambda_q^{\text{mid}}$  is still relatively insensitive to  $P_{\text{NBI}}$ , as shown in Figure N4-3 and as seen in the ELMy discharges without lithium. It is a bit surprising that the peak heat flux did not increase linearly with input power as normally observed – additional time slices are being analyzed to determine if this is a reproducible effect.

A detailed  $\delta_r^{\text{sep}}$  scan was obtained, starting from balanced double-null configuration with  $\delta_r^{\text{sep}} \sim 0$  mm to strongly lower-single null with  $\delta_r^{\text{sep}} \sim -20$  mm, in  $\sim 2.5$  mm increments. The standard convention is used that  $\delta_r^{\text{sep}} < 0$  means the lower divertor is dominant; the ion grad-B drift is toward the lower divertor, here and in all the presented NTSX data. The lower divertor peak heat flux increased with decreasing  $\delta_r^{\text{sep}}$  (Figure N4-4), qualitatively consistent with the single-null/double-null comparison done previously<sup>41</sup> in NSTX. At the two smaller  $\delta_r^{\text{sep}}$  values, the heat flux widths were

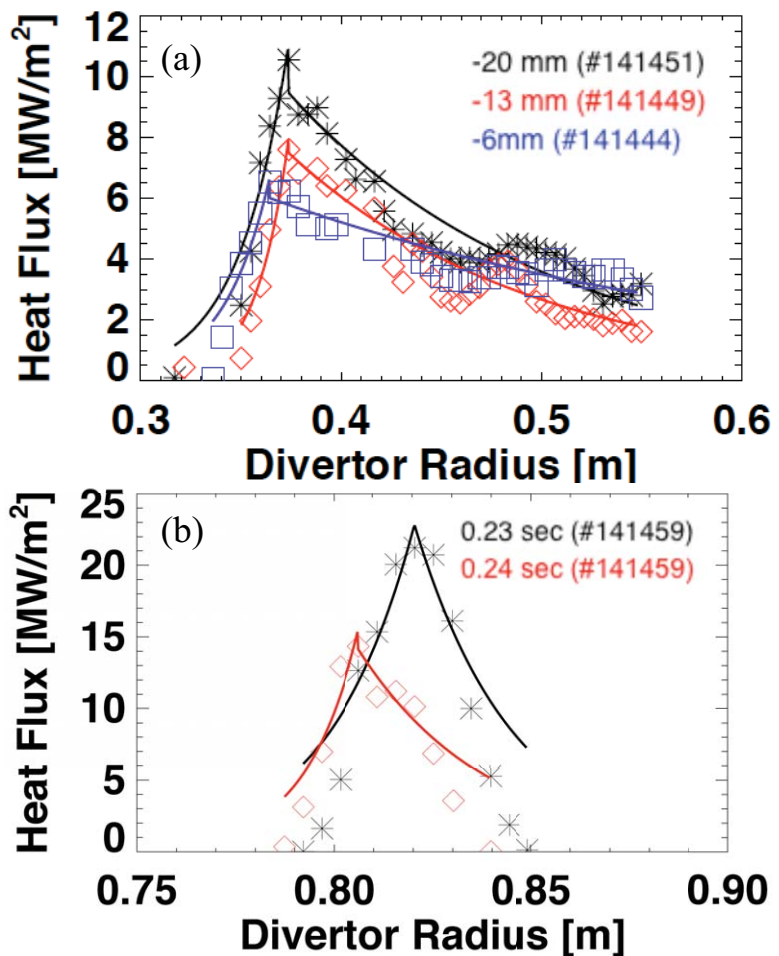


Figure N4-4: Dependence of divertor heat flux profiles for (a) three different  $\delta_r^{\text{sep}}$  values, and (b) two time slices in a low  $\delta$ , low  $f_{\text{exp}}$  boundary shape that matched C-Mod and DIII-D.

similar, while the profile was broadened at the largest  $\delta_r^{\text{sep}}$  closest to double-null. Analysis of the entire dataset is in progress.

Finally a set of low  $\delta$ , low  $f_{\text{exp}}$  discharges were run to match a scaled poloidal cross-sectional shape from Alcator C-Mod and DIII-D, previously used for small ELM similarity studies. Figure N4-4b shows that the divertor heat flux profiles are very narrow because of the low  $f_{\text{exp}}$ . Indeed profiles look more Gaussian than exponential, hence the poor match between the fits (used only to guide the eye) and the data. The  $\lambda_q^{\text{mid}}$  values for these discharges  $\sim 12$  mm, consistent with the low  $I_p$ , low  $\delta$  data presented from the ELMy discharges in section N3.

In summary, the new data obtained in FY 2010 with lithium wall coatings qualitatively supports the dependences from existing older data sets, namely that the  $\lambda_q^{\text{mid}}$  decreases strongly with  $I_p$ , and is largely independent of  $P_{\text{loss}}$ . In addition the new data confirms that the magnitude of  $B_t$  does not affect  $\lambda_q^{\text{mid}}$ , indicating that the observed  $I_p$  dependence is not related to q95 or connection length. Also, we have obtained new data showing that  $\lambda_q^{\text{mid}}$  is independent of  $\delta_r^{\text{sep}}$  for  $\delta_r^{\text{sep}} < -10$  mm; analysis is in progress to see if the observed broadening of  $\lambda_q^{\text{mid}}$  near double null as  $\delta_r^{\text{sep}}$  approaches 0 is a general trend. Finally our preliminary indications are that lithium coatings/ELM-free discharges do indeed reduce  $\lambda_q^{\text{mid}}$  (not shown here), but additional analysis is required to quantify this.

We close with a caution that the data analysis presented in this section should be considered as preliminary. In particular the magnitudes of the heat fluxes are probably too high, but the widths should be ok.

## N5. Associated heat flux profile studies

### a. Snowflake divertor studies

Analysis of divertor characteristics with an innovative divertor configuration, i.e. the “snowflake divertor” (SFD)<sup>21</sup>, represents part of NSTX’s contribution to this milestone from the perspective of improved heat flux handling. This magnetic topology was recently realized in NSTX<sup>22, 23, 42</sup>, resulting in divertor peak heat flux reduction and impurity control. In this case, the divertor heat flux footprint is broadened by easing the access to partial detachment, which leads to a substantial increase in the midplane-equivalent footprint.

In preliminary NSTX experiments with the SFD configuration, a reduction in peak divertor heat flux due to a partially detached strike point region, and a significant reduction in core carbon density and radiated power were observed, in 0.8 MA 4-6 MW NBI-heated H-mode discharges. These initial experiments confirmed the attractive SFD properties predicted by analytic theory<sup>21</sup> and two-dimensional multi-fluid numerical modeling<sup>43</sup>. The SFD concept uses a second-order X-point created by merging, or bringing close to each other, two first-order X-points of a standard divertor configuration. The possibility of forming the SFD configuration has been demonstrated through magnetic equilibria modeling for DIII-D and NSTX, and in experiments on TCV<sup>44</sup>. The SFD-like configuration was generated in NSTX

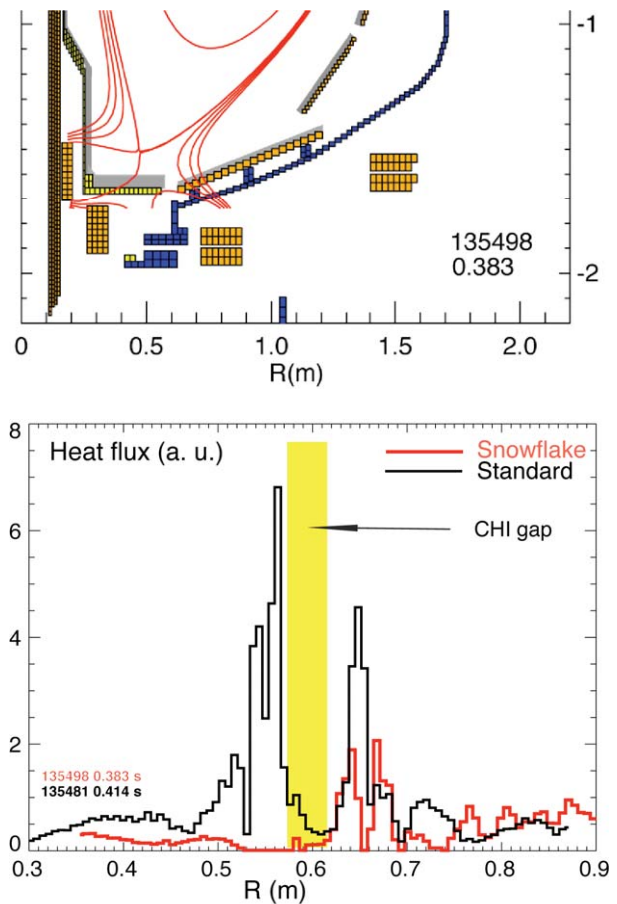


Fig. N5-1. (Top) The “snowflake” divertor configuration obtained in NSTX with 3 mm SOL flux surfaces shown; (bottom) Divertor heat flux profiles measured by IR camera in discharges with a standard medium  $\delta$  divertor and with the “snowflake” divertor configurations [V.A. Soukhanovskii, et al., *Phys. Rev. Lett.* (2010) submitted].

using two divertor magnetic coils controlled in real time by the plasma control system, e.g. Figure N5-1. When compared to the high-triangularity ( $\delta=0.7-0.8$ ) standard divertor configuration in NSTX<sup>36</sup>, the obtained SFD configuration with a medium triangularity ( $\delta=0.5-0.65$ ) had a connection length  $l_{||}$  longer by factors of 1.5-2, and a divertor poloidal flux expansion  $f_{exp}$  higher by factors of 2-3. Divertor heat flux profiles showed low relative heat flux in the greatly expanded region near the outer divertor strike point during the SFD periods (Fig. N5-1); not that the inner strike point is not shown in either heat flux profile; the yellow shading is for a tile-free gap, from which there is no IR emission.

Divertor radiation due to carbon impurity was significantly increased in the SFD. As inferred from the spatially-resolved ultraviolet spectroscopy measurements and collisional-radiative and Stark spectral line broadening modeling, a volume recombination region with  $T_e \sim 1.5$  eV,  $n_e > 3 \times 10^{20} \text{ m}^{-3}$  developed in the X-point and strike point regions, suggesting an increase in volumetric momentum losses in the divertor and a partial detachment of the first several mm of the SOL width, as mapped to the midplane. Importantly, the SFD partial detachment was obtained in reduced density discharges with lithium conditioning, in contrast to previous NSTX divertor detachment experiments that

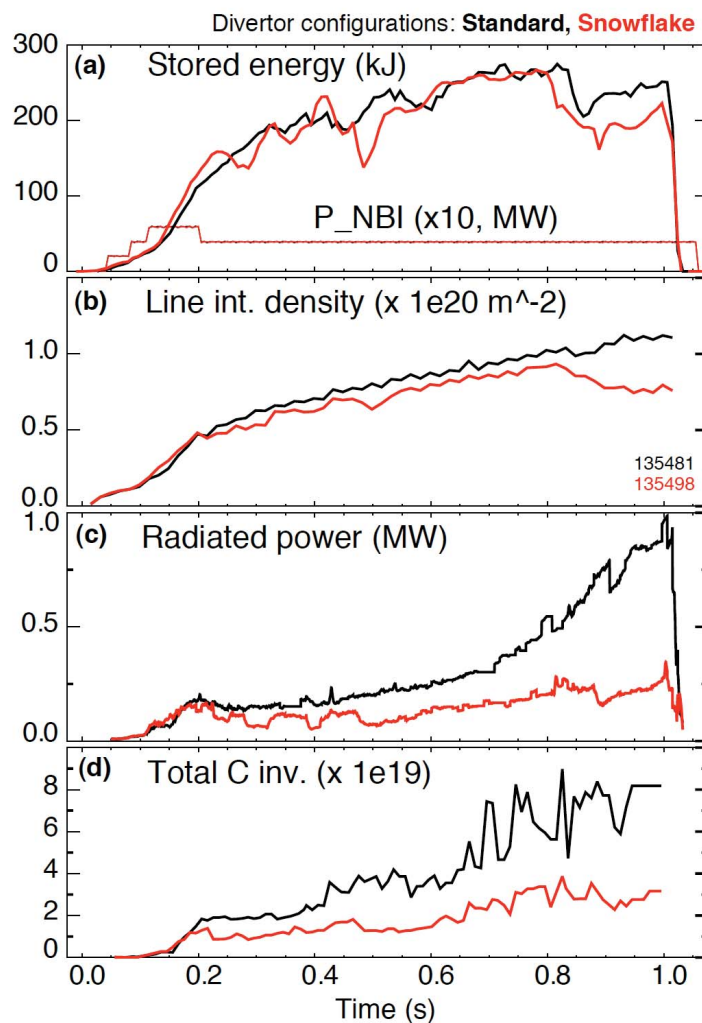


Figure N5-2: Time histories of core and edge plasma quantities of the standard divertor and snowflake divertor discharges: (a) Stored energy  $W_{MHD}$  and  $P_{NBI}$ ; (b) line integrated electron density; (c) Core radiated power  $P_{radi}$ ; (d) Core carbon inventory [V.A. Soukhanovskii, et al., Phys. Rev. Lett. (2010) submitted].

required an additional divertor gas injection<sup>36</sup>.

The core carbon density and core radiated power were reduced by up to 50 % in the SFD discharges, with no degradation of H-mode stored energy and confinement (Figure N5-2). The reduction in carbon density resulted also in a reduction of the line-average density. These good results were obtained in early experiments that achieved the SFD configuration transiently for 50-100ms periods; when added together, these periods represent about 50% of the flattop duration.

The preliminary experiments with the SFD were followed by additional feedback control development, resulting in SFD configurations for the majority of the discharge pulse length. Figure N5-3 compares three discharges: a reference high  $\delta$  discharge, a discharge with the SFD, and a discharge with the SFD and additional divertor gas puffing, all at 0.9 MA, 0.45 T, and 4 MW NBI. Panel N5-3d shows that the reference discharge used only the Pf1a coil. The SFD phase was initiated by use of the Pf1b coil, followed by the Pf2l coil, which were ramped sequentially from 0.3-0.5 sec. Panel N5-3e shows that the divertor  $D_e$  was substantially and steadily higher in the SFD discharges, which is symptomatic of the partial detachment and volume recombination facilitated with the SFD configuration. The core carbon inventory is maintained at a steady level with the SFD, whereas it gradually increased in the reference discharge. The stored

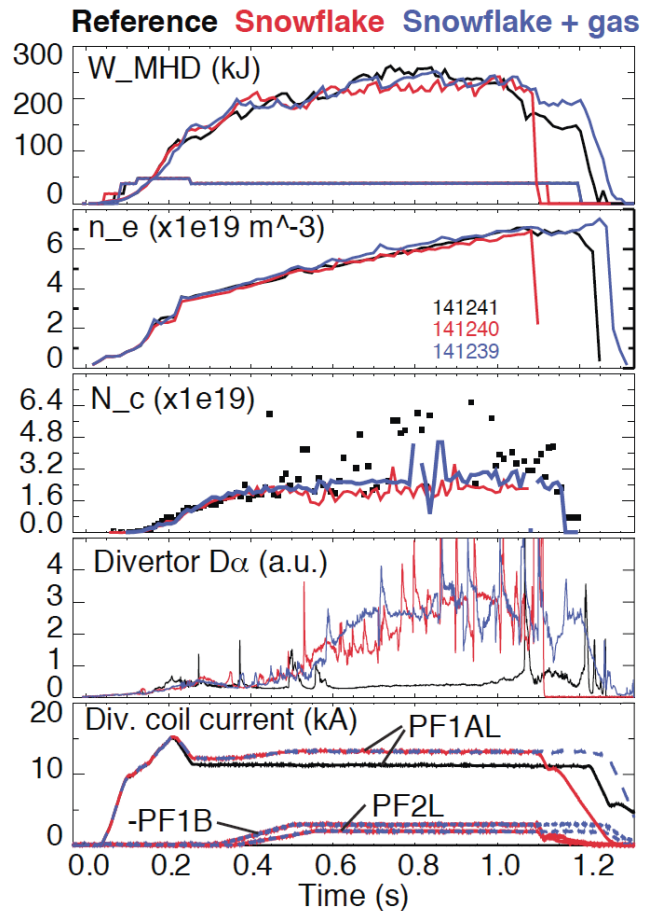


Figure N5-3: Time histories of the standard (reference) divertor, snowflake divertor, and snowflake divertor with divertor gas puffing discharges: (a) Stored energy  $W_{MHD}$ , (b) line-average density from Thomson, (c) Core carbon inventory, (d) Divertor  $D_e$  emission, and (e) Divertor coil currents used to make the SFD. The inset in panel (a) is the common  $P_{NBI}$  waveform.

energy was largely unaffected in the SFD configuration.

Interestingly both of the SFD discharges had ELMs as seen in panel N5-3d, whereas the reference discharge was ELM-free. This makes comparison of the core impurity content difficult, since ELMs are known to flush impurities, i.e. the reduction may not be attributable to the SFD alone in this set of discharges. On the other hand, the periodic heat pulses due to the ELMs provide useful time markers in comparison of the heat flux profiles. Figure N5-4c-e shows that the SFD effectively reduced the peak heat flux between ELMs, but the peak heat flux during the ELMs is still observed, suggesting transient re-attachment between ELMs. Panels N5-4f,g compare the heat flux profiles between ELMs for these three discharges at two different times, demonstrating substantial reduction between the reference and SFD discharges. Thus, the SFD

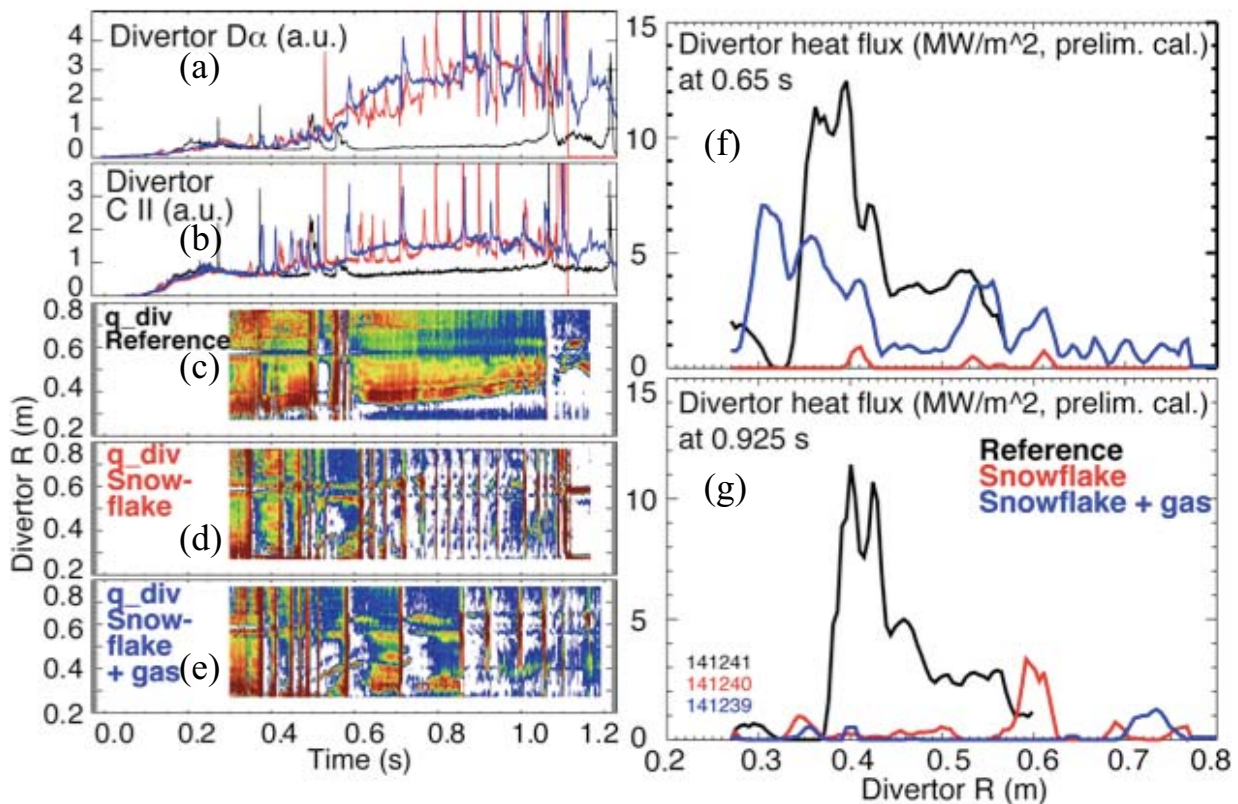


Figure N5-4: Time histories of the standard (reference) divertor, snowflake divertor, and snowflake divertor with divertor gas puffing discharges: (a) Divertor  $D_\alpha$  emission, (b) Divertor C-II emission, (c) contour plot of heat flux from fast IR from reference, (d) contour plot of heat flux from fast IR from SFD, (e) contour plot of heat flux from fast IR from SFD plus gas puffing, (f) radial heat flux profile comparison at 0.65 sec, and (g) radial heat flux profile comparison at 0.925 sec.

configuration is a very promising method to reduce the peak heat flux in existing devices. The simplicity of the SFD, i.e. use of only two divertor coils, should be extrapolable to future devices, thereby partly offsetting the anticipated contraction at higher  $I_p$ .

### N5b. Effect of 3-D fields on profiles

The application of small, 3-D magnetic field perturbations produced by internal or external coils has been found to have significant impact on the plasma performance in tokamaks, i.e. error field and resistive wall mode control<sup>45</sup>, ELM suppression<sup>46</sup> and ELM triggering<sup>47</sup>. At the present time, ITER is considering the use of non-axisymmetric magnetic perturbation for the ELM control; thus, the effect of these intrinsic and imposed 3-D fields on the heat and particle footprints on the divertor plates is of substantial interest.

When external 3-D fields are applied, the modification of the magnetic equilibrium produces a 3-D structure of perturbed magnetic field lines in the plasma edge, where the poloidal magnetic flux is re-organized into topological structures known as homoclinic tangles<sup>48</sup>. The perturbed separatrix is split into multiple invariant manifolds, forming a 3-D “lobe” structure connecting to the open field lines, which are a mixture of long connection length stochastic field lines and short connection length laminar field lines. The lobe structure of the open field lines generates a striated strike point pattern radially across the divertor target surface. This imposed magnetic field structure should be reflected in the measured divertor heat and particle flux profiles, due to the rapid parallel transport along the open field lines. Indeed, such an observation application was recently reported<sup>49, 50</sup> in DIII-D H-mode discharges during the application of Resonant Magnetic Perturbations (RMP). Specifically striated strike point patterns for heat flux were observed in high ( $>0.5$ ) pedestal electron collisionality discharges, while particle flux showed striation was observed for both high and low collisionalities.

In NSTX, striations in the heat and particle flux profiles were observed with the application of 3D fields<sup>51-53</sup>. Here we summarize those results.

Figure N5-5 shows the poloidal cross section of NSTX showing the location of the fast IR camera<sup>26, 54</sup> and  $D_e$  camera diagnostic views, as well as the radial location of one of the six midplane window-frame external 3-D field coil. The magnetic equilibrium for a typical discharge is also overlaid. Also shown in figure N5-5 is the contour plot of the calculated connection lengths at the divertor surface using a vacuum field line following code with the application of external  $n=3$  fields. The formation of the 3-D lobe structure

can be clearly observed. The  $D_\alpha$  emission at the lower divertor target is measured by a 1-D CCD camera<sup>55</sup> installed at toroidal angle  $\phi=255^\circ$ . This camera was operated at 2kHz rate, with sub-mm spatial resolution, and is a part of the system of CCD arrays that are spectrally filtered for deuterium Balmer- $\alpha$  (656.1nm), Balmer- $\gamma$  (433.9nm), and/or HeII Paschen- $\alpha$  (468.5nm) emission lines using  $\Delta\lambda=1.0\text{-}1.5\text{nm}$  bandpass interference filters<sup>55</sup>. It is known that the  $D_\alpha$  emission is closely correlated with the particle flux in attached plasmas, due to its strong dependence on the plasma density; hence, we use  $D_\alpha$  and particle flux interchangeably in this section, noting that one can be converted to the other by use of appropriate S/XB coefficients.

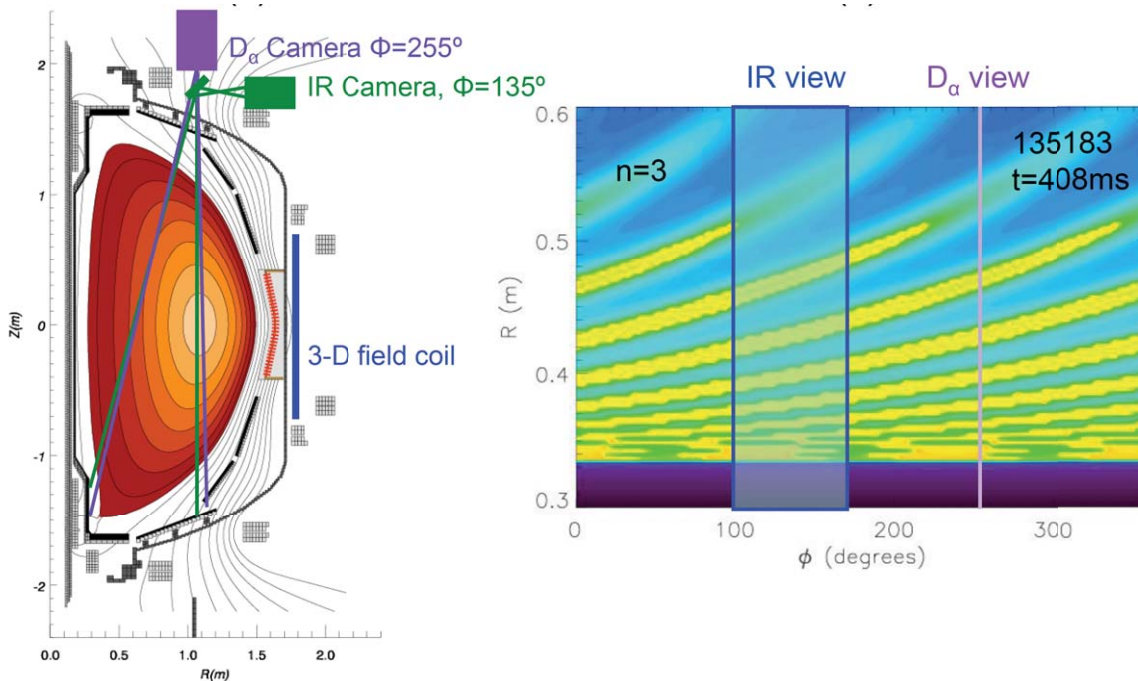


Figure N5-5: (a) Schematic of NSTX cross-section, showing views of the 2D IR camera and the 1-D  $D_\alpha$  cameras, with the location of the external 3D field coil overlaid; (b) shows the contour plot of calculated connection lengths for  $n = 3$  application, showing the formation of the lobe structure as a function of toroidal angle ( $\phi$ ) and radius. The radial and toroidal coverage of the  $D_\alpha$  and IR cameras is also shown [J-W. Ahn, et. al., Nucl. Fusion 50 (2010) 045010].

Figure N5-6 compares the lower divertor IR images before and after the application of  $n=3$  3-D field perturbation at  $t=400\text{ms}$ , along with the heat flux and  $D_\alpha$  profiles. The data along row (a) show that there is negligible strike point splitting at an early stage of the discharge ( $t=180\text{ms}$ ).

In this set of discharges, weak striations become apparent in the IR image before the external magnetic perturbation ( $t=0.398$  sec, figure N5-6b). Both the heat flux and  $D_\alpha$  profiles significantly broadened compared to those in figure N5-6a with modest local peaks in the profile. These multiple peaks and valleys are characteristic of the lobe structure shown in figure N5-5b. We hypothesize that these striations are due to intrinsic error fields, which produce observable strike point splitting. In fact, this ‘intrinsic’ strike point splitting starts to appear even earlier in the discharge, at  $t\sim 0.2$  sec, and is present in the remainder of the discharge. Note that intrinsic strike point splitting is not ubiquitous in NSTX; low  $\delta$  discharges rarely see such splitting. The possible source of intrinsic error fields and the plasma conditions for the intrinsic splitting to occur are presently under detailed investigation.

The application of the 3-D fields augments this intrinsic splitting, making the striations brighter and clearer ( $t=0.432$  sec, figure N5-6c). As the plasma evolves, the striations become more pronounced ( $t=0.482$  sec, figure N5-6d). The widths of the heat flux and  $D_\alpha$  profiles do not change significantly by the ‘augmented’ strike point splitting caused by the 3-D field application. Note also that the peak heat and particle flux values are largely unchanged during the 3-D field application.

Note that the enhancement of the striations can be as fast as 3-4 msec after 3D field application. This is consistent

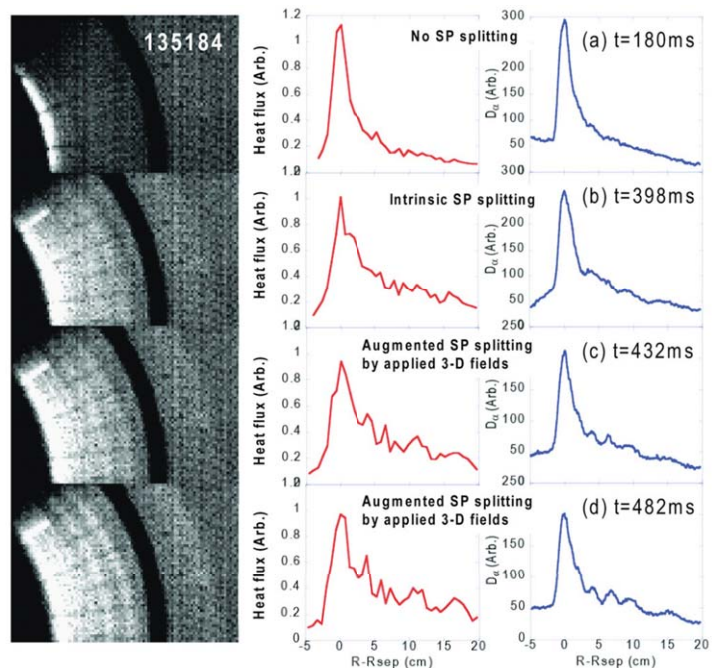


Figure N5-6: Unprocessed images of the IR emission across the lower divertor from the top of NSTX (left column); measured heat flux profiles (middle column), and  $D_\alpha$  profiles (right column) from several time slices for a discharge with  $n = 3$  fields applied at  $t = 0.4$  sec. (Row a) no strike point (SP) splitting early in discharge, (b) ‘intrinsic’ profile splitting 2 msec before the 3D field application and (c), (d) ‘augmented’ profile splitting due to the applied 3D fields [J-W. Ahn, et al., Nucl. Fusion 50 (2010) 045010].

with the measured time for a noticeable perturbation to develop through the vessel and the passive stabilizing plates, detected by the internal magnetic sensors,  $\tau_{\text{vessel}}=3\text{-}4\text{ms}$ .

The observed heat flux striation pattern was compared with the magnetic footprint from a vacuum field line following code, calculated for the toroidal angle of the IR camera. Figure N5-7 shows that the main characteristics of the heat flux profiles do indeed follow the computed vacuum field line structure, both in the number of the observed striations, and in the relative spacing of the peaks. Note however that the precise radial locations of the peak heat flux of the lobes slightly differ from those indicated by the vacuum field line tracing.

A closer look at the structure in the heat and particle flux profiles reveals that the radial separation between consecutive lobes increases with distance from the separatrix along the divertor plate (see figure N5-7c). Note that lobes 1, 2, and 3 (the expected ones from the vacuum field line tracing, in reference to the radial location of the peak at the separatrix as the lobe number 0) appear as a combined local peak in the experimental heat flux and  $D_{\alpha}$  profiles. Thus we have allocated the same value to the radial location for these three lobes in each of the heat flux and  $D_{\alpha}$  profile. In general, the location of these lobes in the profiles is in good agreement with the vacuum field line tracing calculation. Finally the magnitude of the

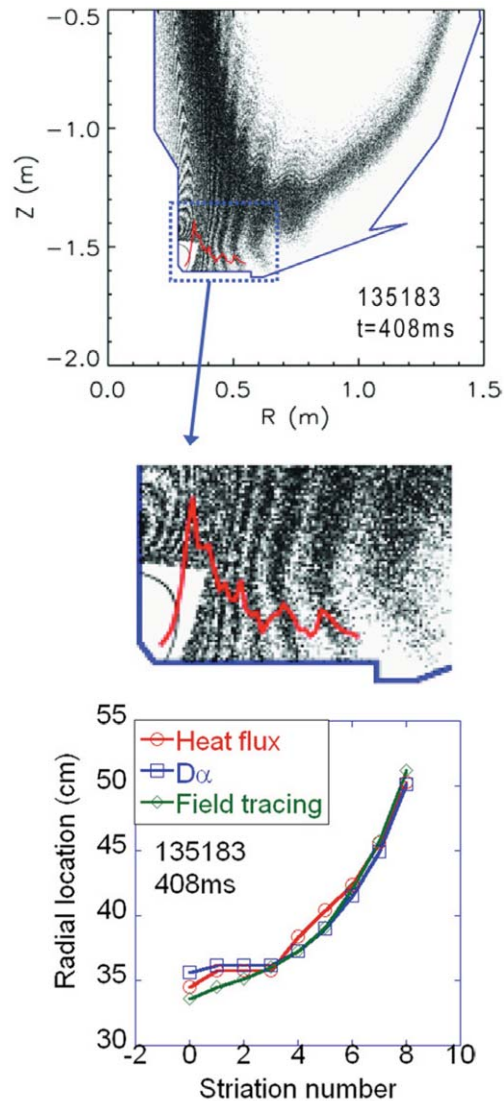


Figure N5-7: (a, b) Magnetic footprints on the divertor target, calculated by a vacuum field line tracing code for the toroidal location of the IR camera at  $\phi = 135^\circ$ , with the measured heat flux profile overlaid; (c) comparison of location of striations with predictions from field line tracing [J-W. Ahn, et. al., Nucl. Fusion 50 (2010) 045010].

peaks and valleys in the IR and  $D_\alpha$  profiles was observed to increase with increasing coil current, i.e. larger perturbing fields generated larger peaks and valleys. On the other hand, the spacing between the lobes and the lobe widths were unaffected.

The last observation we discuss is the effect of applied 3D fields on ELM heat flux. In NSTX, 3D fields are sometimes imposed to trigger ELMs in otherwise ELM-free discharges enabled by lithium wall conditioning. By increasing the applied 3D field above the ELM triggering threshold, the footprint of the ELM heat flux can be compared with the profile before the ELM but with the 3D field. Figure N5-8 shows that the triggered ELM heat flux footprint is nearly identical to the pre-ELM footprint; the ELM merely increases the intensity of the heat flux by  $\sim 300\%$ .

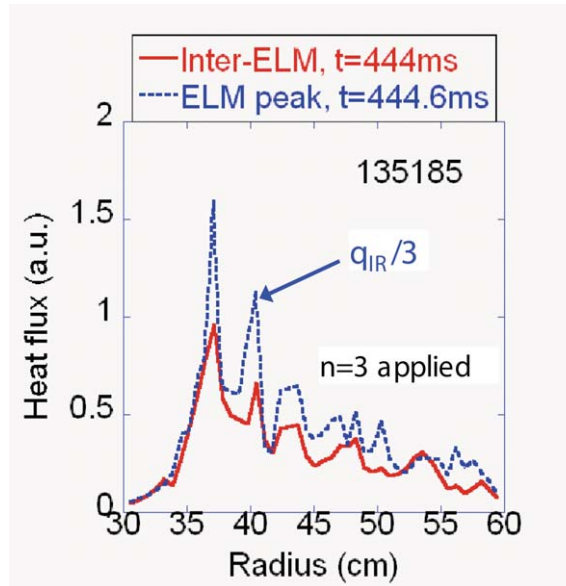


Figure N5-8. Heat flux profiles measured at an ELM peak (blue dotted line - divided by 3), and during the inter-ELM period, 0.6 msec before the peak (red solid line) To appear in J-W. Ahn, et al, J. Nucl. Mater. (2011) at press.

To summarize, intrinsic error fields and applied 3D fields clearly alter the measure heat and particle flux profiles, in a manner qualitatively consistent with vacuum field line tracing in NSTX. Looking ahead, such fields can be rotated in time to increase the time-average wetted area, which should result in reduced time-averaged temperatures and heat fluxes.

**References**

- 1 H. Zohm, et. al., *Plasma Phys. Contr. Fusion* **38** (1996) 1213.  
2 A. Kukushkin, et. al., *Nucl. Fusion* **42** (2002) 187.  
3 A. Kukushkin, et. al., *Nucl. Fusion* **43** (2003) 716.  
4 A. Kukushkin, et. al., *Nucl. Fusion* **49** (2009) 075008.  
5 R. Schneider, et. al., *Contrib. Plasma Physics* **46** (2006) 3.  
6 A. Loarte, et. al., *Nucl. Fusion* **47** (2007) S203.  
7 A. Kallenbach, et. al., *J. Nucl. Materials* **337-339** (2005) 381.  
8 B. Lipshultz, et. al., *Nucl. Fusion* **47** (2007) 1189.  
9 C. J. Lasnier, et. al., *Nuclear Fusion* **38** (1998) 1225.  
10 R. Maingi, et. al., *J. Nucl. Materials* **363-365** (2007) 196.  
11 R. Maingi, et. al., *Proc. 2007 Euro. Conf. on Plasma Phys. and Contr. Fusion, Warsaw, Poland, July 2-6, 2007* (2007) paper P2.020.  
12 T. W. Petrie, et. al., *J. Nucl. Materials* **196-198** (1992) 848.  
13 T. W. Petrie, et. al., *Nuclear Fusion* **37** (1997) 321.  
14 A. Loarte, et. al., *J. Nucl. Mater.* **266-269** (1999) 587.  
15 B. LaBombard, et. al., *J. Nucl. Mater.* (2010) at press.  
16 C. J. Lasnier, et. al., *J. Nucl. Mater.* (2010) at press.  
17 M. Makowski, et. al., *J. Nucl. Mater.* (2010) at press.  
18 T. K. Gray, et. al., *J. Nucl. Mater.* (2010) submitted.  
19 R. Maingi, et. al., *Proc. of 22nd IAEA Fusion Energy Conference, Geneva, SZ, 13-18 Oct. 2008* (2008) paper EX/P6-4.  
20 R. Maingi, et. al., *Nucl. Fusion* (2010) submitted.  
21 D. D. Ryutov, et. al., *Phys. Plasma* **14** (2007) 064502.  
22 V. A. Soukhanovskii, et. al., *J. Nucl. Mater.* (2010) at press.  
23 V. A. Soukhanovskii, et. al., *Phys. Rev. Lett.* (2010) submitted.  
24 D. M. Mastrovito, et. al., *Rev. Sci. Instrum.* **74** (2003) 5090.  
25 R. Maingi, et. al., *J. Nucl. Materials* **313-316** (2003) 1005.  
26 J. W. Ahn, et. al., *Rev. Sci. Instrum.* **81** (2010) 023501.  
27 A. G. McLean, et. al., *Rev. Sci. Instrum.* (2010) to be submitted.  
28 H. W. Kugel, et. al., *Fusion Eng. Design* **84** (2009) 1125.  
29 H. W. Kugel, et. al., *J. Nucl. Mater.* **390-391** (2009) 1000.  
30 H. W. Kugel, M. G. Bell, J.-W. Ahn, et. al., *Phys. Plasma* **15** (2008) 056118.  
31 D. K. Mansfield, et. al., *J. Nucl. Materials* **390-391** (2009) 764.  
32 R. Maingi, et. al., *Phys. Rev. Lett.* **103** (2009) 075001.  
33 T. K. Gray, et. al., *Proc. 23rd Fusion Energy Conference, Daejon, Korea, 11-16 Oct. 2010* (2010) paper EXD/P3-13.  
34 S. F. Paul, et. al., *J. Nucl. Materials* **337-339** (2005) 251.  
35 V. A. Soukhanovskii, et. al., *Phys. Plasma* **16** (2008) 022501.  
36 V. A. Soukhanovskii, et. al., *Nucl. Fusion* **49** (2009) 095025.  
37 V. A. Soukhanovskii, et. al., *Proc. 36th EPS Conf. on Plasma Physics, Europhys. Conf. Abs.* (2009) P2.178.  
38 W. Fundamenski, *Private Comm.* (2010).  
39 R. Maingi, et. al., *Nuclear Fusion* **45** (2005) 1066.  
40 A. Herrmann, et. al. *Plasma Phys. Contr. Fusion* **37** (1995) 17.  
41 D. A. Gates, et. al., *Physics of Plasmas* **13** (2006) 056122.

- 42 V. A. Soukhanovskii, et. al., *Proc. 23rd Fusion Energy Conference, Daejon, Korea, 11-16 Oct. 2010* (2010) paper EXD/P3-32.
- 43 M. V. Umansky, et. al., *Nucl. Fusion* **49** (2009) 075005.
- 44 F. Piras, et. al., *Plasma Phys. Contr. Fusion* **16** (2009) 055009.
- 45 S. A. Sabbagh, et. al., *Nuclear Fusion* **44** (2004) 560.
- 46 T. E. Evans, et. al., *Phys. Rev. Lett.* **92** (2004) 235003.
- 47 J. M. Canik, *Phys. Rev. Lett.* **104** (2010) 045001.
- 48 T. E. Evans, et. al., *J. Physics: Conf. Series* **7** (2005) 174.
- 49 M. W. Jakubowski, et. al., *Nucl. Fusion* **49** (2009) 095013.
- 50 O. Schmitz, et. al., *Phys. Rev. Lett.* **103** (2009) 165005.
- 51 J.-W. Ahn, J. et. al., *Nucl. Fusion* **50** (2010) 045010.
- 52 J.-W. Ahn, et. al., *J. Nucl. Mater.* (2010) submitted.
- 53 J.-W. Ahn, et. al., *Proc. 23rd Fusion Energy Conference, Daejon, Korea, 11-16 Oct. 2010* (2010) paper EXD/P3-01.
- 54 J. W. Ahn, et. al., *Proc. 2009 EPS Conf. on Plasma Physics and Controlled Fusion, Sofia, Bulgaria* (2009) paper P2.175.
- 55 V. A. Soukhanovskii, et. al., *Rev. Sci. Instrum.* **74** (2003) 2094.

# APPENDIX A

## Scaling of Divertor Heat Flux Profile Widths in DIII-D

C.J. Lasnier

Presented at the 19th International Conference on  
Plasma Surface Interactions,  
May 24-28, 2010 in San Diego, California

## Scaling of divertor heat flux profile widths in DIII-D

C.J. Lasnier<sup>a\*</sup>, M.A. Makowski<sup>a</sup>, J.A. Boedo<sup>b</sup>, S.L. Allen<sup>a</sup>, N.H. Brooks<sup>c</sup>,

D.N. Hill<sup>a</sup>, A.W. Leonard<sup>c</sup>, J.G. Watkins<sup>d</sup>, and W.P. West<sup>c</sup>

<sup>a</sup>Lawrence Livermore National Laboratory, Livermore, California 94550, USA

<sup>b</sup>University of California-San Diego, San Diego, California 92093, USA

<sup>c</sup>General Atomics, P.O. Box 85608, San Diego, California 92186-5608, USA

<sup>d</sup>Sandia National Laboratories, Albuquerque, New Mexico 87185, USA

### Abstract

New scalings of the dependence of divertor heat flux peak and profile width, important parameters for the design of future large tokamaks, have been obtained from recent DIII-D experiments. We find the peak heat flux depends linearly on input power, decreases linearly with increasing density, and increases linearly with plasma current. The profile width has a weak dependence on input power, is independent of density up to the onset of detachment, and is inversely proportional to the plasma current. We compare these results with previously published scalings, and present mathematical expressions incorporating these results.

*JNM keywords:* P0500 Plasma-Materials Interaction, P0600 Plasma Properties

*PSI-19 keywords:* Cross-Field Transport, DIII-D, Divertor plasma, parallel transport, Power deposition

*PACS:* 52.25.Fi, 52.40.Hf, 52.55.Fa, 52.55.Rk

*\*Corresponding and presenting author address:* General Atomics, P.O. Box 85608, San Diego, California 92186-5608, USA

*\*Corresponding and presenting author e-mail:* Lasnier@LLNL.gov

## I. Introduction

The width of the divertor heat flux profile  $w_{q,div}$  is of great interest in future large tokamaks as well as many present devices. Previous studies examining the parametric dependence of  $w_{q,div}$  have arrived at diverse scalings [1] in JET [2], ASDEX-Upgrade [3], JT60-U [4,5], DIII-D [6,7], and NSTX [8] with results somewhat at variance with each other. We attempt here to perform a new series of experiments in DIII-D to obtain scaling of the divertor heat flux peak value, profile width, and divertor plate power as a function of plasma input parameters, with the maximum number of divertor and scrape-off layer (SOL) diagnostics brought to bear.

We performed measurements in lower single-null edge localized mode (ELM) H-mode diverted configurations that, due to the strike-point positions, were not strongly pumped. We varied the plasma current  $I_p$  at constant toroidal field  $B_T$ , and varied line-averaged density  $\bar{n}_e$  at constant  $I_p$  and  $B_T$ . The neutral beam injected power  $P_{inj}$  was varied at constant  $I_p$  and  $B_T$ ,  $B_T$  at constant  $I_p$ , and  $B_T/I_p$  at constant  $q_{95}$ . The divertor heat flux was calculated from infrared camera measurements using a new high-resolution fast-framing IR camera.

The IR camera recorded divertor plate surface thermal emission at multi-kilohertz frame rates through the whole discharge to allow measuring time-averaged data as well as rapid changes due to ELMs. The heat flux at each position in the radial profile was calculated at each of the times steps using the THEODOR 2D heat flux analysis code [9]. We show scaling of the divertor peak heat flux and profile width as a function of the parameters varied, and compare with published results from other devices.

## II. Peak divertor heat flux

For each discharge, one or more time intervals of interest were selected where plasma conditions varied little during the interval. The average of each quantity was compiled for each interval. Low-frequency ELMs are included in the average.

Figure 1 shows the peak heat flux  $q_{div,peak}$  at the inner (ISP) and outer strike points (OSP) plotted against the input power  $P_{in}$  (neutral beam heating plus Ohmic heating power), where  $I_p = 1.3$  MA,  $B_T = -1.9$  T were held constant. Density was between  $5.2$  and  $6.5 \times 10^{19} \text{ m}^{-3}$ , except at the highest power, where  $\bar{n}_e = 2.3 \times 10^{19} \text{ m}^{-3}$ . Linear fits are shown. A linear dependence of  $q_{div,peak}$  on input power can reasonably be concluded, with the caveat that not all points were taken at the same density. Without the highest power point, we still see a linear dependence.

Figure 2 again shows  $q_{div,peak}$  at the ISP and OSP, this time plotted against line-averaged density, where  $P_{in} = 4.9\text{-}5.1$  MW except for the densities  $\bar{n}_e = 5.2 \times 10^{19} \text{ m}^{-3}$ , where  $P_{in} = 7.2$  MW, and  $\bar{n}_e = 6.8 \times 10^{19} \text{ m}^{-3}$  where  $P_{in} = 4.1$  MW. Toroidal field was held constant at  $B_T = -1.9$  T, and plasma current was held at  $I_p = 1.3$  MA. Linear fits to the data are shown. If the two density values where  $P_{in}$  varied are eliminated, the dependence of  $q_{div,peak}$  on density still is linear.

Figure 3 depicts the  $q_{div,peak}$ , now plotted against plasma current, showing a linear dependence. Toroidal field was held at  $B_T = -1.9$  T, and  $P_{inj} = 4.7\text{-}5.0$  MW except for the point at  $I_p = 1.3$  MA where  $P_{inj} = 4.1$  MW. Density was not held constant, but allowed to vary at the natural H-mode density, because of practical difficulty measuring the heat flux at the OSP during the plasma pumping that would have been required to

maintain constant density. Figure 4 shows the line-averaged density variation during the  $I_p$  scan. Because of the density variation in this set, this plot does not prove the variation with  $I_p$  alone. In combination with the density scan at constant  $I_p$ , the dependence on  $I_p$  will be extracted from a multi-parameter fit to a larger data set in a later analysis.

Figure 5 shows  $q_{div,peak}$  plotted against  $B_T$  at nearly constant safety factor  $q_{95} = 3.6-3.7$ , with linear fits. Density ranged from  $\bar{n}_e = 3.2 \times 10^{19} \text{ m}^{-3}$  at the lowest field to  $\bar{n}_e = 5.8 \times 10^{19} \text{ m}^{-3}$  at the highest field. There are not enough data points to conclusively show a linear dependence, but that would be consistent with the data. Since we know from Fig. 2 that the  $q_{div,peak}$  decreases with increasing density, this indicates that if density were held constant,  $q_{div,peak}$  would increase faster than linearly with increasing toroidal field magnitude at constant  $q_{95}$ .

The work of Makowski [10] indicates that the heat flux profile width does not depend specifically on the toroidal field. If the width does not change the peak cannot change, by conservation of energy. Therefore most likely the dependence of the peak heat flux directly on toroidal field is weak if any, and the dependence shown in Fig. 5 is a result primarily of the  $I_p$  variation required for maintaining fixed  $q_{95}$ . The fits to  $q_{div,peak}$  vs input power in Fig. 1 nearly pass through the origin, which we expect it should since there will be no steady-state heat flux at zero input power. We will assume here that the correct fit should pass through zero. We also know from previous work [7] that the heat flux depends as expected on flux expansion from the outer midplane to the divertor plate. This means the dominant dependence of  $q_{div,peak}$  at the outer strike point as found above is expressed by

$$q_{div,peak,out} = aP_{in}(9.9 - 9.3n_e)(-1.5 + 3.9I_p)\left(R_{div}B_{div}/R_{mp}B_{mp}\right) \quad , \quad (1)$$

where  $n_e$  is the line-averaged density in units of  $10^{20} \text{ m}^{-3}$ ,  $B_{mp}/B_{div}$  is the ratio of poloidal magnetic fields at the outer midplane separatrix and divertor, and  $R_{mp}$  and  $R_{div}$  are the major radii at the outer midplane and divertor respectively. The factor  $R_{mp}B_{mp}/R_{div}B_{div}$  gives the flux expansion,  $I_p$  is in megamperes, and  $q_{div,peak,out}$  is in units of  $\text{MW}/\text{m}^2$ . For the inner strike point,

$$q_{div,peak,in} = bP_{in}(3.8 - 3.7n_e)(-0.7 + 1.5I_p)\left(R_{div}B_{div}/R_{mp}B_{mp}\right) \quad . \quad (2)$$

For the discharges used here, the flux expansion at the outer strike point was 6.7 and at the inner strike point, 3.1 (again referenced to the outer midplane separatrix). By plotting  $q_{div,peak,outer}$  vs the [right hand side of (1)]  $/a$  and drawing a line through the data and the origin, we find  $a = 0.006 \pm 0.001$  and an analogous procedure for equation (2) gives  $b = 0.05 \pm 0.008$ . Other fitting parameters in equations (1-4) have a comparable fractional margin of error. The parameters  $a$  and  $b$  include some geometry dependence such as scaling with size of the tokamak, which is constant within this data set.

### III. Divertor heat flux profile width

Profile widths discussed here are full width at half maximum (FWHM) values for the ISP and OSP respectively. Widths are obtained at each time point and averaged over the time intervals of interest. Here  $w_{q,div}$  shows no dependence on  $P_{in}$  (not shown). This is consistent with  $q_{div,peak}$  varying linearly with  $P_{in}$  in the sense that energy is conserved when  $P_{in}$  changes.

Figure 6 shows the outer and inner  $w_{q,div}$  plotted against density, for the same density scan as above. There is no effect at low density, but there is a threshold density where the profile becomes wider. Radiated power increases at higher density, but not enough to account for the decreased peak heat flux at the measured widths. It is likely that some energy is deposited in locations that are not measured.

In Fig. 7 is seen  $w_{q,div}$  plotted against  $I_p$ , for the current scan already described. We see that widths become larger at low current. The fitted curve for the ISP is linear, but for the OSP, a better fit goes inversely as nearly the first power of the plasma current. No ISP heat flux peak was seen at the lowest  $I_p$ . We expect the current dependence of the inner width would be of a similar functional form to that of the OSP if more data were available. In Fig. 3, the peak heat flux for this case at the ISP is very small. The dependence  $w_{q,div} \propto 1/I_p$  at least at the OSP from Fig. 7 is consistent with  $q_{div,peak} \propto I_p$  from Fig. 3 so that total power is preserved when  $I_p$  varies.

Because the density scan was performed at constant  $I_p$ , we know the effect of density on the heat flux profile width independent of  $I_p$ . Fig. 6 shows that the effect of density on  $w_{q,div}$  is very weak below the detachment threshold. As shown in Fig. 4, the  $I_p$  scan was performed at densities below this threshold so that density dependence does not enter significantly in the  $I_p$  dependence depicted in Fig. 7.

The plot in Fig. 8 shows  $w_{q,div}$  versus toroidal field at constant  $q_{95}$  for the same discharges as described for the peak heat flux scaling. The widths decrease linearly with the magnitude of the toroidal field. This decrease in  $w_{q,div}$  is consistent with the increase in  $q_{div,peak}$  with increasing magnitude of toroidal field at constant  $q_{95}$ .

As with the discussion of Fig. 5, we know from the work of Makowski [10] that the width does not depend specifically on the toroidal field, and therefore the variation seen in Fig. 8 results primarily from the  $I_p$  variation required for maintaining fixed  $q_{95}$ . The dependence of the width on power and density are weak (for densities below the detachment threshold). Again taking into account the flux expansion, the dominant  $w_{q,div}$  scaling from Fig. 7 for the outer divertor heat flux can be expressed as

$$w_{q,div,out} = 0.0049 \left( R_{mp} B_{mp} / R_{mp} B_{div} \right) / I_p^{1.06} , \quad (3)$$

where,  $I_p$  is in megamperes, and  $w_{q,div,out}$  is in meters. The very small range of variation of inner strike point width in this data set does not yield a useful scaling.

#### IV. Comparisons with other empirical scalings

Loarte summarized several empirical scalings in Ref. 1, pointing out the areas of disagreement. Here we compare the functional dependences seen above with those scalings.

The linear dependence of  $q_{div,peak}$  on power seen above is in agreement with the JET, ASDEX-Upgrade (DIVIII), and previous DIII-D scaling, but not the ASDEX-U (DIVI) scaling. We note that several of those studies use divertor or target power rather than input power. We find the same linear correlation of peak heat flux with target power as with input power.

We have not observed a clear dependence of peak heat flux on toroidal field at fixed  $I_p$  in the present data, unlike the previous DIII-D study which found a variation of  $1/B_T^{0.5}$ . The linear increase in peak heat flux with  $I_p$  peak agrees with the previous

DIII-D result.

The ASDEX-U scaling found  $q_{div,peak}$  varied inversely with density, which we also see.

The  $w_{q,div}$  we use here is different than the  $\lambda_q$  of the referenced studies, which defined an effective width by dividing the strike point power by the peak heat flux. We find in agreement with NSTX, JET IR and ASDEX-Upgrade (DIVII), essentially no (or very weak) dependence of the width on power. We find in agreement with NSTX that the width decreases with increasing plasma current, approximately as  $1/I_p$ .

## V. Conclusion

In the present study we find that peak heat flux varies linearly with input power, inversely as density, linearly with plasma current with a caveat that density was not fixed, and linearly with the magnitude of the toroidal field with  $q_{95}$  held constant (primarily because of the change in  $I_p$  and not  $B_T$ ).

We find FWHM  $w_{q,div}$  depends not at all on power, and not on density at low density. There is a density threshold for profile broadening associated with the onset of detachment. We see  $w_{q,div}$  varies inversely with the  $I_p$  and decreases linearly with increasing  $B_T$  at constant  $q_{95}$ .

We expect to examine this data set further with other fitting techniques as well as making a study of the ELM heat flux profiles from the parameter scans above.

## **Acknowledgment**

This work was supported by the U.S. Department of Energy under DE-AC52-07NA27344, DE-FG02-07ER54917, DE-FC02-04ER54698, and DE-AC04-94AL85000.

## References

- [1] A. Loarte, *et al.*, Nucl Fusion **47** (2007) S203.
- [2] T. Eich, *et al.*, J. Nucl. Mater. **333–339** (2005) 669.
- [3] A. Herrmann, Plasma Phys. Control. Fusion **44** (2002) 883.
- [4] ITER Physics Basis Editors, Nucl. Fusion **39** (1999) 2137.
- [5] A. Loarte, *et al.*, J. Nucl. Mater. **266–269** (1999) 587.
- [6] D.N. Hill, *et al.*, J. Nucl. Mater. **196–198** (1992) 204.
- [7] C.J. Lasnier, *et al.*, Nucl. Fusion **38** (1998) 1225.
- [8] R. Maingi, *et al.*, J. Nucl. Mater. **363–365** (2007) 196.
- [9] A. Herrmann, *et al.*, Plasma Phys. Control. Fusion **37** (1995) 17.
- [10] M.A. Makowski, *et al.*, “Comparison of upstream  $T_e$  profiles with downstream heat flux profiles and their implications on parallel heat transport in the SOL in DIII-D,” these proceedings.

## Figure Captions

Fig. 1: Peak heat flux at the ISP and OSP plotted against the input power. Linear fits to the data are plotted, with fitting parameters shown in the boxes. The dependence on input power appears to be linear.

Fig. 2: Peak heat flux at the ISP and OSP plotted against line-averaged density. As density increases,  $q_{div,peak}$  decreases linearly.

Fig. 3: Peak heat fluxes, now plotted vs  $I_p$ . As  $I_p$  increases,  $q_{div,peak}$  increases linearly.

Fig. 4: Line-averaged density variation during the  $I_p$  scan. All the densities are below the detachment threshold.

Fig. 5: Peak heat fluxes plotted against  $B_T$  at constant  $q_{95}$ , showing a reasonable fits to a line. The heat flux variation is primarily due to the change in  $I_p$  and not  $B_T$ .

Fig. 6: OSP and ISP heat flux profile widths plotted against density. Density variations below the detachment threshold have no effect on the width.

Fig. 7: Profile widths plotted against plasma current. The OSP shows a clear inverse dependence of width on  $I_p$ . The inner strike point dependence is less clear, in part because the heat flux is very small at low plasma current.

Fig. 8: Profile widths versus toroidal field at constant  $q_{95}$ . The trend is described by linear fits. The width variation is primarily due to the change in  $I_p$  and not  $B_T$ .

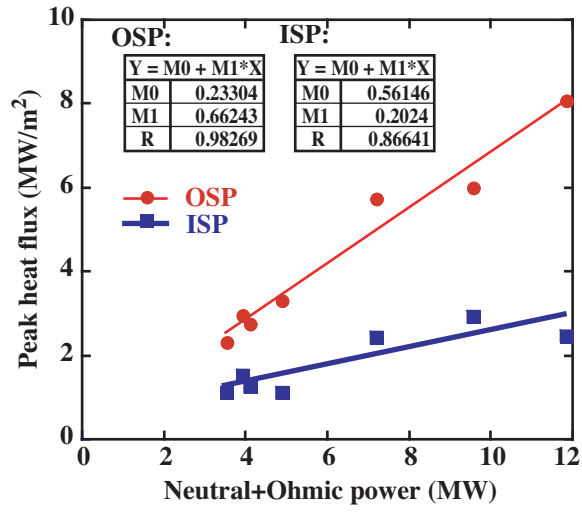


Figure 1

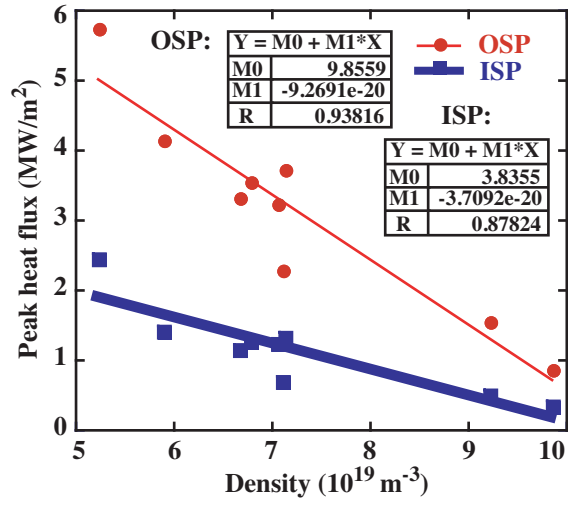


Figure 2

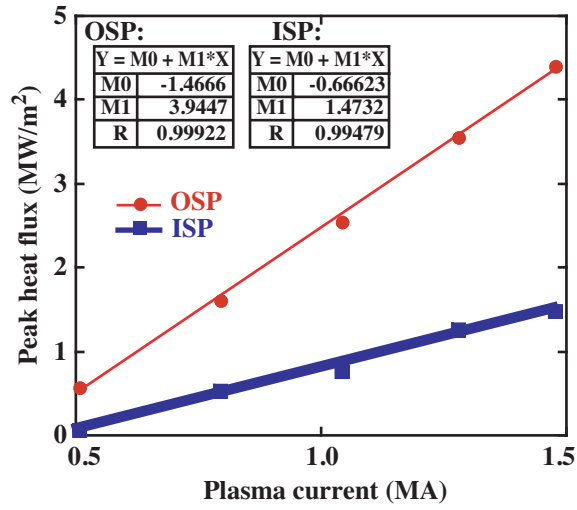


Figure 3

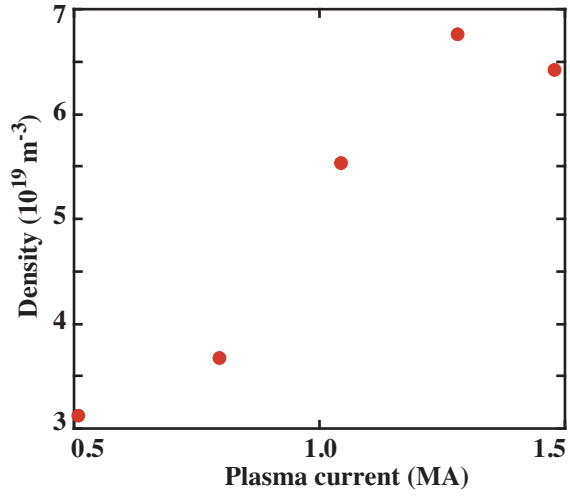


Figure 4

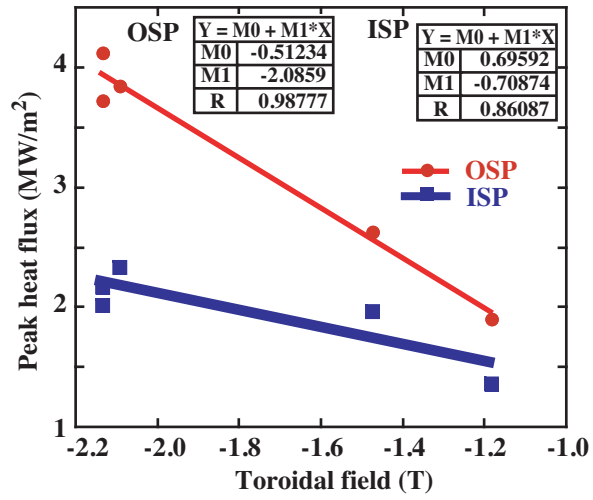


Figure 5

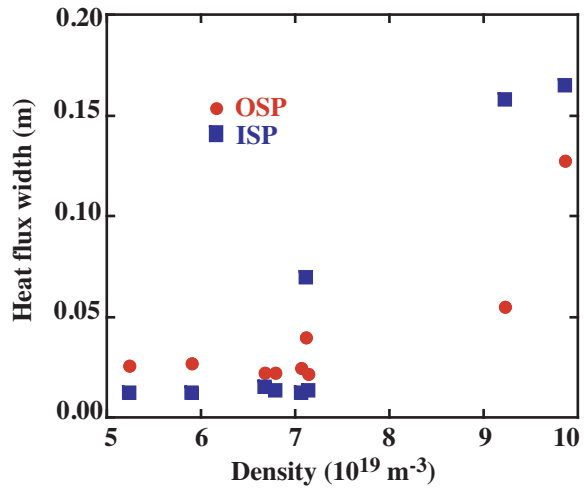


Figure 6

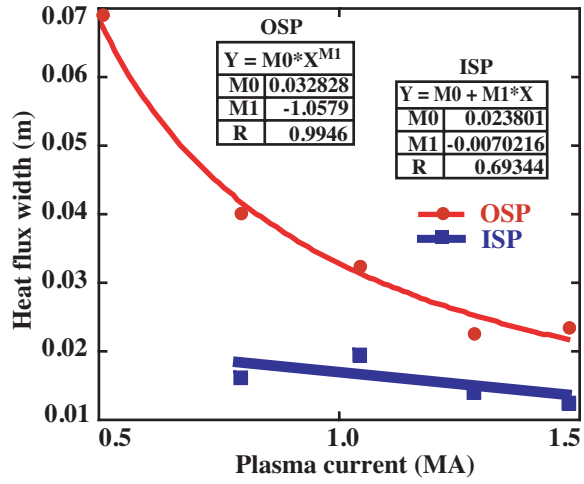


Figure 7

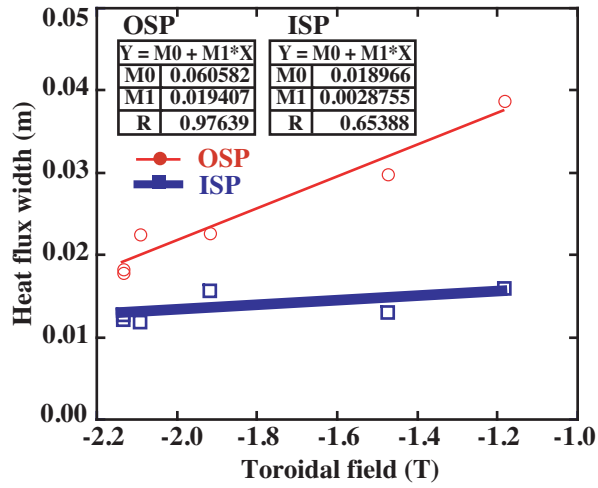


Figure 8

## APPENDIX B

# Comparison of Upstream $T_e$ Profiles with Downstream Heat Flux Profiles and Their Implications on Parallel Heat Transport in the SOL in DIII-D

M.A. Makowski

Presented at the 19th International Conference on  
Plasma Surface Interactions,  
May 24-28, 2010 in San Diego, California

## Comparison of upstream $T_e$ profiles with downstream heat flux profiles and their implications on parallel heat transport in the SOL in DIII-D

M.A. Makowski<sup>a\*</sup>, C.J. Lasnier<sup>a</sup>, A.W. Leonard<sup>b</sup>, J. Boedo<sup>c</sup>, J.G. Watkins<sup>d</sup>, and D.N.  
Hill<sup>a</sup>

<sup>a</sup>Lawrence Livermore National Laboratory, Livermore, California 94550, USA

<sup>b</sup>General Atomics, P.O. Box 85608, San Diego, California 92186-5608, USA

<sup>c</sup>University of California-San Diego, La Jolla, California 92093, USA

<sup>d</sup>Sandia National Laboratories, Albuquerque, New Mexico 87185, USA

### Abstract

In DIII-D, we measure the downstream target plate heat flux and relate it to Thomson and Langmuir probe profile measurements of  $n_e$  and  $T_e$  in the scrape-off layer (SOL) by projecting all measurements to the out-board midplane in order to assess the competition between parallel and cross-field heat transport. We analyze the measured characteristic widths associated with the SOL and model the results with the UEDGE code to provide insight into the mechanisms defining the various widths and the implications they have on transport.

Analysis of the scaling of the heat flux width reveals an essentially inverse dependence on  $I_p$ . The  $B_t$  dependence is extremely weak to non-existent. No dependence was found on the shear and normalized pressure gradient at the 95% flux surface ( $s_{95}$ ,  $\alpha_{95}$ ), nor on  $P_{sol}$ ,  $n_e$  or  $P_{inj}$ .

*JNM keywords:* P0500, P0600

*PSI-19 keywords:* DIII-D, Divertor, Edge modelling, Power Deposition, UEDGE

PACS: 52.40.Hf, 52.55.Rk, 52.55.Fa

*\*Corresponding and presenting author address: General Atomics, P.O. Box 85608,*

*MS 13-153, San Diego, California 92186-5608, USA*

*\*Corresponding and presenting author e-mail: [makowski1@llnl.gov](mailto:makowski1@llnl.gov)*

## I. Introduction

Experiments were carried out in H-mode plasmas to measure the heat flux width,  $\lambda_q$ , as a function of various plasma parameters including magnetic field,  $B_t$ , plasma density,  $n_e$ , and injected power,  $P_{inj}$ . Care was taken to reduce the influence of ELMs through the use of ELM synchronization, a method of conditionally averaging results between ELM spikes over many ELM cycles. Heat flux and Thomson temperature and density profiles were all analyzed in this fashion.

Using this method, we have extracted gradient scale lengths of electron density and temperature at the midplane, and divertor heat flux widths. These, in turn, have been used to derive scaling relations and to examine parametric dependencies such as the relation of the heat flux width to the upstream electron temperature gradient scale length.

We have also started to model the experimental results with the UEDGE [1] code in an effort to understand the relative importance of cross-field and parallel transport.

## II. Upstream Profiles

Upstream, ELM synchronized, edge profiles of  $n_e$  and  $T_e$  were measured with the Thomson scattering system, located at the upper outer region of the plasma at a major radius of 1.94 m. The profile typically consisted of 10-20 measurements within the 200 ms analysis window. The Thomson data was then mapped to the outer midplane. Simple exponential fits to the data immediately inside and outside the separatrix were made to obtain a measurement of the electron temperature gradient scale length,  $\lambda_{T_e}$ , which was then correlated with the heat flux width. Figure 1 shows typical profiles and exponential fits to both the core- and SOL-side data. It can be seen that the core-side exponential fit is

influenced by the top of the pedestal. Scrape-off layer (SOL) widths from tanh-fits [2] were also considered in the analysis. The trends reported below are independent of which parameter was used as the gradient scale length. To be consistent with other published data, the SOL width has been used in the following.

### III. Heat flux results

Heat flux to the lower divertor was measured with an IRTV camera mounted on the top of the vessel. Typically, a set of  $\sim 300$  profiles were averaged to form a single heat flux profile. To facilitate comparison of the various profiles, they have all been mapped to the outer midplane.

These data were used to create a database by dividing each shot into segments 200 ms in length. Each of the plasma parameters was averaged over this interval. ELM synchronization was used to eliminate their influence on the measurements. Additional parameters were also computed such as the shear and normalized pressure gradient at the 95% flux surface  $(s_{95}, \alpha_{95})$ . Other parameters were included in the database to select good segments, since not all shot segments contained usable data.

Figure 2 shows a typical outer divertor heat flux profile as measured with the IRTV camera for  $I_p = 0.52$  MA. The THEODOR code [3] was used to convert the temperature measured by the IRTV camera to a heat flux. For the profile shown, the THEODOR calculation was performed without including the effect of thermal resistance due to surface carbon layers. Also shown are independent offset exponential  $(a_0 + a_1 e^{x/\lambda})$  fits to both sides of the heat flux profile. This procedure was necessitated since the low and high field sides of the heat flux profile had different baselines, likely resulting from

radiative heating of the private flux region. This made the application of the standard definition of the Loarte width [4]

$$\lambda_q^{loarte} = \frac{\int q_{div}(r)2\pi R dr}{2\pi R_{div} q_{div}^{peak}} \cdot \frac{R_{div} B_{\theta}^{div}}{R_{mp} B_{\theta}^{mp}},$$

difficult to apply. The heat flux width  $\lambda_q$  was taken as  $\lambda_q = \lambda_{left} + \lambda_{right}$  which can be shown to be closely related to the Loarte width.

The measured heat flux width,  $\lambda_q$ , shows a very weak dependence on the upstream  $T_e$ -profile regardless which of the inferred gradient scale lengths was used. Figure 3 shows a plot of heat flux width versus the midplane  $T_e$  gradient scale length in the SOL. Due to the scatter in the upstream widths, the correlation coefficient is only 0.124 though, implying that the trend itself is weak. The observed trend is in strong disagreement with simple two-point models that predict  $\lambda_{T_e} = (7/2)\lambda_q$  [5]. Given that the slope of the fit is almost zero, a slope of 7/2 predicted by the two-point model, appears to be nearly excluded by the data, despite the low correlation coefficient. The observed weak dependence of  $\lambda_{T_e}$  on  $\lambda_q$  is not an unreasonable result since radial transport, SOL radiation, and divertor recycling affect heat flux within flux tubes; effects not taken account of in the models leading to the cited scaling law.

A variety of multi-parameter fits were attempted to establish scaling laws between the heat flux width,  $\lambda_q$ , and  $I_p$ ,  $q_{95}$ ,  $n_e$ ,  $B_t$ ,  $P_{sol}$ ,  $P_{inj}$ ,  $s_{95}$ , and  $\alpha_{95}$ . The only significant dependence found was on  $I_p$ . The dependence of  $\lambda_q$  is nearly inverse, scaling as  $I_p^{-1.24}$  as shown in Fig. 4. The  $B_t$  scaling previously reported [6] was not observed in this data. This may be due to the fact that the influence of ELMs was eliminated in this data set

through the use of inter-ELM averaging. Also, there were only a limited number of low-field data points in the current data set.

#### IV. Other scaling laws

There are a number of multi-machine scaling laws in existence. Here we consider two. The first is the JET conduction limited scaling relation [7] given by

$$\lambda_q^{JET} \text{ (mm)} = 2.41 \times 10^{-5} B_T^{-1}(\text{T}) P_{SOL}^{-1/2}(\text{MW}) n_e^{1/4} (\text{m}^{-3}) q_{95} R^2(\text{m}) \quad .$$

This is in quite good agreement with data from the DIII-D experiment. Figure 5 shows a plot of  $\lambda_q^{DIII-D}$  versus  $\lambda_q^{JET}$ . The bulk of the dependence results from the variation in  $q_{95}/B_t \sim 1/I_p$ . The factor  $n_e^{1/4}$  has little influence on the scaling law and no dependence on  $n_e$  has been found in our data. The  $n_e^{1/4}$  scaling on density is quite weak at any rate. Further, we also observe no dependence on  $P_{sol}$ , though the scaling law has a  $P_{sol}^{-1/2}$  dependence. Since  $R$  is a constant for our data, the scaling law reduces to  $\lambda_q^{JET} \sim B_t^{-1} q_{95} \sim 1/I_p$ , which essentially the scaling shown in Fig. 4.

We have also considered the multi-machine scaling law from reference [4]:

$$\lambda_q^{H-2} \text{ (mm)} = 5.3 P^{0.38}(\text{MW}) B_T^{-0.71}(\text{T}) q_{95}^{0.30} \quad .$$

This is in extremely poor agreement with the DIII-D data and predicts profile widths a factor of 10 lower than those measured in DIII-D. There is no size dependence and the dependence on  $q_{95}$  is rather weak.

## V. UEDGE simulations

Efforts are underway to model four representative points on the  $I_p$  scan of Fig. 4 with UEDGE [1] in order to determine what underlying physics might be changing with  $I_p$  to affect  $\lambda_q$ . Inputs to UEDGE are the power flux through the SOL and the midplane electron temperature and density profiles. Transport coefficients are adjusted within UEDGE to obtain a match between the upstream experimental Thomson profiles and UEDGE profiles and held fixed thereafter. Results are preliminary but still offer some insight. The results reported below are with the flows partially turned on (20% of their full value). Figure 6 shows a comparison of the measured heat flux profile and that obtained from a UEDGE simulation as a function of distance along the target plate for  $I_p = 1.5$  MA. The measured profile is scaled by a factor of 5.2 and is thus much lower than that predicted by UEDGE.

With the drifts turned off only  $\sim 90$  kW of power is radiated in the divertor, which is much less than the experimentally measured value of 350 kW. This is caused by a very high value of electron temperature and low value of electron density at the target plate. The high temperature also leads to a large radial electric field that in turn leads to a strong  $\mathbf{E} \times \mathbf{B}$  poloidal flow. The flow, in turn, increases  $n_e$  at the plate with a corresponding increase in radiated power. With the flows partially turned on better agreement in the power balance is obtained with  $\sim 300$  kW of radiated power predicted by UEDGE in this case. The UEDGE heat flux profile width is about 25% narrower than the measurement without the flows turned on. With the flows partially turned on, the heat flux width broadens, but is still narrower than the experimental profile. Note that a shoulder is developing on the right hand side corresponding to the shoulder in the experimental data.

No in/out asymmetry of the baseline is present on the UEDGE profile in contrast to the measurement.

## **VI. Summary**

We have measured upstream electron temperature and density profiles and derived gradient scale lengths from them. These have been related to the measured downstream heat flux widths and a very weak dependence between them has been found between the two quantities. The dependence is much weaker than simple two-point models would predict. A scaling law for the DIII-D heat flux width has been developed and is only dependent on  $\Gamma_p^{-1.24}$ . This is in very good agreement with JET scaling law that takes size into account. UEDGE runs are currently in progress and beginning to yield some insight into the mechanisms influencing the heat flux width. It is already clear that the plasma flows play a significant role in the shaping of the heat flux profile.

## **Acknowledgment**

This work was supported by the U.S. Department of Energy under DE-AC52-07NA27344, DE-FC02-04ER54698, DE-FG02-07ER54917, and DE-AC04-94AL85000. Thanks goes to Gary Porter for his time and patience helping with the UEDGE simulations.

## References

- [1] T. Rognlien, *et al.*, J. Nucl. Mater. **196-198** (1992) 347-351.
- [2] G.D. Porter, *et al.*, Phys. Plasmas **5** (1998) 1410.
- [3] A. Hermann, *et al.*, Plasma Phys. Control. Fusion **37** (1995) 17.
- [4] A. Loarte, *et al.*, J. Nucl. Mater. **266-269** (1999) 587-592.
- [5] C.S. Pitcher and P.C. Stangeby, Plasma Phys. Control. Fusion **39** (1997) 779.
- [6] C. Lasnier, *et al.*, in Proc. 36th EPS Conf. on Plasma Physics, Sofia, Bulgaria, June 29 - July 3, 2009 ECA Vol.33E, P-4.140 (2009).
- [7] G. Kirnev, *et al.*, Plasma Phys. Control. Fusion **49** (2007) 689.

**Figure Caption**

Fig. 1. Upstream  $T_e$  and  $n_e$  profiles mapped to the outer midplane. Fits to exponentials on both the core and SOL sides of the profile are shown. The SOL side fit was used as a measure of the upstream profile gradient scale length.

Fig. 2. Typical heat flux profile as a function of major radius relative to the location of the separatrix at the midplane,  $R - R_{sep,mp}$ . Also shown in red are offset exponential fits to both sides of the profile.

Fig. 3. Plot of the heat flux width,  $\lambda_q$ , versus the Thomson profile e-folding length in the scrape off layer,  $\lambda_{Te,sol}$ . Solid red line is a linear fit between the two parameters. The slope,  $s$ , is 1/10th that predicted by simple two-point models.

Fig. 4. Plot of the heat flux width,  $\lambda_q$ , versus  $I_p$  for two ranges of  $B_t$  (red and blue curve fits). Due to the weak dependence of  $\lambda_q$  on  $B_t$ , the two curves nearly overlap. The black line is fit to all the data (red and blue circles).

Fig. 5. Plot of  $\lambda_q^{DIII-D}$  versus  $\lambda_q^{JET}$  showing that the DIII-D fits the JET scaling law.

Fig. 6. Comparison of measured heat flux (blue, multiplied by 5.2) and that predicted by UEDGE (blue). For this case  $I_p = 1.5$  MA.

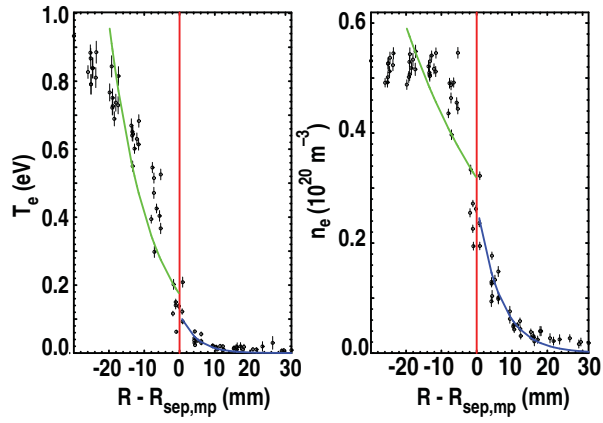


Figure 1

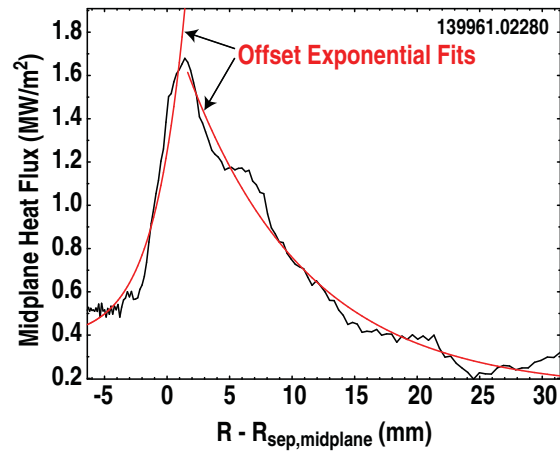


Figure 2

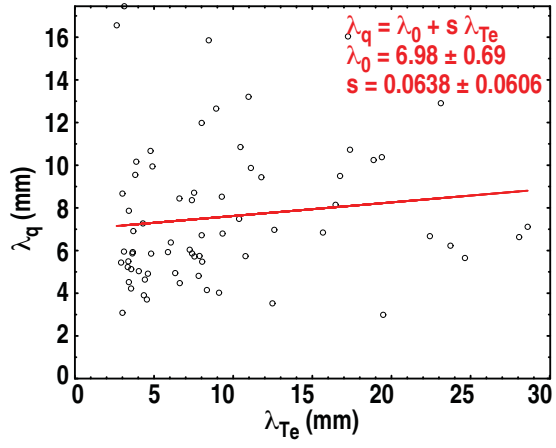


Figure 3

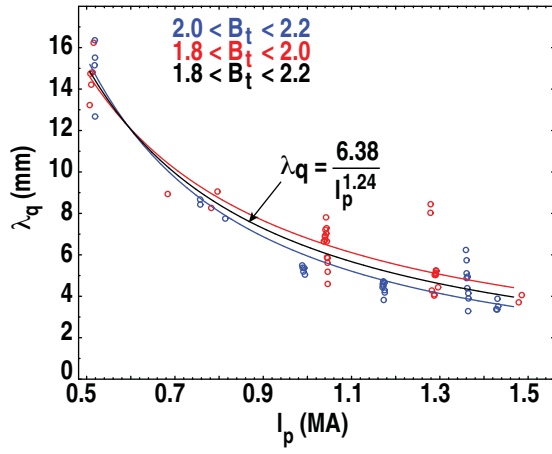


Figure 4

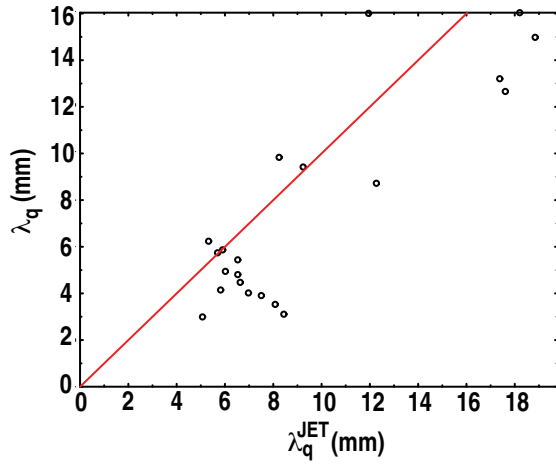


Figure 5

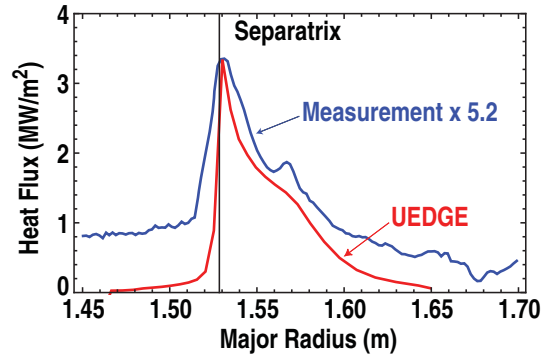


Figure 6

## APPENDIX C

# Two Dimensional Transport Effects in the Tokamak Scrape-off Layer Plasma

D.N. Hill

Presented at the 19th International Conference on  
Plasma Surface Interactions,  
May 24-28, 2010 in San Diego, California

## Two dimensional transport effects in the tokamak scrape-off layer plasma

D.N. Hill<sup>a\*</sup>, G.D. Porter<sup>a</sup>, and T.D. Rognlien<sup>a</sup>

<sup>a</sup>*Lawrence Livermore National Laboratory, Livermore, 94550, USA*

### Abstract

The effect of 2D transport in the tokamak scrape-off layer (SOL) on relating measured divertor heat flux profiles to midplane plasma profiles is explored with the UEDGE code for a range of transport assumptions. The relationship between the divertor heat flux profile and the midplane plasma temperature profile as determined from UEDGE is compared to commonly used predictions from 1D and “2-point” analytic relation. Results show that the parametric variation in  $\lambda_{q,div}$  with midplane separatrix values follows the conduction-limited 2-point model, though the actual value of  $q_{||}$  on a given flux surface is much lower than implied by the midplane  $T_{e,sep}$ , and  $\lambda_{q,div}$  is ~ twice as wide as expected from these models. Poloidal variations in  $\chi$  result in minimal change to radial profiles and probably can't be distinguished experimentally from cases with uniform  $\chi$  having the same flux-surface average value.

*JNM keywords:* T0100 Theory and modeling, P0500 Plasma-material interaction

*PSI-19 keywords:* Scrape-off layer simulation, UEDGE, DIII-D, heat flux

*PACS:* 52.55.Rk, 52.55.Fa, 52.40.Hf, 52.25.Fi

*\*Corresponding and presenting author address:* General Atomics, PO Box 85608,

*San Diego, California 92186-5608, USA*

*\*Corresponding and presenting author e-mail:* hilldn@fusion.gat.com

## I. Introduction

The prediction of peak steady-state heat loads on divertor surfaces is an important element for the design of next generation tokamak burning plasma fusion experiments. Predictions can be based on extrapolation from existing measurements and/or numerical simulations which incorporate relevant scrape-off layer (SOL) physics. Due to the complexity of simulations which accurately treat the SOL geometry and the broad range of relevant physical effects, trends in experimental data are often compared against simple 1D or 1.5D analytic approximations.

In this paper we use the UEDGE 2D scrape-off layer simulation code [1] to examine how well the simple models reproduce the properties of the SOL plasma as determined by the more complete treatment. At the same time, we examine the scaling of peak divertor heat flux and profile width with upstream parameters such as electron temperature, power, density, toroidal field (connections length) and transport coefficients. The purpose of this activity is not to evaluate the validity of UEDGE in matching experiment as in [2-4], but rather to use it as a tool to understand the effect of the 2D geometry as it impacts the behavior of the SOL for only the simplest of effects; namely, thermal transport in the absence of large radiative losses, high impurity concentrations, strong flows, and transients.

In the following sections we examine several aspects of SOL thermal transport, first summarizing basic transport equations and the assumptions that result from considering parallel thermal transport as “dominant.” Then, UEDGE is used to compute basic SOL parameters and the UEDGE output is compared to the simple model. Finally, the effects

of the 2D divertor tokamak geometry and of spatially varying transport coefficients are examined.

## II. The SOL dominated by parallel thermal conduction

It is well known that the heat conduction along magnetic field lines is much larger than cross-field thermal conduction [5,6]. At  $n_{e,mid} = 2 \times 10^{19} \text{ m}^{-3}$  and  $T_{e,mid} = 100 \text{ eV}$  with  $\chi_e = 1 \text{ m}^2/\text{s}$ , parallel and perpendicular power densities are  $1.0 \times 10^9$  and  $6.4 \times 10^4$  ( $\text{W}/\text{m}^2$ ), for 20 m and 0.5 cm gradient scale lengths, respectively. Parallel thermal conductivity is independent of density, but depends strongly on temperature ( $T^{3/2}$ ), while perpendicular conductivity depends on the product of density ( $n$ ) times the anomalous radial thermal diffusivity for ions (electrons),  $\chi_{e,i}$ . For electrons, the relations are [5]:

$$q_{\parallel}(\text{W}/\text{m}^2) = -2050 T_e^{5/2} \frac{dT_e(\text{eV})}{ds(\text{m})} , \quad (1)$$

for  $Z=1$ , and

$$q_{\perp,e}(\text{W}/\text{m}^2) = 3200 n (10^{20} \text{ m}^{-3}) \chi_e (\text{m}^2/\text{s}) \frac{dT_e(\text{eV})}{dy(\text{cm})} , \quad (2)$$

where  $s$  is the distance along field lines and  $y$  is the distance perpendicular to a flux surface. While the ratio of parallel to perpendicular power density is large, the total plasma surface area on the separatrix is much larger ( $\sim 25 \text{ m}^2$  in the DIII-D tokamak) than the cross sectional area of the SOL perpendicular to  $\mathbf{B}$  ( $0.017 \text{ m}^2$ ), so both components are important on a flux surface.

Frequently, for qualitative scaling purposes, the radial transport on a flux tube is

neglected, so the energy balance can be integrated along field lines, giving the well-known relationship between upstream and downstream electron temperatures for plasmas subject to collisional thermal conduction,

$$q_{\parallel} = \left( T_{e,mid}^{7/2} - T_{e,div}^{7/2} \right) / L_{\parallel} . \quad (3)$$

Given the large exponent, the downstream temperature can be neglected. If this relationship holds on flux surfaces, the ratio of the heat flux to electron temperature scale lengths immediately follows:  $\lambda_{q,mid} \propto 2/7 \lambda_{T,mid}$ , with the divertor heat flux related to the midplane heat flux by magnetic flux expansion.

The integrated 1D model can be expanded by including integrated radial energy transport in the entire SOL, thereby finding the overall  $e$ -folding width of the SOL at the midplane,  $\lambda_{q,mid}$ ,

$$\lambda_{q,mid} \propto \frac{q_{95}^{4/9} n_{e,mid}^{7/9} \chi_{\perp}^{7/9}}{P_{SOL}^{7/9}} , \quad (4)$$

where  $q_{95}$  is the safety factor at the 95% flux surface. This is the so-called 2-point SOL model, as discussed in Ref. 2. When the parallel heat flux is limited by the sheath at the divertor plate, the divertor temperature is not much lower than the midplane temperature, and a much weaker dependence on density and power results

$$\lambda_{q,mid} \propto \frac{q_{95}^{2/5} n_{e,mid}^{1/5} \chi_{\perp}^{3/5}}{P_{SOL}^{1/5}} . \quad (5)$$

These relations will now be compared with UEDGE simulations.

### III. UEDGE Simulation Methodology

The UEDGE code solves the 2D transport equations for particles (fuel and impurity ions), momentum, and energy on a  $50 \times 30$  mesh (poloidal x radial) spanning the edge plasma from 3 cm inside the separatrix to 1.8 cm outside the separatrix at the plasma midplane. The UEDGE code calculates the ionization source and radiative and charge exchange losses throughout the plasma. Flux limits to ion and electron parallel thermal conductivity were enabled, but neither particle drifts nor impurity transport were turned on for this study. The calculated divertor heat flux includes electron and ion conduction, convection, classical sheath physics, and recombination energy [2].

The computational mesh was generated from DIII-D MHD equilibria provided by EFIT. Thomson scattering data from lower-single-null discharges used in a divertor experiment provided initial starting point for the density (134079 through 134082) at the top of the pedestal; the total power from the core plasma was set equal to the neutral beam heating power. The plasma shape was nearly identical for these discharges.

Scans with UEDGE were carried out by varying only the single parameter of interest rather than trying to mimic or match how all the midplane parameters vary when one parameter is changed. Once the run was complete, all relevant quantities were available for plotting and analysis, making it a simple matter to determine gradient scale lengths as a function of position in the SOL, which then could be used to evaluate Eqs. (4), (5), and (6). In all, over 50 UEDGE runs were completed, which included scans of power, density, toroidal field, carbon impurity fraction/radiative loss, and radial transport coefficients.

#### **IV. Analysis of power balance on SOL flux surfaces**

Power flows into the tokamak SOL through radial transport across the whole plasma

separatrix surface, whereas the basic analysis of Eqs. (4)-(6) assume that power flows into the SOL at a single location. As the full 2D UEDGE simulation shows, the immediate consequence is that Eq. (4) no longer strictly applies globally in the SOL, and so knowing the midplane electron temperature does not directly specify the parallel heat flux on a flux surface. Figure 1 shows that the poloidal distribution of the perpendicular heat flux across the separatrix into the SOL ( $q_{\perp}$ ) is strongly peaked at the outboard midplane (defined as  $\theta_{pol} = 270^{\circ}$ ) due to the radial compression of flux surfaces there, even when the radial transport ( $\chi_e$  and  $\chi_i$ ) is spatially uniform. Further, the parallel heat flux does not peak at the same place as  $q_{\perp}$ , but down near the x-point, closer to the divertor targets, and there is a stagnation point (zero parallel heat flux) near the top of the plasma, opposite the x-point. Yet, as shown, the electron temperature in the SOL remains high around the whole boundary.

Another effect also comes into play which further breaks the relation between downstream heat flux (near the divertor targets) and midplane  $T_e$  implied by Eq. (4). Radial transport removes energy from higher temperature flux surfaces to neighboring, cooler flux surfaces further out in the SOL. For example, with  $\chi_e = 0.5 \text{ m}^2/\text{sec}$  (a common value derived from fitting  $T_e$  profiles in DIII-D H-mode discharges), half the power crossing the separatrix is transported radially outward from the first 2 mm of the SOL, leaving only half to arrive at the divertor target. In Fig. 2 we plot the heat flux at the outer divertor target as determined from UEDGE (2D solution) and the heat flux as determined from Eq. (4) using  $T_{e,mid}$  from UEDGE vs the radial distance from the separatrix strike point. As shown, the actual divertor heat flux across the SOL is only about 30% implied by the simple 1D analysis. This ratio is fairly independent of  $\chi_e$  in

the SOL.

Below the x-point, additional energy loss from flux tubes occurs by radial transport into the private flux region (PFR). The effect is not as large as might be imagined considering that the private region has no source of energy, because magnetic flux expansion is large near the x-point, reducing the radial temperature gradient. For typical DIII-D divertor configurations, UEDGE predicts only about 10-12% of the outer-divertor SOL power diffuses into the PFR, and reducing  $\chi_e$  nearly to zero in the private region reduces this fraction to just less than 10%, with a corresponding rise in peak heat flux of less than 20%.

## V. Relationship between midplane temperature profiles and divertor heat-flux profiles

The large uncertainties in the divertor heat flux database for ITER, as well as projections of very high heat flux for DEMO, have motivated increased interest in quantifying the dependence of the divertor heat flux profile width on core plasma parameters and upstream/midplane SOL temperature profiles. Figure 3 shows that the full  $1/e$  width of the outer divertor heat flux profile, when mapped back to the midplane, is nearly a factor of two larger than the electron temperature e-folding length  $\lambda_{q,mid} / \lambda_{T,mid} = 0.6$ , as compared to  $2/7=0.28$ ). Here we have computed the slope of the temperature profile over the range 0 to 0.4 cm just outside the separatrix, in the region where the divertor heat flux peaks and begins to fall off. As shown, the ratio  $\lambda_{q,mid} / \lambda_{T,mid}$  is relatively insensitive to  $\chi_e$ .

Moving beyond comparisons with 1D conduction, we have also examined the parameter dependence of the divertor heat flux profile width as predicted from the 2-DIII-D contribution to the FY2010 JRT final report: C.J. Lasnier, *et al.*

point SOL model. Using the output from the full set of UEDGE parameter scans to determine  $n_{e,sep}$ ,  $T_{e,sep}$ , and  $\lambda_{q,mid}$ , we evaluated the two-point model results [Eqs. (5) and (6)] to obtain  $\lambda_{q,mid} \equiv \lambda_{q,2point}$  for comparison. Midplane separatrix values for  $n_e$  and  $T_e$  were taken from UEDGE. As shown in Fig. 4, where we plot normalized  $\lambda_{q,2point}$  vs.  $\lambda_{q,mid}$  from UEDGE, the conduction-limited two-point model reproduces the full 2D solution reasonably well. Note that, to account for geometrical factors missing from Eq. (5), all  $\lambda_{q,2point}$  values have been normalized by a single constant factor to match the UEDGE value at  $\lambda_{q,mid} = 0.256$  cm. Note that, for  $\lambda_{q,mid} \leq 0.4$  cm, the ratio of  $T_{e,mid}$  to  $T_{e,div}$  falls below 2, suggesting that the SOL should transition from the conduction-limited to sheath limited regime; this transition is much more evident when comparing UEDGE against Eq. (5), which is cannot be shown here due to space limitations.

## VI. Effect of spatially varying transport coefficients

It is widely recognized that assuming spatially uniform radial transport coefficients for particles and energy is likely an oversimplification for the scrape-off layer. Indeed, a radial variation in  $\chi_e$  is often required to match simulation with experimental profiles in the SOL. It may be argued that SOL model validation will require a complete 2D map of the edge turbulence, but such measurements will not be available soon.

Here we explore how varying the poloidal distribution of the radial energy flux across the separatrix may affect both the divertor heat flux and midplane electron temperature profiles. We note that the larger surface area and compression of the outboard flux surfaces due to the Shafranov shift will peak radial transport at the outboard midplane

significantly even with spatially uniform  $D$  and  $\chi$  [2]. Giving the transport coefficients a ballooning character ( $\chi \propto 1/B^2$  or even  $1/B^3$ ) will lead to additional peaking of the radial transport at the outboard midplane ( $B_T \propto 1/R$ ). In all cases considered, the radial energy flow ( $\text{W/m}^2$ ) is peaked at the outboard midplane ( $\theta = 270^\circ$ ), with half the total power coming out within a full-width at half-maximum varying from  $\pm 50^\circ$  (uniform  $\chi = 0.5 \text{ m}^2/\text{s}$ ) to  $\pm 40^\circ$  ( $\chi \propto 1/B^3$ ,  $0.18 \leq \chi \leq 1.5 \text{ m}^2/\text{s}$ ).

Poloidal peaking of the radial transport acts in the same manner as reducing a spatially uniform transport coefficient. In effect, radial transport is turned down everywhere except in one section of the SOL, and turning down  $\chi$  leads to a narrower heat flux profile. Thus, if data is only available at midplane and divertor locations, it appears extremely hard to see any measurable difference in basic SOL properties resulting from poloidally non-uniform transport coefficients. Fig. 5 compares computed midplane electron temperature profiles and divertor heat flux profiles for two cases having nearly the same field-line average  $\chi_{ave} = (1/L_{\parallel}) \int \chi(\ell) d\ell_{\parallel}$  but very different form for  $\chi$ : 81bb has uniform  $D$ ,  $\chi = 0.5 \text{ m}^2/\text{s}$  and ii has  $\chi \propto 1/B^3$  with  $\chi_{ave} = 0.49 \text{ m}^2/\text{s}$ . The differences between the profiles are smaller than variations in typical DIII-D data.

## VII. Conclusions

This work reemphasizes that physics validation of the tokamak scrape-off layer physics requires application of comprehensive 2D analysis tools to make quantitative comparisons between midplane and divertor parameters. Using midplane (“upstream”) temperatures near the separatrix or temperature scale length coupled with 1D or “2-point” models to predict the peak divertor heat flux and profile widths can introduce significant

systematic error unless the models are calibrated by a full 2D calculation. Further uncertainties will almost certainly arise when impurity transport, detachment physics, and particle drifts are added to the problem. For quantities of interest such as the divertor heat or particle flux, parameter variations and cross-tokamak comparisons should focus on these quantities, mapped back to the midplane to account for topological considerations, rather than introducing additional complexity by relating data via secondary quantities.

The weak dependence of divertor heat flux and midplane temperature profiles on the poloidal variation of radial transport coefficients suggests that validating SOL models by aiming forever more comprehensive diagnostic coverage around the boundary may be of limited value. On the other hand, the robustness of the basic scaling obtained from the simple 2-point model should motivate increased emphasis on parameter variations to validate the physics of the scrape-off layer. The value of using 2D simulation tools to explore the physics of the scrape-off layer and to identify and motivate new diagnostics and experiments cannot be overemphasized.

### **Acknowledgment**

This work was supported by the U.S. Department of Energy under DE-FC02-04ER54698 and DE-AC52-07NA27344.

### **References**

- [1]. T.D. Rognlien, *et al.*, Contrib. Plasma Phys. **34**, (1994) 362, and T. Rognlien, *et al.*, J. Nucl. Mater. **196-198** (1992) 347.
- [2] Gary .D. Porter, *et al.*, Phys. Plasmas **3** (1996) 1967-1975.
- [3] G.D. Porter, *et al.*, Phys. of Plasmas, **7** (2000), 3663-3690.

- [4] G.D. Porter, *et al.*, *Fusion Sci. Technol.* **48** (2005) 1127-1140.
- [5] C.S. Pitcher, *et al.*, *Plasma. Phys. Control. Fusion* **39** (1997) 779-930.
- [6] P. Stangeby, *The Plasma Boundary of Magnetic Fusion Devices*, Institute of Physics Publishing, Bristol and Philadelphia, 2000.

## Figure Captions

Fig. 1. Poloidal distribution of parallel and perpendicular heat flux into the SOL as a function of parallel length along a field line 1.7 mm outside separatrix: total parallel energy flux  $Q_{\parallel}$  ( $\circ$  dashed), parallel heat flux  $q_{\parallel}$  ( $\blacklozenge$ ) on 1.7 mm field line, and radial heat flux  $q_{\perp}$  across separatrix ( $\bullet$  solid). Inboard midplane is at  $L=28.8$  m.

Fig. 2. Outer-leg divertor heat flux profiles from UEDGE ( $\bullet$ ), Eq. (5) ( $\circ$ ), and their ratio ( $\blacktriangle$ ).

Fig. 3. Midplane scale lengths for electron temperature,  $\lambda T_e$ , divertor heat flux,  $\lambda Q$ , and value predicted from 2-point model ( $0.28 \lambda T_e$ ).

Fig. 4. Comparison between equivalent midplane heat flux profile as determined from conduction limited 2-point model [Eq. (5)] and 50 UEDGE divertor heat flux calculations mapped to midplane. Normalization for 2-point model data as indicated by arrow at  $y = 0.216$ ).

Fig. 5. Comparison of midplane electron temperature profiles and outer divertor heat flux profiles for case ii: uniform  $\chi = 0.5 \text{ m}^2/\text{s}$  and case bb:  $\chi \propto 1/B^3$  with  $\chi_{ave} = 0.49 \text{ m}^2/\text{s}$ .

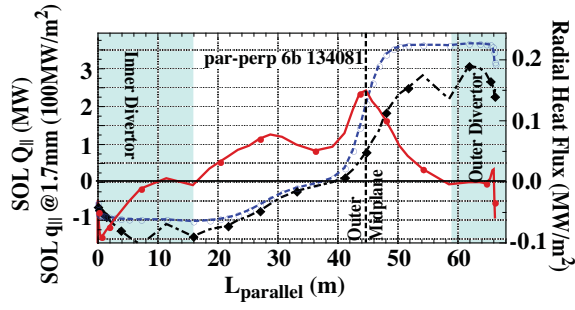


Figure 1

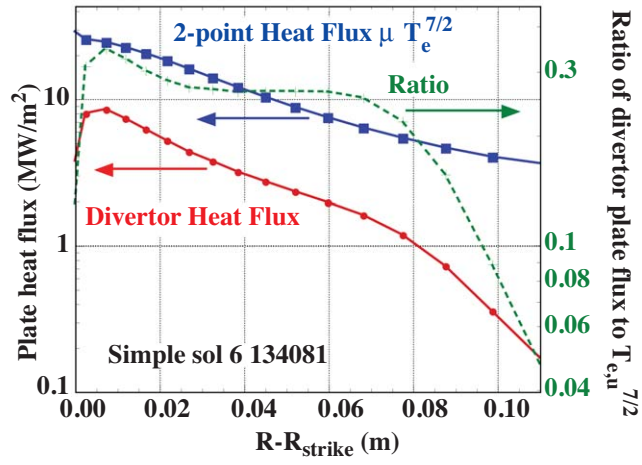


Figure 2

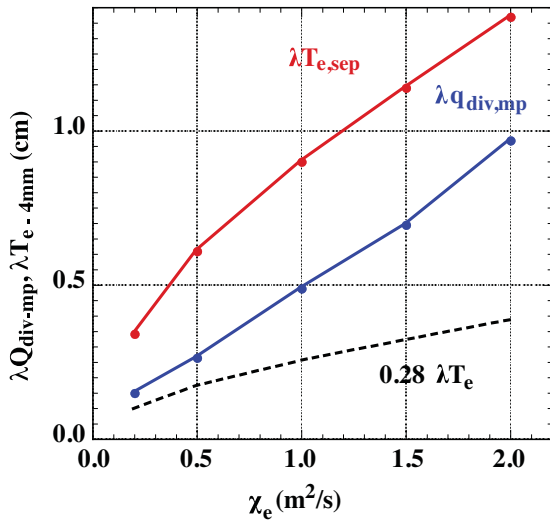


Figure 3

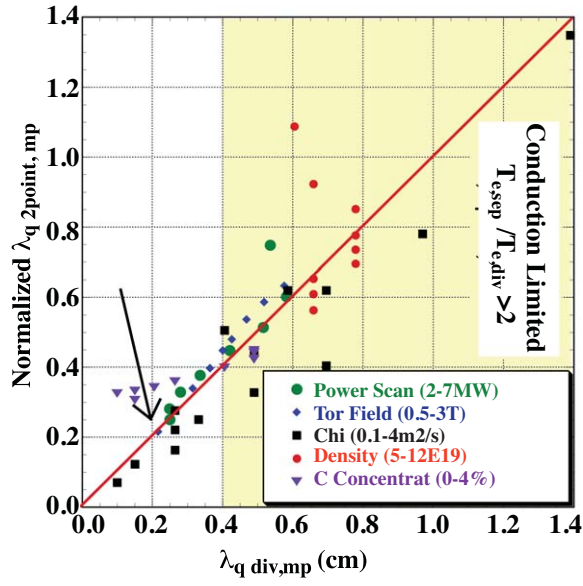


Figure 4

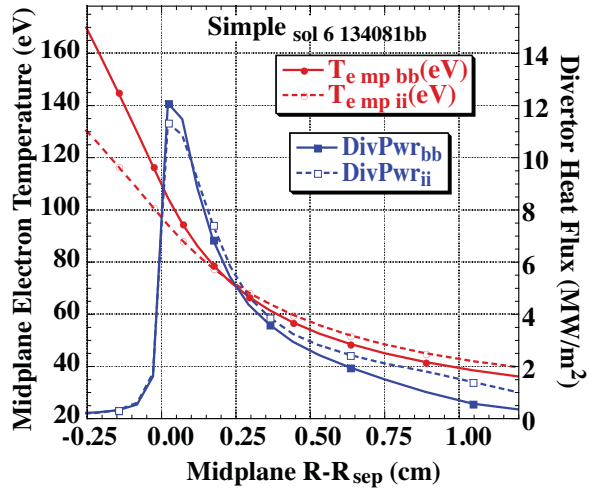


Figure 5

## APPENDIX D

### Scaling of Divertor Heat Flux Profile Widths in DIII-D IAEA 2010 Paper, EXD/P3-20

C.J. Lasnier

## Scaling of Divertor Heat Flux Profile Widths in DIII-D

C.J. Lasnier<sup>1</sup>, M.A. Makowski<sup>1</sup>, J.A. Boedo<sup>2</sup>, N.H. Brooks<sup>3</sup>, D.N. Hill<sup>1</sup>, A.W. Leonard<sup>3</sup>,  
and J.G. Watkins<sup>4</sup>

<sup>1</sup>Lawrence Livermore National Laboratory, Livermore, California 94550, USA

<sup>2</sup>University of California-San Diego, La Jolla, California 92093-0417, USA

<sup>3</sup>General Atomics, PO Box 85608, San Diego, California 92186-5608, USA

<sup>4</sup>Sandia National Laboratories, Albuquerque, New Mexico 87185, USA

e-mail:Lasnier@LLNL.gov

**Abstract.** Recent experiments in DIII-D have led to a new empirical scaling of divertor heat flux width  $\lambda_{q,\text{div}}$  as a function of plasma parameters. Previous scaling efforts around the world have produced results that are not in agreement with each other. We controlled conditions during parameters scans as closely as possible to prevent other complicating variations. We varied  $B_T$  at constant  $I_p$ ,  $I_p$  at constant  $B_T$ , and  $B_T/I_p$  at constant  $q_{95}$ . The neutral beam injected power was changed at constant  $I_p$  and  $B_T$ . Line-averaged density was varied at constant  $I_p$  and  $B_T$ . We find  $\lambda_{q,\text{div}}$  is principally dependent on the plasma current to the -1.24 power. Our results agree with previous conduction-limited scalings from JET and NSTX, and exclude other scalings from both JET and other devices.

### 1. Introduction

The width of the divertor heat flux profile  $\lambda_{q,\text{div}}$  is of great interest in future large tokamaks as well as many present devices. Previous studies examining the parametric dependence of  $\lambda_{q,\text{div}}$  have arrived at diverse scalings [<sup>1</sup>] in JET [<sup>2</sup>], ASDEX-Upgrade [3], JT60-U [4,5], DIII-D [6,7], and NSTX [8]. With the aim of resolving this disagreement, we performed measurements in lower single-null edge localized mode (ELM)ing H-mode diverted configurations. We varied toroidal field ( $B_T$ ) at constant plasma ( $I_p$ ),  $I_p$  at constant  $B_T$ , and  $B_T/I_p$  at constant  $q_{95}$ . The neutral beam injected power  $P_{\text{inj}}$  was changed at constant  $I_p$  and  $B_T$ . Line-averaged density  $\bar{n}_e$  was varied at constant  $I_p$  and  $B_T$ . The divertor heat flux was calculated from infrared camera measurements using a new high-resolution fast-framing IR camera.

The IR camera recorded divertor plate surface thermal emission at multi-kilohertz frame rates through the whole discharge, so that time-averaged data as well as rapid changes due to ELMs were obtained. The heat flux at each position in the radial profile was calculated at each of the times steps using the THEODOR 2D heat flux analysis code [9]. The THEODOR code has a capability of including a surface layer of arbitrary effective thickness to account for fast surface cooling often observed during transients. This layer must be chosen empirically using the surface temperature history. In order to make the simplest possible assumptions, no surface layer effects were assumed in the heat flux calculation. This results in some overshoot when the surface temperature falls after an

ELM pulse. Consequently, we avoid the time slices immediately after an ELM in this analysis.

In an effort to separate the physics of ELM heat flux scaling from the scaling of the inter-ELM heat flux, we chose time slices least affected by ELMs. Therefore heat flux data was averaged from a time 20% into the inter-ELM interval until 95% of the way to the onset of the subsequent ELM, prior to exponential profile fitting. This fixed fraction of the ELM period was chosen so as to reduce the impact of overshoot in the heat flux calculation resulting from the previous ELM, due to the effect of surface layers mentioned above. The overshoot is most pronounced immediately after the ELM heat flux peak and then falls off with time.

The heat flux profiles were coherently averaged for these inter-ELM times over multiple inter-ELM intervals of nearly fixed conditions.

The outer strike point heat flux profile was mapped to outer midplane and fitted on the public and private flux side with separate exponential ( $a_0 + a_1 e^{x/\lambda}$ ) profiles (Fig. 1) [10]. The heat flux width  $\lambda_{q,div,midplane}$  is taken to be the sum of the two exponential widths. This is different from the integral width proposed by Loarte [11], in which the integral of the profile is divided by the peak. Our heat flux profiles show plateau values in the private flux and far scrape-off-layer (SOL), at a level too large to be accounted for by absorbed radiation or plasma interaction. It is possible that there is some effect of internal optical reflections. The plateau effect is still being investigated. Due to these flat areas in the common and the private flux areas far from the separatrix, the Loarte width would depend on the arbitrary width of the integration window, and so is unsatisfactory measure here whereas the sum of the exponential widths is not sensitive to this parameter.

Heat flux data was averaged from a time 20% into the inter-ELM interval until 95% of the way to the onset of the subsequent ELM, prior to exponential fitting. This fixed fraction of the ELM period was chosen so as to reduce the impact of overshoot in the heat flux calculation resulting from the previous ELM, due to the effect of surface layers mentioned above. The overshoot is most pronounced immediately after the ELM heat flux peak and then falls off with time.

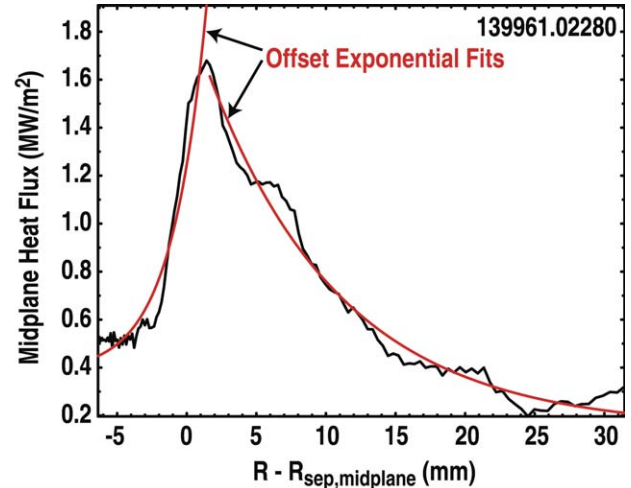


FIG. 1. Typical heat flux profile after mapping to the midplane as a function of distance from the separatrix at the midplane,  $R - R_{sep,mp}$ , showing offset exponential fits.

We show scaling of the profile width as a function of the parameters varied, and compare with published results from other devices.

## 2. Variation in $\lambda_{q,\text{div}}$ with Plasma Parameters

Multi-parameter fits were made to investigate the scaling of  $\lambda_{q,\text{div}}$  with  $I_p$  (plasma current),  $q_{95}$  (safety factor at the 95% flux surface),  $n_e$  (electron density),  $B_T$  (toroidal field),  $P_{\text{SOL}}$  [power flow into the SOL],  $P_{\text{inj}}$  (neutral beam injected power),  $s_{95}$  (magnetic shear at the 95% flux surface), and  $\alpha_{95}$  (dimensionless pressure gradient at the 95% flux surface).

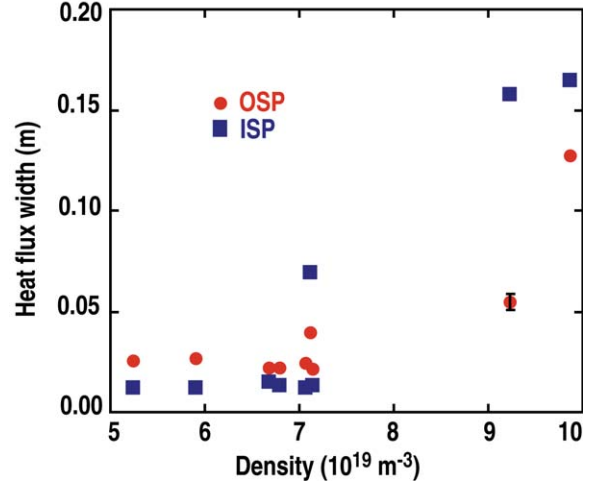


FIG. 2. Dependence of divertor heat flux profile width on density. There is essentially no effect below the detachment threshold. A representative error bar is shown on the red point at lower right.

In Fig. 2, for the case with averaging over ELMs [12], the full widths at half maximum (FWHM) of the heat flux in the divertor are shown plotted against line-averaged density. The FWHM is used here because the heat flux profiles at higher density are not well-fit by the exponentials defined above. At low density,  $\lambda_{q,\text{div}}$  is independent of  $\bar{n}_e$ , but there is a threshold density of  $\sim 7 \times 10^{19} \text{ m}^{-3}$  where the profile becomes wider, representing the onset of detachment. In the density scan from which this data was extracted,  $P_{\text{in}}$  was 4.9–5.1 MW, except for the densities  $\bar{n}_e = 5.2 \times 10^{19} \text{ m}^{-3}$  and  $\bar{n}_e = 6.8 \times 10^{19} \text{ m}^{-3}$  where  $P_{\text{in}} = 7.2 \text{ MW}$ , and  $P_{\text{in}} = 4.1 \text{ MW}$ , respectively. Since we found  $\lambda_{q,\text{div}}$  does not depend on input power, this power variation does not affect the widths obtained from the density scan at these densities. Toroidal field was held constant at  $B_T = -1.9 \text{ T}$ , and plasma current was held at  $I_p = 1.3 \text{ MA}$ .

The effect of radiation from the outboard divertor on the strike point heat flux profile is small for the low-density attached discharges. It becomes significant at the onset of detachment where we see the profile broadening, and in fully detached strike points not considered here, the radiated power absorbed by the divertor plate accounts for nearly all the measured heat flux.

We find that  $\lambda_{q,\text{div},\text{midplane}}$  is larger at low plasma current, as shown in Fig. 3 [10], where  $\lambda_{q,\text{div},\text{midplane}}$  is plotted against  $I_p$ . The width decreases inversely as a power of the plasma current close to unity, namely  $\lambda_{q,\text{div},\text{midplane}} (\text{mm}) = 6.38/I_p^{1.24} (\text{MA})$ . Similar behavior is seen in NSTX [8] where the width decreases with increasing plasma current, approximately as  $1/I_p$ .

The error bar for  $\lambda_{q,div,midplane}$  is  $\pm 0.5$  mm. A representative error bar is shown for a data point in Fig. 3, but is otherwise omitted in this and succeeding figures so as not to obscure the data points.

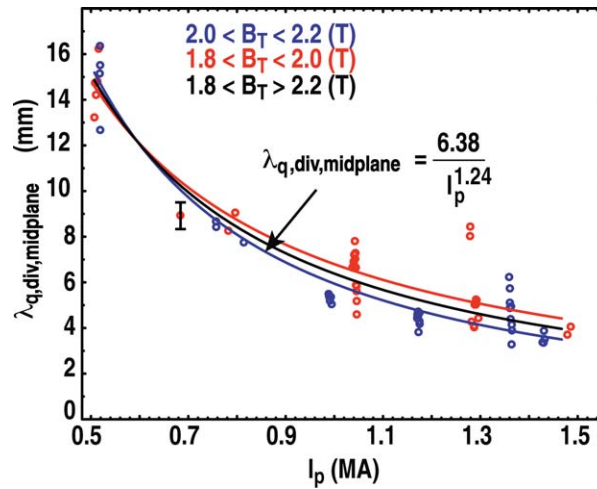


FIG. 3. Dependence of heat flux width (mapped to the midplane) on plasma current. The red and blue symbols denote two ranges of toroidal field, showing little effect from changing  $B_T$ . A representative error bar is shown.

We know that core plasma confinement improves at higher plasma current [13], and the behaviour observed is consistent with cross-field SOL transport also being reduced as plasma current increases. For this scan of plasma current, toroidal field was held fixed at  $B_T = -1.9$  T, and  $P_{inj} = 4.7\text{--}5.0$  MW, except for the point at  $I_p = 1.3$  MA where  $P_{inj} = 4.1$  MW. Density was not held constant, but allowed to vary at the natural H-mode density, because of practical difficulty measuring the heat flux at the OSP during the plasma pumping that would have been required to maintain constant density. Figure 4 [12] shows the line-averaged density variation during the  $I_p$  scan. Note that the range of densities is within the zone of Fig. 2 where the density variation shows little effect on the heat flux width. Also, the density remains at low Greenwald fraction as  $I_p$  is raised and consequently the detachment threshold is raised along with the density. Therefore the density variation during the  $I_p$  scan does not affect the heat flux width.

For the inter-ELM data, the widths  $\lambda_{q,div,midplane}$  showed no discernable trend in the multi-parameter fits with toroidal field  $B_T$ , in contrast to the case where the data was averaged over ELMs [12]. We varied  $B_T$  from 1.2 to 2.1 T (ion  $\nabla B$  drift toward the lower divertor). No correlation was seen between  $\lambda_{q,div}$  and  $B_T$ . The dependence on plasma current but not toroidal field is not fully understood.

We found both in the present analysis between ELMs and the previous analysis averaged over ELMs [12] only very weak dependence of  $\lambda_{q,div}$  on total input power  $P_{in}$ , which in these discharges is the sum of  $P_{inj}$  and the Ohmic heating power.

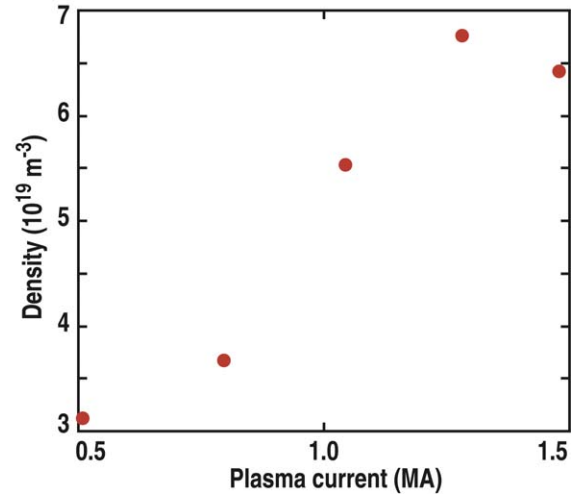


FIG. 4. Variation of line-averaged electron density during the plasma current scan. All these densities are at the low end of Fig. 3, so there was little effect of the density variations on the heat flux width.

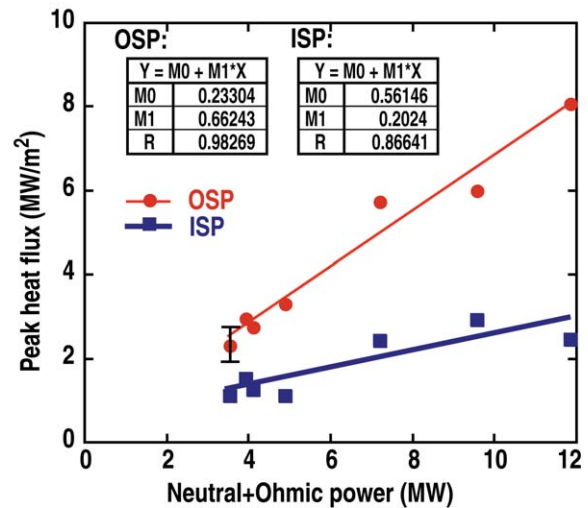


FIG. 5. ELM-averaged peak heat flux at the ISP and OSP plotted against the input power. Linear fits to the data are plotted, with fitting parameters shown in the boxes. The dependence on input power appears linear. A representative error bar is shown.

We illustrate this in Fig. 5, where peak heat flux averaged over ELMs is plotted against input power. The peak heat flux increases linearly with input power. By conservation of energy, the heat flux profile width stays fixed. As found on NSTX, JET and ASDEX-Upgrade (DIVII), we find essentially no (or very weak) dependence of the width on input power.

### 3. Divertor Heat Flux Profile Width in Relation to Upstream Temperature

Figure 6 [10] shows typical  $T_e$  (electron temperature) and  $n_e$  (electron density) profiles at the outer midplane derived from Thomson scattering measurements in the upper outer SOL. Typically 10–20 profiles were coherently averaged over a 200 ms window, from time slices just before ELMs. The Thomson profile data were mapped along field lines to the outer midplane. For each parameter ( $n_e$  and  $T_e$ ) exponential fits were made to the data near the separatrix, from inside and outside, which gave the electron temperature gradient scale lengths,  $\lambda_{T_e}^{\text{int}}$  and  $\lambda_{T_e}^{\text{SOL}}$ , respectively. The  $\lambda_{T_e}^{\text{SOL}}$  was found to have less scatter than either the  $\lambda_{T_e}^{\text{int}}$  or a hyperbolic tangent fit width. The fitted  $\lambda_{T_e}^{\text{SOL}}$  is not sensitive to the method of determining the separatrix location. The divertor heat flux profile widths  $\lambda_{q,\text{div,midplane}}$  were compared with upstream  $\lambda_{T_e}^{\text{SOL}}$ , showing a very weak correlation (Fig. 7) [10]. This is contrary to two-point models that give that predict  $\lambda_{T_e} = (7/2) \lambda_q$  [14].

We can conclude that the heat flux profiles for the most part are wider than predicted by the two-point model. Departures from that model are to be expected due to the presence of radial transport, radiation within the transport volume, and neutral transport in the divertor, which these two-point models neglect.

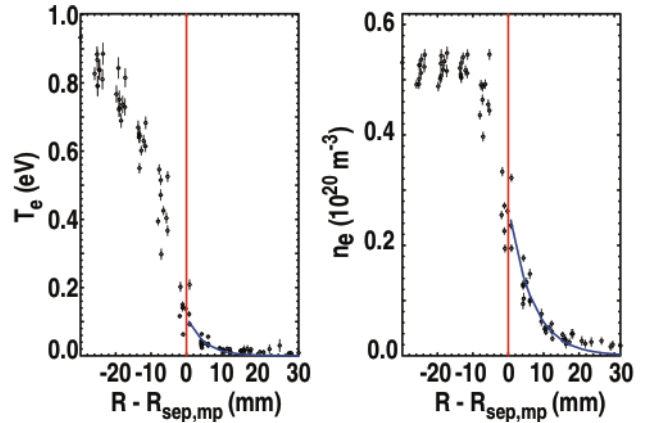


FIG. 6. Typical outer midplane electron temperature and density profiles mapped from Thomson scattering measurements to the outer midplane. The curves show the exponential fits.

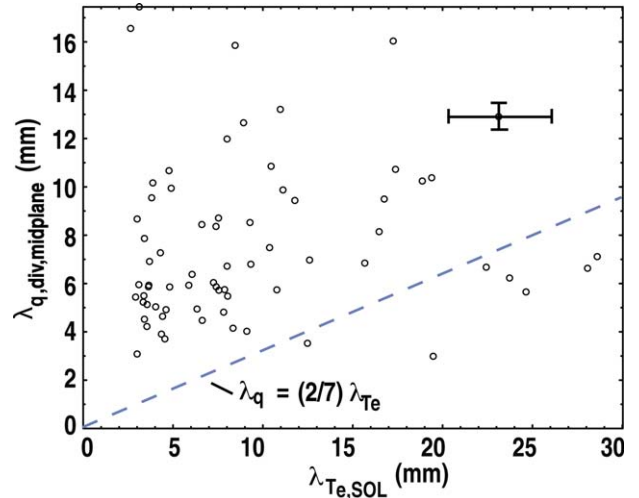


FIG. 7. Plot of the heat flux width,  $\lambda_{q,\text{div,midplane}}$ , versus the Thomson electron temperature profile e-folding length in the scrape off layer,  $\lambda_{T_e}^{\text{SOL}}$ . The widths are larger than expected from a two point model,  $\lambda_q = (2/7) \lambda_{T_e}$  which is shown by the blue dashed line.

#### 4. Comparison with Other Scaling Results

The results of the present scaling study are in rough agreement with the JET scaling of conduction limited heat flux widths [15], given by

$$\lambda_{q,\text{div,midplane}}^{\text{JET}} \text{ (mm)} = 2.41 \times 10^{-5} B_T^{-1} \text{ (T)} P_{\text{SOL}}^{-1/2} \text{ (MW)} n_e^{1/4} \text{ (m}^{-3}) q_{95} R^2 \text{ (m)} \quad (1)$$

The comparison between the present DIII-D scaling and Eq. (1) is shown in Fig. 8 [10]. The dominant dependence is in  $q_{95}/B_T \sim 1/I_p$ . The density dependence is weak in the JET scaling law, in agreement with our observations. However, our fits show no dependence on  $P_{\text{SOL}}$ , the power crossing the separatrix. With no machine size variation in our data to compare with the  $R^2$  dependence from JET, we are left with  $1/I_p$  from Eq. (1), which is similar to our finding. Our finding of no dependence of the width on input power is in direct contrast to Eq. (1).

The heat flux width prediction from Ref. [5] was also considered:

$$\lambda_{q,\text{div,midplane}}^{\text{H-2}} \text{ (mm)} = 5.3 P^{0.38} \text{ (MW)} I$$

The widths predicted by Eq. (2) are 10 times smaller than those found in DIII-D [10]. Equation (2) contains no scaling for machine size.

#### 5. Comparison of Divertor Heat Flux Profiles with UEDGE Modeling

Modeling of discharges from the plasma current scan using the UEDGE code [16] has been initiated, in an attempt to identify what physical mechanism causes the heat flux width to change with plasma current. The power flow through the SOL, and the midplane electron temperature and density profiles are taken from the experimental data. However, there is sufficient scatter in the experimental electron temperature and density data that widely varying profiles could be chosen that are all within the error bars. Transport coefficients in UEDGE are adjusted until the upstream profiles agree with the experiment. In the results reported here, best agreement with the heat flux width was obtained when drifts were turned on at 20% of full value, and poor agreement when drifts were turned

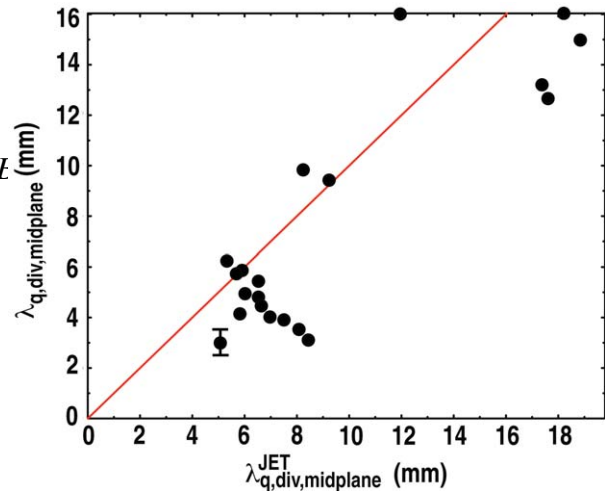


FIG. 8. Comparison of DIII-D heat flux profile width with the JET conduction-limited scaling applied to the same DIII-D data. The red line has a slope of unity. The DIII-D results are in reasonable agreement with the JET scaling. A representative error bar is shown.

off. The comparison between the experimentally determined heat flux profile and the UEDGE output for  $I_p = 1.5$  MA, the highest plasma current reached in the  $I_p$  scan, is shown in Fig. 9 [10] as a function of poloidal distance along the horizontal divertor surface. The experimental data are much lower than the UEDGE prediction, and the data are multiplied by a factor of 5.2 in the plot to match the UEDGE prediction at its peak value. The uncertainty in the upstream profiles creates a large margin of error in the UEDGE predictions of divertor heat flux and other divertor parameters. In addition, it is possible in the experiment to have heat deposited in unobserved locations whereas UEDGE, to achieve power balance, places that heat at the outer strike point. Further work is needed to reconcile these differences.

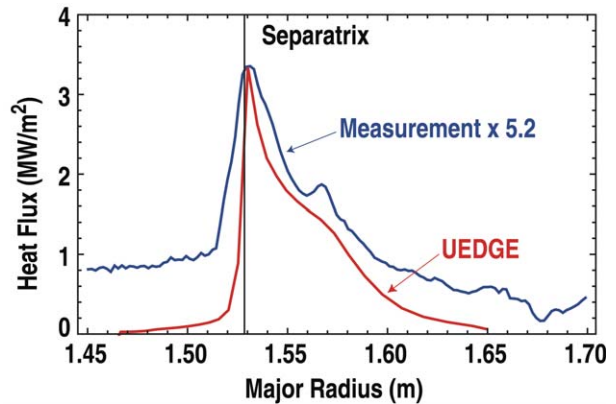


FIG. 9. Comparison of measured heat flux (blue, multiplied by 5.2) and that predicted by UEDGE (red) [10]. For this case  $I_p = 1.5$  MA.

The measured radiated power was 350 kW. This value was approximately matched in UEDGE (300 kW) when the flows were turned on at 20%, but the code greatly underestimated the radiated power (90 kW) when drifts were turned off. The heat flux profile in the model was narrower than in the experiment. Some degree of shoulder is seen in both the measured and experimental profile.

These preliminary attempts at UEDGE modeling are the beginning of a more in-depth effort to compare these measurements with modeling and to aid in understanding the physical origin of the scaling with plasma current. It is clear that drifts are important in interpreting the result, but we must obtain agreement with experimental data with drifts fully turned on.

## 6. Conclusion

In DIII-D, we find the strongest dependence of the divertor heat flux profile width is on the plasma current. The heat flux width varies inversely as the 1.24 power of the plasma current and not at all with input power. Our result is in substantial agreement with the conduction-limited JET scaling of Ref. [15] for plasma current but not for power, but not at all with the multi-machine scaling of Ref. [5]. We are not able to confirm any dependence of the heat flux width on the near-separatrix SOL fall-off length of the outer midplane temperature profile, although we find the simple two-point models do not provide an adequate description of the heat flux transport. Our heat flux profiles are substantially wider than predicted by the two-point model. We find no evidence in the

multi-parameter fitting of a significant dependence on  $B_T$  or  $P_{\text{SOL}}$ . The lack of change in heat flux profile width in spite of the change in field line connection length with  $B_T$  indicates reduction in cross-field SOL transport with  $B_T$ . The physical mechanism leading to the scaling of  $\lambda_q$  with  $I_p$  is not yet understood, but we note that increasing  $I_p$  is known to reduce radial transport inside the separatrix and we suspect a similar effect in the SOL. Attempts to compare the data with the UEDGE modeling code have begun, and we find that drifts are important in matching the heat flux profile width. At this point we still see substantial differences between the model and experiment. Further modeling will be done to help understand the  $I_p$  dependence of the heat flux profile.

This work was supported by the US Department of Energy under DE-AC52-07NA27344, DE-FG002-07ER4917, DE-FC02-04ER54698, and DE-AC04-94AL85000.

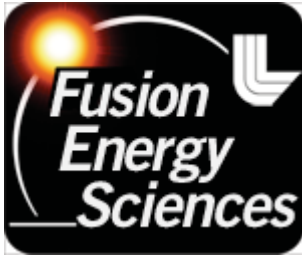
## References

- [1] LOARTE, A., *et al.*, Nucl Fusion **47** (2007) S203
- [2] EICH, T., *et al.*, J. Nucl. Mater. **333-339** (2005) 669
- [3] HERRMANN, A., Plasma Phys. Control. Fusion **44** (2002) 883
- [4] ITER Physics Basis Editors, Nucl. Fusion **39** (1999) 2137
- [5] LOARTE, A., *et al.*, J. Nucl. Mater. **266-269** (1999) 587
- [6] HILL, D.N., *et al.*, J. Nucl. Mater **196-198** (1992) 204
- [7] LASNIER, C.J., *et al.*, Nucl. Fusion **38** (1998) 1225
- [8] MAINGI, R., *et al.*, J. Nucl. Mater **363-365** (2007) 196
- [9] HERRMANN, A., *et al.*, Plasma Phys. Control. Fusion **37** (1995) 17
- [10] MAKOWSKI, M.A., *et al.*, “Comparison of Upstream  $T_e$  Profiles with Downstream Heat Flux Profiles and Their Implications on Parallel Heat Transport in the SOL in DIII-D,” Proc. of 19<sup>th</sup> International Conference on Plasma-Surface Interactions, San Diego, CA, 2010 and submitted for publication in J. Nucl. Mater.
- [11] LOARTE, A., *et al.*, J. Nucl. Mater. **266-269** (1999) 587
- [12] LASNIER, C.J., *et al.*, Proc. of 36th EPS Conference on Plasma Phys., Sofia, 2009 ECA Vol. 33E, P-4.140
- [13] CORDOY, J.G. and ITER Confinement Database and Modeling Working Group, Plasma Phys. Control. Fusion **39** (1997) B115–B127
- [14] PITCHER, C.S. AND STANGEBY, P.C., Plasma Phys. Control. Fusion **39** (1997) 779
- [15] KIRNEV, G., *et al.*, Plasma Phys. Control. Fusion **49** (2007) 689
- [16] ROGNLIEN, T., *et al.*, J. Nucl. Mater. **196-198** (1992) 347

# APPENDIX E

## UEDGE Modeling of DIII-D Discharge from C-Mod/DIII-D Similarity Experiment

M.E. Rensink



**MEMORANDUM**  
**TR-456336**

**LLNL-**

To: DIII-D 2010 Joint Research Task Team  
From: M E Rensink  
Date: 21 September 2010  
Subject: UEDGE simulation of DIII-D shot 141628 at 2490 msec

---

## **1 Introduction**

Experiments on CMOD and DIII-D have been run for similar plasma shapes to facilitate comparison of divertor heat loads. We have also run UEDGE simulations of the edge plasmas for these similarity shots. As previously identified, the relevant time slices are CMOD shot number 1100212024 at 1360 msec and DIII-D shot number 141628 at 2490 msec. The corresponding plasma shapes are shown in Figure 1 together with the divertor target surfaces. The principal qualitative difference is in the outer target configuration which is "open" for DIII-D and "closed" for CMOD.

## **2 Discharge Description**

DIII-D discharge 141628 is part of a series of shots for inter-machine comparisons for heat flux scaling. It has a shape that CMOD and NSTX can run. It was run with 3 + 4 gyrotron-equivalent beams running at 43 kV accelerating voltage, and no gyrotrons. Total power input was about 2.0 MW with 1.6 MW from beams and 0.4 MW ohmic heating.  $B_t = 1.7$  T,  $I_p = 0.76$  MA. The timeslice

2500 msec was selected for simulation because the plasma configuration was not “breathing” so TS data could be averaged over a longer time. This time slice is in the middle of an X-point sweep. Several diagnostics on the experiment can be used to benchmark the UEDGE simulations: Thomson Scattering (TS), reflectometer and Charge-Exchange Recombination (CER) profiles near the outer midplane, Infra-Red TV (IRTV) heat flux profiles on the divertor plates and visible TV images of D $\alpha$  and CIII radiation in the divertor region.

### **3 UEDGE Inputs**

The UEDGE mesh is generated using data from the EFIT reconstruction for shot 141628 at 2490 msec. The scatter in the TS data did not justify re-locating the separatrix for this reconstruction. The mesh shown in Figure 2 was used for all UEDGE simulations in this report. The mesh contains 61 cells in the poloidal direction and 23 cells in the radial direction. The divertor target surfaces are quite simple in this configuration, so mesh resolution should not be an issue.

The UEDGE simulations solve time-dependent fluid equations for the plasma and neutral species. Several model options are available. For DIII-D we include carbon impurities due to both physical and chemical sputtering in the divertor. Cross-field drifts are included, but for these simulations at an artificially reduced level of 10%. This allows the runs to converge more robustly during parameter variations. Later we will increase the drifts to full strength. Most of the simulations used spatially uniform anomalous radial transport coefficients with particle diffusivity  $0.10 \text{ m}^2/\text{sec}$  and thermal diffusivities  $0.25 \text{ m}^2/\text{sec}$  for electrons and ions. Radially varying particle diffusivity can be used to introduce a transport barrier near the separatrix and control the upstream density profile. This was briefly explored. Core plasma boundary conditions are set to be consistent with experimental data: for most of these simulations the plasma density is  $6e19 /\text{m}^3$  and total input power is 1.6 MW.

### **4 UEDGE Base Case Results**

We have a base case simulation, JRT25a, with input parameters described in the previous section. Here we compare simulation results from this case with the available experimental data. In the simulation we observe that the plasma is detached from the inner target with temperatures less than 1 eV at the plate; the power flow to the outer target is sheath-limited with high temperature (48 eV) at the outer strike point. Due to the "open" divertor configuration, recycling neutrals produced by SOL ions striking the outer divertor plate are directed away from the separatrix. This reduces the recycling near the strike point and leads to higher electron temperature. Impurities radiate about 0.7 MW of the total 1.6 MW input power. For this simulation there is a large ion current (700 Amps) from the core plasma which ultimately gets pumped at the vessel wall, mainly in the divertor region. This large particle throughput in steady state should be consistent with beam fueling of the core plasma. We have not yet made this assessment for the gyrotron-equivalent beams used in this discharge.

The simulated midplane electron density profile (in units of  $10^{20} / \text{m}^3$ ) is compared with TS data and reflectometer data in Figure 3. The horizontal axis is the normalized magnetic flux. The "x" are TS data points and "o" are reflectometer data points; these do not seem to correlate very well. The simulated profile does not exhibit the pedestal characteristic of H-mode plasmas. One possible remedy is to use radially varying particle diffusivity, essentially introducing a particle transport barrier at the separatrix. This variation is discussed later in this report. Another remedy is to reduce the particle throughput for this simulation by reducing the wall pumping, but a change in the wall albedo (discussed later) did not have the desired effect.

The simulated midplane electron temperature is compared with TS data in Figure 4. The core boundary temperature in the simulation could be reduced by increasing the electron thermal diffusivity. The high degree of scatter in the TS data does not provide much of a constraint on the shape of the electron temperature profile in UEDGE simulation. The midplane ion temperature is even

less constrained by the CER data in Figure 5. No attempt was made to extract more meaningful data from the automated CER data that was collected.

The simulated divertor heat flux is compared with IRTV data in Figure 6. The horizontal axis is normalized magnetic flux,  $\psi_{\text{in}}$ , with  $\psi_{\text{in}} < 1$  in the private flux region and  $\psi_{\text{in}} > 1$  in the SOL region. The heat flux near the inner strike point is in "blue" and the heat flux near the outer strikepoint is in "red". The solid lines are the UEDGE simulations and the circles are the IRTV data points. The IRTV data shows a very weak peak on the outer target whereas the simulation has a strong peak of about  $4 \text{ MW/m}^2$ . In the simulation, global power balance shows 0.9 MW radiated by impurities, 0.2 MW radiated by hydrogenic species and 0.7 MW incident on the outer divertor plate.

The visible TV images of Dalpha radiation at 6356Å and CIII radiation at 4650Å provide clues as to the temperatures in the divertor region. The simulated Dalpha emissivity is compared with the emissivity deduced from camera image data in Figure 7. The simulated CIII emissivity is compared with that from camera data in Figure 8. Absolute intensities are not available from the camera images. The strong Dalpha emissivity (due to recombination?) on the inner divertor leg is indicative of a detached plasma in both the simulation and the camera data. The absence of a strong CIII emission at the inner target also indicates a low electron temperature in this region.

## 5 Parameter Variations

The base case described above could be made more realistic by adjusting some input parameters in the model, such as anomalous radial diffusivities, input power and drift strength. Some of these changes make it very difficult to

advance the time-dependent fluid equations to a steady state solution. We have a few simulations that exhibit the effects of varying a single input parameter. These may be useful in guiding future modelling efforts.

### **5.1 input power**

Simulation JRT25b had the input power increased from 1.6 MW to 2.0 MW relative to our base case, JRT25a. The peak electron temperature at the outer strike point increased from 48 eV to 82 eV, but no other significant changes were noted.

### **5.2 wall pumping**

Simulation JRT26 had the outer wall albedo reduced from 0.98 in our base case to 0.95. This change did not affect the particle throughput because the neutral hydrogen density near the wall decreased and the net pumping by the wall was essentially unchanged. This did have the unexpected effect of reducing the level of carbon impurities because of reduced chemical sputtering by neutral hydrogen. The associated reduction in carbon radiation caused the inner leg of the divertor to re-attach.

### **5.3 drift strength**

Simulation JRT15a had the drifts turned on relative to simulation JRT15. These runs did not include impurities. The drifts are artificially reduced to 10% of their classical value to allow easy convergence to steady state. At this level, the drifts do not significantly change the simulation. Further increases in drift strength will be necessary to assess the issue.

### **5.4 impurities**

Simulation JRT15f included carbon impurities, whereas simulation JRT15a did not. The carbon is due to physical and chemical sputtering in the divertor region (target plates and private flux wall). The sputtering rates are those given by

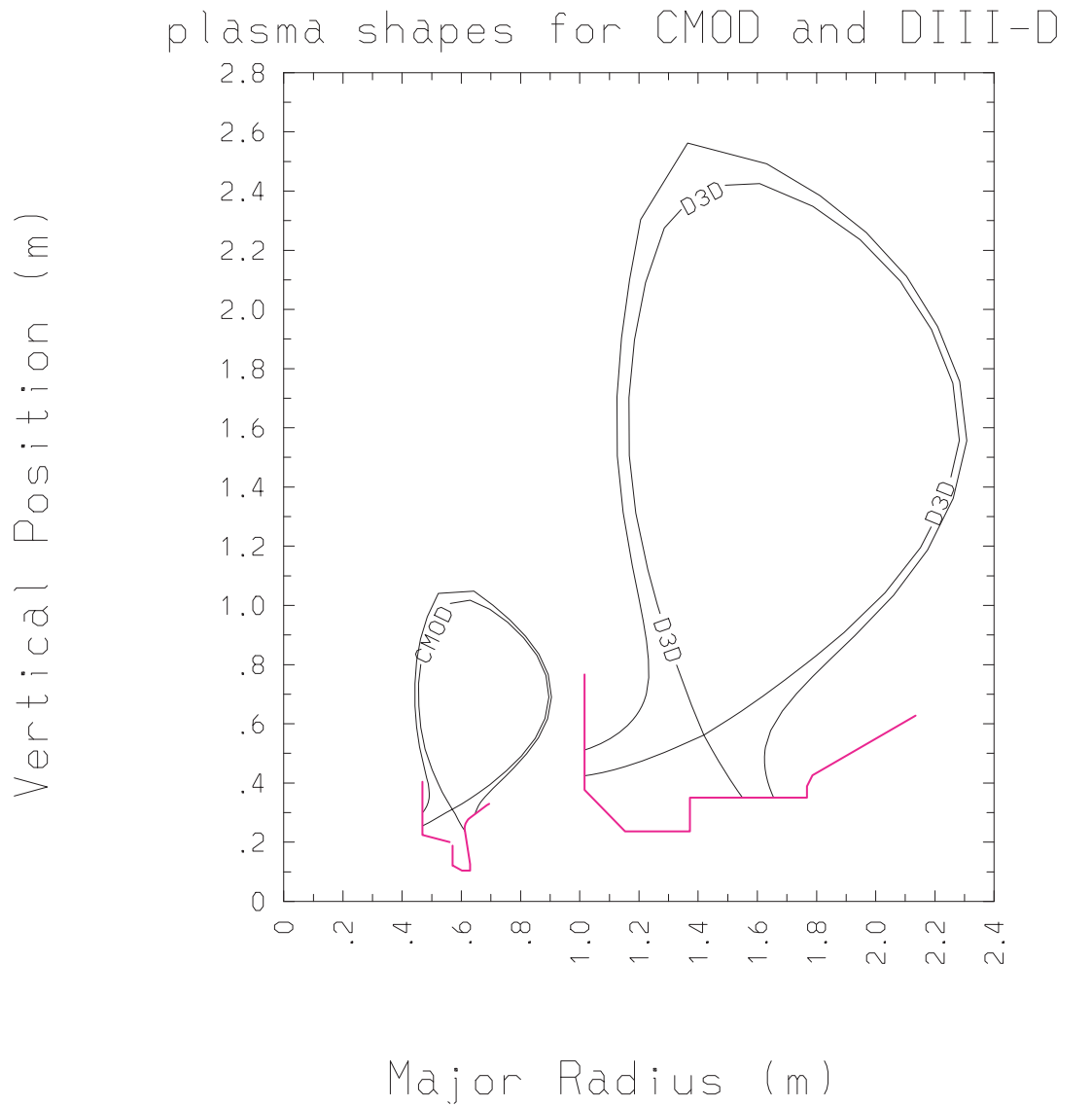
Haasz, et al. The impurities radiate about 0.7 MW of the total 1.6 MW input power. This has the effect of detaching the plasma from the inboard target where most of the power is radiated.

### **5.5 radially varying particle diffusivity**

Most of the simulations use a spatially uniform particle diffusivity,  $D_{\text{particle}}=0.1 \text{ m}^2/\text{sec}$ . An example is simulation JRT15 which had no drifts and no impurities. This simulation was re-run as JRT16 with a spatially varying particle diffusivity similar to that used by Porter in the CMOD simulations, i.e., the particle diffusivity was reduced to  $0.015 \text{ m}^2/\text{sec}$  on flux surfaces within about 1 cm of the separatrix at the outboard midplane. The uniform diffusivity produces an upstream electron density which decreases linearly with radial position from the core boundary to the outer wall. In contrast, the varying diffusivity yields a flattened density profile in the core plasma and a rapid drop at the separatrix near the transport barrier. The reduced transport across the separatrix leads to reduced density and increased temperatures at the divertor plates.

## **6 Acknowledgement**

This work performed under the auspices of the U.S. Department of Energy by Lawrence Livermore National Laboratory under Contract DE-AC52-07NA27344.



```

CMOD: plot zm(i,ysptrx,3) rm(i,ysptrx,3) scale=equal labels="CMOD"
plot zm(.ny,3) rm(.ny,3) scale=equal labels=blank
plot zplate1 rplate1 color=magenta thick=3 labels=blank
plot zplate2 rplate2 color=magenta thick=3 labels=blank
D3D: plot zm(i,ysptrx,3) rm(i,ysptrx,3) scale=equal labels="D3D"
plot zm(.ny,3) rm(.ny,3) scale=equal labels=blank
plot zplate1 rplate1 color=magenta thick=3 labels=bl
plot zplate2 rplate2 color=magenta thick=3 labels=bl
    
```

*Fig. 1: Comparison of CMOD and DIII-D plasma size and shape*

EFIT 05/12/98 #141628 2490

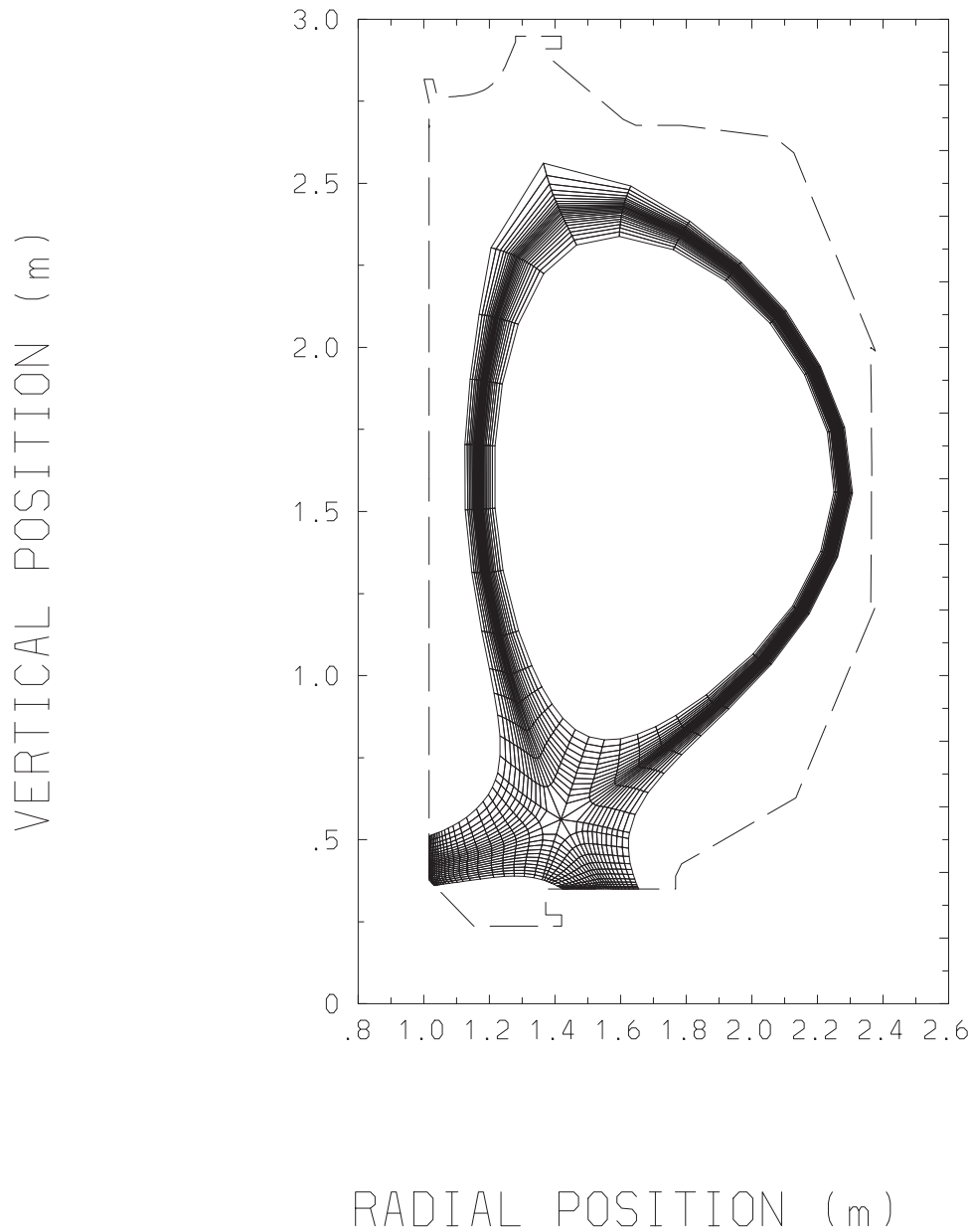
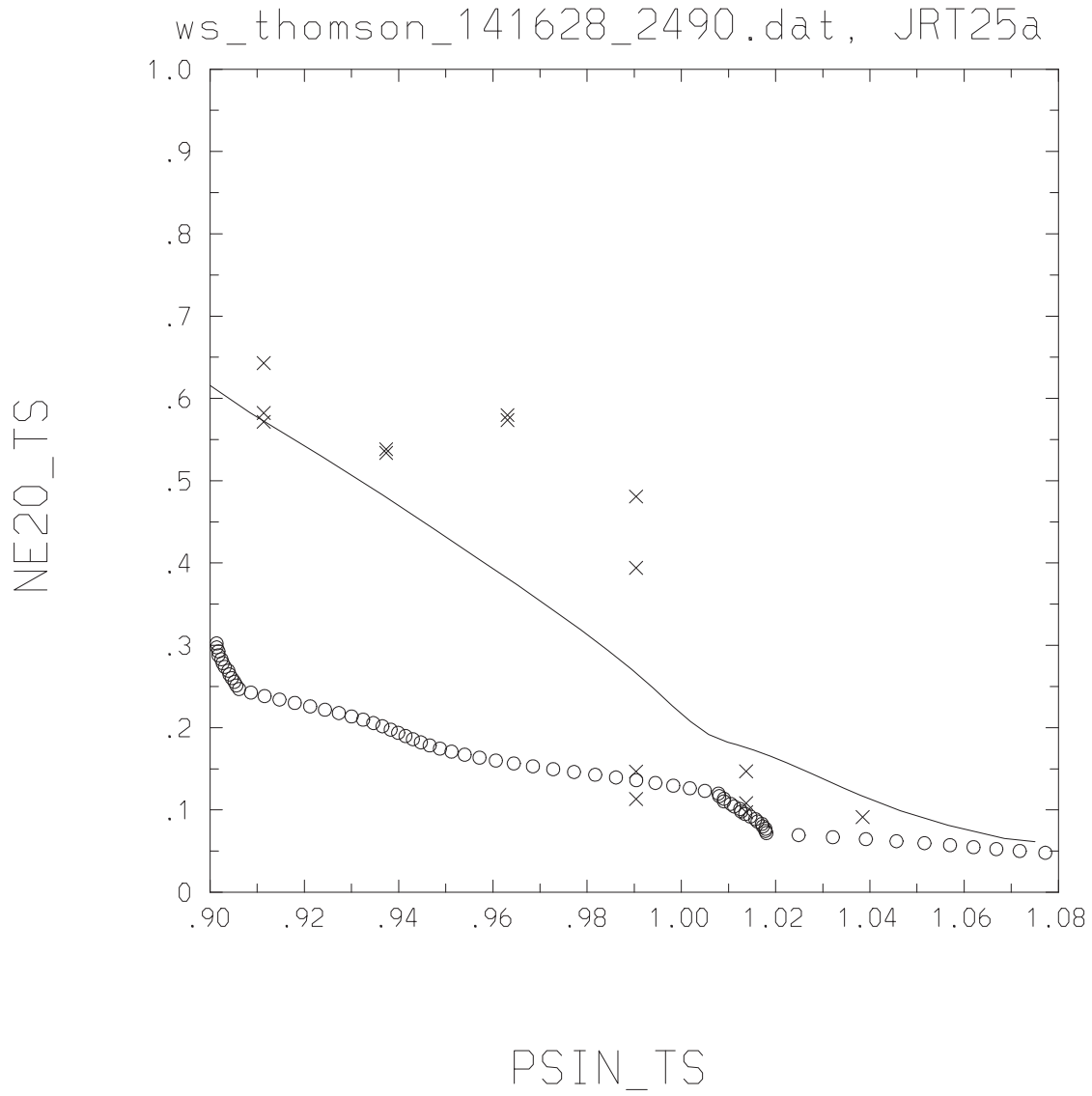
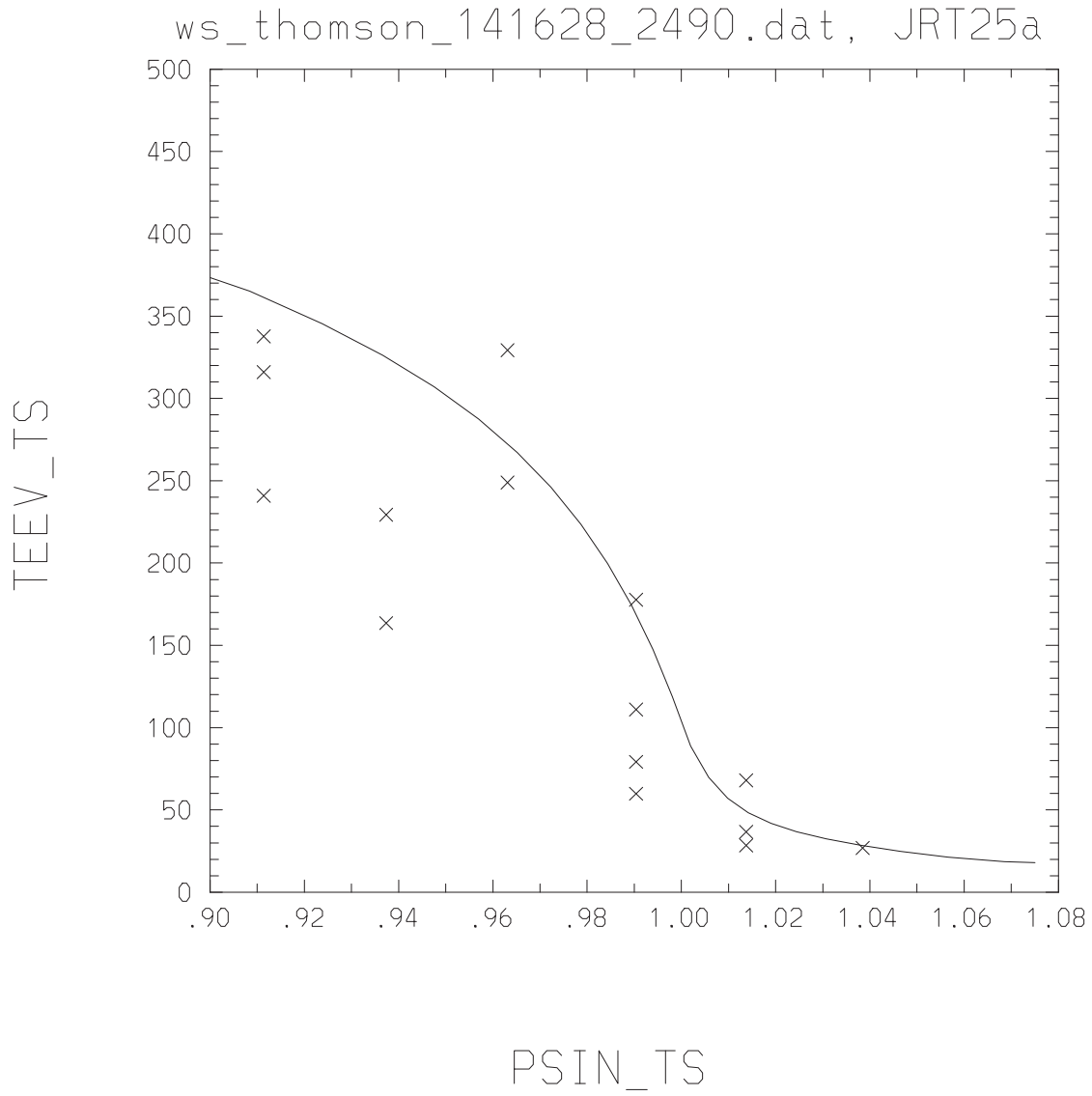


Fig. 2: Mesh for UEDGE simulations



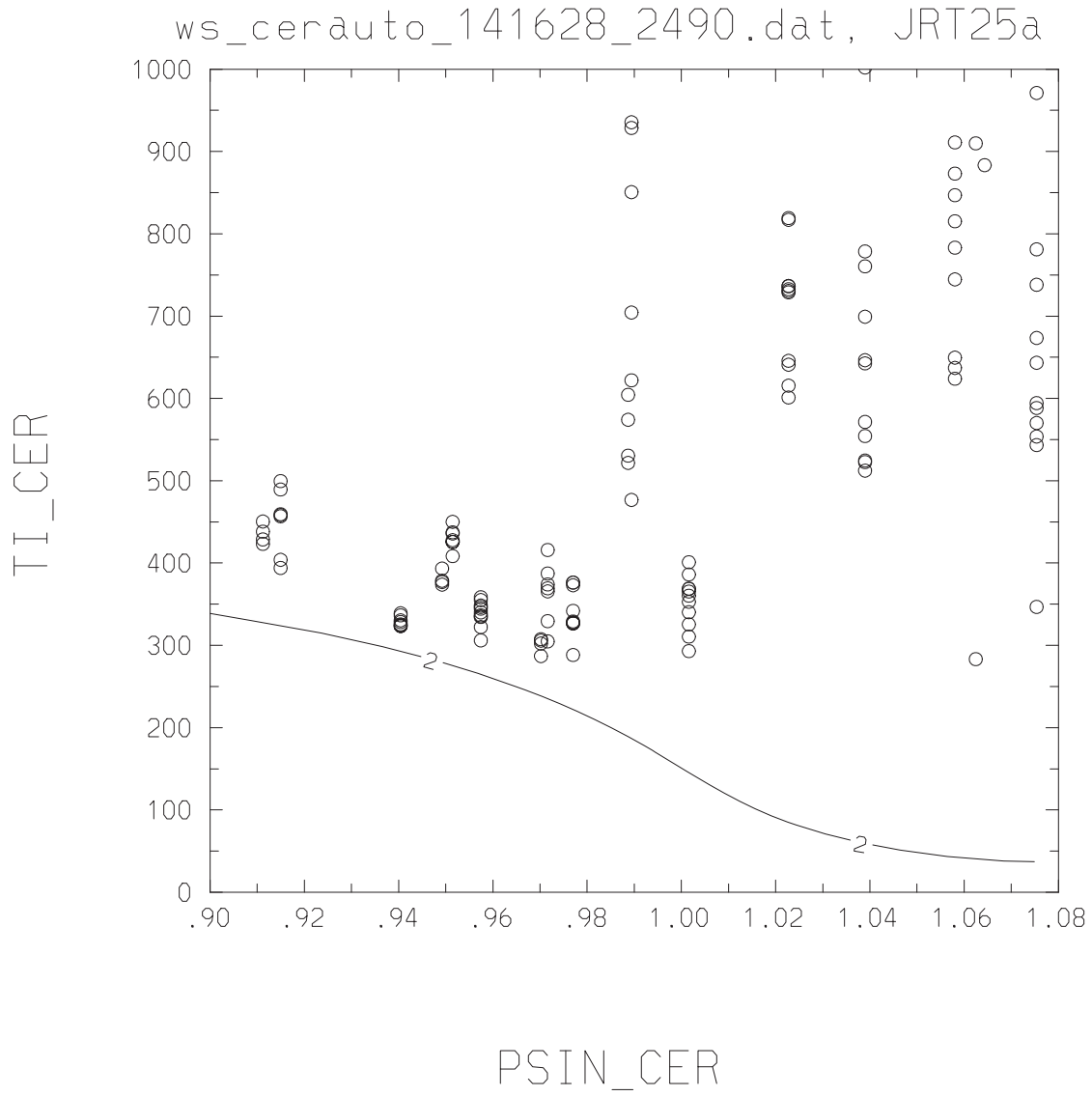
```
plot ne20ts psints mark=cross
plot tsne20 tspsin labels=blank
plot densrefl psinrefl mark=circle
```

*Fig. 3: Upstream electron density profile vs. normalized magnetic flux. The "x" are Thomson Scattering data points and "o" are reflectometer data points. The curve is the UEDGE electron density profile.*



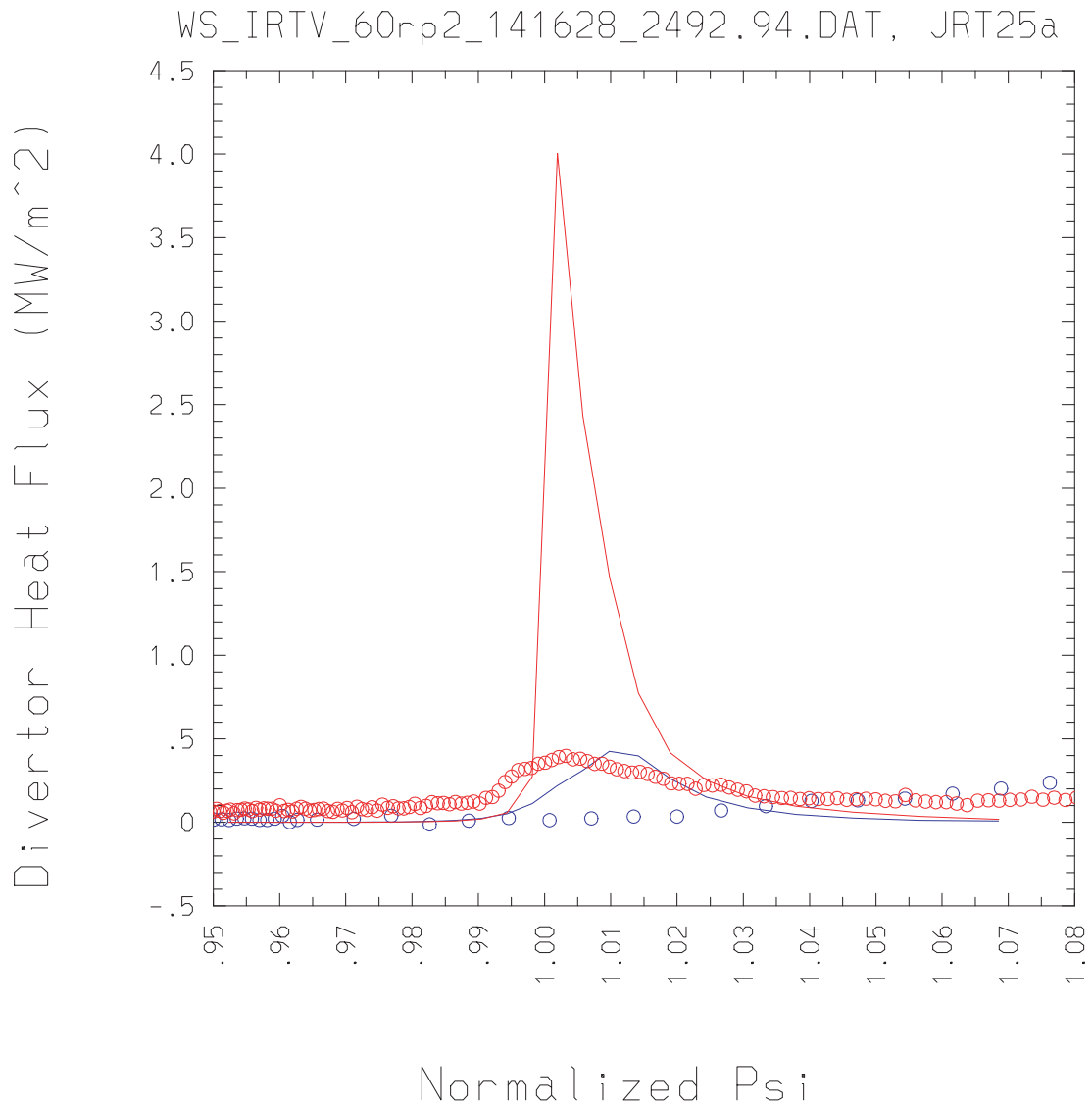
```
plot tets psints mark=cross
plot tsteev tpsin labels=blank
```

*Fig. 4: Upstream electron temperature profile vs. normalized magnetic flux. The “x” are Thomson Scattering data points and the curve is the UEDGE electron temperature profile.*



```
plot ticer psincer mark=circle
2: plot tis(ixmp,)/ev psin(ixmp,,0)
```

*Fig. 5: Upstream ion temperature profile vs. normalized magnetic flux. The circles are CER ion temperature data points and the curve is the UEDGE ion temperature profile.*



```

plot pwrcirtvl(1:162) psinirtvl(1:162) mark=circle color=blue
plot 1e-6*sdtin(1:ny) psin(0,1:ny) labels=blank color=blue
plot pwrcirtvl(163:490) psinirtvl(163:490) mark=circle color=red
plot 1e-6*sdtout(1:ny) psin(nx+1,1:ny) labels=blank color=red
    
```

*Fig. 6: Divertor heat flux profile vs. normalized magnetic flux,  $\psi_{\text{in}}$ , with  $\psi_{\text{in}} < 1$  in the private flux region and  $\psi_{\text{in}} > 1$  in the SOL region. The heat flux near the inner strike point is in blue and the heat flux near the outer strikepoint is in red. The solid lines are the UEDGE simulations and the circles are the IRTV data points.*

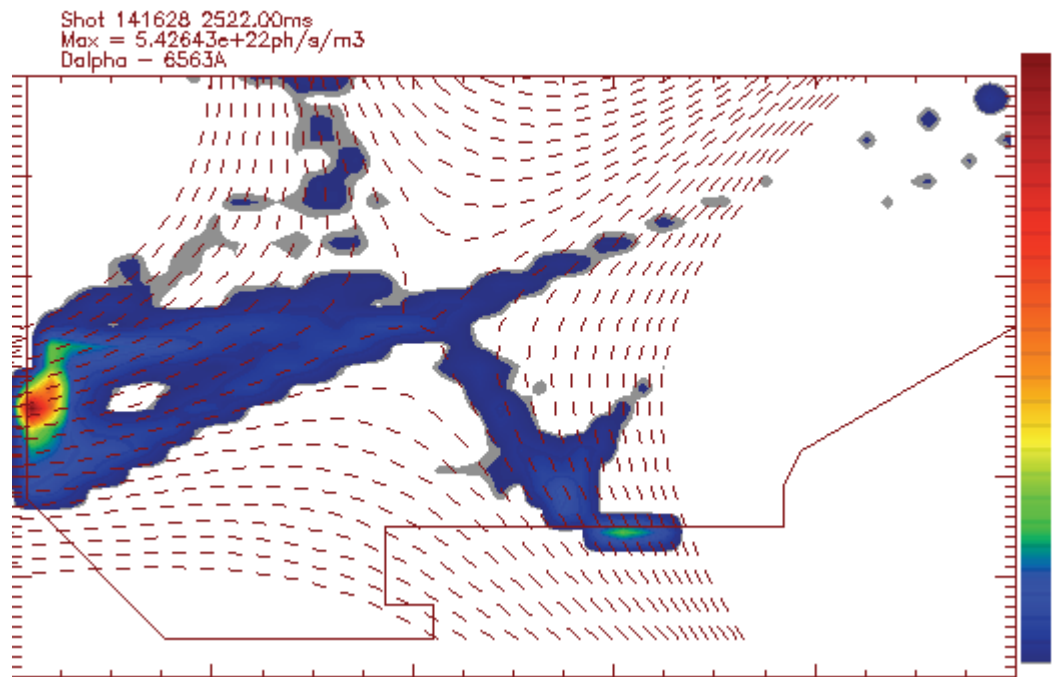


Fig. 7: *Dalpha* emissivity from visible TV

Dalpha 6563A, JRT25a

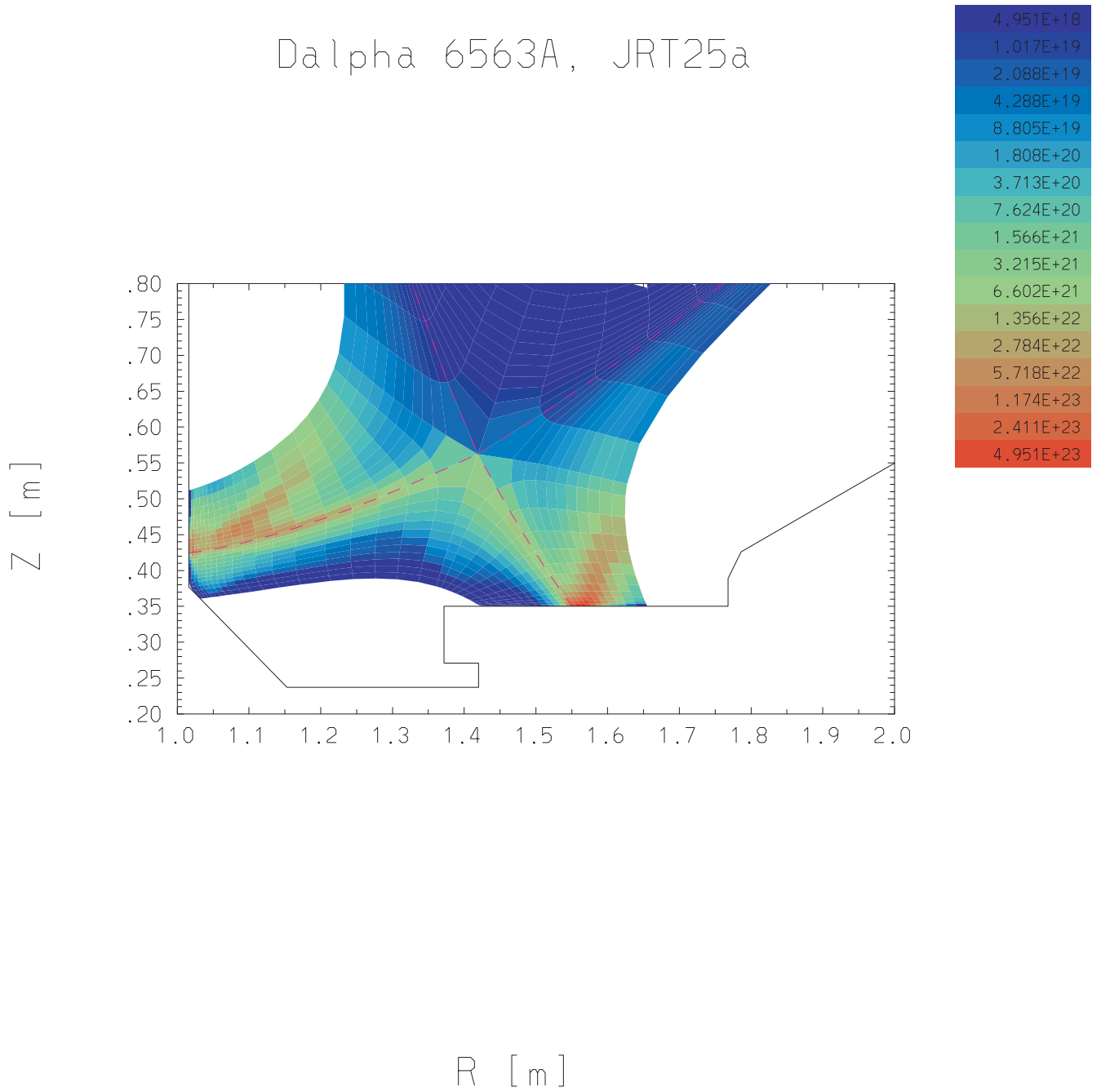


Fig. 8: Dalpha emissivity from UEDGE simulation JRT25a

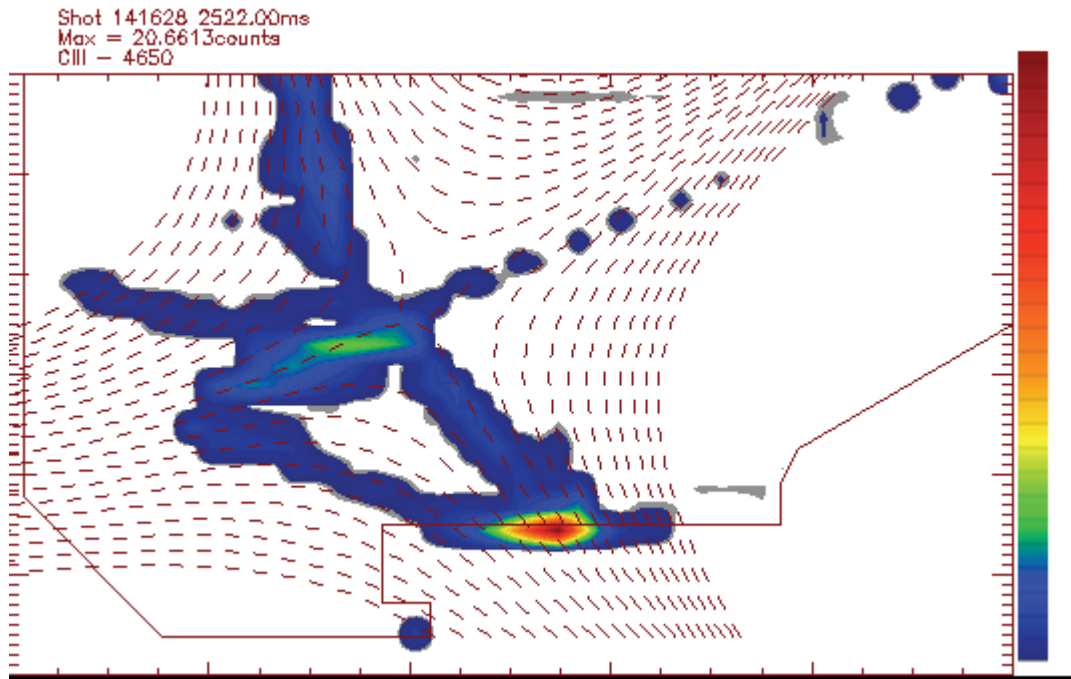


Fig. 9: CIII emissivity from visible TV

CIII 4650A, JRT25a

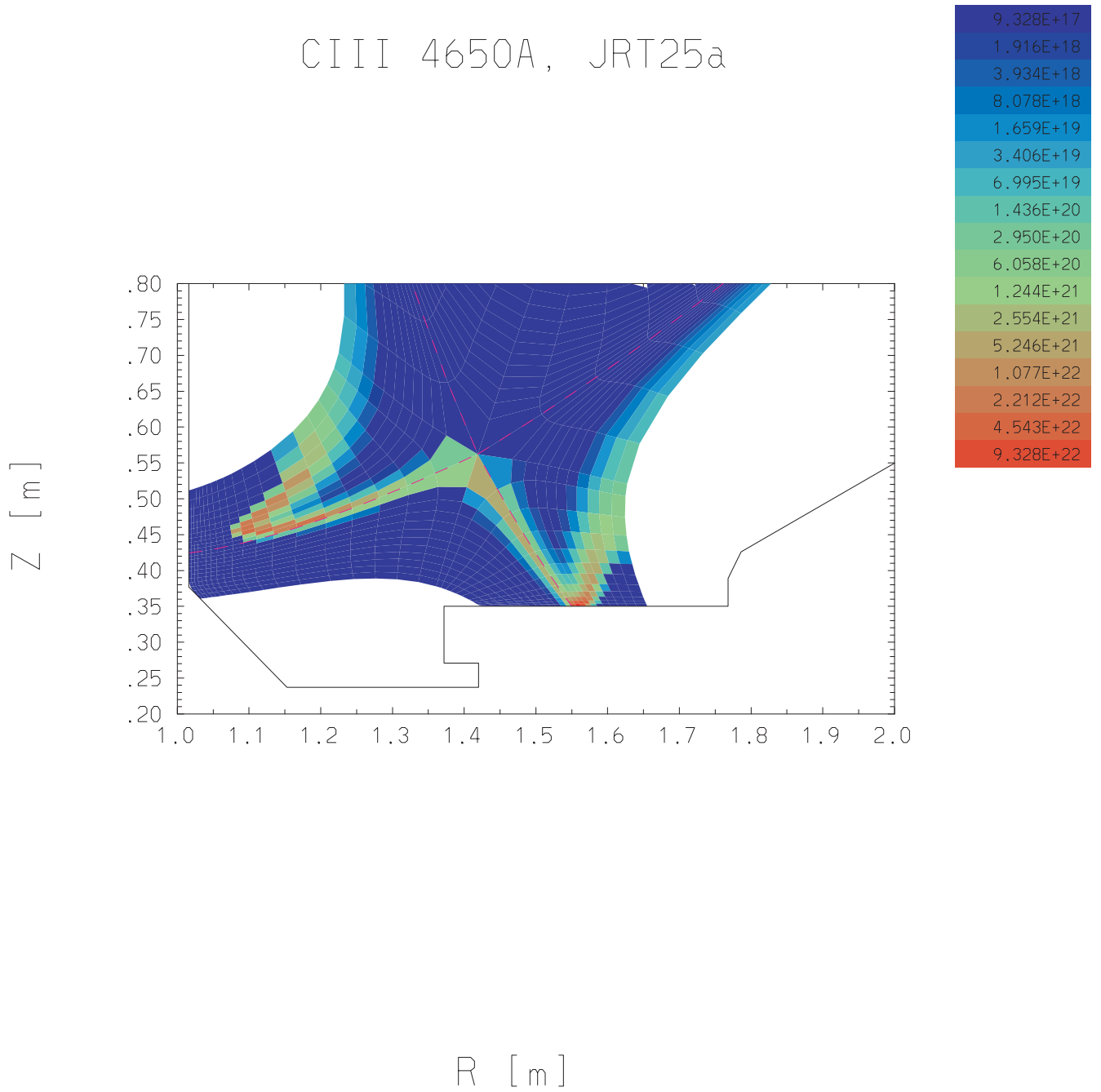


Fig. 10: CIII emissivity from UEDGE simulation JRT25a

# APPENDIX F

## UEDGE Modeling of C-Mod Discharge from C-Mod/DIII-D Similarity Experiment

G.D. Porter



To: DIII-D 2010 Joule Milestone Team  
 From: G D Porter  
 CC: Brian LaBombard  
 Date: 27 September 2010  
 Re: UEDGE simulation of CMOD discharge  
 1100212024.01360

## 1 Introduction

We report here initial UEDGE[1] simulations of CMOD discharge 1100212024. This discharge was taken as part of Joint Research Task (JRT), i.e. a coordinated effort between several diverted tokamaks to characterize the heating flux on the divertors when the devices were operated in similar geometries. The tokamaks included in this exercise were CMOD, DIII-D and NSTX. Discharges taken as part of this coordinated effort on DIII-D are also being analyzed using UEDGE and will be reported elsewhere.

This report begins with a brief description of the CMOD discharge in Section 2, followed by a detailed description of the simulation results with a variety of different physics assumptions in Section 3.

## 2 Discharge Description

CMOD discharge 110212024 was taken 12 February, 2010 as part of a campaign to obtain data with dimensionless similar discharges with DIII-D and NSTX. This CMOD discharge was described in some detail at the 2010 PSI conference in San Diego.[2] The discharge is an "Enhanced  $D_\alpha$ " (EDA) high confinement (H-mode) discharge. The magnetic reconstruction obtained using EFIT[3] indicates this discharge is a Lower Single Null (LSN) with a fairly narrow gap, i.e. the limiter surfaces maps to only 8.1 mm from the separatrix at the Low Field Side (LFS) midplane. The UEDGE mesh obtained using this EFIT reconstruction will be shown in the next section. The plasma is heated with a combination of Ohmic (0.63 MW) and ICRH (3.86 MW). There is 1.92 MW of radiated power on the closed field lines yielding an estimated power into the Scrape-off layer (SOL) of 2.17 MW ( $0.9 \cdot \text{PICRF} - \text{Prad\_core}$ ). Diagnostics that are available to guide the UEDGE simulations include an edge Thomson Scattering (TS) system measuring the electron density and temperature near the separatrix, an array of Langmuir probes in the divertor region that nominally determine the plasma density, ion saturation current, plasma potential and electron temperature at the divertor floor; and an Infra-red TV system (IRTV) measuring the heat flux profile on the outer divertor. These data are provided by Brian LaBombard with the proviso that data not be distributed without permission of the C-mod experiment. We will show comparisons of the experimental data and UEDGE simulations in this report.

## 3 UEDGE simulations

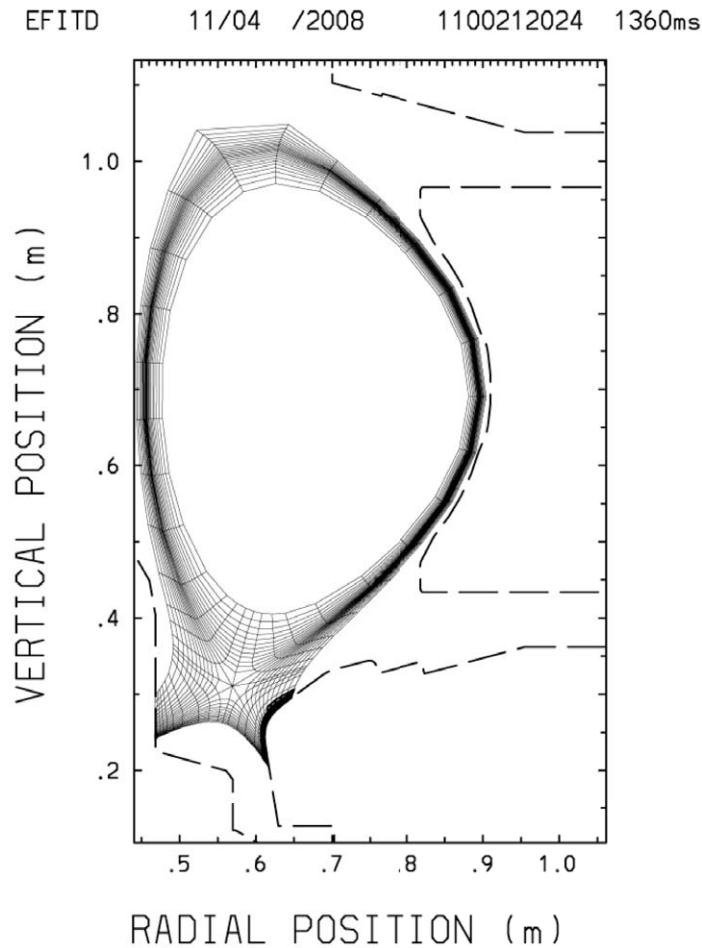


Figure 3-1 UEDGE mesh used for simulation of CMOD discharge 1100212024.

The UEDGE mesh obtained using the data from the EFIT reconstruction of CMOD discharge 1100212024 is shown in Figure 3-1. The radial region used for the simulations extends inside the last closed flux surface (LCFS) to the 90% poloidal flux ( $\Psi_N=0.90$ ) and out to the limiting surface at  $\Psi_N=1.05$ . We use a non-orthogonal mesh that closely matches the divertor geometry of the machine. The mesh contains 49 poloidal cells, concentrated near the divertor plates where we expect plasma parameters to vary most quickly, and 23 radial cells, concentrated near the separatrix.

The UEDGE code requires a variety of options for physics to be included and the use of boundary conditions at all surfaces that define the calculation domain. These include:

- We use the mesh described previously and shown in Figure 3-1 for all simulations discussed in this memo.
- We solve plasma fluid equations for the ion density, the ion and electron thermal transport, the ion parallel momentum and the plasma potential. A simple model for potential, which solves Ohm's law on the open surfaces of the SOL, but which is probably not accurate on the closed surfaces in used in Section 3.1. A more accurate potential model is incorporated when

we include the effect of plasma drifts[4] in Section 3.2. All equations are iterated to obtain a steady state solution with residuals less than  $10^{-8}$ .

- The radial power across the inner-most flux surface,  $\Psi_N=0.90$ , is specified as a boundary condition (BC). We assume the experimentally determined power is distributed equally between power flowing in the electron channel and that flowing in the ion channel, i.e. 1.1 MW in each.
- The ion density on the inner-most flux surface is specified as a BC and is assumed constant on that surface. We use the value measured with the TS diagnostic to specify this density.
- We specify the BC on the ion density at the outermost and private flux (PF) surfaces by assuming the radial scale length of the density falls off with a 10 cm scale length. The ion flux resulting from this assumption is recycled as neutral deuterium atoms.
- We use a fluid model for simulating the neutral density. This model includes the effect of momentum exchange with the deuterium ions and inertial effects, i.e. we include simulation of the parallel neutral momentum.[5] The ion flux flowing to the outer-most and PF surfaces as well as that flowing to the divertor plates is assumed to recycle as neutral atoms. The BC used for the neutral density at these surfaces is specified as a neutral albedo at each surface. The assumed albedo at both the inner and outer plate is assumed to be 0.99 (1% of the neutral flux to these surfaces is removed or pumped); that at the outermost flux surface is assumed to be 0.95 and that at the PF surface is assumed to be 1.0.
- We assume all anomalous transport is diffusive. Initial simulations, discussed in Section 3.1.1, assume that the electron and ion thermal diffusivity and the particle diffusivity are spatially constant. Subsequent simulations assume a radially varying particle diffusivity. The value of all diffusivities is varied to obtain better agreement with experimental data.
- The BC used for the neutral density at the boundary of the calculation means that all surfaces are pumped. Initially the only ion source that is required to obtain steady state is an ion flux across the innermost flux surface. We note that the neutral density at the LFS midplane is quite high so we introduce a gas puff at that point. The amplitude of this gas puff is assumed to be 100 atom A. We discuss the effect of this gas puff in Section 3.1.3, and use it in Section 3.2.
- 

### 3.1 Simulations without drift effects

#### 3.1.1 Initial simulations, spatially constant particle and thermal diffusivity

The upstream and divertor profiles obtained in the initial UEDGE simulation, BLc02, (run BLc01 mistakenly used an old geometry for the inner divertor plate) are compared with experiment in Figure 3-2. This simulation was done with spatially constant thermal, particle and momentum diffusivities of:

$$\begin{aligned}\chi_i &= \chi_e = 0.1m^2/s \\ D &= 0.1m^2/s\end{aligned}$$

Equation 1

All parameters are mapped to the LFS midplane and plotted versus the distance from the separatrix at that poloidal position. Although there are discrepancies between experiment and simulation on all the profiles, the density profile is most poorly fit with the assumptions used for this simulation. Based on experience in simulating DIII-D discharges we chose to introduce a radially dependent particle diffusivity to improve the density profile.

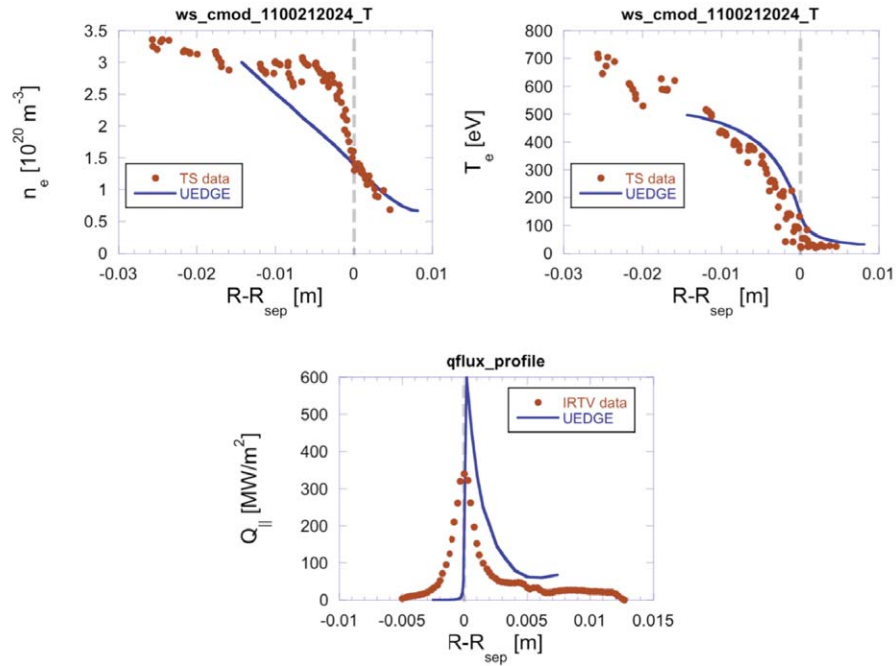


Figure 3-2 Comparison of measured upstream plasma profile and divertor heating profile with UEDGE simulation B1c02. Only the heating profile at the outer divertor is shown, corresponding to the experimental measurement.

### 3.1.2 Effect of radially dependent particle diffusivity

The problem was divided into three radial zones to modify the particle diffusivity. Zone 1 is from the innermost flux surface to the surface that lies 0.4 cm inside the separatrix at the LFS midplane. Zone 2 goes from 0.4 cm inside to 0.3 cm outside the separatrix and zone 3 extends from there to the edge of the calculation domain, 8 cm outside the separatrix. We show two simulations in Figure 3-3 to demonstrate that although the density profile can be made more consistent with experiment by simply introducing the particle transport barrier in zone 2, we had to modify the thermal diffusivity to bring the electron temperature back to the experiment after reducing the diffusivity in zone 2. The first simulation, B1c05, used the particle diffusivity in zone 2 of  $0.015 \text{ m}^2/\text{s}$ , leaving all other diffusivities the same as in Equation 1. This simulation has a significantly higher electron temperature on the core surface than the experiment. We had to increase the thermal and momentum diffusivities to  $0.16 \text{ m}^2/\text{s}$  to make the electron temperature more consistent with experiment (run B1c05b). It is interesting to note that simulation of DIII-D plasmas typically do not require iteration of the thermal diffusivity after introducing a radially dependent particle diffusivity. The radial power flow is composed of a convective part, associated with the power carried by the radial particle flux, and a conductive flow associated with the radial transport due to anomalous diffusion, as shown in Equation 2. One can solve the simplified form of this equation for the temperature on the core surface for a specified power (recall that the power is used as a BC in UEDGE) showing that the core temperature is determined by the sum of the inverse scale length of the temperature and density on that surface. In DIII-D the convective term,  $D/\lambda_n$ , is small. The density scale length increases for both CMOD and DIII-D when one introduces a particle transport barrier at the separatrix (the density flattens), but since the convective term is small in DIII-D, the electron temperature on the core typically does not change. However, the convective and conductive contributions to the radial power are more equal for CMOD so that one has to modify the thermal diffusivity when the core density flattens out.

$$\begin{aligned}
 P_r &\propto -\chi n \frac{\partial T_e}{\partial r} - 2.5TD \frac{\partial n}{\partial r} \\
 &\propto -nT \left( \frac{\chi}{\lambda_T} + \frac{D}{\lambda_n} \right)
 \end{aligned}$$

Equation 2

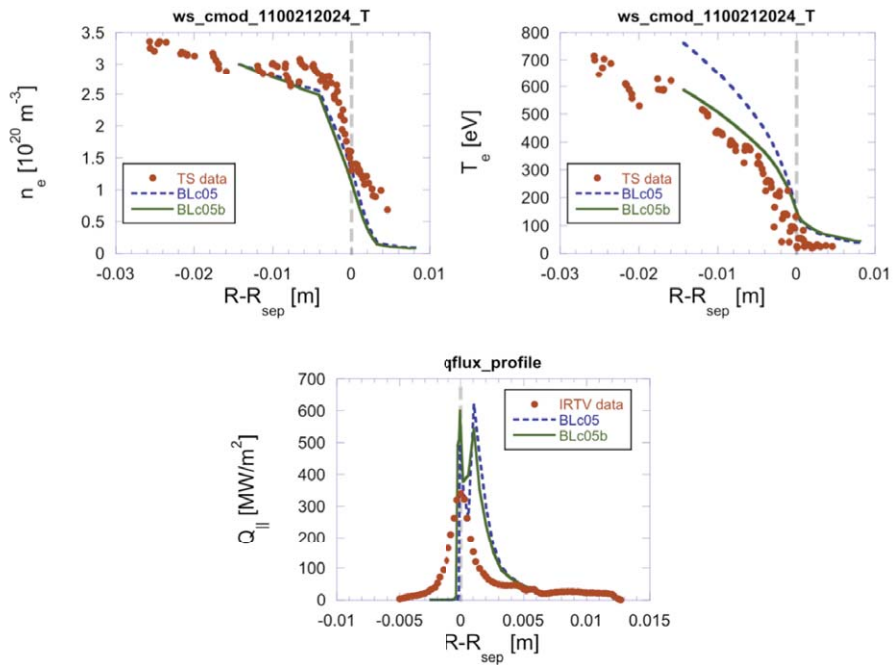


Figure 3-3 Comparison of measured upstream plasma profiles and divertor heating profiles with UEDGE simulations with radially dependent particle diffusivity.

The simulated density profile on the closed field lines is more consistent with experiment when a particle transport barrier is introduced near the separatrix. However, the SOL density is much lower than experiment. Upon examining the data Brian LaBombard sent us we noticed that the neutral density near the LFS midplane was quite high. We therefore introduced a neutral gas puff in a region near the midplane, extending about 20 cm poloidally. The effect of this gas puff is discussed in the next section

### 3.1.3 Effect of gas puff at LFS midplane

The effect of a 100 atom Amp (about 1000 Torr l/s) gas puff is shown in Figure 3-4. There is remarkably little effect on the upstream plasma profiles. The effect of the gas puff on the ion saturation plate is also shown in this figure. The UEDGE sign convention is that a current flowing clockwise (from the inner plate toward the outer plate) is positive. Hence ion current flowing to the inner plate appears negative and that to the outer plate is positive. The divertor heat flux in a very narrow region near the strike point increases more than a factor of 2 with the gas, arising from the sharp spike in  $J_{sat}$ . The ion flux across the core surface is about 270 atom Amp so the 100 A introduced by the gas puff is only a perturbation which increases the recycling currents a bit. There is very little effect on the SOL density. All subsequent simulation results described in this memo include this gas puff.

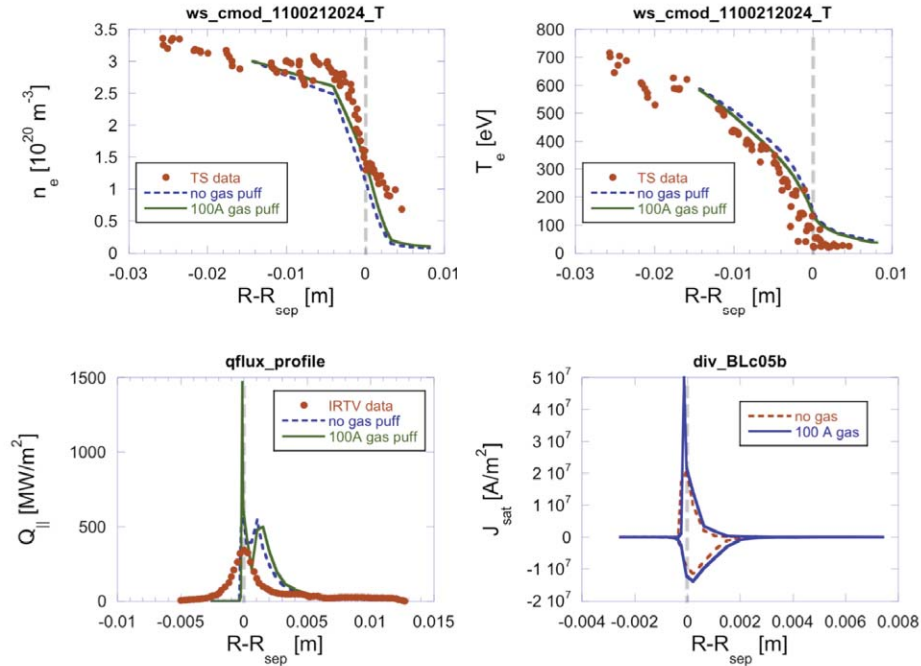


Figure 3-4 Comparison of upstream plasma profile and divertor heating profile with UEDGE simulations with and without a 100A gas puff at the LFS midplane.

### 3.2 Simulations with drift effects

The final set of physics that we have implemented for these simulations of CMOD has been the inclusion of the effect of all plasma drifts, ExB,  $\nabla B$  and  $\nabla P$ . [4] It has been proposed that the effect of these drifts is important for DIII-D. [6] We find that they are even more important for CMOD. The cross field diffusivities had to be modified to keep the upstream plasma profiles more or less consistent with experiment. The upstream and divertor profiles are compared with experiment in Figure 3-5. The diffusivities used for this simulation are:

$$\begin{aligned}\chi_i &= \chi_e = 0.05 \text{ m}^2 / \text{s} \\ D_1 &= D_3 = 0.05 \text{ m}^2 / \text{s} \\ D_2 &= 0.075 \text{ m}^2 / \text{s}\end{aligned}$$

Equation 3

Note that the scale used for the ordinate of the divertor parameters in Figure 3-5 has been expanded to better see the profiles obtained with drifts. The high divertor heating flux near the strike point is therefore not obvious, nor is the peak in the ion saturation current. The level of these features without drifts can be seen in Figure 3-4. The amplitude and shape of the divertor heating flux and ion saturation current are more consistent with measurement for the simulation that includes the effect of drifts. The experimental ion saturation current appears to peak in the PF region that seems unlikely and may indicate some uncertainty in the location of the strike point. Unfortunately the probe data on the inner plate has a wide gap where UEDGE shows the largest flux to the plate.

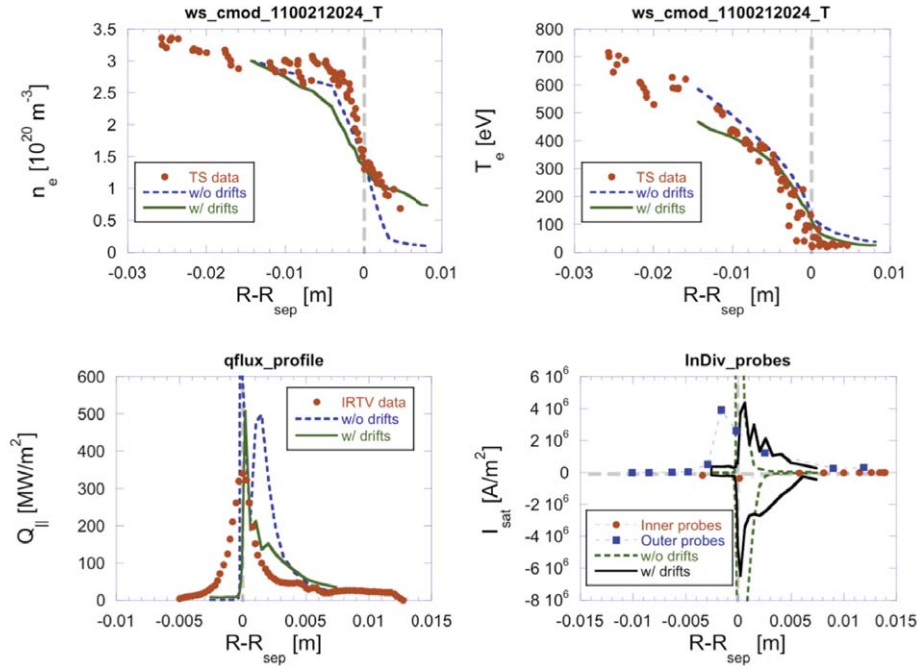


Figure 3-5 Comparison of upstream and divertor parameters with UEDGE simulations without drifts (BLc07) and with drifts (BLc13).

$$\begin{aligned}
 nT &\propto \beta B^2 \\
 v_{drift} &\propto 1/B \\
 \Gamma_{drift} &= nv_{drift} \propto \frac{\beta B}{T}
 \end{aligned}$$

Equation 4

One possible view of the importance of the effect of drifts is seen by examining the scaling of the drift flux with the total field  $B$ , as shown in Equation 4. Plasma drift velocities scale as  $1/B$ , suggesting that the drifts are less important for high field devices such as CMOD. However, if one chooses to maximize the use of the expensive magnetic field, i.e. operate near a MHD limited plasma pressure, the drift fluxes will scale as  $B$  and therefore are more important for high field devices such as CMOD (and ITER). One should compare these drift fluxes with those expected from anomalous diffusion. However, that would bring in the unknown particle diffusivity. The size scaling of particle diffusivity is not known. Furthermore there is fear that the diffusive fluxes obtained in these simulations are dominated by numerical diffusion associated with the use of “upwind differencing”. This concern is particularly worrisome for a case with the extremely small diffusivities needed to match the upstream profiles for the CMOD simulation with drifts (see Equation 3) The numeric diffusion problem is currently understudy by not only UEDGE developers, but by developers of other fluid edge plasma codes.

Finally, we show the effect of drifts on the 2D profile of  $D_\alpha$  emission in Figure 3-6. We show these profiles in the hope there might be some experimental data which can be compared with the simulations and therefore confirm the importance of including drifts in simulations of the edge plasmas.

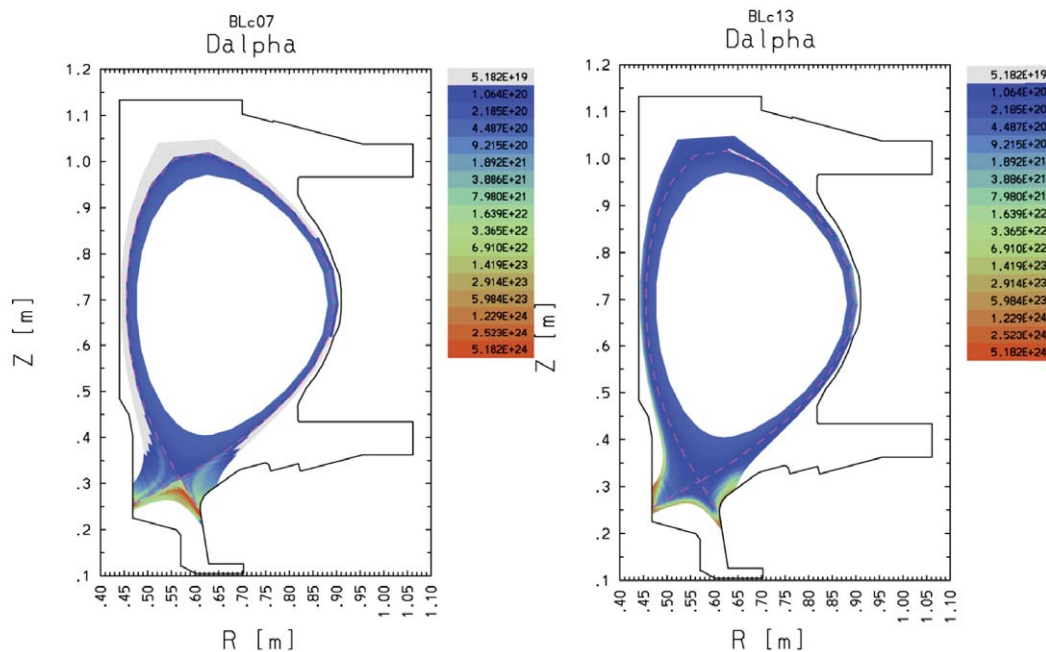


Figure 3-6 Comparison of  $D_{\alpha}$  emissivity for a simulation without drifts (left, BLC07) and one with drifts (right, BLC13).

#### 4 Summary and conclusions

We report initial results of UEDGE simulations of a CMOD discharge taken as part of coordinated research effort to characterize the divertor heating characteristics on several devices. We have discussed the sensitivity of the simulation results to numerous UEDGE input parameters and physics models. We find that the code is able to reproduce the experimentally measured divertor heating profile when all relevant physics are turned on, viz. when the effect of plasma drifts is included. Reproduction of the measured upstream plasma profiles on CMOD requires use of a radially dependent transport model for particle diffusivity. We find that the high density of CMOD discharges requires iteration of the thermal transport diffusivity when the particle transport model is modified. This is not characteristic of simulations of DIII-D data and indicates that convective power flow in CMOD is a larger fraction of the total cross-field power flow in CMOD. Furthermore we find that inclusion of plasma drifts in CMOD has a dramatic difference in the nature of the divertor plasmas. We show that one expects drifts to be more important for a high field device when operated near a plasma  $\beta$  limit. Thus the higher density of a high field device makes the inclusion of plasma drifts essential. This should be a concern for simulations of the ITER device.

CMOD simulations with plasma drifts require use of very small cross-field diffusivities since much of the radial plasma flow arises from the effect of drifts. The use of small diffusivities is problematic for UEDGE since numeric diffusion associated with the differencing scheme becomes larger than that determined from the assumed transport model. The resulting numerical problem has led to CMOD simulations which have spatial oscillations which we do not believe are real. This numeric diffusion has been a recognized problem in all fluid edge plasma codes. Recently a re-formulation of the numerical scheme used for these simulations has been proposed as a solution to this problem. This scheme has been implemented in UEDGE. We have not yet applied the newer version of the code to these CMOD simulations.

Finally we note that all simulations discussed in this memo assume significant pumping by the plasma facing surfaces. Such pumping is not expected for an all metal device such as CMOD. However we seek fully steady state solutions so we would require a density profile which has zero gradient on the inner most surface (no ion current across this surface), and no externally introduced neutrals.

That is we can not allow any particle input to the calculation domain if we eliminate all pumping. This does not seem consistent with the experiment, so we have introduced the wall pumping. This issue should be examined in more detail in future simulations.

## 5 Acknowledgement

This work performed under the auspices of the U.S. Department of Energy by Lawrence Livermore National Laboratory under Contract DE-AC52-07NA27344.

## 6 References

- [1] T. Rognlien, J. Milovich, M. Rensink, and G. Porter, *J. Nucl. Mater.* 196-198 (1992) 347.
- [2] B. LaBombard, J. L. Terry, J. W. Hughes, D. Brunner, J. Payne, M. L. Reinke, Y. Lin, and S. Wukitch, *J. Nucl. Mat.* submitted (2010)
- [3] L. L. Lao, H. S. John, R. D. Stambaugh, A. G. Kellman, and W. Pfeiffer, *Nucl. Fusion* 25 (1985) 1611.
- [4] T. D. Rognlien, G. D. Porter, and D. D. Ryutov, *J. Nucl. Mat.* 266-269 (1999) 654.
- [5] F. Wising, D. A. Knoll, S. I. Krasheninnikov, T. D. Rognlien, and D. J. Sigmar, *Contrib. Plasma Phys.* 35 (1996) 136.
- [6] G. D. Porter, J. A. Boedo, T. N. Carlstrom, R. J. Groebner, M. J. Schaffer, P. C. Stangeby, T. D. Rognlien, M. E. Rensink, and N. S. Wolf, in 28th European Physics Society Conference on Controlled Fusion and Plasma Physics, Madeira, Portugal, 2001.

# APPENDIX G

## *Theory and simulation modeling of the scrape-off layer heat flux width:*

### *Lodestar work in support of the FY2010 US DOE Joint Research Target*

J.R. Myra,<sup>a</sup> D.A. Russell,<sup>a</sup> D.A. D'Ippolito<sup>a</sup>

*in collaboration with*

R. Maingi,<sup>b</sup> J-W. Ahn,<sup>b</sup> R.J. Maqueda,<sup>c</sup> D.P. Lundberg,<sup>c</sup> D.P. Stotler,<sup>c</sup>

S.J. Zweben,<sup>c</sup> J. Boedo,<sup>d</sup> M. Umansky,<sup>e</sup> and the NSTX Team;

B. LaBombard,<sup>f</sup> J.L. Terry,<sup>f</sup> S. J. Zweben,<sup>c</sup> and the C-Mod Team.

*a) Lodestar Research Corporation, b) Oak Ridge National Laboratory, c) Princeton  
Plasma Physics Laboratory, d) Univ. of California at San Diego, e) Lawrence Livermore  
National Laboratory, f) MIT Plasma Science and Fusion Center*

September 2010

---

DOE/ER/54392-61

LRC-10-138

---

**LODESTAR RESEARCH CORPORATION**

*2400 Central Avenue  
Boulder, Colorado 80301*

*Introduction and executive summary* – In support of experimental investigations of the size and scaling of the heat flux width for the FY2010 US DOE Joint Research Target (JRT), Lodestar has carried out simulation modeling to better understand the role of cross-field turbulent heat transport in the scrape-off layer (SOL). These studies were carried out using the Scrape-Off-Layer Turbulence (SOLT) code.<sup>1</sup> The next sub-section describes the physics basis of the SOLT code and how it was used in the present studies. The remaining sub-sections give results from simulations of NSTX and C-Mod discharges and our conclusions.

For NSTX we simulated the scaling of the near-SOL heat flux width,  $\lambda_q$ , with power,  $P$ , and plasma current,  $I_p$ , for several H-mode shots. The simulated  $\lambda_q$  as well as midplane SOL profiles of density and temperature were compared with gas-puff imaging (GPI), probe and midplane-mapped divertor infrared thermography (IRTV) data. It was concluded that the midplane turbulence simulated in SOLT explains some, but not all, of the experimentally observed  $\lambda_q$  scaling. We identified a new convective cell mechanism that determines the SOL width in our simulations of NSTX H-mode discharges. In related theoretical work, we found a transition from a diffuse to a convective SOL heat transport regime at critical values of power and connection length.

For C-Mod, an EDA H-mode shot was simulated. The SOLT code produced a heat flux SOL width of about  $\lambda_q \sim 1$  mm, not far from the experimental result. Most of the edge turbulence was in a single mode with a poloidal wavelength of order 6 cm, which might be related to the quasi-coherent mode.

*The SOLT code* – SOLT is a fluid code that models turbulence in a two-dimensional region perpendicular to the magnetic field  $B$  at the outboard midplane of the torus. SOLT implements classical parallel physics using closure relations<sup>2</sup> for the midplane parallel current and parallel fluxes for collisional regimes ranging from sheath-connected to conduction limited. The SOLT code can describe arbitrarily strong nonlinear plasma dynamics ( $\delta n/n \sim 1$ ), including blob formation, and the physics model supports interchange-type curvature-driven modes, sheath instabilities, and drift waves. SOLT also includes the self-consistent evolution of zonal (i.e., poloidally-averaged) flows and has been used to demonstrate the control of turbulence by sheared flows and

the radial transport of zonal momentum by turbulent Reynolds' stress. For comparison with experimental gas puff imaging (GPI) data,<sup>3</sup> SOLT includes a synthetic GPI diagnostic which has recently been upgraded to simulate both He and D gas puffs.

SOLT has flexible sources for plasma density, temperature, and flows ( $n_e$ ,  $T_e$ ,  $v_y$ ). In the present work, artificial sources for  $n_e$  and  $T_e$  are configured to maintain the experimentally observed profiles in the steep pedestal region inside the separatrix. These artificial sources are set to zero in the SOL, so that the SOL profiles themselves are determined self-consistently by the balance between perpendicular turbulent transport and parallel losses. Using the SOLT model, we are able to assess the role of electrostatic turbulence at the midplane in determining the cross-field transport fluxes and midplane profiles. Midplane turbulence gives rise to fluctuating  $\mathbf{E} \times \mathbf{B}$  convection near the separatrix which can result in both diffusive and convective transport processes.

Previously, SOLT has been used to model blob generation and turbulence in L-mode plasmas on NSTX.<sup>4</sup> Detailed comparisons of simulation and experimental results for the distribution of blob sizes and speeds were made possible by using the simulated and experimental GPI diagnostic. For the FY2010 Joint Research Target (JRT) work, it was necessary to simulate H-mode discharges. The primary difference between H-mode and L-mode simulations in SOLT was the use of an imposed mean sheared flow inside the separatrix in the H-mode case. The radial profile of the poloidal flow was taken to be proportional to the ion diamagnetic drift, with a constant of proportionality  $\tau$ . This imposes an  $E_r$  well inside the separatrix which regulates the turbulence. The value of  $\tau$  was chosen such that the SOLT power flow across the separatrix,  $P_{sep}$ , matched the experimental value. In this way, we were able to achieve a heat-flux-driven boundary condition at the separatrix for our SOL simulation, which gives a first principles calculation of the turbulent transport in the SOL, i.e. without any ad-hoc sources or sinks of particles, momentum or energy.

Simulation power scans were performed, where the imposed flows were varied and the resulting simulated  $P_{sep}$  was determined from

$$P_{sep} = 2\pi R b_{\theta} \int dr q_{\parallel}$$

where  $b_\theta = B_p/B$  and the integral is taken across the entire SOL. The simulation for which  $P_{sep}$  most closely matched the experimental value was employed for comparison.

*Results for NSTX simulations* – Table 1 shows comparisons of the SOLT simulated heat flux width  $\lambda_q$  with NSTX midplane-mapped divertor infra-red thermography (IRTV) footprint data for a power (P) scan and a plasma current ( $I_p$ ) scan. More details of how these comparisons were done are available elsewhere.<sup>5,6</sup> Shots 135009 and 135038 are low power ELM-free H-modes in lithium-walled shots.<sup>7</sup> Shots 128013 and 128797 are higher power shots in the pre-lithium phase of NSTX.<sup>8</sup>

shot	$I_p$ (MA)	P(MW)	$\lambda_{q,NSTX}$ (cm)	$\lambda_{q,SOLT}$ (cm)
135009	0.8	0.8	0.36	0.30
135038	0.8	1.3	0.50	0.41
128013	0.8	5.8	1.73	0.76
128797	1.2	6.1	0.56	0.58

Table 1. Scaling of the SOL heat flux width for the power and current scans in NSTX. The last column is the midplane heat flux width from the SOLT simulations, and is to be compared with the experimental value in column 3. All widths are field-line-mapped to the outboard midplane.

From Table 1, we conclude that midplane turbulence simulated in SOLT explains some, but not all, of the experimentally observed  $\lambda_q$  scaling. Absolute agreement is within modeling uncertainties (factor of 2). Both simulation and experiment (shots 135009 and 135038) show a weak positive scaling of  $\lambda_q$  with power, but the scaling with  $I_p$  (shots 128013 and 128797) appears to be different, with the most significant discrepancy at the lowest  $I_p$ .

In SOLT, the parallel heat flux width is determined by the midplane turbulence. To check the role of this mechanism against experiment, we compared SOLT profiles of density, temperature and fluctuations directly against midplane NSTX data. This provides

a more direct check on the role of midplane turbulence than comparison of the midplane-mapped heat flux width which is measured at the divertor plate, and is therefore potentially subject to broadening by other mechanisms.

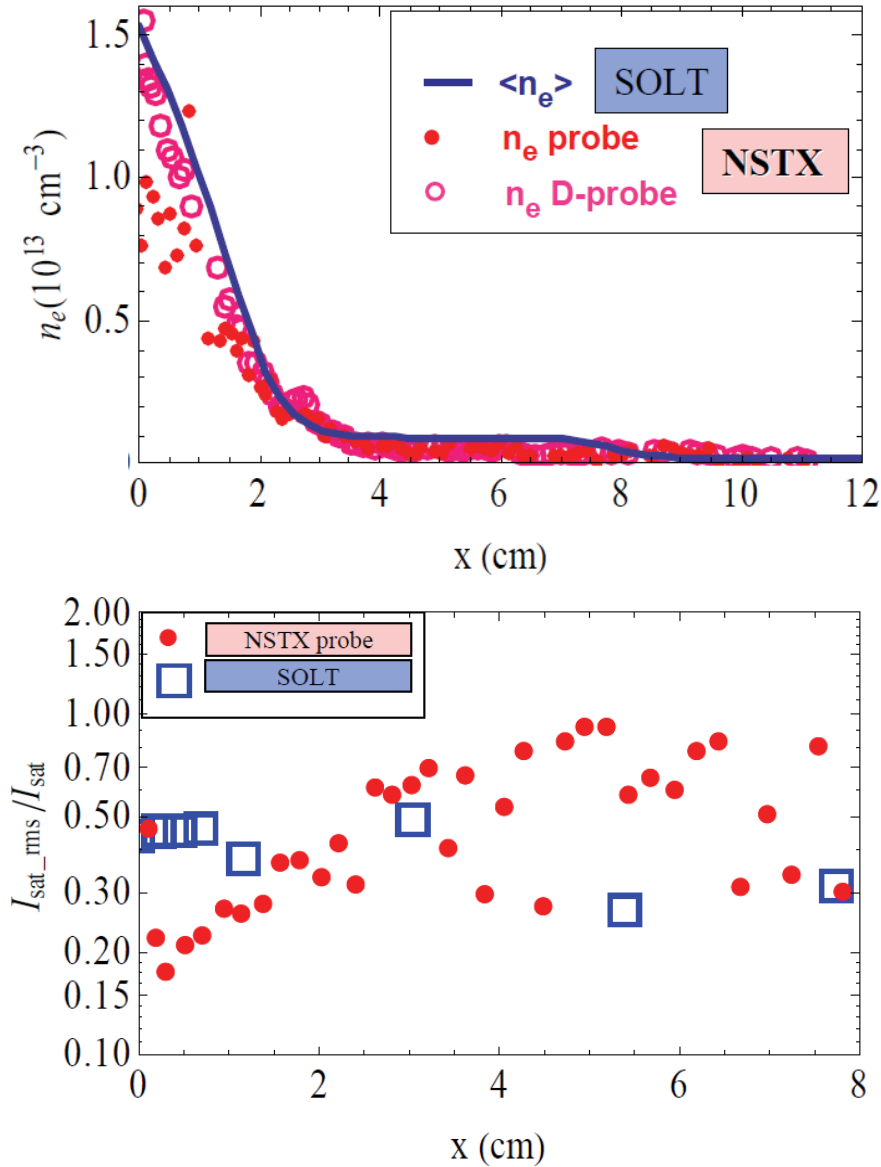


Fig. 1. (upper) Comparison of SOLT density profile with NSTX probe data; (lower) comparison of SOLT and NSTX probe  $I_{\text{sat}}$  fluctuation levels. [Fig. from Ref. 5]

For the low power shots, midplane reciprocating probe data was available for this comparison. Fig. 1 illustrates the comparison of SOLT and NSTX probe data for the average density profile and saturation current fluctuations, for shot 135009. The level of agreement is well within modeling uncertainties. Similar results were obtained for 135038. This validates the midplane turbulence calculations by SOLT, and together with the agreement in Table 1 for these shots (135009 and 135038) suggests that midplane turbulence is indeed responsible for the observed heat flux width seen at the divertor.

A somewhat different conclusion was reached for the  $I_p$  scan shots (128013 and 128797). Since probe data was not available for these high power shots, we compared SOLT fluctuation levels from synthetic GPI, with midplane NSTX GPI data. This comparison (not shown here, see Ref. 5) showed good agreement. Furthermore, the NSTX data, like the simulations, showed little difference in fluctuation levels with  $I_p$ . Consequently, it seems that the strong  $I_p$  scaling of the heat flux width seen in the NSTX data (Table 1) cannot be explained by midplane turbulence alone. Possible additional mechanisms include divertor leg instabilities,<sup>9</sup> ELM and MHD effects which could cause strike point motion,<sup>10</sup> and X-point loss of ions due to drift-orbit effects<sup>11</sup> which might be expected to be a particularly strong effect at low  $I_p$ . Caveats in our analysis include possible differences in downstream sheath conditions for the two shots and MHD activity not included in these electrostatic simulations.

An interesting spin-off from the modeling work was the identification of a new convective cell mechanism that appears to determine the SOL width in our simulations of NSTX H-mode discharges. This mechanism is the presence of intermittent separatrix-spanning convective cells. Figure 2 shows a snapshot of the turbulent density field in color shades, on top of which is superimposed some contours of electrostatic potential, giving the stream lines for the  $\mathbf{E} \times \mathbf{B}$  flow. The potential shows an up-down flow pattern that is sheared from left to right. The flow pattern has embedded within it closed vortex structures (island convective cells) that can transport plasma radially. In the figure, finger-like structures (e.g. indicated by the arrow) have been ejected from the main plasma, but in the presence of the strong H-mode sheared flow, these structures cannot penetrate far radially into the SOL. Rather they are sheared downwards by the flow.

Intermittently, the extra plasma gets carried across the LCS by the convective cells. The resulting cross-field motion competes with parallel flow to establish the SOL width.

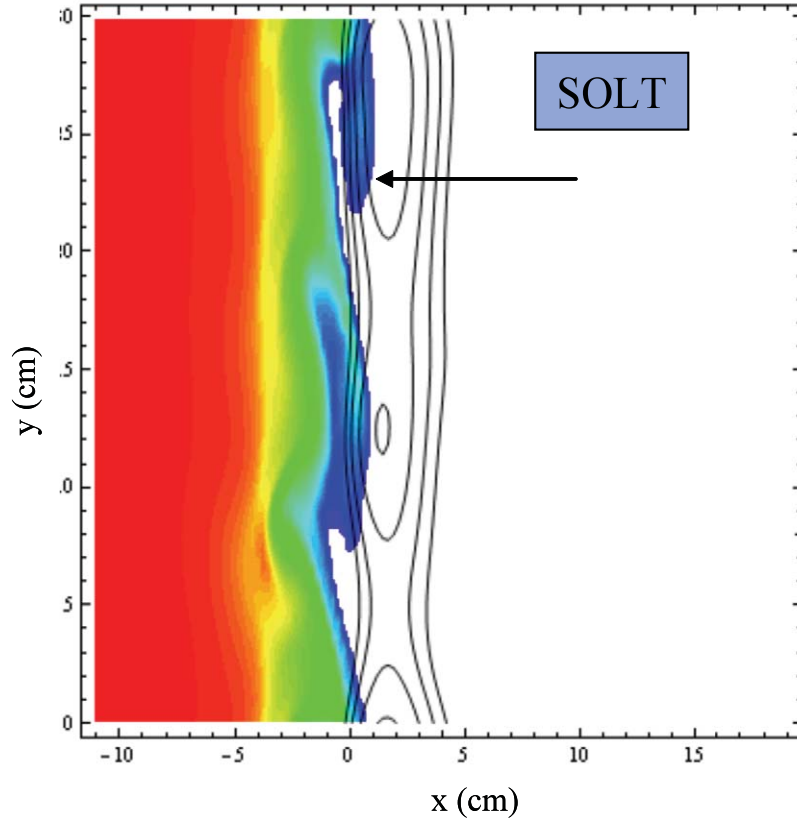


Fig. 2. Turbulent fields of density (log palette, truncated to white for  $n/n_{ped} < 0.3$ ), and potential (contours). The arrow points to a downward-sheared finger structure

Other, ongoing theoretical scaling studies, were stimulated by the JRT work. One important example is that for certain parameters, the SOLT results were found to transition from a diffusive dominated near-SOL structure to one that is convection dominated, and much broader.<sup>6</sup> In the latter case, some of the intermittent separatrix-spanning convective cells start to form structures which break free as blobs. Qualitatively similar trapping and release of blobs is evident in the NSTX GPI data.

*Results for C-Mod simulations* – The SOLT code was employed<sup>12</sup> to simulate an EDA H-mode shot<sup>13</sup> that was part of the JRT campaign, using a similar procedure to that employed for NSTX. Results of a SOLT code power ( $\tau$ ) scan for Alcator C-Mod are shown in Fig. 3. For this time slice, the experimental power is 1.79 MW and the observed midplane-mapped heat flux e-folding width is  $\lambda_{q,\text{exp}} = 1.3$  mm. Comparing with the e-folding widths in Fig. 3, we find that absolute agreement is well within factor-of-two modeling uncertainties. The measured integral heat flux width (Loarte width)<sup>14</sup> mapped to the outboard midplane for this same case is  $\lambda_{q,\text{int}} = 3.7$  mm due to the presence of a tail in the heat flux extending into the far SOL, while the SOLT  $\lambda_{q,\text{int}} = 1.13$  because the tail is not present. This point will require further study. Nevertheless, it is satisfying that the same SOLT code physics model provides rough agreement in the near-SOL  $\lambda_q$  for both NSTX and C-Mod cases, where outboard-midplane B is different by more than an order of magnitude. The scaling of  $\lambda_q$  with power in C-Mod using another time slice is presently under study.

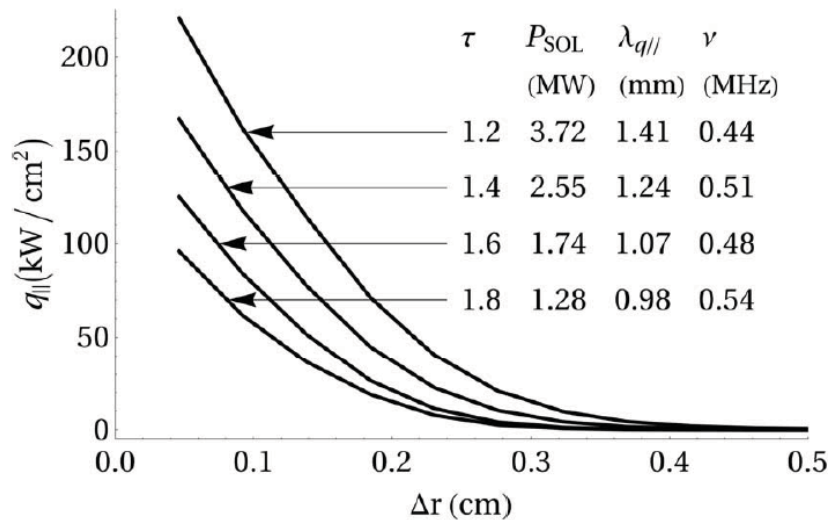


Fig. 3. Heat flux width variation in a SOLT power ( $\tau$ ) scan for a C-Mod EDA H-mode. The dominant mode frequency  $\nu$  is also tabulated.

An intriguing result from the SOLT simulations of the C-Mod EDA is the appearance of a mode that has at least some qualitative similarities to the quasi-coherent

(QC) mode that is observed experimentally in the EDA regime.<sup>15,16</sup> The frequency spectrum of density fluctuations from SOLT is shown in Fig. 4. A “quasi-coherent” feature at 480 kHz is evident for this case. (See the legend in Fig. 3 for the variation of the frequency during a SOLT power scan.) This feature results from density fluctuations at a wavelength of about 6 cm which originate in the strong gradient region just inside the separatrix, and are convected and Doppler shifted by the  $\mathbf{E} \times \mathbf{B}$  flows. The QC mode frequency in the lab frame is affected by the radial electric field and toroidal rotation. Although SOLT does not provide a first principles model of these effects, it is encouraging that simulated frequencies are in the range of several hundred kHz, which is characteristic of QC mode frequencies seen experimentally. In SOLT, the “QC” mode is responsible for cross-field transport fluxes, and is a key player in setting the SOL width. Finally, the inset in Fig. 4 shows the same spectrum on a log-log scale. The broad features (low-frequency plateau and algebraic high-frequency decaying tail) are typical of both simulation and experimental data for intermittent edge turbulence.

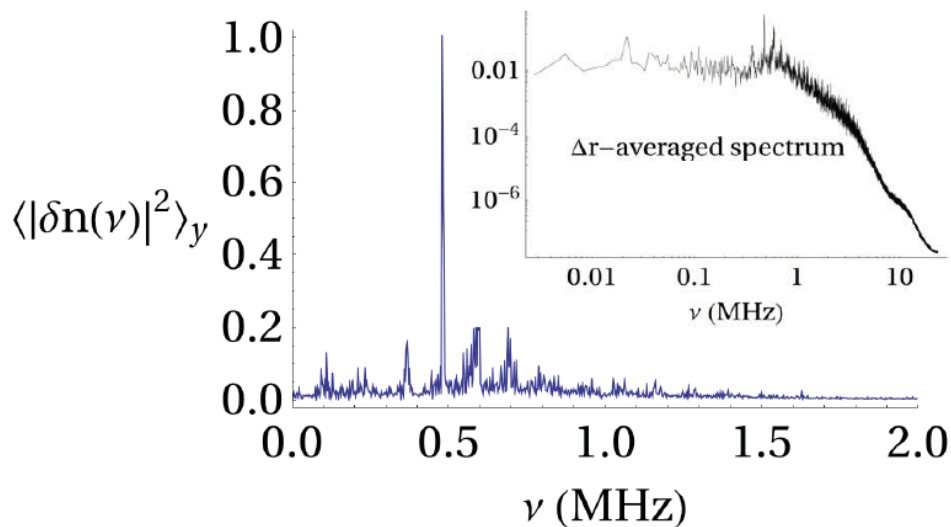


Fig. 4. Density fluctuation spectrum for the SOLT EDA simulation at  $\tau = 1.6$

*Conclusion* – Modeling of JRT-relevant discharges in NSTX and C-Mod using the SOLT turbulence code have made some important qualitative and quantitative connections of theory with heat flux experimental data. Simulated and experimentally

measured heat flux widths were found to agree for all cases investigated within factor-of-two modeling uncertainties. Modeled and NSTX experimental scaling trends were similar, however scaling with plasma current was stronger in the experiment than in the simulations, suggesting the importance of additional broadening mechanisms beyond midplane region turbulence. Physics mechanisms which set the SOL width were elucidated, such as the role of intermittent separatrix-spanning convective cells, and quasi-coherent modes. The experimental JRT data both validates some aspects of the modeling and raises additional challenges for theory.

*Acknowledgments* – This work was supported by the US DOE under grants DE-FG02-02ER54678 and DE-FG02-97ER54392, and by PPPL under subcontract S009625-F; however, such support does not constitute an endorsement of the views expressed herein.

---

### **References**

- 1 D. A. Russell, J. R. Myra and D. A. D'Ippolito, Phys. Plasmas **16**, 122304 (2009); and refs. therein.
- 2 S. I. Krasheninnikov, D. A. D'Ippolito, and J. R. Myra, J. Plasma Physics **74**, 679 (2008).
- 3 S.J. Zweben, R.J. Maqueda, D.P. Stotler et al, Nucl. Fus. **44**, 134 (2004).
- 4 D. A. Russell, J. R. Myra, D. A. D'Ippolito, T. L. Munsat, Y. Sechrest, R. J. Maqueda, D. P. Stotler, S. J. Zweben and the NSTX Team, Lodestar Report # LRC-10-135, [www.lodestar.com/LRCreports/](http://www.lodestar.com/LRCreports/), submitted to Phys. Plasmas.
- 5 J.R. Myra, D.A. Russell, D.A. D'Ippolito, J-W. Ahn, R. Maingi, R.J. Maqueda, D.P. Lundberg, D.P. Stotler, S.J. Zweben, J. Boedo, M. Umansky and the NSTX team, Lodestar Report # LRC-10-136, [www.lodestar.com/LRCreports/](http://www.lodestar.com/LRCreports/), submitted to Phys. Plasmas.
- 6 J.R. Myra, D.A. Russell, D.A. D'Ippolito, J.-W. Ahn, R. Maingi, R.J. Maqueda, D.P. Lundberg, D.P. Stotler, S.J. Zweben, J. Boedo, M. Umansky and the NSTX team, Lodestar Report #LRC-09-132, [www.lodestar.com/LRCreports/](http://www.lodestar.com/LRCreports/), to be published in J. Nucl. Mater.
- 7 J. W. Ahn (private communication, 2010); and manuscript in preparation.
- 8 T. K. Gray, R. Maingi, J. E. Surany, V. A. Soukhanovskii, J-W. Ahn and A. G. McLean, presented at the 2010 PSI meeting; and to be published in J. Nucl. Mater.; R. Maingi, C.E. Bush, R. Kaita, H.W. Kugel, A.L. Roquemore, S.F. Paul, V.A. Soukhanovskii, and NSTX Team, J. Nucl. Mater **363-365**, 196 (2007).
- 9 D.D. Ryutov and R.H. Cohen, Contrib. Plasma Phys. **48**, 48 (2008).
- 10 E. R. Solano et al., J. Nucl. Mater. **337-339** 747 (2005).
- 11 S. Ku, H. Baek, and C. S. Chang, Phys. Plasmas **11**, 5626 (2004).
- 12 D.A. Russell et al., in progress (2010).

- 
- 13 B. LaBombard, J.L. Terry, J.W.Hughes, et al., to be published in J. Nucl. Mater.;  
B. LaBombard, et al., *Boundary Layer Heat Transport Experiments in Alcator C-  
Mod in Support of the FY2010 US DoE Joint Research Target*, PSFC/RR-10-14
  - 14 A. Loarte, et al., J. Nucl. Mater. **266-269**, 587 (1999).
  - 15 M. Greenwald et al., Phys. Plasmas **6**, 1943 (1999).
  - 16 J.L. Terry et al., Nucl. Fusion **45**, 1321 (2005).

# APPENDIX H

## *XGC-0 modeling of the divertor heat flux*

AY. Pankin

*CPES work in support of the  
FY2010 US DOE Joint Research Target*

**Contribution of the CPES project to the Joint Research Target:  
XGC0 modeling of divertor heat load fluxes in  
the Alcator C-Mod, DIII-D and NSTX tokamaks**

A.Y. Pankin<sup>1</sup>, G.Y. Park<sup>2</sup>, J. Cummings<sup>3</sup>, C.S. Chang<sup>2</sup>, D. Brunner<sup>4</sup>,  
R.J. Groebner<sup>5</sup>, J.W. Hughes<sup>4</sup>, B. LaBombard<sup>4</sup>, R. Maingi<sup>6</sup>, and J.L. Terry<sup>4</sup>

<sup>1</sup>Lehigh University, Bethlehem, PA

<sup>2</sup>New York University, New York, NY

<sup>3</sup>Caltech, Pasadena, CA

<sup>4</sup>MIT Plasma Science and Fusion Center, Cambridge, MA

<sup>5</sup>General Atomics, San Diego, CA

<sup>6</sup>ORNL, Oak Ridge, TN

E-mail: [pankin@lehigh.edu](mailto:pankin@lehigh.edu)

The XGC0 kinetic guiding-center code [1] is used in this study to investigate the basic kinetic neoclassical behavior of the heat and particle fluxes on divertor plates in tokamaks with a realistic divertor geometry. The neoclassical divertor heat load fluxes are computed with the XGC0 code and a relation for the dependence of the divertor heat load width on the plasma current is derived. In the development of this relationship, effects of neutral collisions and anomalous transport are taken into account. Changes in the neoclassical divertor heat load fluxes associated with the introduction of the neutral collision and anomalous transport effects are described. For the anomalous transport, a radial random-walk is superposed in the Lagrangian neoclassical particle motion.

Understanding physical effects that contribute to divertor heat load fluxes is important for experiment planning, design of future tokamaks, and development of new models for the SOL region. In this study, the neoclassical effects and effects related to neutral collisions and anomalous transport are investigated. A series of four DIII-D discharges that represent plasma current scan [2] is analyzed in this study. In this series of DIII-D discharges, the total plasma current is varied from 0.51 to 1.50 MA with an approximately fixed toroidal magnetic field ( $B_T \approx 2.1$  T), plasma shape ( $\delta \approx 0.55$ ), and normalized toroidal beta ( $\beta_n \approx 2.1-2.4$ ). The discharges differ by total plasma current, auxiliary heating power, and plasma densities that are given in Table 1 and Fig. 1 correspondingly.

Discharge #	EFIT time, msec	Plasma current, MA	Auxiliary heating power, MW
132016	3023	1.50	8.12
132014	3023	1.17	7.36
132017	2998	0.85	8.50
132018	1948	0.51	7.10

Table 1. DIII-D discharges analyzed in this study and their parameters.

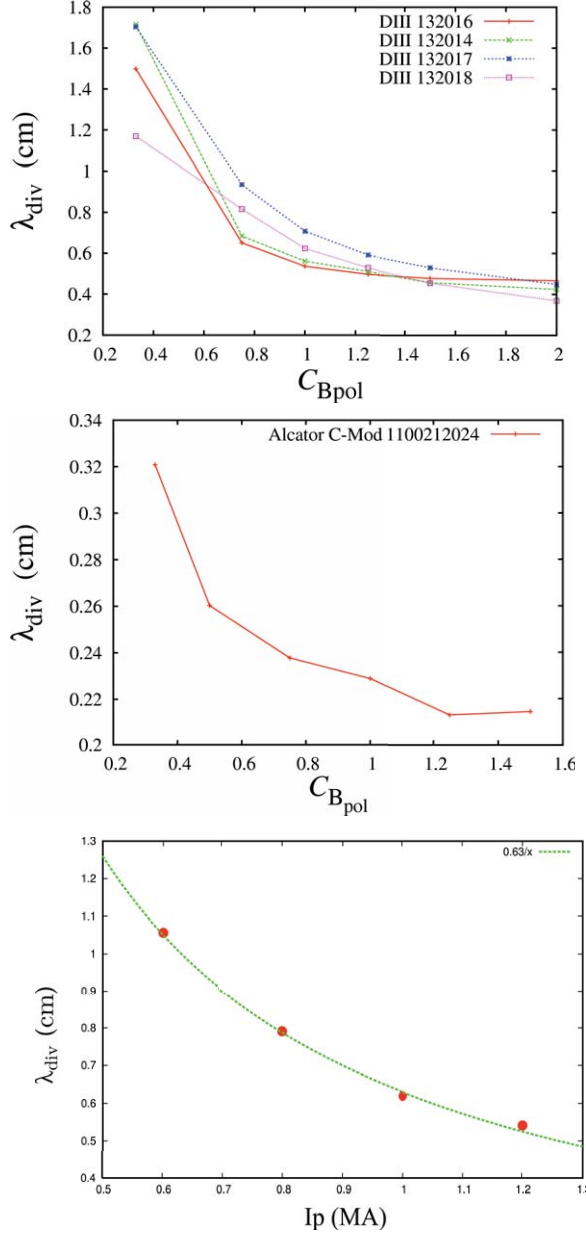


Fig. 2: The divertor heat load widths for four DIII-D discharges (top panel), one Alcator C-Mod discharge (middle panel), and one NSTX discharge (bottom panel) as functions of poloidal magnetic field scaling factor and plasma current (for NSTX discharge).

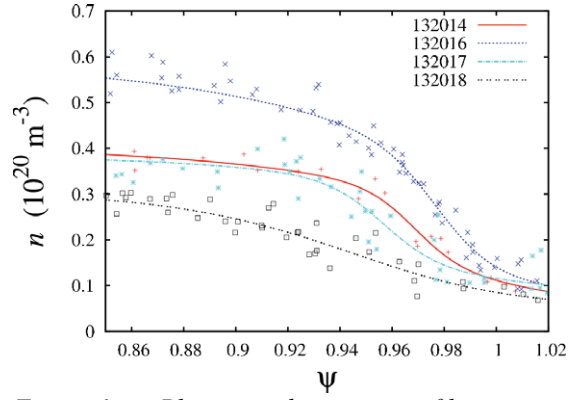


Fig. 1: Plasma density profiles in the DIII-D discharges that represent plasma current scan. The experimental data are shown as dots and fitted profiles are shown as solid and dashed curves.

In addition, one Alcator C-Mod discharge 1100212024 that was a part of Alcator C-Mod/DIII-D similarity campaign and one NSTX discharge 128013 are analyzed. The divertor heat load widths,  $\lambda_{div} \equiv \int q_{\parallel} d\rho / q_{\parallel}^{max}$ , as functions of the poloidal magnetic field amplification factor  $C_{Bp}$  are shown on Fig. 2. This scaling factor is an internal numerical multiplier introduced in the XGC0 code in order to alter the initial equilibrium by scaling the poloidal flux. If the toroidal flux is not modified,  $I_{pl} \propto B_p \propto \partial\psi/\partial\rho$ , where  $\psi$  is the normalized poloidal flux. Thus, the amplification factor  $C_{Bp}$  can be also considered as a scaling factor for the total plasma current  $I_{pl}$ .

The neoclassical divertor heat load width in the Alcator C-Mod discharge is found to be approximately 2.3 mm, which is about 40% below the experimentally observed value of 3.13 mm in the base case ( $C_{Bp}=1$ ) [3]. As it will be shown below, the anomalous effects

typically increase the divertor heat load width bringing the simulation results and experimental data closer to each other. It has been found that the neoclassical heat load width for all four DIII-D discharges follows approximately the  $1/I_p$  dependence.

There is neither anomalous transport nor neutral effects included in these simulations. The difference in the slopes of the predicted divertor heat load widths vs  $C_{Bp}$  for different DIII-D discharges might be attributed to different collisionality in these discharges. The differences in slopes are especially noticeable if two set of discharges with lower (DIII-D discharges 132017 and 132018) and higher plasma densities (DIII-D discharges 132014 and 132016) are compared. This computational result on the effect of collisionality on divertor heat fluxes still needs to be confirmed in further computational and analytical analysis. In the meantime, there is no doubt that the neoclassical divertor heat load width is decreasing with increasing

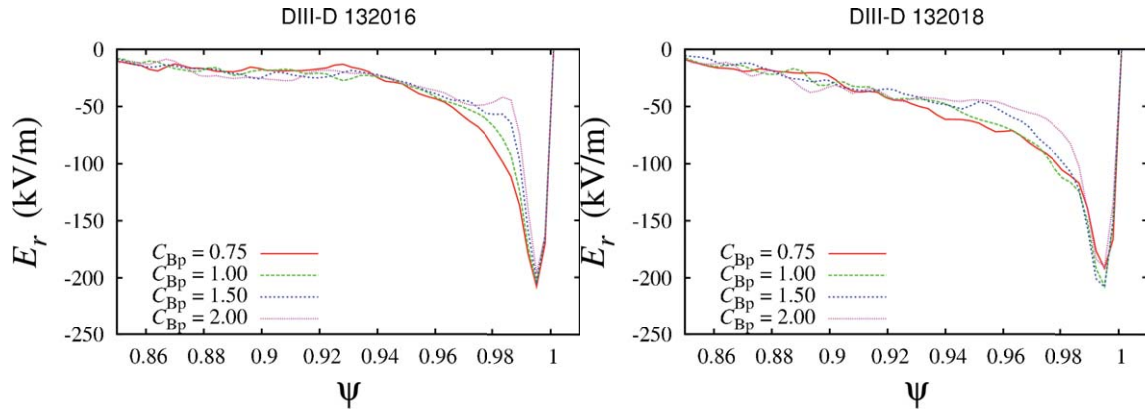


Fig. 3: The radial electric field profiles in low and high plasma current DIII-D discharges 132016 and 132018 for different values of plasma current scaling factor  $C_{Bp}$ .

plasma current for all DIII-D discharges studied in this research.

Correlation between the divertor heat load width and the width of radial electric field profiles in the pedestal region is found. The width of radial electric field profiles is reduced with increased plasma current. Fig. 3 shows the radial electric field profiles for low and high plasma current DIII-D discharges 132017 and 132018. The width of radial electric field profiles in the H-mode pedestal region reduces when the plasma current scaling factor  $C_{Bp}$  is increased.

Simulation results that are shown on Fig. 4 demonstrate the effects of neutral collisions and anomalous transport. The dependence of the divertor heat load width is weakly affected by neutral collisions, but it can be completely modified when the anomalous transport is introduced and is applied uniformly for all poloidal angles. The effective diffusivities that are used here are derived in the form so that when they are combined with the neoclassical transport computed with XGC0 the experimental profiles are reproduced (see Figs. 5 and 6). There are three regions of constant diffusivities that are separated by two narrow transitional regions that use *tanh*-fit. The levels of anomalous transport in all three regions, locations of transitional regions and their widths are adjustable parameters. The profiles for the particle diffusivities as well as for the electron and ion thermal diffusivities are independent from each other. These profiles are adjusted to find a steady state solution that

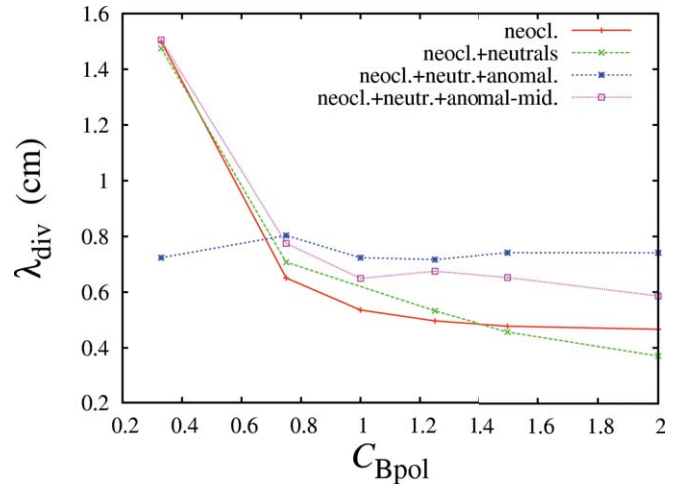


Fig. 4: Effects of neutral collisions and anomalous transport on the divertor heat load width scaling in the XGC0 simulations of the DIII-D discharge 132016. The red curve shows the neoclassical scaling that does not include the effects of neutral collision and anomalous transport. The green curve shows the effect of neutral collisions. The anomalous transport that is applied uniformly for all poloidal angles in used in the simulations resulted in the blue curve. The purple curve shows the divertor heat load width scaling when the anomalous transport is applied within  $45^\circ$  from the midplane.

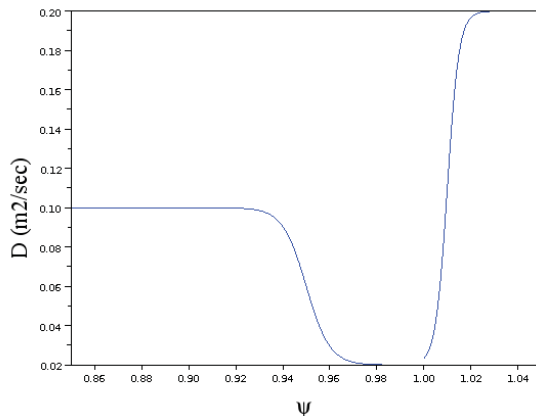


Fig. 5: Typical particle diffusivity profile that is used in the modeling with the XGC0 code.

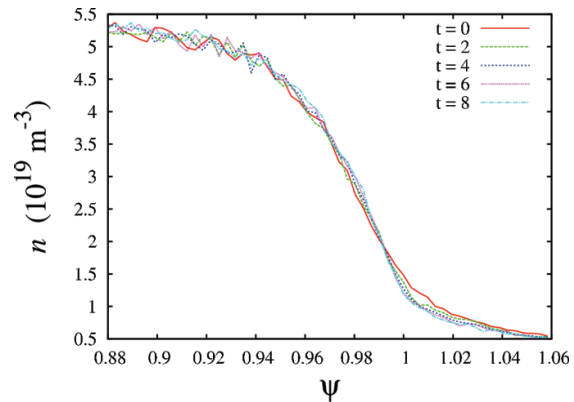


Fig. 6: Simulation results of the plasma density profile in the DIII-D discharge 132016 for the first eight ion transit periods. The experimental plasma density profile is shown in red.

reproduces the experimental profiles. The anomalous diffusivity profiles are selected so that the resulting profiles remains close to the experimental profiles at least up to eight ion transit

periods. It has been found that particle and thermal pinches play an important part in the pedestal regions of all discharges analyzed in this study.

Changes to the divertor heat load width scaling related to the ballooning nature of resistive-ballooning modes, that are likely to be major players in the region near the separatrix, are shown as purple curve on Fig. 4. In these simulations, the anomalous transport is applied in the region within  $45^\circ$  from the midplane. The neoclassical dependence of the divertor heat load width on the total plasma current is preserved for the high-density DIII-D discharge 132016 and almost vanished for the low-density DIII-D discharge 132018 (not shown on Fig. 4). The dependence of divertor heat load width on the current density was weakest for the DIII-D discharge 132018 among discharges studied in this research (see Fig. 1). The

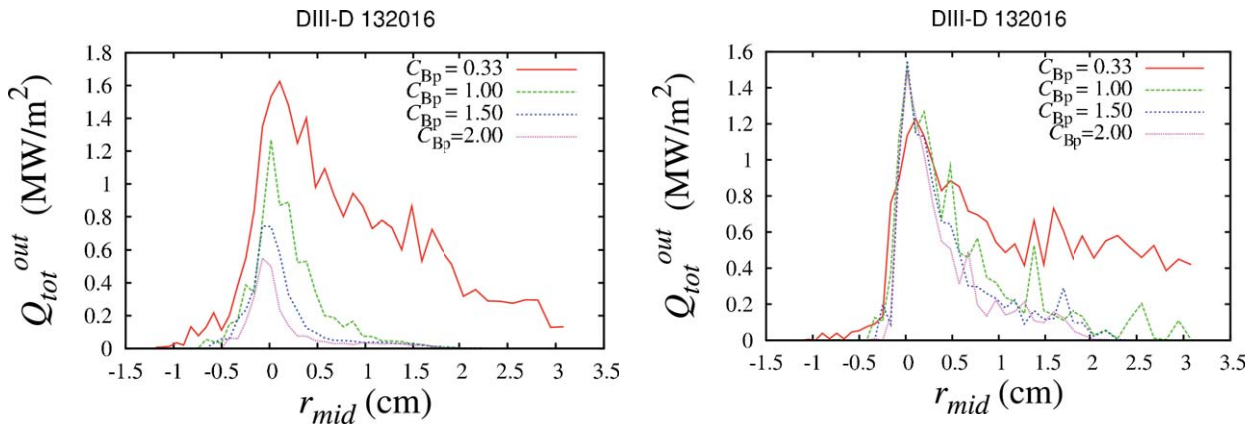


Fig. 7. The heat fluxes on the divertor plates in the DIII-D discharge 132016 for different values of the plasma current scaling factor  $C_{Bp}$ . The left panel shows the heat fluxes computed without the anomalous transport. The right panel shows the anomalous fluxes when the anomalous transport is applied within  $45^\circ$  from the midplane.

introduction of anomalous transport effects typically widens the divertor heat load width. This observation becomes evident, when red and purple plots on Fig. 4 are compared. The heat fluxes on the divertor plates with and without anomalous transport are compared for the DIII-D discharge 132016 on Fig. 7. The peak values of heat fluxes typically increase when the anomalous effects are included.

The neoclassical scaling of divertor heat load width with the plasma in DIII-D and Alcator C-Mod discharges is studied in this report. It has been found that the divertor heat load width is broader for lower plasma currents for all discharges simulated in this work. The DIII-D and NSTX discharges have similar scaling for the divertor heat load width with the plasma current. The Alcator C-Mod discharge has weaker scaling of the width of the divertor heat load with the plasma current relative to the four DIII-D discharges that were analyzed in this study. This trend reproduces the experimental observations [3, 4]. The differences in neoclassical scaling of divertor heat load width might be attributed to difference in

collisionality in Alcator C-Mod and DIII-D discharges. This hypothesis will be verified in future studies with the XGC0 code. The effect of neutral collisions does not significantly modify this dependence, while the inclusion of anomalous transport typically widens the divertor heat load width and enhances the heat load fluxes on the divertor.

**References:**

- [1] C.S. CHANG *et al.*, Phys. Plasmas **11** (2004) 2649.
- [2] R. GROEBNER *et al.*, Nucl. Fusion **49** (2009) 085037.
- [3] B. LABOMBARD *et al.*, J. Nucl. Materials (in press).
- [4] C.J. LASNIER *et al.*, Nucl. Fusion **38** (1998) 1225; D.N. HILL *et al.*, J. Nucl. Materials **196-198** (1992) 204; C.J. LASNIER *et al.*, Proc. of 36th EPS Conference (Sofia, Bulgaria, 2009).

---

<sup>§</sup> This work supported by the U.S. Department of Energy under DE-SC0000692, DE-FC02-08ER54985, DE-FG02-06ER54845, DE-FG02-92ER54141, DE-FG03-98ER54461, DE-FG02-94ER54084, DE-FC02-04ER54698, DE-FC02-99ER54512.